Insights into the mechanism of electrocatalytic CO2 reduction and concomitant catalyst degradation pathways

Raaijman, S.J.

Citation

Raaijman, S. J. (2022, January 19). *Insights into the mechanism of electrocatalytic CO2 reduction and concomitant catalyst degradation pathways*. Retrieved from https://hdl.handle.net/1887/3250500

Insights into the mechanism of electrocatalytic CO_2 reduction and concomitant catalyst degradation pathways

Proefschrift

ter verkrijging van
de graad van doctor aan de Universiteit Leiden,
op gezag van de rector magnificus prof.dr.ir. H. Bijl,
voorzitter van het college voor promoties,
ter verdedigen op 19 januari, 2022
klokke 10:00 uur

door

Stefan Johannes Raaijman

Dit proefschrift is goedgekeurd door de

promotor: prof.dr. M.T.M. Koper
copromotor: prof.dr. G. Mul

Overige commissieleden:

Prof.dr. H.S. Overkleeft,	voorzitter
Prof.dr. S.A. Bonnet,	secretaris
Dr. R.V. Mom	
Dr. B.S. Yeo,	National University of Singapore
Prof.dr. B. Roldán Cuenya,	Fritz Haber Institute

Financial support was provided by the Dutch Research Council (NWO), the Netherlands Organisation for applied scientific research (TNO) and Shell Global Solutions B.V.

ISBN 978-94-6423-593-7

Contents

1

Introduction

The purpose of this chapter is to introduce key concepts related to how- and why the research in this thesis was conducted, linking individual chapters together. As for 'why', the broader purpose of this work is to take (renewable) electrical energy, carbon dioxide and water as the inputs to generate products of higher value as the output (a process colloquially referred to as the CO_2 reduction reaction, CO2RR).[1] We specifically focus on investigating products consisting of multiple carbon atoms (C2+ products) as they are in high demand and thus of increased value.[2–4] The problem is that CO2RR to C2+ products is not a reaction that is easy to do with currently existing electrocatalysts[5], generally resulting in multiple products forming simultaneously[6, 7] and/or low specific activities for products of interest[6, 8], high energy losses[9–11] and decreasing reaction performance with time.[6, 12, 13] In other words: with the current state of the technology we have many unwanted byproducts, high electricity costs, and need a lot of catalyst materials together with theoretically requiring frequent servicing of such systems.

Therefore, we investigate in this thesis i) how we can perform the act of creating carbon-carbon bonds (believed to be the limiting step in generating C2+ products[14, 15]) to search for methods to make only the products of interest without large energy losses and ii) what is the role of a particular degradation mechanism (called cathodic corrosion[16]) in catalyst deactivation during CO2RR, in an attempt to better understand and possibly address the time-dependent performance issues. The main techniques we used for conducting these studies involved studying system response (e.g., current, products) when varying the reaction conditions (e.g., pressure, potential, electrolyte conditions), voltammetric surface titration methods for determining (changes in) the catalyst nature, and various surface imaging methods to visualize nano-/mesoscale catalyst morphologies. By combining data acquired via these different techniques together with reported literature results, we were able to obtain important new insights regarding both the mechanism of CO_2 reduction and the role of cathodic corrosion as a degradation mechanism in changes in catalyst performance during CO_2 reduction.

At this point, I will take the opportunity to manage reader expectations regarding this chapter.

For my scientific readership:
It is likely you are of the opinion that perhaps this introduction thus far is a little too concise and too superficial. This was done intentionally. Please find yourself better informed by reading the introductions associated with each individual chapter, and possibly the accompanying experimental sections to satiate your intellectual curiosity.

For those of you who are not trained to be scientists:
Probably this brief 'pre-introduction' was quite unlike what you are used to, possibly somewhat intimidating even, especially when considering that it is written in English. Therefore, for the rest of this chapter we forego using scientific jargon and use instead everyday concepts to explain the contents of this thesis. Therefore, the remainder of the introduction is written such that it should contain sufficient background information to at least get a grasp of the contents of this thesis even though the individual chapters are not written with a general audience in mind.

1.1. Outline introduction

To make the rest of the introduction easier to follow (and less scary), science-related words are kept to a minimum, and important concepts are explained when and where they occur in the text. To accomplish this, let me start with explaining the title: *"Insights into the mechanism of electrocatalytic CO_2 reduction and concomitant catalyst degradation pathways"*. The central part, 'electrocatalytic CO_2 reduction', represents a total of four concepts that form the foundation for the chapters in this thesis, and mean the following.

- To start, we have the term 'CO_2', which is the chemical notation of carbon dioxide, with C representing carbon, di meaning 2 and O representing oxygen (somewhat confusingly called 'oxide' instead of oxygen in this instance). Giving us: one carbon and two oxygen, C & O & 2.
- Secondly, we have the word 'electrocatalytic', which is a combination of 'electro' as in electricity and/or electrochemistry, and 'catalytic' as in something involving a catalyst. Here, electrochemistry is a subdivision within the field of chemistry and can be defined as *"[...] chemical phenomena associated with charge separation, [which] often [...] leads to charge transfer, which can occur homogeneously in solution, or heterogeneously on electrode surfaces."*[17] Or simply the combination of electricity ('electro', charge) and chemistry.
- The third concept comes from the second half of the word 'electrocatalytic', namely 'catalytic', which refers to the use of a catalyst. A catalyst, in turn, is defined as: *"... [A] substance that accelerates the attainment of thermodynamic equilibrium without itself being consumed in the process. It does this by providing an alternative mechanism or pathway for the reaction, with lower*

activation energy. [...] It does not change the conditions of equilibrium in a reaction; it changes only the speed of getting there."[18] Simplified, a catalyst is any material that can improve the 'performance' of a reaction between substances while not being used up in the process. In this instance, performance can mean things like: to make the reaction go faster, or to change the (types of) products that form, or to decrease the amount of energy that is consumed. However, although a catalyst can improve reaction performance (specifically, by changing the path via which reactants are converted into products, discussed later), it is not capable of breaking the laws of nature: a certain minimum of energy is always associated with any reaction.

- The last concept is 'reduction', which simply indicates the direction in which electricity flows, and (in the case of CO_2 reduction) means that we start combining hydrogen atoms (chemical notation: H) and CO_2 to make different products.

Therefore, the key phrase 'electrocatalytic CO_2 reduction' means that we force electricity to go through a catalyst that then influences the reaction in such a way that it becomes easier to combine hydrogen atoms and carbon dioxide, resulting into the formation of products. As for why we are interested in making products out of CO_2, it is a consequence of the fact that in the majority of cases in our everyday life we actually do the opposite: produce it.[19] For example; when we breathe and convert sugars into energy, when we burn coal to generate electricity or heat, when we burn gasoline to propel automotive vehicles, or when we poor concrete during construction work. This, in turn, has resulted in steadily increasing levels of carbon dioxide in the atmosphere over the past decades, which is impacting our environment. And research indicates that it would be preferable to reduce the overall quantity of carbon dioxide we emit, possibly going so far as to have net-negative levels of 'emission' (to mean more CO_2 exiting the atmosphere than being introduced).[20] There exists only two ways of doing this. Firstly, we can decrease those activities which produce carbon dioxide as a product. Or, secondly, we can prevent the CO_2 that is being produced from becoming an integral part of the atmosphere by making it 'inactive' (which we can do either before enters the atmosphere, or after we remove it from the atmosphere). Inactivating carbon dioxide can be as simple as 'storing away' (say by putting it in a bottle, or in an enormous underground cave). Or, it can be done by chemically converting it into something else, which is what we mean by CO_2 reduction and what we investigate in this work. This latter option makes sense from the following point of view: carbon dioxide is cheap because it is unwanted, and, therefore, makes for a good reactant for adding carbon functionality to products – in theory.

It is at this point, having explained the meaning of the key phrase, that the research described in this thesis splits into two parts. There is the first part related to obtaining 'insights into the mechanism of electrocatalytic CO_2 reduction' as stated in the title, which is regarding how exactly a catalyst is able to help with converting carbon dioxide into products more easily – where we focus specifically on C2+ products. And there is the second part, 'concomitant catalyst degradation pathways', which is about why catalysts keep breaking down while they are making products out of CO_2.

1.2. The mechanism of CO_2 reduction to multiple-carbon products

For the first topic (how exactly does a catalyst help convert CO_2 into C2+ products), some additional information is required regarding what is already known about catalysts and how they are able to improve reaction performance. As we saw previously, a catalyst is a material that is capable of changing the route between the starting point (reactants) and the destination (products). In chemistry, this is called the reaction mechanism. You can think of the concept as follows. Imagine you have a map, with your hometown and various different cities located in different places on the map. Home represents the reactants (or, the starting point), while the different cities are possible products (destinations). Between the cities, we have roads which are the paths through which we can make products (the mechanism). Effectively what a catalyst does, is to change which roads are available between cities, together with the quality of those roads. Depending on the catalyst, there is may not be a road available to a certain city (say because of a broken bridge), and thus you will not be able to reach that city: you will not make this product. And maybe we have roads to two different cities, but one road is made out of cobblestones and is very long, having many twists and turns. The other road, however, is like the German autobahn: beautifully flat and straight. The German highway is considerably better, and thus it will be quicker to reach the city it connects to, meaning it is easier to make this product and therefore the catalyst will produce more of it.

In our comparison, the time it takes to reach a city (which depends on distance and road conditions) can be used to represent the amount of energy it takes to make a certain product (reach the destination). However, although the roads are influenced by the catalyst, the geographical distance between every city is fixed (as cities obviously do not move), meaning there is a minimum distance you have to drive to go from one city to another. This distance between cities has a chemical analogue called 'thermodynamic equilibrium'. Thermodynamics basically tell us that the catalyst can change the road, but the shortest road is a straight line and no matter what, a catalyst will not be able to make a road shorter than this. Now, the chemical method by which a catalyst is capable of changing the hypothetical road is via binding to i) the reactants, ii) the 'intermediates' (anything that exists between reactants and products) and iii) the products. Although this may sound complicated, you can imagine there exist a whole bunch of possible chemicals that look like either the reactants, the products, or kind of resemble both products and reactants at the same time (things in-between, if you will: intermediates). And, a catalyst will hug with every single one of these possible chemicals when it gets close to them. However, some of them it hugs very tightly (aggressive hugging), others it barely touches (unloving hugging), and some it may even push away (let's call it negative hugging). The strength at which a catalyst hugs any of these chemicals is called the binding strength, and every different chemical it hugs represents a different possible ‘reaction step’ (section of a road). The roads that a catalyst ends up making depend on which combination of reaction steps (hugging which chemicals) are necessary to reach each destination, and the exact binding strength of each individual step (how strongly the catalyst hugs each individual chemical).

And with this we reach the quintessential (most important) concept of catalysis, called the Sabatier principle[21]: an ideal catalyst binds optimally for each individual step, not too weak and not too strong. If a catalyst binds too strongly for any of the steps that make up a road, it takes longer to reach our destination (think of introducing a traffic light in one spot, slowing you down). If a catalyst binds too weakly for any of the steps, it will take longer as well (think of introducing a narrow bridge with no guard rail where you have to slow down or you might fall off). Only if every step is optimal, will the journey be as fast as theoretically possible. This principle results in two commonly accepted truths about catalysts. Firstly, because every step has to be perfectly balanced, a catalyst is generally best at catalyzing one specific reaction (though it may still be capable of catalyzing other reactions). Secondly, the more different steps we have to go through (the longer the road), the more difficult it is to optimally bind during every individual step, making it harder to find a good catalyst for more complex reactions. Simply put, if more steps are required, then a catalyst has to work harder to make every single one optimal whilst simultaneously having more opportunities to get it wrong.

From the previous sections, it (hopefully) comes as no surprise that knowing exactly how a catalyst converts reactants into products – via which steps, and with which amount of binding for each step – is of great help with searching for and designing of new catalysts with better performance. And exactly this question is what we study in one of the chapters: what is the catalytic pathway (road) via which we can form products that have more than one carbon atom. Such products are also sometimes called carbon-coupled products or C2+ products, and are of interest because they are generally more valuable. However, they are also more complicated to make as our starting material only has a single carbon atom (remember, CO_2 means one carbon and two oxygen), therefore requiring extra steps if we want to form products that have more than one carbon atom. Additionally, a logical implication of the fact that we start with a reactant that only has one carbon is that the pathway leading to C2+ products must include a step where we form a bond between two separate chemicals that have one carbon each. For now, there is much debate on exactly what this step looks like.

Considering that the currently known best electrocatalyst for producing C2+ products is metallic copper (chemical notation: Cu, from the Latin word ‘cuprum’), much research has been conducted on understanding the exact path via which copper catalyzes the formation of such products. However, for every new publication (meaning people writing down their research findings in a magazine), there tends to be a new theory for the exact mechanism (roads), with currently more than 10 separate pathways proposed to lead to various experimentally reported products. Some of these suggested pathways are similar, while others are radically different. The resulting situation makes for a very complicated roadmap and there is much debate on the correct pathway or possibly pathways.

In order to be able to gain new insights, we turned our attention to a piece of conventional wisdom: if one wishes to solve a particular problem, it is sometimes beneficial to take a step back and look at the bigger picture. In terms of mechanistic studies regarding C2+ product formation (the C-C coupling mechanism), we discussed previously that copper is most often used because it has the highest performance of all known electrocatalysts for CO_2 reduction. However, it is possible to increase our understanding of the overall situation by looking at other catalytically active materials (catalysts) capable of producing similar types of products and comparing the (proposed) mechanisms of both systems to each other. Therefore, we studied the reaction mechanism on a silver catalyst (chemical notation: Ag, from the Latin word 'argentum') and compared the results to copper systems to gain additional insights into exactly how electrocatalysts perform the act of making carbon-carbon bonds.

We used silver for our studies because theoretical calculations predict that this electrocatalyst may be even better than copper for making one specific C2 product (alcohol, chemical name: ethanol), although at that time this had not been observed experimentally. Considering the disagreement with the theoretical expectations and existing experimental reports, we opted to investigate the reduction of a key 'in-between' chemical intermediate, namely carbon monoxide (chemical notation: CO) instead of CO_2 as it was hypothesized that after its formation on silver, carbon monoxide may be released by the catalyst (to desorb, in chemical terms) rather than react further into ethanol. (You can imagine desorption as the catalyst hugging a chemical very weakly, easily letting go.) By increasing the amount of available CO (through increasing the pressure, together with using a special type of electrode called a gas diffusion electrode) we increased the chance of further reaction rather than desorption and studied what types of products silver was capable of making under such conditions. Comparing the mechanisms on silver and copper, we propose an important step for making carbon-carbon bonds after having taken into account our results plus recent experimental and theoretical studies.

1.3. (Metallic) catalyst stability during CO_2 reduction

Although the most important aspect of a catalyst is generally assumed to be its catalytic performance, there is another fundamental (catalyst-related) aspect to take into consideration when investigating CO_2 reduction: deactivation. By definition, a catalyst is something that can influence the path of a reaction, but is itself regenerated after reaching the destination (making a product). Therefore, in theory, a catalyst should not change its performance in time as it just keeps returning to its initial state and start over anew. Though, obviously, theory is theory; and when does ever theory apply in practice? Within the boundaries of our topic of study (converting CO_2), there do exist catalysts that can operate for extended periods of time without the catalyst and/or its performance changing. However, this is more of an exception rather than the norm. Instead, it is more commonly reported that during CO_2 reduction, catalyst performance goes down rapidly as time goes on.[7] Such decreased performance results in less products related to (or, more accurately; derived from) CO_2, and a shift towards the formation of unwanted (in this case) molecular hydrogen (chemical notation: H_2).[12] And many theories have been proposed to explain why such deactivation takes place, with (as is common in science) no universally agreed-upon answer.[7]

Specifically with regards to catalysts capable of reducing CO_2, there exists currently the belief that changes in the morphology during the reaction could lead to the catalyst becoming worse over time.[13, 22] Here, you can think of the morphology of a catalyst as the landscape that you see if you look at it under a very good microscope: perhaps it looks like a forest, or like the dunes, or like a desert, or maybe like a volcanic landscape. And this geometry of the surface affects the binding strength of the catalyst (how strongly it hugs), which in turn influences the catalytic pathway (the roads it forms). Therefore, changes in morphology can be related to changes in the binding strength which affect the products we make, and therefore the time dependence of catalyst performance during CO_2 reduction has been hypothesized to be related to observed changes in surface morphology with respect to time. However, this is rather intriguing because we keep using the word 'reduction' in concert with CO_2. Looking back at the start of the introduction, reduction signifies (besides adding hydrogen atoms to make products) the direction of flow of electricity. And it just so happens that under reducing conditions metals are believed to be in their most stable state. Actually, exactly the principle of applying a reducing potential (forcing electricity to flow in a specific direction) is a very common method for increasing the stability of metals (called cathodic protection), used for example for protecting bridges and ships. Therefore, the theory that a metallic surface is changing during CO_2 reduction goes against conventional wisdom that metals are protected against change under exactly such conditions.

It turns out there does exist a (recently 'rediscovered') mechanism by which a metal surface actually can change is morphology under exactly such reducing conditions, called cathodic corrosion.[16] However, this particular mechanism requires relatively special circumstances: extremely reducing potentials (think of needing a high voltage and high current), high cation concentrations (think of needing a lot of dissolved salts surrounding your catalyst) and very alkaline conditions (think of needing a bath of very aggressive drain cleaner fluid). And it turns out that many of these conditions are actually, to a certain degree, applicable during CO_2 reduction. Therefore, the second line of investigation in this thesis is if whether cathodic corrosion perhaps plays an important role in the reported catalyst deactivation during CO_2 reduction. To this end, we study the possible effects of cathodic corrosion on changing the catalytic activity of two catalyst materials, namely gold (chemical notation: Au, from the Latin word 'aurum') and copper. Gold is a good catalyst for forming exactly a single product from CO_2, namely carbon monoxide (CO) whereas copper is relatively less good of a catalyst (in terms of energy efficiency) but capable of making many chemically important types of carbon-coupled (C2+) products which are highly sought-after.

Studying gold allowed us to study the applicability of cathodic corrosion as a degradation mechanism during CO_2 reduction under strictly controlled conditions, where the properties of gold itself (specifically its stability in air and the large quantity of available information regarding the electrochemistry of gold) allowed for an in-depth investigation into the specifics of Au degradation under CO_2 reduction-like conditions. Here, note we append the suffix '-like' as we ended up approximating real-world conditions in order to simplify the system and remove sources of errors. In contrast to gold, the electrochemical properties of copper are less well-documented and still under debate owing to the fact that copper is inherently much less stable than gold, making such studies more difficult. Because of this, less (reliable) information is available regarding the electrochemical properties of copper. Consequently, before we could systematically investigate the role of cathodic corrosion as a potential degradation mechanism for copper, we first had to develop appropriate methodologies and procedures as existing literature at that moment was insufficient for our studies. After going through this process, using the knowledge we acquired during the development of these procedures, we investigated if cathodic corrosion is a viable degradation mechanism resulting in the reported changing morphology of copper during CO_2 reduction.

The exact method we used for studying the degradation for gold and copper catalysts during CO_2 reduction is a little intimidating when put in writing. Namely: we used a combination of surface titration techniques and surface imaging techniques together with spherical and cut single crystalline surfaces to investigate where catalyst degradation occurs and what the final catalyst looks like. This requires some additional explanation. Surface titration is a methodology that allows us to determine which types of 'active sites' are located on the catalyst, where active sites are the places that are responsible for hugging (binding to) chemicals, and different types of active sites hug (bind) with different strength. Changes in the morphology (landscape) actually mean that the types of active sites change, which is eventually responsible for changing catalytic performance, and surface titration allows us to investigate which sites are available. Surface imaging techniques allow us to look at the morphology of the catalyst from above, but provide us with more of a general overview rather than in-depth information. Finally, single crystals are catalysts that contain only a small number of different types of active sites (with a spherical single crystal being a special case thereof). Using these special catalysts allow us to see exactly which sites are changing the most during the experiment. The combination of looking at the catalyst and measuring which types of active sites are present before and after degradation helped us to determine the role of cathodic corrosion in the degradation of gold and copper, which can be summarized as follows. A large effect, in the case of gold (made worse by having CO near the surface) and no effect at all, in the case of copper.

1.4. Outline of this thesis

The research objective of this work was to investigate methods to improve the conversion of CO_2 to C2+ products. The resulting chapters making up this thesis are a rather liberal interpretation of this goal. This can be directly attributed to the properties inherent to the best catalyst for producing such products – copper, as these properties make studies regarding the catalytic behavior of copper poorly reproducible and data easily misinterpreted due to the ever-changing nature of this material during CO_2 reduction. However, a combination of "practicing" on simplified systems and some perseverance have finally yielded the following chapters in which we shed light on long-debated aspects of CO2RR albeit not all directly related to the formation of C2+ products.

In Chapter 2, we study the reaction mechanism (catalyst roadmap) by which we can form C2+ products (products containing 2 or more carbon atoms). This chapter looks at silver as a catalyst material, in a special shape called a gas diffusion electrode (a shape that has many very small holes to allow gas to go inside/through). Using this silver catalyst, we investigated the reduction of carbon monoxide (CO, a chemical that is sort of in-between step as CO_2 converts to products) at elevated pressures. Increased pressure was used in order to make it easier for two CO molecules (or chemicals somewhat resembling CO: intermediates related to CO) to react together. We compare our results to results predicted by density functional theory (DFT) calculations[23] (complicated math that can be used to estimate reaction parameters such as catalyst binding/hugging strength), and find that our experimental results match with those calculations. The agreement between the results in Chapter 2 and the DFT calculations can be interpreted to mean that the pathway that is proposed by the people who performed those calculations is likely true. From the products we could (and could not) detect during our experiments, and the similar trends of the different detected products as a function of experiment settings, we believe that ethylene glycol, ethanol and propanol (our observed C2+ products) follow the same pathway (share part of the same roads on our catalyst roadmap). Likely, an acetaldehyde-like surface-bound intermediate is an important shared intermediate for all these products.

In Chapter 3, we study the cathodic stability of gold (meaning under reducing conditions), and if having CO on/near the surfaces influences the stability under such conditions. We found that a gold catalyst quickly changes under strongly cathodic conditions. Specifically, we found it dissolved, and, depending on exact reaction and catalyst conditions, particles of specific shapes could also form. These catalyst conditions depended on the types of 'active sites' (places that hug with different strengths) on the surface. Such active sites can be imagined as being places on the catalyst having different shapes if you zoom in really far, and because they have different shapes they bind (hug) with a different strength. We observed that some types of sites (shapes) get destroyed by the cathodic corrosion process and by destroying these shapes, new sites (shapes) form. As the particular sites (shapes) that are lost in this process are actually most active for the CO2RR out of the three basal planes[24] (denoting three relatively simple shapes), the cathodic corrosion (degradation) mechanism leads to the catalyst changing under specific circumstances, which may in turn result in catalytic performance becoming worse as time goes on. Additionally, if carbon monoxide is located close to/on the catalyst, the catalyst was found to change quicker. This observation is important, as gold is a good catalyst material for making CO, meaning it will always be present in high concentration on and near the catalyst during CO_2 reduction on gold.

In Chapter 4, investigations into the electrochemical adsorption behavior of copper electrodes with commonly used surface structures are reported. Such adsorption measurements provide information about how the catalyst looks like, and tells us what types of 'active sites' are present on the catalyst. Experiments were performed on copper catalysts prepared under reductive atmosphere (in hydrogen gas) via induction annealing (a special type of heating). We compare the adsorption experiment results obtained via this method to literature-reported results for copper surfaces prepared via other methods, including crystals prepared under ultra-high vacuum (UHV) conditions. This last method yields high quality crystals. We found that, if we use a set of precise instrument settings in combination with heating and cooling our copper surfaces in hydrogen gas, the adsorption measurement results are better than most results normally reported for copper, while also being more reproducible. This indicates that the quality of our surfaces is improved with respect to other literature-methods, although it is still worse than the best preparation method: UHV-preparation. However, because our methodology is relatively much simpler and more accessible (requiring cheaper machinery and shorter preparation time) it provides for a good balance between quality and speed. Besides showing our methodology works rather well, we also show a number of new adsorption-related peaks that have not been previously reported. These new features are related to oxygen adsorption on specific copper 'active sites' (shapes), and can be used together with the already-known adsorption peaks to (better) understand the structure of the copper catalyst surface.

In Chapter 5, we study the stability of copper surfaces of various crystallographic orientations under purely cathodic conditions. We show that copper morphology is stable against change under such conditions. In simple terms: our experiments indicate that cathodic corrosion does not happen on copper, with copper active sites of many different shapes not changing. It is only when we start introducing periods of oxidation (comparable to exposing our catalyst to air) that surface morphology starts to evolve (change with time), requiring only brief periods at potentials very close to the open circuit potential. However, these results were obtained under very special reaction conditions that are very good for making cathodic corrosion take place, and not standard CO_2 reduction reaction conditions. To prove our result also applies under normal conditions, we performed by performing identical-location surface morphological studies using scanning electron microscopy after doing 1 hour of CO_2 reduction (in simple terms, we took pictures of a copper surface through an advanced microscope before and after doing CO_2 reduction and compared the results). In agreement with previous experiments, also this experiment showed no change of the copper catalyst to within the accuracy of our instrument. From these combined results we conclude that copper does not, in fact, change due to the cathodic potential applied during CO_2 reduction (cathodic corrosion), but rather due to improper experiment design allowing for brief periods of oxidation which result in the copper catalyst changing rapidly.

References

[1] Jiujun Zhang, editor. *Electrochemical reduction of carbon dioxide: Fundamentals and Technologies*. CRC Press, Taylor & Francis Group, 2016.

[2] Matthew Jouny, Wesley Luc, and Feng Jiao. General techno-economic analysis of CO2 electrolysis systems. *Industrial & Engineering Chemistry Research*, 57(6):2165–2177, 2018.

[3] Md Golam Kibria, Jonathan P. Edwards, Christine M. Gabardo, Cao-Thang Dinh, Ali Seifitokaldani, David Sinton, and Edward H. Sargent. Electrochemical CO2 reduction into chemical feedstocks: From mechanistic electrocatalysis models to system design. *Advanced Materials*, 31(31):1807166, 2019.

[4] Sumit Verma, Byoungsu Kim, Huei-Ru "Molly" Jhong, Sichao Ma, and Paul J. A. Kenis. A gross-margin model for defining technoeconomic benchmarks in the electroreduction of CO2. *ChemSusChem*, 9(15):1972–1979, 2016.

[5] Jingjie Wu and Xiao-Dong Zhou. Catalytic conversion of CO2 to value added fuels: Current status, challenges, and future directions. *Chinese Journal of Catalysis*, 37(7):999–1015, 2016.

[6] Y. Hori. *Electrochemical CO2 Reduction on Metal Electrodes*, book section 3, pages 89–189. Springer New York, New York, NY, 2008.

[7] Stephanie Nitopi, Erlend Bertheussen, Soren B. Scott, Xinyan Liu, Albert K. Engstfeld, Sebastian Horch, Brian Seger, Ifan E. L. Stephens, Karen Chan, Christopher Hahn, Jens K. Nørskov, Thomas F. Jaramillo, and Ib Chorkendorff. Progress and perspectives of electrochemical CO2 reduction on copper in aqueous electrolyte. *Chemical Reviews*, 119(12):7610–7672, 2019.

[8] Yansong Zhou and Boon Siang Yeo. Formation of C–C bonds during electrocatalytic CO2 reduction on non-copper electrodes. *Journal of Materials Chemistry A*, 8(44):23162–23186, 2020.

[9] Kendra P. Kuhl, Etosha R. Cave, David N. Abram, and Thomas F. Jaramillo. New insights into the electrochemical reduction of carbon dioxide on metallic copper surfaces. *Energy & Environmental Science*, 5(5):7050–7059, 2012.

[10] Hori Yoshio, Murata Akira, Takahashi Ryutaro, and Suzuki Shin. Electrochemical reduction of carbon monoxide to hydrocarbons at various metal electrodes in aqueous solution. *Chemistry Letters*, 16(8):1665–1668, 1987.

[11] Hori Yoshio, Kikuchi Katsuhei, Murata Akira, and Suzuki Shin. Production of methane and ethylene in electrochemical reduction of carbon dioxide at copper electrode in aqueous hydrogencarbonate solution. *Chemistry Letters*, 15(6):897–898, 1986.

[12] Y. Hori, H. Konishi, T. Futamura, A. Murata, O. Koga, H. Sakurai, and K. Oguma. "deactivation of copper electrode" in electrochemical reduction of CO2. *Electrochimica Acta*, 50(27):5354–5369, 2005.

[13] Stefan Popović, Milutin Smiljanić, Primož Jovanovič, Jan Vavra, Raffaella Buonsanti, and Nejc Hodnik. Stability and degradation mechanisms of copper-based catalysts for electrochemical CO2 reduction. *Angewandte Chemie International Edition*, 59(35):14736–14746, 2020.

[14] Qun Fan, Mingli Zhang, Mingwen Jia, Shizhen Liu, Jieshan Qiu, and Zhenyu Sun. Electrochemical CO2 reduction to C2+ species: Heterogeneous electrocatalysts, reaction pathways, and optimization strategies. *Materials Today Energy*, 10:280–301, 2018.

[15] Yao Zheng, Anthony Vasileff, Xianlong Zhou, Yan Jiao, Mietek Jaroniec, and Shi-Zhang Qiao. Understanding the roadmap for electrochemical reduction of CO2 to multi-carbon oxygenates and hydrocarbons on copper-based catalysts. *Journal of the American Chemical Society*, 141(19):7646–7659, 2019.

[16] Alexei I. Yanson, Paramaconi Rodriguez, Nuria Garcia-Araez, Rik V. Mom, Frans D. Tichelaar, and Marc T. M. Koper. Cathodic corrosion: A quick, clean, and versatile method for the synthesis of metallic nanoparticles. *Angewandte Chemie International Edition*, 50(28):6346–6350, 2011.

[17] Christopher M. A. Brett and Ana Maria Oliveira Brett. *Electrochemistry: principles, methods, and applications*. Oxford University Press, 1993.

[18] Richard E. Dickerson, Harry B. Gray, and Gilbert P. Haight. *Chemical principles*. The Benjamin/Cummings Publishing Company, Inc., 1979.

[19] Mette Mikkelsen, Mikkel Jørgensen, and Frederik C. Krebs. The teraton challenge. A review of fixation and transformation of carbon dioxide. *Energy & Environmental Science*, 3(1):43–81, 2010.

[20] Johan A. Martens, Annemie Bogaerts, Norbert De Kimpe, Pierre A. Jacobs, Guy B. Marin, Korneel Rabaey, Mark Saeys, and Sebastian Verhelst. The chemical route to a carbon dioxide neutral world. *ChemSusChem*, 10(6):1039–1055, 2017.

[21] Enrique Herrero, Juan M. Feliu, and Antonio Aldaz. *Electrocatalysis*, book section 5.1, pages 443–465. John Wiley & Sons, Ltd, 2007.

[22] Youn-Geun Kim, Jack Hess Baricuatro, Alnald Javier, John Mathew Gregoire, and Manuel P. Soriaga. The evolution of the polycrystalline copper surface, first to Cu(111) and then to Cu(100), at a fixed CO2RR potential: A study by operando EC-STM. *Langmuir*, 30(50):15053–15056, 2014.

[23] Selwyn Hanselman, Marc T. M. Koper, and Federico Calle-Vallejo. Computational comparison of late transition metal (100) surfaces for the electrocatalytic reduction of CO to C2 species. *ACS Energy Letters*, 3(5):1062–1067, 2018.

[24] Stefano Mezzavilla, Sebastian Horch, Ifan E. L. Stephens, Brian Seger, and Ib Chorkendorff. Structure sensitivity in the electrocatalytic reduction of CO2 with gold catalysts. *Angewandte Chemie*, 131(12):3814–3818, 2019.

2

High-pressure CO electroreduction at silver produces ethanol and propanol

Reducing CO_2 to long-chain carbon products is attractive considering such products are typically more valuable than shorter ones. However, the best electrocatalyst for making such products from CO_2, copper, lacks selectivity. By studying alternate C2+ producing catalysts we can increase our mechanistic understanding, which is beneficial for improving catalyst performance. Therefore, we investigate CO reduction on silver, as density functional theory (DFT) results predict it to be good at forming ethanol. To address the current disagreement between DFT and experimental results (ethanol vs. no ethanol), we investigated CO reduction at higher surface coverage (by increasing pressure) to ascertain if desorption effects can explain the discrepancy. In terms of product trends, our results agree with the DFT-proposed acetaldehyde-like intermediate, yielding ethanol and propanol as C2+ products – making the CO_2 electrochemistry of silver very similar to copper at sufficiently high coverage.

This chapter has been published in
Raaijman, S. J.; Schellekens, M.P.; Corbett, P.J.; Koper, M. T. M., *Angewandte* **2021**, *60* (40), 21732-21736.

2.1. Introduction

Few electrocatalytic systems are known to be capable of generating carbon-coupled products from the CO_2 reduction reaction (CO2RR) and/or the CO reduction reaction (CORR).[1–4] Out of these, copper is by far the most capable electrocatalyst for making C2+ molecules, yielding ethylene,[5, 6] ethanol[7] and n-propanol[8] as its primary multi-carbon products.[3, 9] Other catalysts (in aqueous media) include molybdenum disulfides[10], enzymatic nitrogenases with a vanadium/molybdenum active center[11] (and its organo-metallic homologues[12]), bimetallic palladium/gold nanparticles[13], heteroatom (N, B) doped nanoparticles[14–16], transition-metal (Ni, Fe) doped carbon xerogels[17], certain surfaces when coated with functionalized films,[18, 19] nickel/gallium alloys,[20] nickel phosphides,[21] and metallic nickel and silver.[22–24] However, these non-copper catalysts exhibit comparatively low (on the order of a few %) faradaic efficiencies (FEs) for C2+ products.

As for the currently existing theories on the C-C coupling mechanism, an in-depth review concerning non-copper systems has recently been published by Zhou and Yeo[25], whilst comprehensive reviews regarding the mechanism on copper can be found in e.g. [26–29], with a review by Fan *et al.*[30] comparing mechanisms on a per-product basis. For comprehensibility, summaries of the main theories for making C2 and C3 products on metallic Cu in aqueous media are also provided in the supporting information in schemes A-C2 to I-C2 (with, where applicable, reaction paths to C3 products in accompanying schemes A-C3 to J-C3).

To increase molecular-level understanding of the formation mechanism for C2+ products, Hanselman *et al.* carried out Density Functional Theory (DFT) calculations on CO reduction to C2 products for various transition metal surfaces (including silver), suggesting two reaction pathways: one to ethylene and one to ethanol, bifurcating from a surface intermediate that is one hydrogen short of acetaldehyde.[31] This mechanism, where acetaldehyde is the precursor to ethanol, agrees with experiments on copper single-crystal electrodes.[32] Their DFT calculations indicate that, among nine transition-metal surfaces, only copper has a reasonably low onset potential for ethylene formation whilst ethanol has a slightly later onset. The former agrees well with literature as copper is reported to yield reasonable FE towards C_2H_4 at overpotentials of a few hundred mV[6, 33, 34], although experimentally no large differences are observed between the formation onsets of ethylene and ethanol.[5, 35, 36] Importantly, their calculations also indicate silver should have a lower onset potential for ethanol formation than copper whilst being incapable of producing ethylene. In chemical terms, silver is seemingly too noble to break the last C-O bond.

This prediction is, however, in apparent disagreement with experimental studies as the maximum reported FE of CO_2 to ethanol is ca. 0.1% on silver vs. 40% on copper.[7, 23, 35] Hanselman *et al.* hypothesized this disagreement may be a consequence of CO desorbing rather than reacting further on silver due to its unfavorable adsorption strength.[31] Hence, herein we probe the validity of the theory that silver can produce ethanol if the CO coverage on the surface is sufficiently high. To this end, we study CO reduction at elevated pressure as a means of increasing surface coverage which enhances the likelihood of (intermolecular) reactions involving CO_{ads}. In line with DFT calculations we observe ethanol (whose formation is positively influenced by increasing the pressure) and no ethylene during CORR. Furthermore, ethylene glycol and n-propanol are also observed and found to exhibit an similar pressure dependency as ethanol, providing us with additional insight into carbon-carbon bond formation and the mechanistic aspects of C3 production.

2.2. Experimental

Experiments were carried out in three-compartment electrochemical cell inside an autoclave that could be pressurized up to $60\ barg$, with the gaseous products leaving the cell analyzed by gas chromatography, and liquid products analyzed by NMR. The working electrode was a silver gas diffusion electrode (GDE) with a $1\ cm^2$ exposed geometrical area. Alkaline conditions were employed as these promote C2 formation from CO on copper.[37–39] A Ag|AgCl|KCl (3M) reference was used as a reference electrode and potentials are reported on this scale unless denoted otherwise. Reported potentials are not IR-corrected because of the inherent inhomogeneity of the interfacial potential on a GDE, rendering the nominal reported potentials unrepresentative of the 'real' potential. As a figure of merit, the nominal IR-corrected potential of the most negative potential employed in this work ($-4.5\ V$) was calculated to be ca. $-1\ V$ vs. RHE (see supporting information; SI). A comprehensive description of the experimental setup can be found in the SI, including control experiments conducted in the absence of CO and in the absence of applied potential in the presence of CO to prove that the products we report are indeed the result of electrochemical CO reduction.

2.3. Results and discussion

Absolute formation rates of CORR-related products obtained for CO reduction in $0.5\ M$ KOH on a silver GDE at various potentials are depicted in Figures 2.1a, b and c, for reactant (carbon monoxide) pressures ranging between 10 and $60\ barg$. Investigated reaction times were between 2.6 and $73\ hours$, with more positive potentials necessitating longer times to guarantee a minimum of charge had passed. The CORR products depicted in Figure 2.1 are minority species, with hydrogen and formate (Figures A.3a and b, respectively) being the main products. As we study the carbon-carbon bond formation mechanism on silver, we will disregard H_2 and $HCOO^-$ as neither is the result of CO reduction or contains a C-C bond. However, to briefly address the possible origin of formate (being in equal oxidation state as CO), we refer the reader to literature wherein formate is proposed to form through a solution phase reaction between CO and hydroxide, which may occur in this work given the high electrolyte alkalinity and elevated carbon monoxide pressures.[40–42]

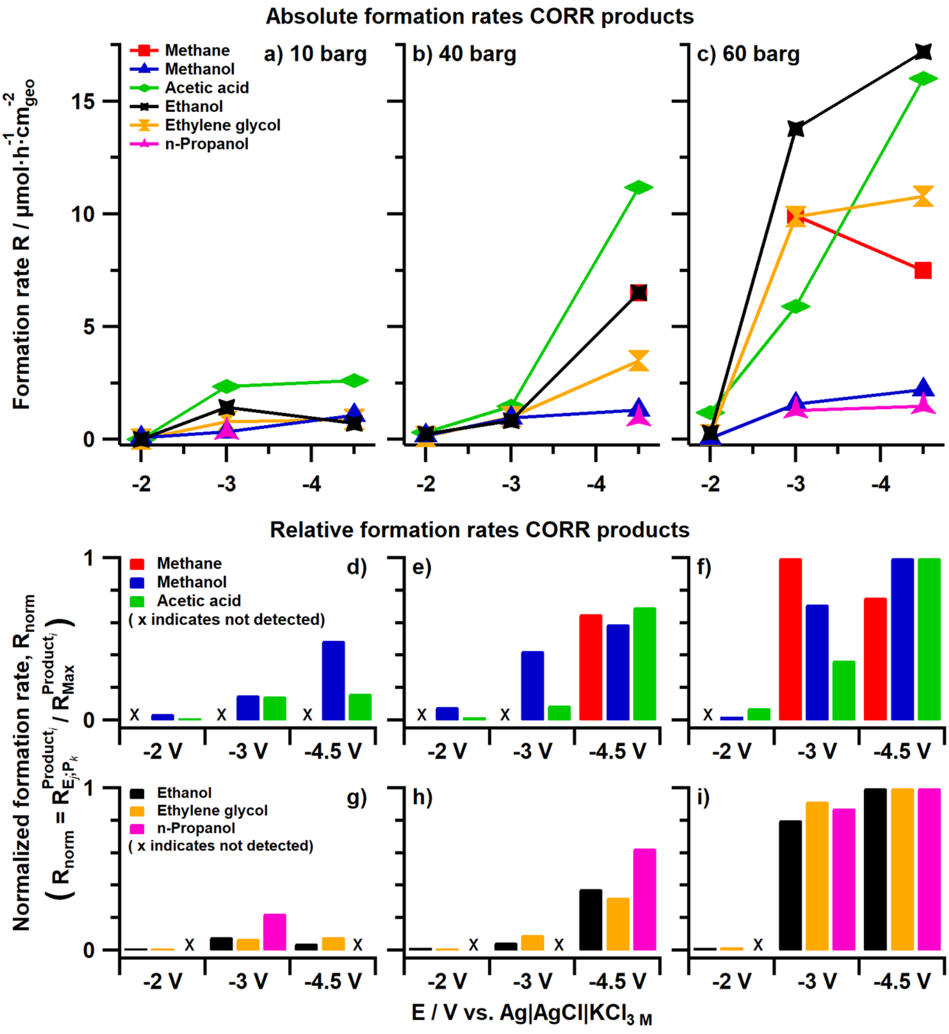

Figure 2.1: Color-coded formation rates for CORR products (methane: red, methanol: blue, acetic acid: green, ethanol: black, ethylene glycol: orange, n-propanol: pink) plotted as a function of applied potential (non-IR corrected) for three different reactant pressures; $10\ barg$ (a,d & g), $40\ barg$ (b, e & h) and $60\ barg$ (c, f & i) expressed in absolute rates (a, b & c) and relative rates (d, g & e, h & f, i). All axes in a given row are of equal magnitude. Not detected products are marked by an 'x' in the subfigures depicting relative rates.

Specifically, the CORR-related products (Figure 2.1) comprise a product with carboxylic acid functionality (acetic acid, green), the simplest hydrocarbon (methane, red) and four compounds with alcohol functionality (methanol, ethylene glycol, ethanol and n-propanol; blue, orange, black and purple, respectively). Notably, ethylene, which is very commonly observed on copper electrodes[3], was not observed. The predominance of oxygenates (excluding methane) agrees with the DFT predictions of Hanselman *et al.*, who computed silver to be a poor catalyst for breaking C-O bonds.[31] Unconventionally, formation rates rather than partial current densities are depicted in Figure 2.1. This approach allows for directly comparing molar product rations, which is valuable from a mechanistic point of view considering certain reaction pathways yielding C2 species (e.g., Cannizzaro disproportionation[43]) would result in equimolar concentrations of particular types of products. Partial current densities are provided in Figures A.4 (for CORR products) and A.5 (for hydrogen), whilst the overall current response of the system is depicted in Figure A.6. Faradaic efficiencies are given in Table A.1.

Pressure and potential dependencies for these CORR products can be determined from Figures 2.1a, b and c. Overall, formation rates increase when either the overpotential or CO pressure is increased, although formation rates at $10\ barg/{-3}\ V$ and methane formation at $60\ barg/-3\ V$ are exceptions. However, because the products' formation rates overlap to a considerable degree, these figures can only provide us with general trends. To better distinguish individual trends, each product has been normalized to its highest observed formation rate and is depicted on a per-pressure-basis in Figures 2.1d, e and f (for methane, methanol and acetic acid) and Figures 2.1g, h and i (for ethanol, ethylene glycol and n-propanol) for $10, 40$ and $60\ barg$ from left to right, respectively. The first group (methane, methanol and acetic acid) comprises products weakly correlating to pressure, potential and one another whereas the second group (ethanol, ethylene glycol and n-propanol) is comprised of products that show fairly straightforward trends that are shared between them.

The behavior of these latter three higher alcohols yields important insights into the C-C formation mechanism since they all exhibit very similar trends: at the lowest applied pressure and potential ($10\ barg, {-2}\ V$) they are just barely detectable. Then, as the potential is decreased ($-3\ V$) their formation rates go through a maximum and subsequently slightly decrease again for higher overpotentials ($-4.5\ V$). Increasing the CO pressure from 10 to $40\ barg$ results in this maximum disappearing, with observed relative formation rates increasing rapidly as higher overpotentials are applied. However, this potential dependency becomes weaker as the pressure is increased further, with more moderate increases of ca. $5 - 25\%$ observed between successively more negative potentials at CO pressures of $60\ barg$.

Exhibiting such strong similarities in their potential and pressure dependency indicates commonalities in their formation mechanism, separate from the pathway via which methanol and acetic acid form (to be discussed later). The absence of ethylene (which cannot be explained by insufficient hydrogen coverage, considering the still high rate of H_2 formation) in concert with the comparable behavior of ethanol and n-propanol is especially interesting. Namely, this observation makes it unlikely that the coupling of CO and ethylene (“hydroformylation”) is responsible for the formation of C3 products on silver, as hypothesized to occur on copper by Ren *et al.*[44] Instead, acetaldehyde, being both reactive and difficult to detect via standard NMR techniques (especially in alkaline media)[45], is known to only reduce to ethanol and not ethylene (on copper).[46, 47] Its high reactivity would facilitate further reduction rather than desorption. This possibility would agree with recent work by Xu *et al.* who showed that propanol is formed on copper via the coupling between CO and a surface-bound methylcarbonyl, an intermediate which is one hydrogen short of acetaldehyde.[46] This latter observation agrees well with DFT calculations conducted by Hanselman *et al.*, who propose ethanol formation takes place via a surface-bound acetaldehyde species.[31]

The fact that both ethylene glycol and ethanol are observed and exhibit similar behavior proves that silver is capable of breaking one of the C-O bonds in a molecule comprised of two carbon atoms containing two C-O bonds. However, the absence of ethylene shows that silver is indeed a poor catalyst for breaking the final C-O bond, as predicted by DFT calculations. From these observations, our results suggest that an oxygenated intermediate, probably surface-bound methylcarbonyl (as proposed by Hanselman *et al.* and Xu *et al.*)[31, 46] is involved in the formation of ethanol, as well as in the coupling with adsorbed CO to lead to the formation of n-propanol (through propanal).

Additional insights regarding C-C coupling on silver can be derived from the behavior of the other ‘group’ of products (methane, methanol and acetic acid) whose trends with regards to potential, pressure and one another are more inconsistent. Of these, the methane ‘trends’ disagree with all other observed CORR products. The most notable observation that can reasonably be made is that it is more prevalent at increased CO pressures and more cathodic potentials. More important are methanol and acetic acid, as they exhibit some similarities although their correlation is much weaker than the previously discussed alcohols. Comparing these products, we find that methanol generally exhibits higher relative formation rates than acetic acid at lower overpotentials, and for all investigated potentials in the case of $10\ barg$ of CO pressure. However, when the pressure is increased (from 10 to 40 or $60\ barg$), relative acetic acid formation rates start to become very similar to those of methanol formation for the most cathodic potentials investigated ($-4.5\ V$). This results from the fact that methanol formation rates are relatively invariant with potential and pressure, whereas acetic acid is strongly influenced by both of these parameters. (This observation that acetic acid formation remains strongly potential dependent also at increased pressures is what makes its behavior different from the previously discussed ‘alcohol group’ as they exhibit much weaker relative increases in formation rate with potential at $60\ barg$ of CO).

The strong pressure dependency of acetic acid suggest that CO is involved in its formation. Furthermore, the fact that this dependency persists even at elevated reactant pressures, signifies that the C-C coupling step for its formation has a significant barrier. Additionally, the (weak) correlation observed between methanol and acetic acid can be interpreted as them sharing a common intermediate. Hence we speculate there may exist a pathway where CO couples with a methanol-like moiety

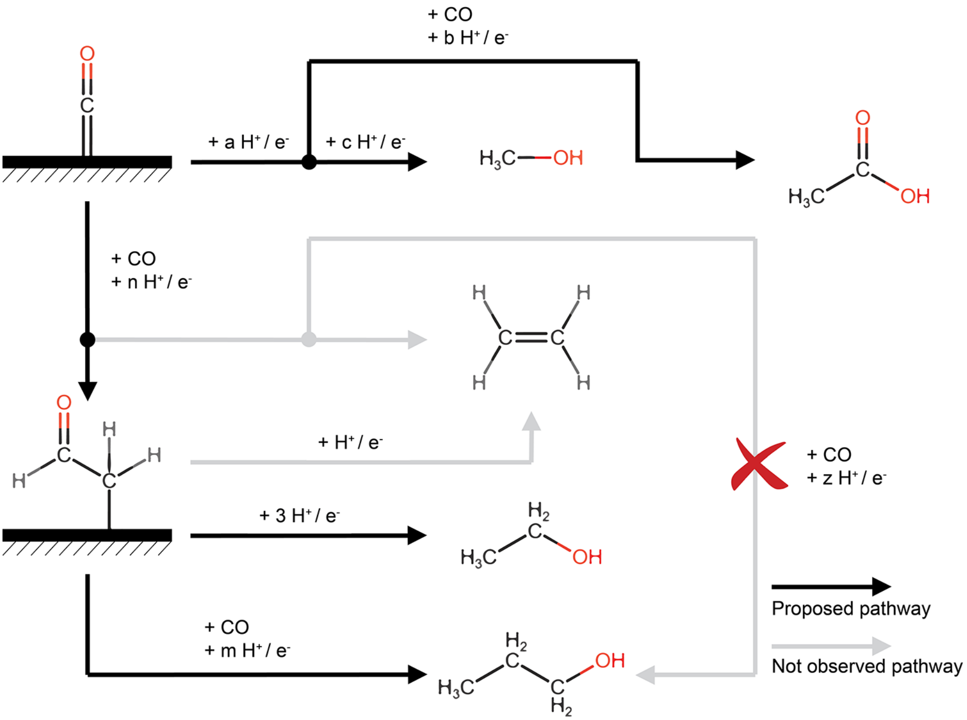

Figure 2.2: Proposed mechanistic pathway based on literature and the products (and their trend similarities) observed in this study.

to form acetic acid. Some plausibility for this hypothesis can be derived from the existence of a rhodium-catalyzed industrial process for acetic acid synthesis involving the carbonylation of methanol called the Monsanto process.[48, 49] However, we emphasize that the most important observation from Figure 2.1 is that the pathway for the formation of acetic acid differs from the pathway via which ethanol, ethylene glycol and n-propanol are formed.

2.4. Conclusions

In summary, high-pressure CO electroreduction experiments reveal that silver is capable of further reducing carbon monoxide if the CO surface coverage is sufficiently high, with the total production rates of C2+ CORR products (ethanol, ethylene glycol and propanol) increasing as the pressure is increased. Contrary to one literature report[22], ethylene formation was not observed in this work. The fact that silver is capable of reducing CO to ethanol but not to ethylene is in agreement with DFT calculations.[31]

The comparable potential and pressure dependence of the formation of ethanol, n-propanol and ethylene glycol indicates a commonality in their formation pathways. An oxygenated surface species is likely to be the shared intermediate between ethanol and n-propanol, and this species is likely to be one hydrogen short of acetaldehyde, as suggested by Hanselman *et al.* and Xu *et al.*[31, 46] We propose it is the coupling of this species with adsorbed CO that is responsible for the formation of propanal, which is then further reduced to n-propanol, as opposed to a reaction between a surface bound ethylene molecule with carbon monoxide (Figure 2.2).

If the CO coverage is sufficiently high, as can be achieved by increasing CO pressure, the product spectrum of silver starts to resemble that of copper under CO2RR conditions.[9] However, the formation rates for CORR products on silver are orders of magnitude lower than what is observed on copper, making detecting minority products beyond the scope of this work. The main difference between the two systems seems twofold. Firstly, due to the rather unfavorable adsorption energy of CO, silver has the propensity for desorbing CO rather than reducing it further, even though thermodynamically speaking it is capable of doing so. Secondly, due to silver being a poor catalyst for breaking C-O bonds[31], no ethylene (nor ethane) formation is observed although the rest of the products observed compare favorably with copper-catalyzed CO(2) reduction.

References

[1] Y. Hori. *Electrochemical CO2 Reduction on Metal Electrodes*, book section 3, pages 89–189. Springer New York, New York, NY, 2008.

[2] Qi Lu, Jonathan Rosen, and Feng Jiao. Nanostructured metallic electrocatalysts for carbon dioxide reduction. *ChemCatChem*, 7(1):38–47, 2015.

[3] Stephanie Nitopi, Erlend Bertheussen, Soren B. Scott, Xinyan Liu, Albert K. Engstfeld, Sebastian Horch, Brian Seger, Ifan E. L. Stephens, Karen Chan, Christopher Hahn, Jens K. Nørskov, Thomas F. Jaramillo, and Ib Chorkendorff. Progress and perspectives of electrochemical CO2 reduction on copper in aqueous electrolyte. *Chemical Reviews*, 119(12):7610–7672, 2019.

[4] Jinli Qiao, Yuyu Liu, Feng Hong, and Jiujun Zhang. A review of catalysts for the electroreduction of carbon dioxide to produce low-carbon fuels. *Chemical Society Reviews*, 43(2):631–675, 2014.

[5] Cao-Thang Dinh, Thomas Burdyny, Md Golam Kibria, Ali Seifitokaldani, Christine M. Gabardo, F. Pelayo García de Arquer, Amirreza Kiani, Jonathan P. Edwards, Phil De Luna, Oleksandr S. Bushuyev, Chengqin Zou, Rafael Quintero-Bermudez, Yuanjie Pang, David Sinton, and Edward H. Sargent. CO2 electroreduction to ethylene via hydroxide-mediated copper catalysis at an abrupt interface. *Science*, 360(6390):783–787, 2018.

[6] F. Sloan Roberts, Kendra P. Kuhl, and Anders Nilsson. High selectivity for ethylene from carbon dioxide reduction over copper nanocube electrocatalysts. *Angewandte Chemie*, 127(17):5268–5271, 2015.

[7] Christina W. Li, Jim Ciston, and Matthew W. Kanan. Electroreduction of carbon monoxide to liquid fuel on oxide-derived nanocrystalline copper. *Nature*, 508(7497):504–507, 2014.

[8] Yuanjie Pang, Jun Li, Ziyun Wang, Chih-Shan Tan, Pei-Lun Hsieh, Tao-Tao Zhuang, Zhi-Qin Liang, Chengqin Zou, Xue Wang, Phil De Luna, Jonathan P. Edwards, Yi Xu, Fengwang Li, Cao-Thang Dinh, Miao Zhong, Yuanhao Lou, Dan Wu, Lih-Juann Chen, Edward H. Sargent, and David Sinton. Efficient electrocatalytic conversion of carbon monoxide to propanol using fragmented copper. *Nature Catalysis*, 2(3):251–258, 2019.

[9] Kendra P. Kuhl, Etosha R. Cave, David N. Abram, and Thomas F. Jaramillo. New insights into the electrochemical reduction of carbon dioxide on metallic copper surfaces. *Energy & Environmental Science*, 5(5):7050–7059, 2012.

[10] Sonja A. Francis, Jesus M. Velazquez, Ivonne M. Ferrer, Daniel A. Torelli, Dan Guevarra, Matthew T. McDowell, Ke Sun, Xinghao Zhou, Fadl H. Saadi, Jimmy John, Matthias H. Richter, Forrest P. Hyler, Kimberly M. Papadantonakis, Bruce S. Brunschwig, and Nathan S. Lewis. Reduction of aqueous CO2 to 1-propanol at MoS2 electrodes. *Chemistry of Materials*, 30(15):4902–4908, 2018.

[11] Yilin Hu, Chi Chung Lee, and Markus W. Ribbe. Extending the carbon chain: Hydrocarbon formation catalyzed by vanadium/molybdenum nitrogenases. *Science*, 333(6043):753–755, 2011.

[12] Kazuki Tanifuji, Nathaniel Sickerman, Chi Chung Lee, Takayuki Nagasawa, Kosuke Miyazaki, Yasuhiro Ohki, Kazuyuki Tatsumi, Yilin Hu, and Markus W. Ribbe. Structure and reactivity of an asymmetric synthetic mimic of nitrogenase cofactor. *Angewandte Chemie*, 128(50):15862–15865, 2016.

[13] R. Kortlever, I. Peters, C. Balemans, R. Kas, Y. Kwon, G. Mul, and M. T. M. Koper. Palladium-gold catalyst for the electrochemical reduction of CO2 to C1-C5 hydrocarbons. *Chemical Communications*, 52(67):10229–10232, 2016.

[14] Yanming Liu, Shuo Chen, Xie Quan, and Hongtao Yu. Efficient electrochemical reduction of carbon dioxide to acetate on nitrogen-doped nanodiamond. *Journal of the American Chemical Society*, 137(36):11631–11636, 2015.

[15] Yanming Liu, Yujing Zhang, Kai Cheng, Xie Quan, Xinfei Fan, Yan Su, Shuo Chen, Huimin Zhao, Yaobin Zhang, Hongtao Yu, and Michael R. Hoffmann. Selective electrochemical reduction of carbon dioxide to ethanol on a boron- and nitrogen-Co-doped nanodiamond. *Angewandte Chemie International Edition*, 56(49):15607–15611, 2017.

[16] Jingjie Wu, Sichao Ma, Jing Sun, Jake I. Gold, ChandraSekhar Tiwary, Byoungsu Kim, Lingyang Zhu, Nitin Chopra, Ihab N. Odeh, Robert Vajtai, Aaron Z. Yu, Raymond Luo, Jun Lou, Guqiao Ding, Paul J. A. Kenis, and Pulickel M. Ajayan. A metal-free electrocatalyst for carbon dioxide reduction to multi-carbon hydrocarbons and oxygenates. *Nature Communications*, 7:13869, 2016.

[17] Agustín F. Pérez-Cadenas, Cornelia H. Ros, Sergio Morales-Torres, María Pérez-Cadenas, Patricia J. Kooyman, Carlos Moreno-Castilla, and Freek Kapteijn. Metal-doped carbon xerogels for the electro-catalytic conversion of CO2 to hydrocarbons. *Carbon*, 56:324–331, 2013.

[18] Kotaro Ogura, Kenichi Mine, Jun Yano, and Hideaki Sugihara. Electrocatalytic generation of C2 and C3 compounds from carbon dioxide on a cobalt complex-immobilized dual-film electrode. *Journal of the Chemical Society, Chemical Communications*, (1):20–21, 1993.

[19] Jun Tamura, Akihiko Ono, Yoshitsune Sugano, Chingchun Huang, Hideyuki Nishizawa, and Satoshi Mikoshiba. Electrochemical reduction of CO2 to ethylene glycol on imidazolium ion-terminated self-assembly monolayer-modified Au electrodes in an aqueous solution. *Physical Chemistry Chemical Physics*, 17(39):26072–26078, 2015.

[20] Daniel A. Torelli, Sonja A. Francis, J. Chance Crompton, Alnald Javier, Jonathan R. Thompson, Bruce S. Brunschwig, Manuel P. Soriaga, and Nathan S. Lewis. Nickel–gallium-catalyzed electrochemical reduction of CO2

to highly reduced products at low overpotentials. *ACS Catalysis*, 6(3):2100–2104, 2016.

[21] Karin U. D. Calvinho, Anders B. Laursen, Kyra M. K. Yap, Timothy A. Goetjen, Shinjae Hwang, Nagarajan Murali, Bryan Mejia-Sosa, Alexander Lubarski, Krishani M. Teeluck, Eugene S. Hall, Eric Garfunkel, Martha Greenblatt, and G. Charles Dismukes. Selective CO2 reduction to C3 and C4 oxyhydrocarbons on nickel phosphides at overpotentials as low as 10 mV. *Energy & Environmental Science*, 2018.

[22] Abhijit Dutta, Carina Elisabeth Morstein, Motiar Rahaman, Alena Cedeño López, and Peter Broekmann. Beyond copper in CO2 electrolysis: Effective hydrocarbon production on silver-nanofoam catalysts. *ACS Catalysis*, 8(9):8357–8368, 2018.

[23] Toru Hatsukade, Kendra P. Kuhl, Etosha R. Cave, David N. Abram, and Thomas F. Jaramillo. Insights into the electrocatalytic reduction of CO2 on metallic silver surfaces. *Physical Chemistry Chemical Physics*, 16(27):13814–13819, 2014.

[24] Akihiko Kudo, Shinji Nakagawa, Akira Tsuneto, and Tadayoshi Sakata. Electrochemical reduction of high pressure CO2 on Ni electrodes. *Journal of The Electrochemical Society*, 140(6):1541–1545, 1993.

[25] Yansong Zhou and Boon Siang Yeo. Formation of C–C bonds during electrocatalytic CO2 reduction on non-copper electrodes. *Journal of Materials Chemistry A*, 8(44):23162–23186, 2020.

[26] Kayode Adesina Adegoke, Rhoda Oyeladun Adegoke, Asiata Omotayo Ibrahim, Samson Ademola Adegoke, and Olugbenga Solomon Bello. Electrocatalytic conversion of CO2 to hydrocarbon and alcohol products: Realities and prospects of Cu-based materials. *Sustainable Materials and Technologies*, 25:e00200, 2020.

[27] Haochen Zhang, Jing Li, Mu-Jeng Cheng, and Qi Lu. CO electroreduction: Current development and understanding of Cu-based catalysts. *ACS Catalysis*, 9(1):49–65, 2019.

[28] Qiang Zhang, Shuihui Tao, Jun Du, Anbang He, Yong Yang, and Changyuan Tao. A cold plasma-activated in situ AgCo surface alloy for enhancing the electroreduction of CO2 to ethanol. *Journal of Materials Chemistry A*, 8(17):8410–8420, 2020.

[29] Yao Zheng, Anthony Vasileff, Xianlong Zhou, Yan Jiao, Mietek Jaroniec, and Shi-Zhang Qiao. Understanding the roadmap for electrochemical reduction of CO2 to multi-carbon oxygenates and hydrocarbons on copper-based catalysts. *Journal of the American Chemical Society*, 141(19):7646–7659, 2019.

[30] Qun Fan, Mingli Zhang, Mingwen Jia, Shizhen Liu, Jieshan Qiu, and Zhenyu Sun. Electrochemical CO2 reduction to C2+ species: Heterogeneous electrocatalysts, reaction pathways, and optimization strategies. *Materials Today Energy*, 10:280–301, 2018.

[31] Selwyn Hanselman, Marc T. M. Koper, and Federico Calle-Vallejo. Computational comparison of late transition metal (100) surfaces for the electrocatalytic reduction of CO to C2 species. *ACS Energy Letters*, 3(5):1062–1067, 2018.

[32] Isis Ledezma-Yanez, Elena Pérez Gallent, Marc T. M. Koper, and Federico Calle-Vallejo. Structure-sensitive electroreduction of acetaldehyde to ethanol on copper and its mechanistic implications for CO and CO2 reduction. *Catalysis Today*, 262:90–94, 2016.

[33] Jinmo Kim, Woong Choi, Joon Woo Park, Cheonghee Kim, Minjun Kim, and Hyunjoon Song. Branched copper oxide nanoparticles induce highly selective ethylene production by electrochemical carbon dioxide reduction. *Journal of the American Chemical Society*, 141(17):6986–6994, 2019.

[34] Hemma Mistry, Ana Sofia Varela, Cecile S. Bonifacio, Ioannis Zegkinoglou, Ilya Sinev, Yong-Wook Choi, Kim Kisslinger, Eric A. Stach, Judith C. Yang, Peter Strasser, and Beatriz Roldan Cuenya. Highly selective plasma-activated copper catalysts for carbon dioxide reduction to ethylene. *Nature Communications*, 7:12123, 2016.

[35] Xiaofeng Feng, Kaili Jiang, Shoushan Fan, and Matthew W. Kanan. A direct grain-boundary-activity correlation for CO electroreduction on Cu nanoparticles. *ACS Central Science*, 2(3):169–174, 2016.

[36] Lei Wang, Stephanie A. Nitopi, Erlend Bertheussen, Marat Orazov, Carlos G. Morales-Guio, Xinyan Liu, Drew C. Higgins, Karen Chan, Jens K. Nørskov, Christopher Hahn, and Thomas F. Jaramillo. Electrochemical carbon monoxide reduction on polycrystalline copper: Effects of potential, pressure, and ph on selectivity toward multicarbon and oxygenated products. *ACS Catalysis*, 8(8):7445–7454, 2018.

[37] Federico Calle-Vallejo and Marc T. M. Koper. Theoretical considerations on the electroreduction of CO to C2 species on Cu(100) electrodes. *Angewandte Chemie International Edition*, 52(28):7282–7285, 2013.

[38] N. S. Romero Cuellar, K. Wiesner-Fleischer, M. Fleischer, A. Rucki, and O. Hinrichsen. Advantages of CO over CO2 as reactant for electrochemical reduction to ethylene, ethanol and n-propanol on gas diffusion electrodes at high current densities. *Electrochimica Acta*, 307:164–175, 2019.

[39] Klaas Jan P. Schouten, Zisheng Qin, Elena Pérez Gallent, and Marc T.M. Koper. Two pathways for the formation of ethylene in CO reduction on single-crystal copper electrodes. *Journal of the American Chemical Society*, 134(24):9864–9867, 2012.

[40] Maitland C. Boswell and J. V. Dickson. The action of sodium hydroxide on carbon monoxide, sodium formate and sodium oxalate. *Journal of the American Chemical Society*, 40(12):1779–1786, 1918.

[41] J. Hietala, A. Vuori, P. Johnsson, I. Pollari, W. Reutemann, and H. Kieczka. *Formic Acid*, pages 1–22. 2011.

[42] Susan Topham, Alexis Bazzanella, Sebastian Schiebahn, Sebastian Luhr, Li Zhao, and Alexander Otto. *Carbon Monoxide*. 2001.

[43] Yuvraj Y. Birdja and Marc T. M. Koper. The importance of cannizzaro-type reactions during electrocatalytic reduction of carbon dioxide. *Journal of the American Chemical Society*, 139(5):2030–2034, 2017.

[44] Dan Ren, Nian Tee Wong, Albertus Denny Handoko, Yun Huang, and Boon Siang Yeo. Mechanistic insights into the enhanced activity and stability of agglomerated Cu nanocrystals for the electrochemical reduction of carbon dioxide to n-propanol. *Journal of Physical Chemistry Letters*, 7(1):20–24, 2016.

[45] Erlend Bertheussen, Arnau Verdaguer-Casadevall, Davide Ravasio, Joseph H. Montoya, Daniel B. Trimarco, Claudie Roy, Sebastian Meier, Jürgen Wendland, Jens K. Nørskov, Ifan E. L. Stephens, and Ib Chorkendorff. Acetaldehyde as an intermediate in the electroreduction of carbon monoxide to ethanol on oxide-derived copper. *Angewandte Chemie International Edition*, 55(4):1450–1454, 2016.

[46] Xiaoxia Chang, Arnav Malkani, Xuan Yang, and Bingjun Xu. Mechanistic insights into electroreductive C–C coupling between CO and acetaldehyde into multicarbon products. *Journal of the American Chemical Society*, 142(6):2975–2983, 2020.

[47] Bernhard Schmid, Christian Reller, Sebastian Neubauer, Maximilian Fleischer, Romano Dorta, and Guenter Schmid. Reactivity of copper electrodes towards functional groups and small molecules in the context of CO2 electroreductions. *Catalysts*, 7(5):161, 2017.

[48] F. E. Paulik and J. F. Roth. Novel catalysts for the low-pressure carbonylation of methanol to acetic acid. *Chemical Communications*, (24):1578a–1578a, 1968.

[49] James F. Roth. The production of acetic acid. *Platinum metals review*, 19(1):12–14, 1975.

3

Anisotropic Cathodic Corrosion of Gold Electrodes in Absence and Presence of CO

In this work, we investigate gold surface dissolution under cathodic potentials as a function of crystal orientation using cyclic voltammetry, SEM and AFM, to determine to what extent cathodic corrosion is anisotropic in nature. Additional experiments were performed to gain insights into the effect of the presence of CO on cathodic corrosion. Carbon monoxide experiments were conducted to investigate the effect of more realistic reaction conditions on cathodic corrosion as they might be found in gold-driven CO_2-electrolyzers, although effects of the presence of CO_2 (reactant) and carbonate salts (typically present in the reaction medium) were excluded from this study. It was found that cathodic corrosion of gold is strongly anisotropic, with stepped surfaces and the {110} plane being most susceptible to dissolution, whereas the {111} and {100} planes were much more resilient to dissolution. On these more stable surfaces, nanocrystallite growth was observed instead, which we hypothesize originates from redeposition of the gold that dissolves from the more corrosive, more open and/or defective facets. Finally, the presence of carbon monoxide was found to slightly enhance the rate of surface change, as evidenced by increases in charge in cyclic voltammograms after corrosion and an earlier onset of crystallite growth on the {111} and {100} planes, which we ascribe to enhanced gold mobility due to the strong bond formed between CO and gold in alkaline media.

This chapter has been published in
Raaijman, S. J.$^{=}$; Arulmozhi, N.$^{=}$; Koper, M. T. M., *J. Phys. Chem. C* **2020**, *124* (52), 28539-28554.

3.1. Introduction

With the predicted strong growth of renewable energy sources[1], their intermittency will become increasingly problematic. One option for dealing with the intermittency is to electrochemically generate value-added products at times when the supply supersedes demand. The electrochemical conversion of carbon dioxide and water, or the CO_2 reduction reaction (CO2RR), would make a suitable contender for this role as it can yield a plethora of valuable products in the form of hydrocarbons, carbohydrates and (inorganic-) acids. However, the CO2RR requires a suitable catalyst to facilitate the efficient conversion of electrical work into chemical products. Fortunately, catalysts exist that are capable of reducing carbon dioxide to economically interesting products with good selectivity and efficiency: gold[2] and silver[3] are capable of forming carbon monoxide with high selectivity, indium[4] and palladium[5] are selective for the formation of formic acid and, depending on the exact conditions, copper can produce ethylene[6] or ethanol[7] with very reasonable efficiencies.

However, the applicability of a catalyst is subject to stringent performance tolerances for it to be economically viable. Two important metrics are catalyst cost and lifetime[8], since replacement of spent catalyst requires capital and leads to process downtime, reducing overall profitability. Under CO2RR relevant conditions (negative potentials, high current flows, high local pH values and large amounts of product), metals can undergo substantial morphological restructuring and possibly dissolve due to cathodic corrosion (CC).[9] Cathodic corrosion is a degradation pathway that might prove quite relevant for catalyst stability and long term performance in CO_2-electrolyzers. This phenomenon has been mainly studied on platinum electrodes[9–12], leading to the formation of nanoparticles in solution and etch pits on the metal surface, resulting in the generation of specific surface sites.[12] It has been hypothesized that these pits originate from atom clusters being expelled from the surface via the formation of a negatively charged ternary metal hydride complex.[11] The process itself has been shown to depend strongly on cation identity and concentration, and there seems to be good agreement between the onset of corrosion and the specific potential window where adsorption of a full monolayer of hydrogen becomes energetically favorable.[11]

At present, CO_2-electrolyzers focusing on HCOOH or CO production are regarded as closest to commercialization, with CO having a larger market.[13] The best catalysts for producing CO are silver and gold, both exhibiting high selectivity at low overpotentials.[2, 3, 14] However, both metals have been reported to undergo cathodic corrosion.[9]

Therefore, we explore in this work the cathodic corrosion of gold single crystal electrodes, showing evidence for a strong anisotropic effect both with regards to pitting, and for nanocrystal formation. The choice to study gold is based on the fact that the field of gold single crystal electrochemistry is mature and expansive[15–17] and experimentally more accessible.[18, 19] There already exists literature on its cathodic corrosion behavior (for polycrystalline surfaces)[9, 11, 20], showing that gold exhibits a tendency to form (nano-) crystallites on the surface.[20] An additional motivation for the work in this paper is that cathodic corrosion has been studied predominantly under HER conditions, as opposed to CO2RR conditions.[21] Trends in macroscopic pitting and deposition phenomena as a function step type and step density were investigated on spherical single crystals (Au(sphere)), whilst cut crystals (Au(hkl)) enabled us to deconvolute electrochemical signals from Au(sphere) crystals. Finally, experiments were conducted with the addition of gaseous CO to the electrochemical cell as a means to approximate realistic CO2RR conditions.[6]

3.2. Methods

3.2.1. Electrodes, electrolytes, and electrochemical Cells

The experimental work was conducted using monocrystalline bead-type Au(111), Au(110) and Au(100) electrodes (icryst, oriented to $\leq 0.1^{\circ}$), and Au(spherical) working electrodes (WE) prepared using the flame fusion method.[22–24] Prior to each measurement, spherical single crystals were entirely regrown and flame annealed immediately prior to measuring, while cut crystals were annealed at ca. $950\ ℃$ in a pure hydrogen flame for at least $5\ minutes$. A gold mesh (99.999%) was used as a counter electrode (CE), and a reversible hydrogen electrode (RHE) (Hydroflex, Gaskatel) was used as a reference electrode (RE). Two types of custom-made electrochemical cells were employed in this study, namely a Pyrex glass cell and a fluorinated ethylene propylene (FEP) cell. The two-compartment Pyrex glass cell was used in all CV measurements in acid media and the FEP cell was employed in cathodic corrosion measurements in alkaline media. The FEP cell consists of a single compartment with ca. $3\ cm$ of distance between the CE and the WE surface. The H_2SO_4 (96%, ultrapur, Millipore) and NaOH (30%, suprapur, Millipore) electrolyte solutions were prepared using ultra-high purity (UHP) Milli-Q water (Millipore; resistivity $\geq 18.2\ M\Omega \cdot cm$). Glassware and plasticware were cleaned by storing it in aqueous permanganate solution ($0.5\ M$ H_2SO_4 (96%, ACS reagent, Honeywell) and $1\ g \cdot L^{-1}$ $KMnO_4$ (99%, ACS reagent, Sigma Aldrich)). Prior to the experiment, permanganate residue was removed by rinsing with Milli-Q water and washing with diluted piranha solution (3:1 *v/v* mix of H_2SO_4 (96%) and H_2O_2 (30%), diluted with water) to remove manganese dioxide and permanganate residue. Next, glassware was boiled five times in Milli-Q water.

Ultra-high purity argon (Linde, 6.0) was passed through and above the electrolyte to remove any dissolved gases. Prior to establishing electrode-electrolyte contact, argon flow through the electrolyte is stopped while the argon flow above the electrolyte is maintained or initiated. After annealing the monocrystalline gold electrodes, the hot electrode is subsequently transferred to the electrochemical cell and cooled in argon atmosphere. Once cooled to room temperature, the so-called hanging meniscus configuration was used for making electrochemical contact of the Au(111), Au(110), and Au(100) electrodes. In the case of Au(spherical)[25], the electrode was carefully placed in the electrolyte so that the monocrystalline gold sphere was entirely submerged. All electrochemical experiments were conducted using a Bio-Logic SP 300 potentiostat using proprietary software. All surfaces were normalized assuming $390\ \mu C \cdot cm^{-2}$ (the value assigned to polycrystalline gold), which was deemed to best represent the imperfect nature of the cut single crystals, and the fact that many different sites are present on spherical single crystals.[26] CVs obtained post-corrosion were normalized using the surface area calculated from the blank obtained prior to corrosion.

3.2.2. Cathodic corrosion studies

The cathodic corrosion studies were performed at Au(111), Au(110), Au(100) and Au(spherical) electrodes via application of a constant potential (E_p in the range between $-1.10\ V_{RHE}$ and $-1.30\ V_{RHE}$) for a controlled polarization time (t_p, with $2.5 < t_p < 7.5\ minutes$) in $10\ M$ NaOH at room temperature. These conditions were chosen on account of the fact that the least cathodic potential and shortest time was close to the observable onset for surface restructuring from SEM, whereas the upper limit (most cathodic potential and longest time) showed large surface changes but could still be related to the initial faceting. Specifically, shorter times at less cathodic potentials were not tried, as the current least corrosive conditions ($2.5\ minutes$ at $-1.1\ V_{RHE}$) exhibited only minor signs of change in SEM images. More strongly cathodic potentials ($5\ minutes$ at $-1.5\ V_{RHE}$, not shown) were initially tested, but resulted in such drastic changes that it became impossible to correlate the initial substrate structure to the morphology observed in the SEM after corrosion. Some tests were conducted for longer times ($1.5\ hour$ at $-1\ V_{RHE}$, Figure B.4) as well, but corrosion for such long times resulted in significant issues with surface cleanliness, being detrimental to experiment reproducibility. The electrolyte was used for either a maximum of $10\ minutes$ of corrosion time, or a total of three separate measurements (depending on which metric was reached first), after which it was discarded and the cell thoroughly rinsed, and fresh electrolyte added. All corrosion measurements were conducted using a freshly prepared electrode surface. For all corrosion experiments, Ar or CO was bubbled through the solution before *and during* the experiment. Cathodic polarization studies were conducted with the cell submerged in a water bath at room temperature with a magnetic stirrer (in the water bath) to prevent electrolyte heating.

Figure 3.1 displays a potential versus time profile that illustrates the sequence of steps (a through e) involved in the corrosion studies.

- Firstly (step a), a cyclic voltammogram (CV) is measured in $0.05\ M$ H_2SO_4 electrolyte in the potential window $0 \leq E \leq 1.65\ V_{RHE}$ at a scan rate of $\nu = 80\ mV \cdot s^{-1}$ to characterize the initial surface.

- Secondly (step b), the electrode is rinsed with Milli-Q water and flame annealed in either a hydrogen flame of ca. $950\ ℃$ for $5\ minutes$ (cut crystals) or in a butane flame until the gold surface is faintly red hot for $5\ minutes$ (spherical crystals) to remove the defects generated in step a.

- Thirdly (step c), the electrode is immersed in $10\ M$ NaOH (at controlled potential of $0\ V_{RHE}$), but not in hanging meniscus configuration in this instance. Then, the potential is stepped from $E = 0\ V_{RHE}$ to a certain (85%) iR compensated polarization potential E_p (in Figure 3.1, $E_p = -1.30\ V_{RHE}$); for a defined polarization time t_p (in Figure 3.1, $t_p = 2.5\ minutes$).

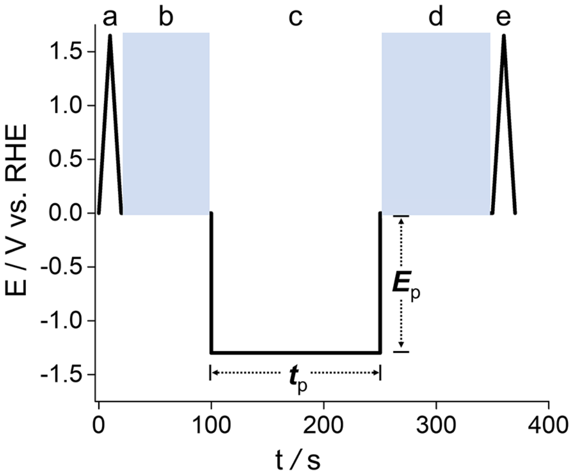

Figure 3.1: The potential program employed in the cathodic corrosion studies. Step a: cyclic voltammetry in the sulfate adsorption/desorption region and gold oxidation/reduction region in $0.05\ M$ H_2SO_4 at a scan rate of $\nu = 80\ mV \cdot s^{-1}$. Step b: Cleaning the electrode in Milli-Q water and annealing for $> 5\ minutes$. Step c: cathodic corrosion in $10\ M$ NaOH aqueous solution at a given potential E_p for a given time t_p. Step d: Cleaning the electrode with Milli-Q water. Step e: cyclic voltammetry in the sulfate adsorption/desorption region and gold oxidation/reduction region in $0.05\ M$ H_2SO_4 at a scan rate of $\nu = 80\ mV \cdot s^{-1}$.

- Thereafter (step d), the cathodically corroded crystal is rinsed with Milli-Q water for sodium hydroxide removal
- Finally (step e), the electrode surface after corrosion is characterized again via cyclic voltammetry as described in step a.

Due to the variation in the potential sensitivity of different facets with regards to adsorption of ions, cyclic voltammetry in H_2SO_4 (in the window $0 \leq E \leq 1.65\ V_{RHE}$)[15–17] can be used to characterize changes in surface structure via comparison of CV profiles obtained prior to and after cathodic treatment.

3.2.3. Microscopic analysis of cathodic corrosion

Surface roughening of the monocrystalline Au(spherical) electrodes brought about by cathodic corrosion was analyzed using Scanning Electron Microscopy (SEM, Apreo SEM, Thermo Scientific) and Atomic Force Microscopy (AFM, JPK Nanowizard 4). After the corrosion experiment, the monocrystalline Au electrode was carefully removed from the electrochemical cell and placed in a custom-made SEM sample holder. Then, the sample was rinsed under a stream of Milli-Q water to remove traces of acid from the electrode. Subsequently, the monocrystalline Au(spherical) electrode was dried in a stream of Ar(g) and placed in the SEM/AFM chamber for analysis. The SEM was operated in high vacuum condition ($< 5 \cdot 10^{-6}\ mbar$) and the images were collected at a beam setting of $10\ kV$ and $0.40\ nA$ using an Everhart-Thornley detector. The AFM measurements were conducted in contact mode, using a gold coated tip (NANOSENSORS™ PPP-FMAuD; tip height $10-15\ \mu m$, tip resonance frequency: $75\ kHz$, tip force constant: $2.8\ N \cdot m^{-1}$) at a scan rate of $0.4\ Hz$. Crystals not being actively measured/used were affixed in a custom holder and stored in a plastic vial so as to minimize ambient exposure.

In order to identify the main surface facets of a Au(spherical) electrode, we compare the FCC unit cell to an SEM image of a corroded Au(spherical) electrode. Figure 3.2a shows an SEM image of an as-imaged monocrystalline Au(spherical) electrode and Figure 3.2b presents the FCC lattice structure of a Au single crystal, with the low Miller index facets depicted using different colors (i.e., {111} in red, {100} in blue, and {110} in green). In the SEM image, stereographic triangles are superimposed using grey, dashed lines. The SEM instrument was equipped with a three-axis goniometer and allowed us to orient the monocrystalline Au(spherical) electrode and to acquire SEM images that were then superimposed on the simulated single crystal. Once superimposed with reasonable accuracy ($\pm 3^{\circ}$), we can identify the location of the main surface facets on the actual monocrystalline Au(spherical) electrode. One stereographic triangle in the actual and simulated single crystals is marked with black lines; it contains all basal, stepped and kinked facets. It is important to add that one FCC single crystal contains forty-eight stereographic triangles. Figure 3.2c presents a partially color-coded visualization of this triangle and shows as solid circles the locations of the facets which are the subject of our study. As explained above, the low Miller index surfaces are marked by red, blue, and green filled circles located at the vertices of the triangle; stepped surfaces are located along edges of the triangle. Kinked surfaces are located inside of the triangle.

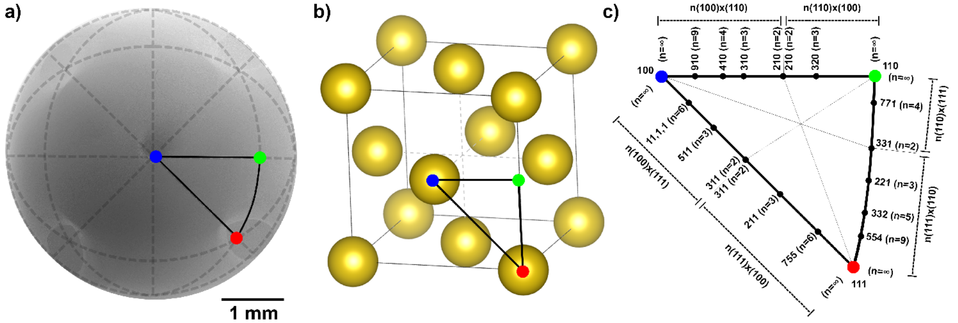

Figure 3.2: The methodology of surface facet identification on a Au(spherical) electrode. a) An SEM image of an actual (corroded) Au(spherical) electrode. b) An image of the FCC lattice that a spherical Au single crystal adopts, with the low Miller index facets depicted using different colors (i.e., (111) in red, (100) in blue, and (110) in green). One stereographic triangle in these two images is marked using a black, solid line. c) Color-coded visualization of a stereographic triangle, showing the locations of the surface structures which are the subject of our study.

Table 3.1: Different potential windows that comprise the gold oxide formation region in $0.05\ M$ H_2SO_4, adapted from work published by Štrbac *et al.*[17]

Potential window	**Sites that contribute**	**Denotation in text**
$1.35 < E < 1.40\ V_{RHE}$	111-, 100- and 110-type step-sites	"step-sites"
$1.39 < E < 1.42\ V_{RHE}$	110 terraces (infinite length, *secondary feature*) • shifts to more negative potentials and combines with primary 110 feature in the case of finite length terraces with 100-type step defects. • increases in peak current but stays in place in the case of finite length terraces with 111-type step defects.	Stepped terraces: "stepped {110}", "finite length {110} terraces"
$1.41 < E < 1.43\ V_{RHE}$	100 terraces (finite and infinite length)	"{100} terraces"
$1.43 < E < 1.46\ V_{RHE}$	110 terraces (infinite length, *primary feature*) • shifts to more negative potentials and combines with secondary feature in the case of finite length terraces with 100-type step defects. • exhibits minor shift to more positive potentials in the case of finite length terraces with 111-type step defects.	"{110} terraces"
$1.46 < E < 1.62\ V_{RHE}$	Finite length 111 terraces terminated by a 111- or 100-type step	"stepped {111}", "finite length {111} terraces"
$1.46 < E < 1.57\ V_{RHE}$	(subset) Small 111 terraces (N < 6 atoms), terminated by a 111- or 110-type step	"small {111} terraces", "small finite length {111}"
$1.57 < E < 1.62\ V_{RHE}$	(subset) Large 111 terraces (N > 6 atoms), terminated by a 111- or 110-type step	"large {111} terraces", "large finite length {111}"
$1.62 < E < 1.64\ V_{RHE}$	'Infinite' length 111 terraces	"{100} terraces"

3.3. Results and discussion

3.3.1. Voltammetric characterization of cathodic corrosion

Cathodic corrosion was investigated on single crystals oriented and cut to expose a specific facet, and on spherical single crystals that were not cut and thus contain a multitude of different types of facets. The changes in the cyclic voltammetry as a function of corrosion potential were investigated for the three basal planes (Au(111), Au(100) and Au(110)) as well as for a spherical single crystal (Au(sphere)), where trends observed on the former will be used to interpret behavior observed on the latter.

Cyclic voltammetry was conducted in $50\ mM$ sulfuric acid electrolyte between $0 < E < 1.65\ V_{RHE}$ at a scan rate of $80\ mV{\cdot}s^{-1}$ to facilitate comparison to literature data.[17] Under such conditions, the gold oxidation region ($1.35 < E < 1.65\ V_{RHE}$) exhibits a number of characteristic zones defined by the hydroxide/oxygen adsorption strength of a particular (set of) surface site(s). In this work, we focus on the gold oxidation region, because the effect of introducing different types of steps at differing step densities on this region has been thoroughly studied and reported. Furthermore, changes in step density result in gradual changes in the gold oxidation region. Hence, we focus on investigating the oxidation region as opposed to the double layer region. Although not discussed herein, close ups of the double layer region are provided in the supporting information (Figure B.5). The different regions, their accompanying potential window, and the way they are referred to in this work are summarized in Table 3.1.

Analysis of CV changes in the hydroxide/oxygen adsorption region will allow for the determination of global trends in the creation and destruction of specific types of facets. Rather than the direct conversion of one site to another, it is the formation of pits and/or nanocrystals that are responsible for the creation of specific sites as will be discussed later in this work. We start by discussing the cyclic voltammetry of the $\{111\}$ plane, which is depicted in Figure 3.3a. For this surface, the characteristic feature of infinite $\{111\}$ terrace sites at $1.63\ V_{RHE}$ is observed to decrease in current density and shift to less positive potentials after cathodic corrosion. From the assignment of the different regions of hydroxide/oxygen adsorption on gold in Table 3.1, this shift is indicative of the creation of large finite length $\{111\}$ terraces with step defects. Thus, this particular change in the CV denotes the introduction of step-site defects in the ‘infinite’ $\{111\}$ plane upon corrosion.

Simultaneously, the charge in the $1.46 < E < 1.57\ V_{RHE}$ region is found to increase as more corrosive potentials are applied, which is again evidence for $\{111\}$ terraces with step defects. However, the terraces in this region are of smaller size (i.e., higher step density). As we will show below, these newly formed stepped facets likely relate to the formation of etch pits and nanocrystallites in and on the surface, respectively. Finally, the defects that were initially present in the cut Au(111) surface ($1.35 < E < 1.40\ V_{RHE}$, Table 3.1) exhibit non-monotonic behavior as a function of corrosion potential. Their quantity (i.e., the charge corresponding to their features) decreases for more moderate (i.e., less negative) corrosive

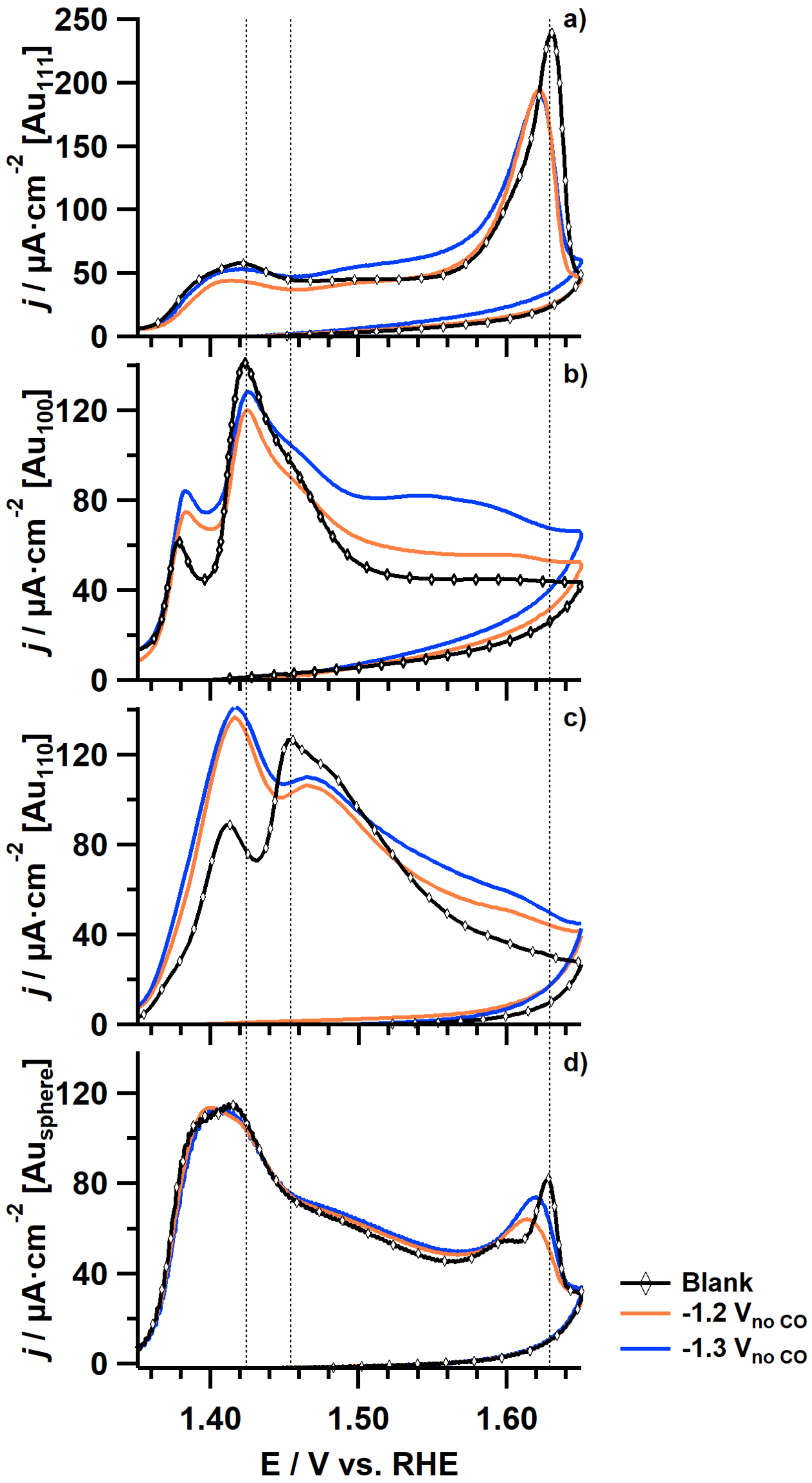

Figure 3.3: Cyclic voltammogram of a) Au(111), b) Au(100), c) Au(110) and d) Au(spherical) after $2.5\ minutes$ of corrosion in $10\ M$ NaOH at $-1.2\ V_{RHE}$ (orange) and $-1.3\ V_{RHE}$ (blue) (85% iR corrected), compared to the blank obtained prior to corrosion (black with diamonds).

potentials, whereas this decrease in the number of these sites is less pronounced for more strongly corrosive potentials (e.g., moderate levels of CC actually result in a reduction of these type of defect sites, but this effect is less at more strongly corrosive conditions).

The voltammetry of the {100} surface is shown in Figure 3.3b. For this facet, the characteristic feature at $1.42\ V_{RHE}$ is found to initially slightly decrease in peak intensity upon corrosion. However, surfaces corroded more vigorously (i.e., having been subjected to increasingly negative potentials) exhibit less of a decrease in the number of {100} terraces than surfaces corroded under milder conditions, although the peak is still lower than for an uncorroded surface. The first observation suggests that under mild cathodic potentials (with respect to the onset of cathodic corrosion, $-0.8\ V$[20]), {100} terrace sites are being transformed and/or destroyed. The second observation can be explained by taking into account that finite length {100} terraces give rise to a broad contribution in the same region as infinite {100} terraces, the two eventually being indistinguishable from one another. Thus, although we are corroding our initially 'perfect' 100 plane, it is still possible to observe a gain in charge in the {100}-terrace-characteristic potential window if we assume that corrosion leads to the creation of finite length {100} terraces. Corrosion of the {100} terraces is further corroborated by an increase of step-site defects (feature at $1.38\ V_{RHE}$, Table 3.1) as increasingly cathodic potentials are applied. Finally, it is observed that corrosion of the {100} plane leads to a substantial increase in the number of stepped {111} terrace sites, as denoted by an increase in charge in the $1.46 < E < 1.62\ V_{RHE}$ region. Apparently, corrosion introduces specifically {111}-type step defects into the {100} surface and thereby transitions the overall surface morphology in the direction of the {111} plane.

Corrosion behavior of the most open of the basal planes, {110}, is shown in Figure 3.3c. Unlike the other two planes, this facet exhibits two characteristic features in the case of infinite terrace lengths: a weaker feature at $1.41\ V_{RHE}$ (denoted from here on as secondary), and a stronger one at $1.45\ V_{RHE}$ (which we shall refer to as primary). Under corrosive conditions, the primary feature decreases in current density. However, similar to what is observed for corrosion of the {100} plane, this decrease in peak current density is actually less when more corrosive potentials are applied. As for the secondary feature, it is found to monotonically increase with corrosion potential instead, without shifting. Finally, an increase in charge is observed for the region characteristic for finite length stepped {111} terraces. Taken together, these observations can only be explained by the transformation of the {110} plane into a surface that is rich in {111}-type sites. The fact that the primary {110} peak exhibits less of a decrease in current density as more corrosive potentials are applied, can be explained by the fact that finite-length {111} terraces contribute charge in a very broad potential range. Although the number of {110} terrace sites is expected to decrease more at stronger corrosive potentials, the contribution of charge by finite-length {111} terraces increases.

Figure 3.3d illustrates the transformation of the CV of a spherical single crystal upon cathodic corrosion. Overall, the changes in the CV of a spherical single crystal appear less pronounced than the changes for the cut single crystals. Notwithstanding, the following changes are observed upon cathodic corrosion. The characteristic feature of the infinitely large {111} terrace sites at $1.63\ V_{RHE}$ is observed to shift to less positive potentials, where it is presumed to (partially) merge with the voltammetric feature characteristic of large finite width stepped {111} terraces, leading to the maximum of the latter feature shifting to more positive potentials. Furthermore, an increase in charge for smaller stepped {111} terraces is observed. This behavior mimics what is observed upon corrosion of the {111} electrode, and can be explained by the creation of step-site defects, leading to finite length stepped {111} terraces with decreasing terrace lengths as the surface corrodes further.

Finally, small changes are observed in the (stepped-) {100} terraces, and step- and kink site regions (Table 3.1). This 'twin peak' feature merges into a single peak, showing only minor changes in peak current density without clear trend. More specifically, depending on corrosion conditions (not depicted), its current density can decrease or increase marginally. Such erratic behavior is in line with the behavior observed for corrosion of Au(111) specifically, where the charge for step-site defects could increase as well as decrease, depending on experimental conditions. Although such inconsistent behavior was not observed upon corrosion of the {100} plane, it can still be reasonably explained by the {111} plane being the dominant facet on gold spherical crystals due to them adopting the equilibrium crystal shape during growth (see Figure 3.2a).[27]

Since voltammetry for stepped {111} terraces is ambiguous ({100}- and {111}-type steps cannot be clearly distinguished via hydroxide/oxygen adsorption in the CV profile), the voltammetry measurements cannot provide direct evidence for the types of steps that are formed upon corrosion of the {111} plane, it might be preferentially one step-type, or both step-types.

3.3.2. Morphological characterization of cathodic corrosion

SEM anisotropy of the basal planes

Further information regarding the facet dependency of cathodic corrosion is derived from SEM images. Because of the Au spherical single crystal adopting the FCC equilibrium crystal shape, it is possible to determine the locations of all facets, so long as one can accurately pinpoint a minimum of two facets and knows the radius of the crystal. Under the effects of corrosion, finding two identification points is straightforward as can be seen in Figures 3.4a-c. From these figures, which depict a global overview of spherical single crystal electrodes corroded for different time intervals at $-1.3\ V_{RHE}$, it can be seen that the {100} and {111} facets are easily identified.

The anisotropy in corrosion that was identified from cyclic voltammetry experiments is also observed macroscopically in the SEM images. This can be seen in the form of differences in time-dependent evolution of the different basal planes, as well as in the differences in contrast for different locations on the surface. However, the anisotropic behavior is much clearer in the images shown in Figures 3.4d-l, where close-ups of the three basal planes are presented. More specifically, Figures 3.4d-f consist of higher magnification images of the {111} plane corroded for $2.5, 5$ and $7.5\ minutes$ at $-1.3\ V_{RHE}$ in $10\ M$ NaOH, respectively, whereas Fig-

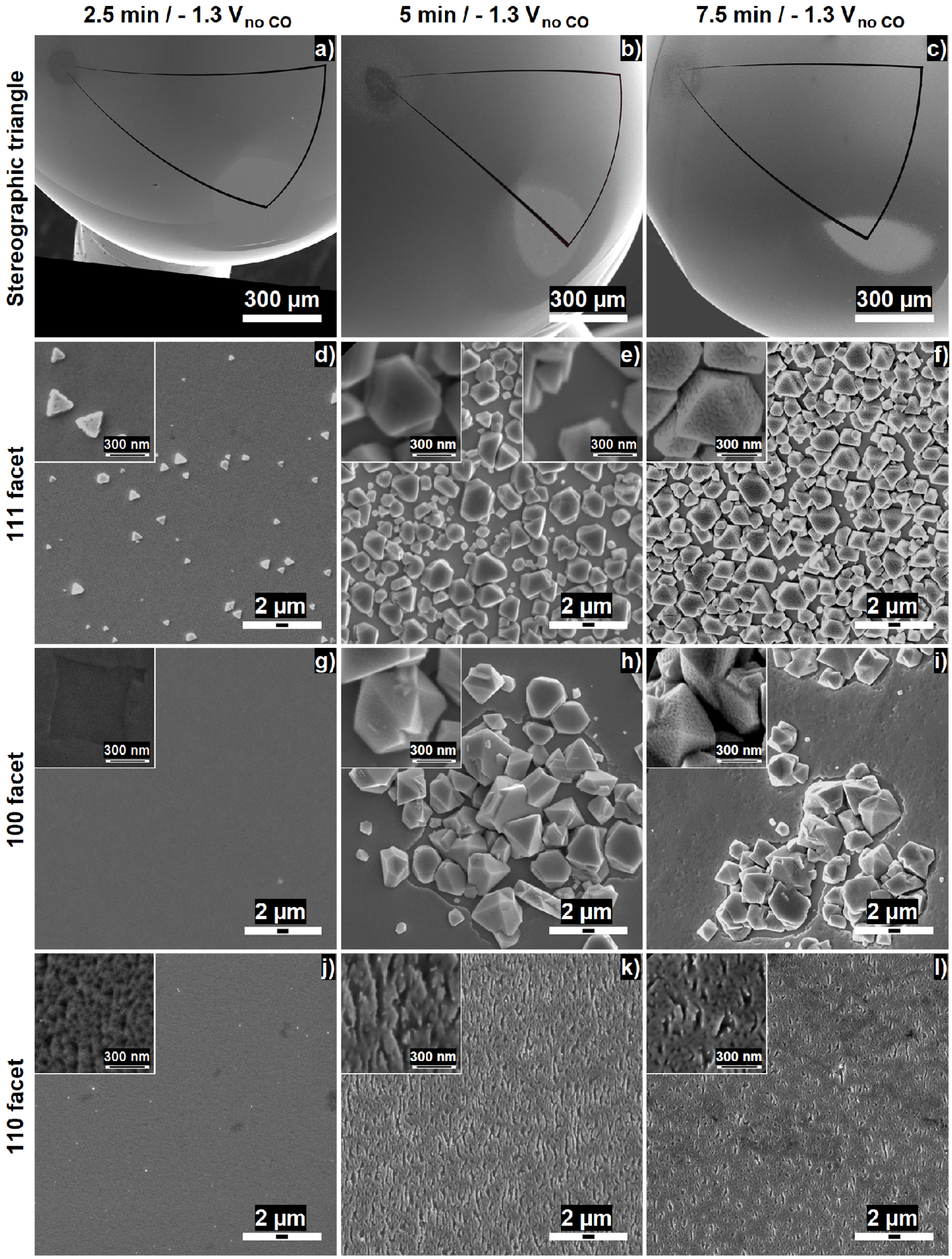

Figure 3.4: SEM images (macroscopic overview, 111 facet, 100 facet and 110 facet, respectively, going from the first to last row) of anisotropic surface corrosion in the form of pitting and nanocrystal formation as a function of time ($2.5\ min$ to $7.5\ min$, respectively, going from the left to right column) at a corrosion potential of $-1.3\ V_{RHE}$ (85% iR corrected) in $10\ M$ NaOH.

ures 3.4g-i and 3.4j-l are SEM images of the {100} and {110} faces under the same conditions.

From the expanded images, it can be seen that the morphological changes of the basal planes as a function of corrosion time differ per facet. The initially flat {111} face shows only very minor signs of pitting and etching, but does exhibit nanocrystal formation when certain corrosion potential and time thresholds are exceeded (specifically, $-1.2\ V_{RHE}$ for $\geq 7.5\ minutes$, Figures B.1a and B.1b). Of course, we realize that SEM cannot image truly nanoscopic changes on the surface. Regarding crystallite formation, uniformly distributed nanocrystals with a clear preference for triangular-prism (with the word prism denoting the top face to be parallel with and equal in shape to the base, like a column) and octahedral geometry start to form (Figures 3.4d and 3.4e), with crystallite density increasing as a function of corrosion time. Although pitting of the flat face is observed (Figure B.2a) after the onset of nanocrystal formation, these newly formed nanocrystals themselves exhibit much more prominent pitting (Figures 3.4e and 3.4f).

Compared to the {111} plane, only minor signs of surface pitting are observed for the {100} facet prior to the onset of nanocrystal formation. The earliest observed signs of pitting can be seen in Figure 3.4g (showing an uncommonly observed pit), but pits become more prevalent when nanocrystals start to grow (Figure B.2b). Again, at sufficiently cathodic conditions, nanocrystals are also observed on the ‘infinite’ {100} plane (specifically, $-1.3\ V_{RHE}$ for $\geq\ 5\ minutes$, compare Figure 3.4g to 3.4h) and these nanocrystals themselves are also susceptible to surface pitting (Figure 3.4i, inset). However, some differences exist when comparing nanocrystal formation on {100} and {111}. Firstly, the onset of nanocrystal formation is shifted to more cathodic potentials. Secondly, rather than depositing uniformly, nanocrystals on the {100} facet tend to cluster together (compare Figures 3.4e and 3.4h). Thirdly, whereas the nanocrystals that deposit on the {111} face preferentially adopt a triangular-prism geometry, the crystallites that form on the {100} face are better described as adopting shapes driven by a truncation process (where truncation refers to the (partial) cutting of the vertices of a polyhedron, resulting in the creation new faces in their stead) and/or aggregates of crystallites, with some of the smaller individual crystallites adopting an octahedral shape.

Cathodic corrosion-induced morphological changes for the {110} plane do not follow what is observed for the {111} and {100} planes. As opposed to mild surface pitting paired with nanocrystal growth under sufficiently corrosive conditions, severe surface pitting takes place without the formation of nanocrystals (see e.g., Figure 3.4l). Corrosion behavior of this facet is dominated by surface etching and pitting as can be seen in Figures 3.4j-l. The onset of pitting in the {110} face as observed in SEM images ($-1.1\ V_{RHE}$ for $\geq\ 5\ min$, Figures B.1c and B.1d) occurs earlier than SEM-observable morphology changes (e.g., pitting and/or nanocrystal formation) for the {111} and {100} faces, with the earliest signs of corrosion for the latter two faces requiring potentials equal to, or more negative than, $-1.2\ V_{RHE}$ at corrosion times exceeding $5\ minutes$.

The observed nanocrystal growth, where applicable, is found to depend on both corrosion time and corrosion potential. In Figures 3.4d-f, the corrosion time is varied for the same applied potential, showing a clear increase in nanocrystal density with respect to time. The potential dependency of nanocrystal formation is evident from comparing the onset potential for nanocrystal formation on the {111} face as discussed previously ($-1.2\ V_{RHE}$ for $\geq 7.5\ minutes$, Figures B.1a and B.1b) with the onset of nanocrystal formation at an applied potential of $-1.3\ V_{RHE}$: $\geq 2.5\ minutes$ (Figure 3.4d). This seems to suggest that nanocrystal formation depends on the buildup of a concentration gradient of dissolved gold ions, which would originate from surface etching under cathodic potentials. More cathodic potentials lead to faster dissolution, resulting in reaching supersaturation values sooner and thus an earlier onset of nanocrystal formation. However, the facets that exhibit nanocrystal deposition during corrosion experiments actually show little surface pitting prior to (and arguably after) the onset of nanocrystal formation. Rather than the flat basal planes being the origin of the gold ions, we hypothesize the gold ions to originate from the dissolution of facets with step defects as we expect them to be more corrosive.

AFM anisotropy of the basal planes

Further insight into surface dissolution and ion redeposition phenomena is derived from AFM imaging, shown for the three basal planes in Figure 3.5. Firstly, in Figures 3.5a-c, a $5x5\ \mu m$ AFM image and accompanying line profile and histogram for a corroded Au(111) surface are depicted. The AFM image agrees with SEM data (Figure 3.4e), showing nanocrystal growth with uniformly distributed nanocrystals with preferential triangular-prism geometry. From the line profile (Figure 3.5b), it becomes evident that these nanocrystals are have fairly flat tops that run parallel to the substrate on which they grow. Furthermore, the spots where nanocrystals are absent (purple-blue colored regions in Figure 3.5a) show little variation in height. Hence, the majority of the roughening occurring for this facet stems from the growth of nanocrystals, rather than from dissolution/corrosion of the surface itself. This also agrees with previously discussed SEM data, where parts of the surface that do not contain crystallites look to be 'smooth'.

An AFM image of the {100} plane, with accompanying line profile and histogram can be seen in Figures 3.5d-f, respectively. Contrary to the behavior of nanocrystal growth on the {111} plane, nanocrystals that grow on the {100} plane have the tendency to form clusters of crystallites, resulting in non-uniform surface coverage. Furthermore, the clustering results in nanocrystals that have seemingly arbitrary shapes, although smaller individual crystallites exhibit preference for an octahedral geometry, as observed from both SEM and AFM. Contrary to the smoothly terminated 'plateau-like' nanocrystals that form on the {111} face, the nanocrystals that grow on the {100} face are better described as 'mountainous'. As for corrosion of the plane underneath the nanocrystals, a fairly smooth surface can be observed; in line with what we find for the etching of Au(111).

The final facet, Au(110), is shown in Figures 3.5g-i, containing respectively an AFM image, and accompanying line profile and histogram. For this plane, no nanocrystal formation is observed upon corrosion, which is in line with what SEM data show (Figure 3.4k). However, the surface clearly exhibits pitting, with these

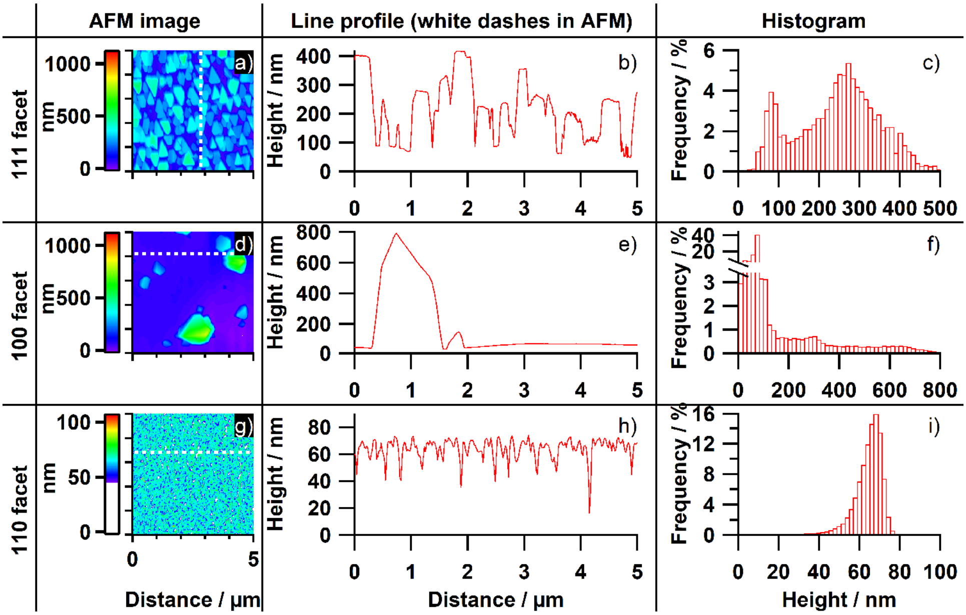

Figure 3.5: AFM images, line profiles and histograms (columns 1, 2 and 3, respectively) for the basal planes ({111}: a-c, {100}: d-f, and {110}: g-i) after cathodic corrosion at –1.3 V_{RHE} (85% iR corrected) for 5 $minutes$, in 10 M NaOH.

pits being distributed uniformly across the surface and reaching depths of several tens of nanometers.

3.3.3. Enhanced corrosion at stepped surfaces

Due to the regularity of spherical single crystals, facets with step- and kink site defects are located between the basal planes on the stereographic triangle, with the step density increasing as one moves further away from any of the three basal planes. As such, it is possible to investigate surface morphology after corrosion as a function of step type and step density by imaging different parts of the three sides of the stereographic triangle as defined by the {111}, {100} and {110} faces. The results of such an experiment are shown in Figure 3.6 (identical corrosion conditions as in Figures 3.4e, h and k), wherein we traverse along the edges of the stereographic triangle and take an image of the surface at equidistant intervals, varying step density and transitioning step types along the way.

Corrosive effect of introducing minor amounts of defects in {100} and {111} planes

The effect of incorporating a small number of step-site defects (i.e., low step density) into 'infinitely large' (unstepped) {100} and {111} terraces can be investigated by comparing Figure 3.4h ('perfect' {100}) with Figures 3.6a and 3.6o (n{100}x{110} and (n{100}x{111}) – and by comparing Figure 3.4e ('perfect' {111})

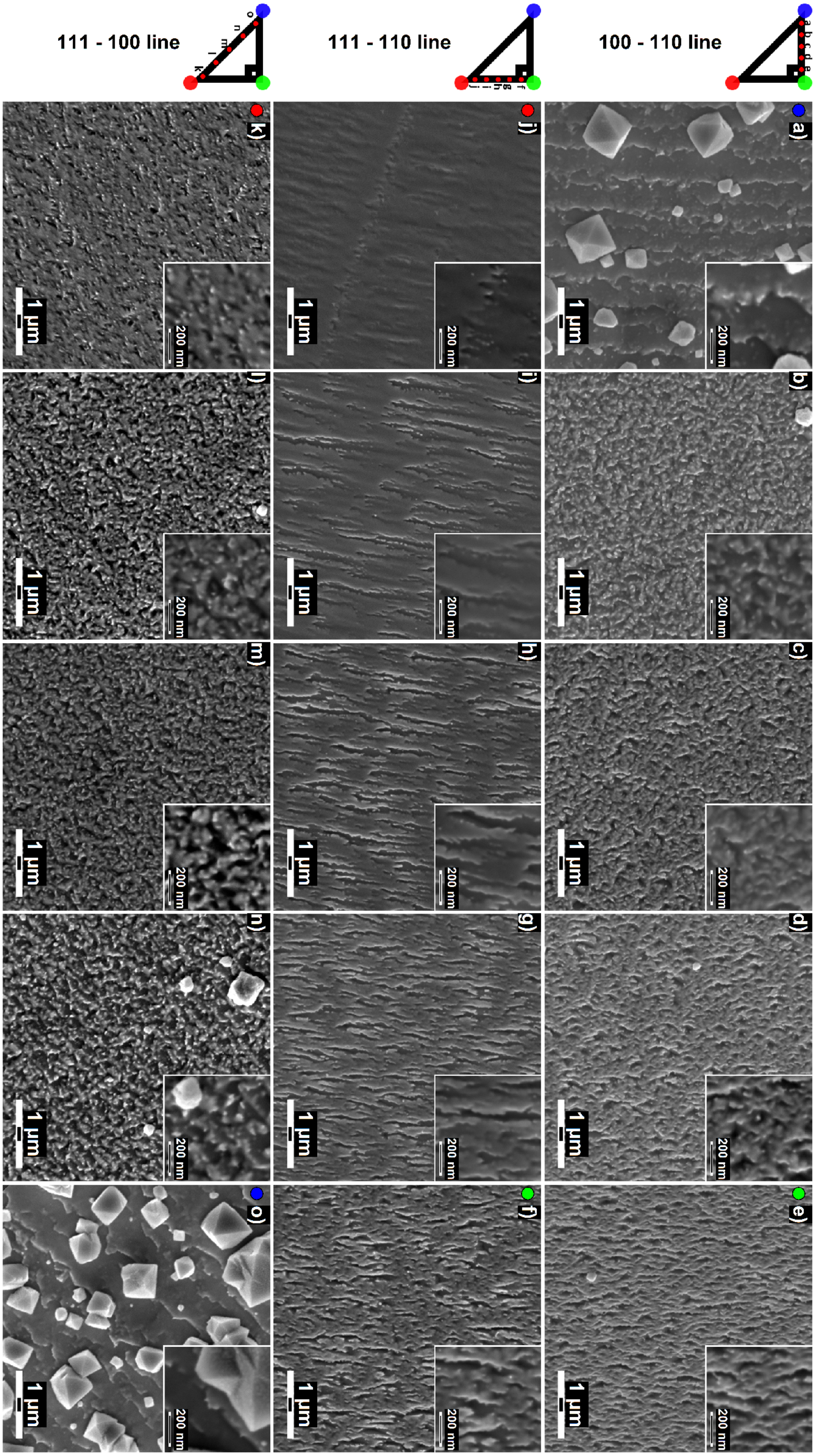

Figure 3.6: Effect of step-type and step density on macroscopic corrosion phenomena at $-1.3\ V_{RHE}$ (85% iR corrected) for $5\ minutes$, as investigated by traversing the stereographic triangle in its entirety.

with Figures 3.6j and 3.6k (n{111}x{110} and n{111}x{100}). For this comparison, we shall neglect nanocrystal growth on the infinite terraces, and focus on the areas in the SEM images that do not contain nanocrystals (e.g., in-between crystallites such as in the right inset in Figure 3.4e and/or nanocrystal-free patches, like the corners in Figure 3.4h). From these images it is found that the infinite {100} and {111} faces yield much smoother surfaces post corrosion as compared to the same surfaces with a minor density of step-site defects, which yield visually coarser surfaces upon corrosion (mind the two-fold difference in magnification between Figures 3.4 and 3.6). Since the presence of small amounts of step-site defects results in visually more roughened surfaces upon corrosion, and due to the fact that these facets with low step density are located in close spatial proximity to their unstepped counterparts, we hypothesize that dissolution of gold atoms at these stepped facets drive the concentration gradient that we think is responsible for nanocrystal formation as observed on the 'infinite' {111} and {100} faces.

Corrosive effect of varying the density of {110}-type steps in {100} and {111} planes

We start the investigation into the effect of step type and step density on corrosion behavior by looking at the effect of {110} step-site defects terminating {100} and {111} terraces (Figures 3.6a, b, c and 3.6h, i, j, respectively). From these images, it can be seen that surfaces that contain {110} step-site defects are highly susceptible towards cathodic corrosion. Interestingly, the mode of corrosion in the presence of this particular step-type seems to depend on the neighboring terrace site: {100} or {111}. Corrosion of {100} terraces next to {110}-type steps with low step density (Figure 3.6a) results in a 'staircase-like' surface with fairly straight step edges on which nanocrystallites grow. However, increasing the number of step-site defects (Figures 3.6b, c) yields a much coarser surface exhibiting uniform micro-roughening without nanocrystal growth during cathodic corrosion. Quite different morphological changes are observed when {111} terraces with {110}-type step defects undergo cathodic corrosion: firstly, both low (Figure 3.6j) and higher (Figures 3.6h, i) step densities result in a similar type of surface. Secondly, corrosion of the steps is found to yield densely packed trenches that are open-ended on one side (Figures 3.6h, i) with the number of trenches per unit area diminishing as step density is reduced (Figure 3.6j). Overall, the surface morphology after corrosion becomes 'smoother' for the facets with fewer step-site defects, leading to the observation that the {111} terraces by themselves are less corrosive than when terminated by {110}-type step defects. This observed difference between corrosion of {111} facets and {100} facets in the presence of {110}-type steps may, in part, originate from redeposition phenomena. Specifically, the onset of nanocrystal formation on the {100} plane is observed to initiate at the edges of this face, where the terraces with low density step defects are located (Figures B.3a and B.3b) before they start to form aggregrates on the defect-free facet, as opposed to crystallite formation on the {111} plane (see e.g., Figures B.1a and B.1b), where nanocrystals are only observed on the defect-free face.

Corrosive effect of varying the density of {100}- and {111}-type steps in {110} plane

The presence of {100}- and {111}-types of step defects in {110} terraces is found to have much less of an enhancing effect on corrosion susceptibility than the presence of {110}-type step defects in {111} or {100} terraces. Specifically, in the case of {100}-type step defects in {110} terraces with low (Figure 3.6e) and higher (Figures 3.6c, d) step density, it is found that step- and terrace-sites cannot be distinguished in the SEM images and that the surface morphology remains virtually identical as step density increases. This, combined with the strong resemblance of the morphology of these surfaces with the morphology of corroded {110} terraces without step-site defects (Figure 3.4k), indicates that post-corrosion morphology is dominated by corrosion of the {110} terrace sites, and indifferent to the presence of {100} step-sites.

Corrosion of {110} terraces in the presence of {111}-type steps of low (Figure 3.6f) and higher (figures 6g, h) density exhibits behavior comparable to the presence of {100}-type steps; yielding in a surface containing many pits that are a few hundred nanometers in size. However, unlike {100} step-sites, increasing the density of {111}-type steps (going from Figure 3.6f to h) does lead to morphological changes. Specifically, the pits become more elongated to yield trenches, which in turn become seemingly open ended on one side as the step density is further increased. Rather than stating that these morphological changes originate from the presence of increased amounts of {111}-type steps, it is more accurate to state that corrosion of the {110} terraces transitions into corrosion of {110}-type step sites. This reasoning can be substantiated by comparing the facets we just discussed to the facets located closer to the {111} basal plane along the same stereographic line (Figures 3.6i and 3.6j). These latter images are of corroded {111} terraces with differing amounts of {110}-type step defects, and exhibit the same types of trenches as the corroded {110} terraces with {111}-type step defects. As the trenches decrease as we get closer to the {111} plane, the {110}-type steps yield the trench-like corrosion feature as opposed to corrosion of {111}-type steps. Therefore, the changes in surface morphology upon increasing the step density of {111}-type defects in {110} terraces are better described by stating that the corrosion behavior of {110} terraces evolves to resemble the corrosion of {110}-type steps as terrace width is decreased.

Corrosive effect of varying the density of {100}-type steps in {111} plane and {111}-type steps in {100} plane

Corrosion of {111} terraces in the presence of low (Figure 3.6k) and higher (Figures 3.6l, m) density of {100}-type steps yields a morphology that is quite different from corrosion in the presence of {110}-type steps. Rather than a relatively smooth surface with trenches, a uniformly roughened surface is obtained instead. Furthermore, the surface morphology does not change much when the density of step-site defects is increased (going from 3.6k to 3.6m). As such, it is concluded that morphology is dictated by corrosion of the ({111}) terrace sites rather than by corrosion of the {100} step-sites.

The final effect that can be studied from these images is the corrosion behavior of {100} terraces with lower (Figure 3.6o) or higher (Figures 3.6m, n) densities of {111}-type step defects. Corrosion of terraces with high amounts of step defects yield a morphology that resembles corrosion of {111} terraces, whereas lowering the step-site density further (Figure 3.6o) results once more into a 'staircase-like' morphology with fairly straight edges and crystallite formation, as was also observed in the case of corrosion in the presence of low step density {110}-type step defects. Hence, the morphology is dominated by corrosion of step-site defects, rather than of the {100} terraces.

Summarizing, corrosion resistivity of the three basal planes and their stepped counterparts is found to increase in the following order:

{110} terraces ≈ stepped {110} terraces < terraces with {110} steps < other stepped terraces < {111} terraces < {100} terraces

where:

- The presence of any type of {110} site leads to the formation of preferentially oriented trenches, which is more pronounced in the case of steps.
- Stepped {111} terraces exhibit homogenous micro-scale roughening in the presence of {100} steps, compared to trench formation in the presence of {110} steps.
- Stepped {100} terraces exhibit uniform roughening at higher step densities, and 'staircase-like' morphology with nanocrystal growth at lower step densities.
- 'Infinite' {111} and {100} basal planes exhibit the highest corrosion resistance, with the latter showing a later onset for nanocrystal formation and surface pitting.

3.3.4. On the location, shapes, and origin of nanocrystallites

In the preceding sections, we have shown that facet-specific morphological changes occur during cathodic corrosion of gold. Specifically, the {110} face and facets with higher Miller indices exhibit cathodically induced surface dissolution resulting in pitting, whereas the {111} and {100} faces mostly show nanocrystallite growth which, we hypothesize, originates from the gold that dissolves at the more corrosive facets. Dissolution from the only other possible source of gold, the counter electrode, was excluded based on the following. Firstly, nanoparticle formation on gold during cathodic corrosion has been reported in the literature before, in a work in which a titanium counter electrode (CE) was used, with crystallite shapes matching what is observed in this work.[20] Secondly, similar crystallite growth was observed over the entire crystal, both for the faces pointing towards the counter electrode and for the faces on the opposite side of the crystal - meaning there is no effect of the placement of the counter electrode on crystallite formation. The non-uniform concentration gradient that would result from dissolution of the counter electrode would most likely not allow for such observed symmetry. Thirdly, although it is known that gold dissolution takes place at anodic potentials, the majority of the dissolution actually occurs following reduction of the oxide rather than during the anodic period of a CV.[28, 29] As a DC signal was applied during measurements, no such cycling occurred on the CE. Furthermore, gold is known to exhibit a decrease in dissolution rate (passivation) as increasingly positive potentials are applied (with commonly observed CE potentials in the $+3\ V_{RHE}$ range in this work).[28] Finally, cathodic corrosion for much longer times ($1.5\ hours$) at a slightly lower cathodic potential ($-1\ V_{RHE}$) in the presence of CO did not yield any NP formation even though the CE for this experiment was still at ca. $+2.5\ V_{RHE}$ (Figure B.4).

Surface dissolution is commonly observed during cathodic conditions for various noble metal surfaces[9, 11, 20, 21, 30], and is hypothesized to occur via the formation of a negatively charged ternary metal hydride complex.[9, 11, 31, 32] Interestingly, for platinum[33] and rhodium[20], solution phase nanoparticles are observed at sufficiently high electrolyte conditions and sufficiently negative potentials, where agglomeration and deposition of these solution-phase formed particles back onto the substrate is hypothesized to be the source of the nanoparticles that are (sometimes) observed on these surfaces after cathodic corrosion.[9] However, in this work no indications for the formation of such solution phase particles (in the form of a color change of the electrolyte, or the formation of a 'particle cloud' during corrosion, or the formation of a precipitate after cathodic corrosion) have been observed, even at applied potentials as negative as $-1.3\ V_{RHE}$. Yet, nanocrystallite growth is observed at such potentials. Furthermore, the crystallites are only observed to grow on facets of specific crytallographic orientations ($\{111\}$ and $\{100\}$), with the underlying surface seemingly having a 'templating effect', influencing the shapes of the crystallites that grow thereon.

It has been reported that for shape manipulation of gold nanoparticles there exist two distinct mechanisms.[34] Firstly, one can control the rate at which a dissolved precursor-ion is converted to the solid state, denoted as kinetic control. The second mechanism is based on selective surface passivation, whereby the growth of a particular facet is retarded due to it being blocked by some adsorbing species. In case of kinetic control, thermodynamics-driven shapes are obtained in the limiting case of infinitely slow growth rates, with thermodynamically less stable particles being formed as growth rate is increased. In case of selective surface passivation, the eventual particle shape will be such that its surface is entirely comprised of the facet that is being blocked.

If the crystallites that we observe herein were directed by selective surface passivation, their shapes should be similar/equal everywhere as the electrolyte contains the same possible adsorbates everywhere. Furthermore, under such circumstances, no substrate directing effects would be expected, yet are observed in this work. Hence, the shapes of the formed nanocrystallites must be under kinetic control instead. This would be plausible if our hypothesis of the origin of the solution-phase gold ions is correct (i.e., stemming from dissolution of more corrosive facets), as then the concentration of gold ions is location specific due to lattice periodicity.

In the case of kinetic control, particles with truncated bitetrahedral (e.g., triangular prism-like) and octahedral shape are expected for slower growth rates, whereas more complex shapes (i.e., containing more edges, having lower symmetry) are expected in the case of faster growth. Slow growth rate particle shapes agree well with the shapes observed in this work for the nanocrystallites that grow on the {111} face, validating our assumption that growth is under kinetic control. However, the shapes of the nanocrystallites that form on the {100} face exhibit a plethora of differing geometries which is difficult to reconcile with a specific expected particle shape (although some of the smaller, individual ones adopt an octahedral geometry). We think the following discussion can reasonably explain such irregular shapes as observed for the {100} face.

The onset for crystallite growth is different on the {111} and {100} faces, with the {111} face exhibiting nanocrystal formation much prior to crystallite growth occurring on the {100} face. As no typical signs of solution phase nanoparticle formation were observed, we hypothesize that seed formation takes place on the substrate, with seeds forming (and growing) earlier on the {111} facet than on the {100} facet. If a seed that forms on the substrate adopts the underlying substrate structure, then seeds that form and grow on the {111} face are thermodynamically more favorable than seeds that grow on the {100} face in the case of gold. We hypothesize this would result in a lower barrier for nucleation of seeds on {111}, thus requiring a lower local ion concentration (i.e., driving force), resulting in (and observed as) an earlier onset for nanocrystallite formation on the {111} face. Crystallite shapes in this instance match the expected shapes for particles forming under kinetic control with a slow growth rate. Considering that seeds forming on the {100} face would by the same reasoning adopt the {100} geometry, their nucleation and growth is thermodynamically less favorable, resulting in a higher barrier of seed formation and slower crystallite growth. In turn, this would decrease the rate at which gold ions are consumed, allowing for a larger local concentration gradient to build up which translates into a higher driving force, leading to more unfavorable particle shapes becoming thermodynamically viable. As a certain threshold concentration is reached, nucleation and growth barriers are overcome and growth rates increase rapidly, resulting in the formation of irregular nanocrystallites with non-equilibrium shapes.

As for why only nanocrystallite formation and growth is observed on the {111} and {100} faces, a simple stability argument can be used. Under cathodic conditions, it is evident that the {110} face and facets with higher Miller indices are unstable, as they are oberved to strongly corrode cathodically. Only the {111} and {100} faces are (relatively) stable, and hence only seeds of these orientations are thermodynamically viable. Thus, nanocrystallites only form on these faces, and not on any others. Hence, for the nanocrystallites in this work to form where they do (and do not), two conditions have to be met. Firstly, seed nucleation must take place only on the substrate (where its orientation is influenced by the substrate) and not in solution. Secondly, a sufficiently high concentration of solution-phase gold ions must be present and/or be allowed to develop.

3.3.5. Effect of carbon monoxide on cathodic corrosion of Au

Voltammetric characterization of CO effect on cathodic corrosion

To investigate the effect that CO_2 reduction taking place on gold would have on cathodic corrosion in a controlled setting, the following experiment was conducted. Cathodic corrosion was carried out $10\ M$ NaOH, to facilitate comparison with prior cathodic corrosion literature as well as to mimic the high local alkalinity expected for CO_2-electrolyzers operated at high current densities.[35] As gold is a good catalyst with high faradaic efficiency and activity for the CO2RR to CO, the concentration of CO near the surface will be high. Hence, CO2RR conditions were approximated by addition of gaseous CO to the cell during corrosion experiments. With these settings, local pH effects on cathodic corrosion can be excluded as pH changes can be neglected due to the high starting pH. Additionally, the continuous purging of the electrolyte with CO (which is not further reduced on gold) yields a constant concentration of carbon monoxide near the surface that is independent of current density. Although fixing the electrolyte pH allows one to determine solely the effect of the presence of CO on catalyst stability at an interface that is mostly independent on current density, this comes at the cost of neglecting any (possible) additional effects of the presence of CO_2 (aq) and bicarbonate/carbonate in the electrolyte. Therefore, any observed changes in the presence of carbon monoxide reflect only part of the stability differences of gold under CO2RR conditions compared to cathodic corrosion during HER. Although strategies involving strongly alkaline electrolytes have been reported as a means of boosting the overall performance of CO_2-to-CO electrocatalytic systems[36], the electrolyte conditions ($10\ M$ NaOH) are not representative of the most commonly reported conditions in established literature (generally in the $0.1 - 0.5\ M$ $KHCO_3$ range)[37]. It does, however, provide for an interface where pH changes due to changes in current can be neglected (whereas the interfacial pH of bicarbonate electrolytes is known to deviate significantly as a function of current density).[38] Furthermore, it significantly enhances the rate at which a surface undergoes changes under cathodic potentials, which allows for shorter experiments.

It is important to note that cathodic corrosion in general is more prevalent at higher cation concentrations, although it has been shown to also occur at lower cation concentrations, albeit at a slower rate.[11, 33] As for gold specifically, there are currently no corrosion data for less concentrated electrolytes ($\leq 1\ M$), but the data available in literature indicates that gold and platinum exhibit comparable behavior, in the sense that corrosion is less pronounced at lower cation concentrations (but still takes place), and that similar types of sites are created irrespective of cation concentration, though the final state of the surface will likely still be different.[11]

In Figures 3.7a-d, CVs obtained after corrosion experiments in the absence (solid lines) and presence (dashed lines) of CO are depicted for the $\{111\}$, $\{100\}$ and $\{110\}$ basal planes and a spherical single crystalline surfaces, respectively. A close up of the double layer region for this figure, which encompasses all CVs discussed in this work, can be found in the supporting information (Figure B.5). It is found that all surfaces exhibit the same trend when comparing CVs of crystals corroded

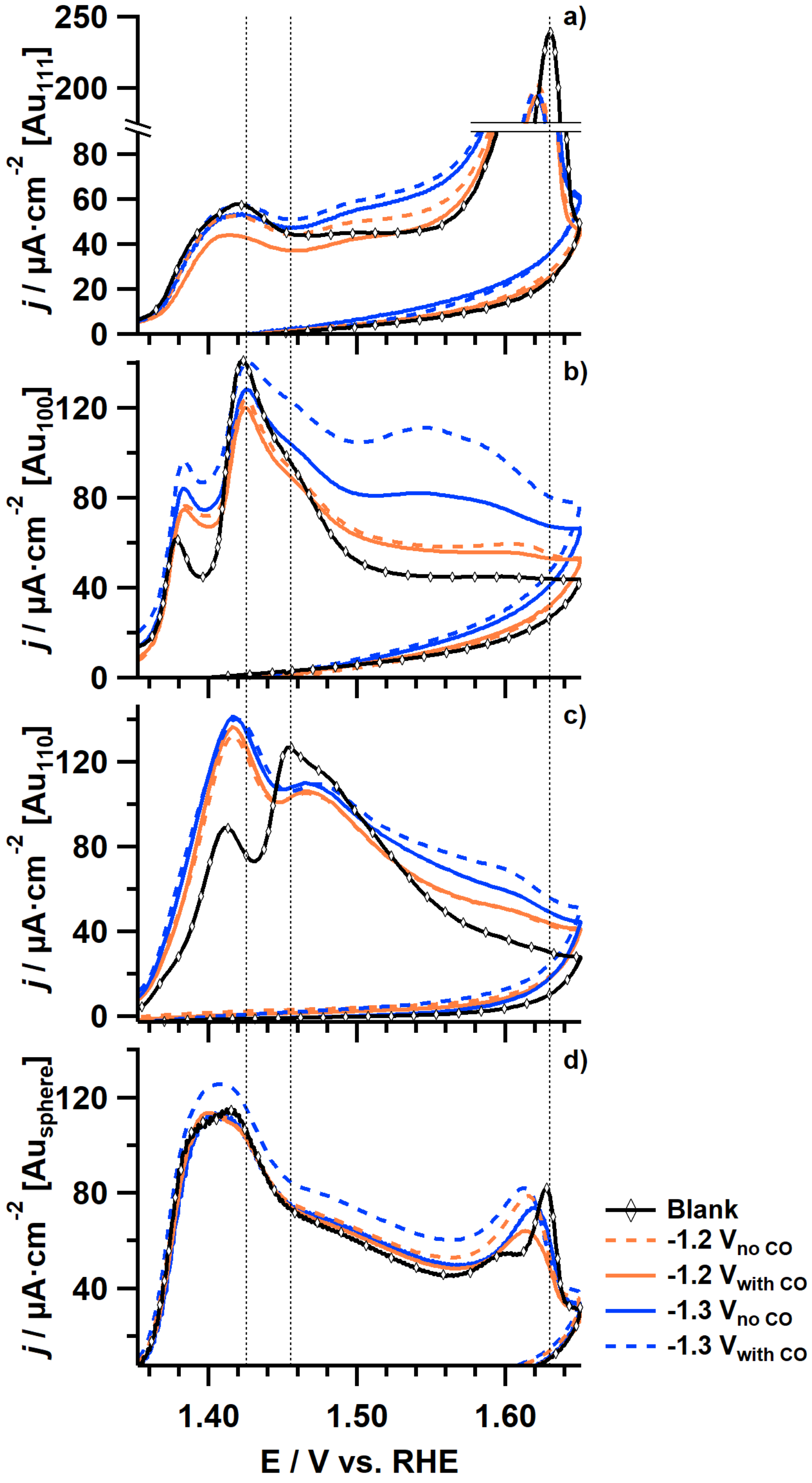

Figure 3.7: CVs of gold single crystals corroded in $10\ M$ NaOH for $2.5\ minutes$ in the absence (solid lines) and presence (dashed lines) of CO at $-1.2\ V_{RHE}$ (orange) and $-1.3\ V_{RHE}$ (blue) (85% iR corrected) for a) Au(111), b) Au(100), c) Au(110) and d) Au(spherical) electrodes, compared with their respective CVs prior to corrosion (black with diamond).

in the absence of CO with CVs of crystals corroded in the presence of CO, and therefore only one facet will be discussed. As the CO effect is most pronounced for the {100} face (Figure 3.7b), that surface will be discussed. When comparing the solid orange line (CV after $2.5\ min$ of corrosion at $-1.2\ V_{RHE}$ without CO) with the dashed orange line (CV after identical corrosion conditions but with CO present), it can be seen that there is a slight excess in charge when CO was present during corrosion. The same is observed when comparing the solid blue curve (CV after $2.5\ min$ corrosion at $-1.3\ V_{RHE}$ without CO) with the dashed blue line (corroded with CO present), albeit more pronounced. However, although the charge under the curves is found to increase (indicative of an increase in active sites), the overall shape remains mostly the same except for some small changes in the stepped-{111} region. Hence it is concluded that the presence of CO enhances the rate of corrosion but the types of sites that are generated during the corrosion process are very similar, with perhaps a small increase in stepped {111} sites. This conclusion is generalizable to the three basal planes as they show the same trend when CO is added as discussed for the {100} face. Spherical crystal surfaces are also found to be similarly influenced by the presence of CO, but from these measurements it is not possible to ascertain whether this is applicable to all the facets that constitute the overall surface, or whether all of the changes are solely due to enhanced corrosion of the {111}, {100} and {110} terrace sites that are present.

A more quantitative proof for the effect of CO on cathodic corrosion is shown in Figure B.6, wherein the roughness factors (RFs) for the crystals corroded under different conditions are depicted. Depending on the exact conditions and initial surface structure, corrosion in the presence of carbon monoxide yields an increase of 2-20% in surface area post-corrosion, compared to the surface area after corrosion in the absence of CO. However, because the effect can be seen to be highly dependent on the initial surface structure and applied potential, we believe it is more appropriate describe the effect in qualitative terms rather than quantitative terms, and hence refer to it as a 'mild enhancement'.

SEM characterization of CO effect on cathodic corrosion

In Figure 3.8, an image is depicted that is mostly identical to Figure 3.4, with the only change being that corrosion was conducted in the presence of CO as opposed to Ar. The same observations as made for surfaces corroded in the *absence of CO* are applicable here. When comparing these two datasets, it is important to be aware of the fact that each SEM image only depicts a selected spot on the surface that we deemed to best portray the particular features of that face. Most notably, on this length scale, there is some variability in nanocrystal density. Hence these particular sets of images (Figures 3.4 and 3.8) do not allow for fair comparison of the average number of nanocrystals per unit area, for which the reader is, instead, referred to Figure 3.9.

Clear evidence for the slight enhancement of surface dissolution in the presence of CO is provided in the SEM images depicted in Figure 3.9. From the micrographs depicted in 3.9a and 3.9b, it can be seen that no nanocrystal growth is observed on {111} for $t_p \leq 5\ minutes$ at a corrosion potential of $-1.2\ V_{RHE}$ when CO is absent. However, nanocrystals are found to be present after $5\ minutes$ when CO

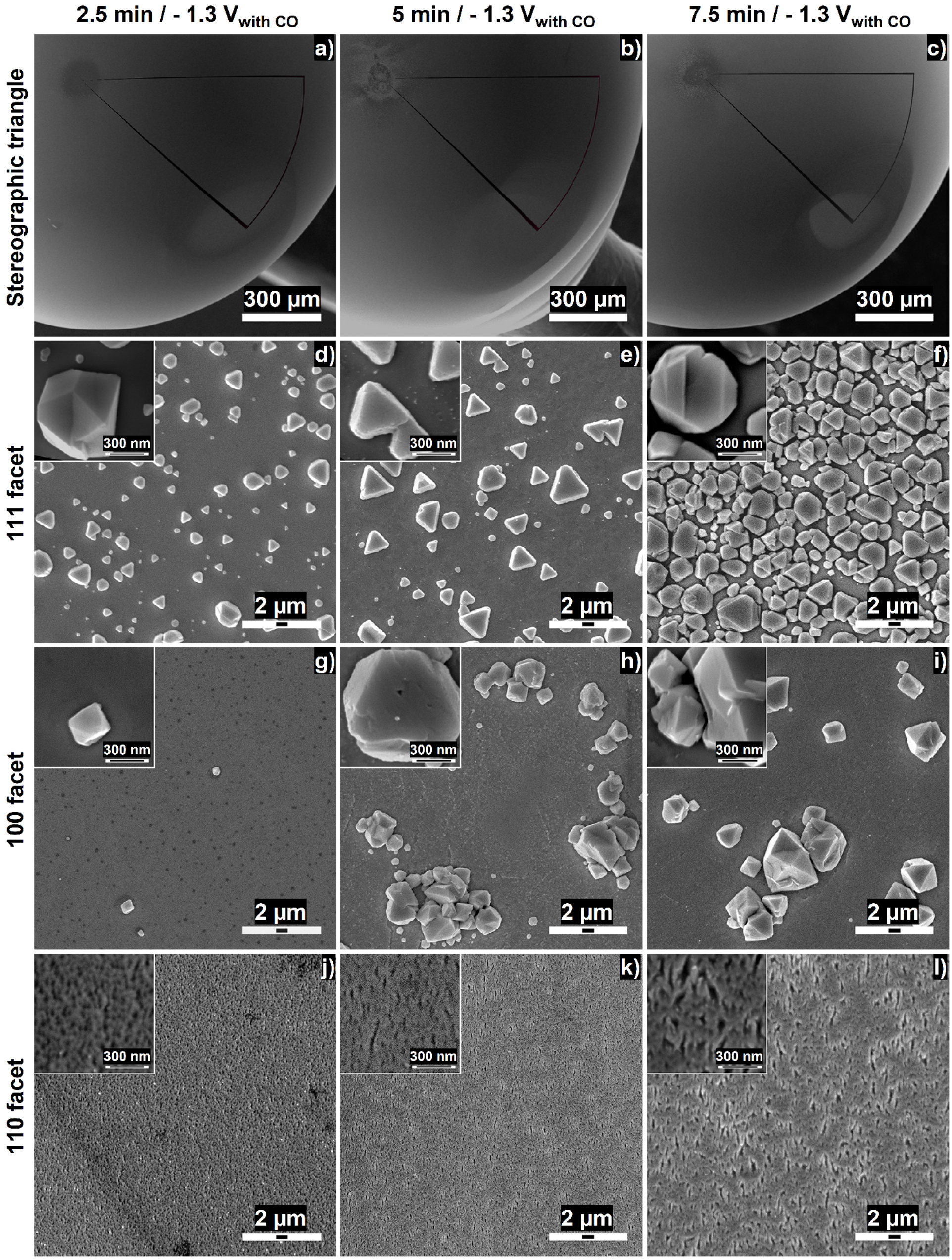

Figure 3.8: SEM images (macroscopic overview, 111 facet, 100 facet and 110 facet, respectively, going from the first to last row) of anisotropic surface corrosion in the form of pitting and nanocrystal formation as a function of time ($2.5\ min$ to $7.5\ min$, respectively, going from the left to right column) at a corrosion potential of $-1.3\ V_{RHE}$ (85% iR corrected) in $10\ M$ NaOH with CO present.

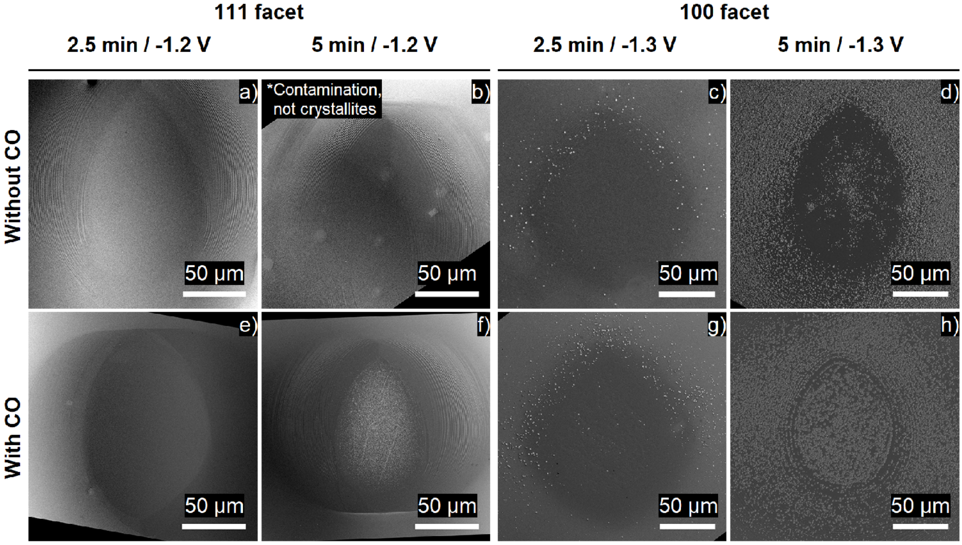

Figure 3.9: Corrosion-time dependent nanocrystal growth during corrosion in the absence (a-d) and presence (e-h) of CO at a potential of $-1.2\ V_{RHE}$ (85% iR corrected) for the 111 facet (a,b and e, f) and $-1.3\ V_{RHE}$ (85% iR corrected) for the 100 facet (c,d and g,h).

is present during corrosion under otherwise identical conditions (Figures 3.9e,f). Although the gold ions that redeposit in the form of nanocrystals likely originate from elsewhere on the surface, the fact that crystallite growth is observed sooner does indicate enhanced dissolution in the presence of CO. Similar behavior is observed for nanocrystal growth on the {100} facet (compare Figures 3.9c,d with 3.9g, h) for more negative applied corrosion potentials ($-1.3\ V_{RHE}$). However, in both instances, this trend is only observed for crystallite formation near the observed onset of growth, and does not apply to longer timeframes and/or more corrosive potentials.

AFM characterization of CO effect on cathodic corrosion

AFM images obtained upon corrosion in the presence of carbon monoxide are depicted in Figure 3.10. Observations pertaining to surface roughening and crystallite shapes are in line with those previously discussed for corrosion in the absence of CO. However, the influence of CO on the growth of nanocrystals on the {111} and {100} faces can clearly be seen from the histograms. In both instances (Figure 3.10c for {111} and Figure 3.10f for {100}), the histograms show that in the absence of CO average height is lower. Thus, the presence of CO yields deposits with similar shapes but overall taller crystallites. The face that does not exhibit crystallite growth (i.e., Au(110)) does not display a strong CO effect, exhibiting only small changes in the histogram on the order of ca. $10\ nm$.

We attribute the slight enhancement of surface corrosion in the presence of CO to the interaction of carbon monoxide with the gold atoms at the surface. As CO is known to bind quite strongly to gold atoms in alkaline media[39, 40], the

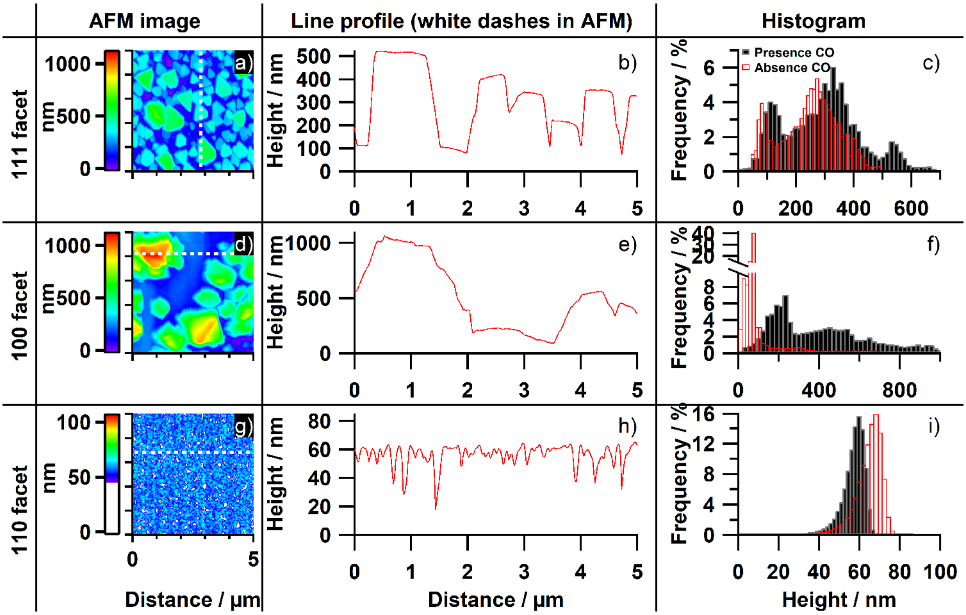

Figure 3.10: AFM images, line profiles and histograms (column 1, 2 and 3, respectively) for the basal planes ({111}: a-c, {100}: d-f, and {110}: g-i) after cathodic corrosion at $-1.3\ V_{RHE}$ (85% iR corrected) for $5\ minutes$, in $10\ M$ NaOH with CO present.

surface mobility of those gold atoms is expected to increase (as binding an adsorbate decreases the binding strength a gold atom has with its neighboring gold atoms).[41, 42] Such effects can negatively influence catalyst stability under cathodic conditions in an industrial setting, as many possible adsorbates will reasonably be present.

3.4. Discussion and conclusions

In this work, cathodic corrosion has been studied on gold surfaces with well-defined surface structures so as to determine the types of surface sites that may be preferentially created when specific types of facets corrode. Specifically, cyclic voltammetry was utilized to study changes in the hydroxide/oxygen adsorption region in $0.05\ M$ H_2SO_4, after corrosion. Voltammetric changes of cut single crystals of the three basal planes; {111}, {100} and {110}, and those of (uncut) spherical single crystalline surfaces, were investigated and compared. The inclusion of spherical single crystal electrodes enabled us to study further, using SEM, not only the macroscopic morphological changes of the three basal planes with corrosion potential (E_p) and corrosion time (t_p), but also the effect of the specific type and density of step defects present in a specific terrace. Additional information regarding the nano/microscale surface morphology for the three basal planes was obtained from AFM imaging. Finally, all parameters were investigated for surfaces corroded in the absence and in the presence of carbon monoxide during corrosion. The inclusion of

CO as a parameter serves as a controlled test environment that is meant to approximate, in part, the local environment of a gold surface if it were to be utilized in a CO_2 -electrolyzer. This parameter serves as an indication whether cathodic corrosion is influenced by the reaction that is occurring at the interface (although the absence of CO_2 (g) and bicarbonate/carbonate salts are artificially imposed simplifications of the system).

From cyclic voltammetry, SEM, and AFM, it was found that cathodic corrosion is anisotropic, i.e., dependent on the specific crystallographic orientation of the substrate. CV data showed that corrosion of {100} facets results in the preferential creation of stepped-{111} surface sites, and the same holds true for corrosion of the {110} plane. Due to the fact that the {111} face itself also undergoes corrosion (resulting also in a surface that, voltammetrically, resembles a stepped-{111} surface), it is concluded that, under cathodic conditions, the surface changes in such a way that more stepped-{111} sites are created at the cost of other types of surface sites. The presence of CO during corrosion seems to accelerate corrosion slightly (as derived from CV charges), but the overall shape of the hydroxide/oxygen adsorption region remained very similar, except for possibly a slight increase in the fraction of stepped-{111}. Therefore, the presence of carbon monoxide enhances the rate of corrosion only mildly and does not lead to a substantial shift in the types of sites that are created.

Further proof for anisotropic corrosion is obtained from both SEM and AFM, by looking specifically at corrosion of the three basal planes. On two of these faces ({111} and {100}), nanocrystal growth is observed after certain threshold potentials and corrosion times are exceeded, whereas crystallite formation is absent entirely for the {110} facet. Additionally, nanocrystal shapes, spatial distribution, and onset of formation are also facet dependent. Specifically, nanocrystals shaped like triangular-prisms that are distributed uniformly on the surface form on the {111} face, whereas smaller individual octahedra and clusters of irregularly shaped crystallites form on the {100} face. Interestingly, nanocrystal formation on the {100} facet requires longer corrosion times and more corrosive potentials than growth on the {111} face. Also, near the onset, crystallite formation on Au(100) is actually observed to start at the edges of this facet on a spherical single crystal, where {100} facets with low step density are located. This is in contrast with nanocrystal formation on the {111} face, which only takes place on the step-defect free facet. Further information regarding the crystallites that form on the two basal planes was obtained via AFM, which shows that the nanocrystals that grow on the {111} face are terminated with a flat top that runs parallel to the base, much like a plateau, as opposed to the agglomerates that form on the {100} face which are better described as irregular mountains. Furthermore, AFM has shown that nanocrystallites that form under corrosion in the presence of CO are higher than crystallites that form in the absence of CO. In a similar direction, SEM data shows that the onset of crystallite growth is shifted to shorter corrosion times or yields higher nanocrystallite densities for the same corrosion times (limited to specifically timeframes near the onset of crystallite formation) when CO is present during cathodic corrosion.

Contrary to the nanocrystal formation observed on Au(111) and Au(100), the

{110} face exhibits strong pitting and no crystallite growth under corrosive conditions. Furthermore, the formation of pits is observed to occur at less strongly corrosive applied potentials and shorter corrosion times from SEM than the conditions required for nanocrystal formation (and surface pitting) on the other two basal planes.

In conclusion, cathodic corrosion of gold can be divided into two corrosion modes: dissolution and pitting, and redeposition. As our experiments show nanocrystallite formation to be a function of corrosion time, we conclude that there must exist a concentration gradient that develops over time, resulting into electrocrystallization at specific surface sites when certain critical values are reached. Rather than gold ions dissolving and redepositing on the same face, SEM imaging shows that facets containing {110} sites (both terraces and steps), and facets with increasing amounts of step-site defects, exhibit more roughening upon corrosion than the {111} and {100} terraces with fewer to no step-site defects (which are the facets where nanocrystal growth occurs). Hence, we conclude that electro-dissolution of more corrosive facets (those containing {110}-type sites and/or having high defect density) results in the build-up of a concentration gradient of gold ions near the surface, which subsequently recrystallize on the faces that are less corrosive (i.e., more stable; defect-free {111} and {100} terraces with little to no defects). The fact that the presence of CO enhances corrosion rates leads to this concentration gradient developing faster, and hence can explain a shift in the onset for crystallite formation. Presumably, the effect of CO is related to the chemisorption of CO on gold in alkaline media[39, 40], thereby slightly weakening the Au-Au bond and enhancing surface atom diffusion.[41, 42]

Anisotropic cathodic corrosion has also been observed for Pt electrodes in alkaline media.[12, 43] However, cathodic corrosion of platinum leads to substantially different surface transformations. For platinum, the {111} facet is the most prone to cathodic corrosion, and the {110} the least, and leads to the preferential formation of {100} surface sites, both steps and terraces. Only etch pits are observed on Pt, without evidence for redeposition, with etch pit shapes reflecting the atomic order of the surface. The observed structures on platinum suggest that the etching process is (surface-) diffusion limited. The fact that gold exhibits very different behavior may suggest that the intermediate of cathodic corrosion (presumably a ternary metal hydride) has a different structure and/or stability in the case of gold, and that the role of mass transport in the generation of the surface roughness is different.

Finally, our experiments have shown that cathodic corrosion is a highly destructive phenomenon that severely impacts the structure of electrodes at negative potentials, specifically during electrocatalytic reduction reactions, such as CO2RR, that run at relatively high overpotential. This may undermine the stability of such electrodes in (future) commercial electrolyzers, as cathodically induced dissolution leads to consumption of the catalyst and furthermore, both dissolution as well as electrocrystallization phenomena result in preferential types of sites being produced, which may not necessarily be the most catalytically active sites for the reaction of interest as different facets generally exhibit different catalytic performance.[44] On the other hand, leaving aside the stability aspect, cathodic corrosion may also lead to a surface site distribution that is actually beneficial for catalysis.[45] We note that this study was conducted in highly concentrated alkaline solution to accelerate cathodic corrosion, and that surface changes are expected to be less severe if electrolytes with lower cation concentrations are employed.

References

[1] Kevin J Warner and Glenn A Jones. The climate-independent need for renewable energy in the 21st century. *Energies*, 10(8):1197, 2017.

[2] Etosha R. Cave, Joseph H. Montoya, Kendra P. Kuhl, David N. Abram, Toru Hatsukade, Chuan Shi, Christopher Hahn, Jens K. Norskov, and Thomas F. Jaramillo. Electrochemical CO2 reduction on Au surfaces: mechanistic aspects regarding the formation of major and minor products. *Physical Chemistry Chemical Physics*, 19(24):15856–15863, 2017.

[3] Qi Lu, Jonathan Rosen, Yang Zhou, Gregory S Hutchings, Yannick C Kimmel, Jingguang G Chen, and Feng Jiao. A selective and efficient electrocatalyst for carbon dioxide reduction. *Nature communications*, 5:3242, 2014.

[4] Masashi Azuma, Kazuhito Hashimoto, Masahiro Hiramoto, Masahiro Watanabe, and Tadayoshi Sakata. Electrochemical reduction of carbon dioxide on various metal electrodes in low-temperature aqueous KHCO3 media. *Journal of the Electrochemical Society*, 137(6):1772–1778, 1990.

[5] Xiaoquan Min and Matthew W. Kanan. Pd-catalyzed electrohydrogenation of carbon dioxide to formate: High mass activity at low overpotential and identification of the deactivation pathway. *Journal of the American Chemical Society*, 137(14):4701–4708, 2015.

[6] Cao-Thang Dinh, Thomas Burdyny, Md Golam Kibria, Ali Seifitokaldani, Christine M. Gabardo, F. Pelayo García de Arquer, Amirreza Kiani, Jonathan P. Edwards, Phil De Luna, Oleksandr S. Bushuyev, Chengqin Zou, Rafael Quintero-Bermudez, Yuanjie Pang, David Sinton, and Edward H. Sargent. CO2 electroreduction to ethylene via hydroxide-mediated copper catalysis at an abrupt interface. *Science*, 360(6390):783–787, 2018.

[7] Christina W. Li, Jim Ciston, and Matthew W. Kanan. Electroreduction of carbon monoxide to liquid fuel on oxide-derived nanocrystalline copper. *Nature*, 508(7497):504–507, 2014.

[8] Sumit Verma, Byoungsu Kim, Huei-Ru "Molly" Jhong, Sichao Ma, and Paul J. A. Kenis. A gross-margin model for defining technoeconomic benchmarks in the electroreduction of CO2. *ChemSusChem*, 9(15):1972–1979, 2016.

[9] Alexei I. Yanson, Paramaconi Rodriguez, Nuria Garcia-Araez, Rik V. Mom, Frans D. Tichelaar, and Marc T. M. Koper. Cathodic corrosion: A quick, clean, and versatile method for the synthesis of metallic nanoparticles. *Angewandte Chemie International Edition*, 50(28):6346–6350, 2011.

[10] Nakkiran Arulmozhi, Derek Esau, Ram P. Lamsal, Diane Beauchemin, and Gregory Jerkiewicz. Structural transformation of monocrystalline platinum electrodes upon electro-oxidation and electro-dissolution. *ACS Catalysis*, 8(7):6426–6439, 2018.

[11] Thomas J. P. Hersbach, Ian T. McCrum, Dimitra Anastasiadou, Rianne Wever, Federico Calle-Vallejo, and Marc T. M. Koper. Alkali metal cation effects in structuring Pt, Rh, and Au surfaces through cathodic corrosion. *ACS Applied Materials & Interfaces*, 10(45):39363–39379, 2018.

[12] Thomas J. P. Hersbach, Alexei I. Yanson, and Marc T. M. Koper. Anisotropic etching of platinum electrodes at the onset of cathodic corrosion. *Nature Communications*, 7:12653, 2016.

[13] Matthew Jouny, Wesley Luc, and Feng Jiao. General techno-economic analysis of CO2 electrolysis systems. *Industrial & Engineering Chemistry Research*, 57(6):2165–2177, 2018.

[14] Xiong Peng, Stavros G. Karakalos, and William E. Mustain. Preferentially oriented Ag nanocrystals with extremely high activity and faradaic efficiency for CO2 electrochemical reduction to CO. *ACS Applied Materials & Interfaces*, 10(2):1734–1742, 2018.

[15] A. Hamelin. Cyclic voltammetry at gold single-crystal surfaces. Part 1. Behaviour at low-index faces. *Journal of Electroanalytical Chemistry*, 407(1):1–11, 1996.

[16] A. Hamelin and A. M. Martins. Cyclic voltammetry at gold single-crystal surfaces. Part 2. Behaviour of high-index faces. *Journal of Electroanalytical Chemistry*, 407(1):13–21, 1996.

[17] S. Štrbac, R. R. Adžć, and A. Hamelin. Oxide formation on gold single crystal stepped surfaces. *Journal of Electroanalytical Chemistry and Interfacial Electrochemistry*, 249(1):291–310, 1988.

[18] Enrique Herrero, Lisa J. Buller, and Héctor D. Abruña. Underpotential deposition at single crystal surfaces of Au, Pt, Ag and other materials. *Chemical Reviews*, 101(7):1897–1930, 2001.

[19] Ludwig A. Kibler. *Preparation and characterization of noble metal single crystal electrode surfaces*. International Society of Electrochemistry, 2003.

[20] Thomas J. P. Hersbach, Vladislav A. Mints, Federico Calle-Vallejo, Alexei I. Yanson, and Marc T. M. Koper. Anisotropic etching of rhodium and gold as the onset of nanoparticle formation by cathodic corrosion. *Faraday Discussions*, 193(0):207–222, 2016.

[21] Jonnathan Medina-Ramos, Weiwei Zhang, Kichul Yoon, Peng Bai, Ashwin Chemburkar, Wenjie Tang, Abderrahman Atifi, Sang Soo Lee, Timothy T. Fister, Brian J. Ingram, Joel Rosenthal, Matthew Neurock, Adri C. T. van Duin, and Paul Fenter. Cathodic corrosion at the bismuth–ionic liquid electrolyte interface under conditions for CO2 reduction. *Chemistry of Materials*, 30(7):2362–2373, 2018.

[22] Nakkiran Arulmozhi and Gregory Jerkiewicz. Design and development of instrumentations for the preparation of platinum single crystals for electrochemistry and electrocatalysis research. Part 1: Semi-automated crystal growth. *Electrocatalysis*, 7(6):507–518, 2016.

[23] J. Clavilier, R. Faure, G. Guinet, and R. Durand. Preparation of monocrystalline Pt microelectrodes and electrochemical study of the plane surfaces cut in the direction of the {111} and {110} planes. *Journal of Electroanalytical Chemistry and Interfacial Electrochemistry*, 107(1):205–209, 1980.

[24] R. Kaischew and B. Mutaftschiew. Uber die elektrolytische keimbildung des quecksilbers. *Electrochimica Acta*, 10(7):643–650, 1965.

[25] Nakkiran Arulmozhi, Derek Esau, Julia van Drunen, and Gregory Jerkiewicz. Design and development of instrumentations for the preparation of platinum single crystals for electrochemistry and electrocatalysis research. Part 3: Final treatment, electrochemical measurements, and recommended laboratory practices. *Electrocatalysis*, 9(1):113–123, 2018.

[26] S. Trasatti and O. A. Petrii. Real surface area measurements in electrochemistry. *Journal of Electroanalytical Chemistry*, 327(1):353–376, 1992.

[27] T. L. Einstein. *Equilibrium Shape of Crystals*, book section 5, pages 215–264. Elsevier, Boston, 2015.

[28] Serhiy Cherevko, Aleksandar R. Zeradjanin, Gareth P. Keeley, and Karl J. J. Mayrhofer. A comparative study on gold and platinum dissolution in acidic and alkaline media. *Journal of The Electrochemical Society*, 161(12):H822–H830, 2014.

[29] Maximilian Schalenbach, Olga Kasian, Marc Ledendecker, Florian D. Speck, Andrea M. Mingers, Karl J. J. Mayrhofer, and Serhiy Cherevko. The electrochemical dissolution of noble metals in alkaline media. *Electrocatalysis*, 9(2):153–161, 2018.

[30] Jicheng Feng, Dong Chen, Ahmad S. Sediq, Stefan Romeijn, Frans D. Tichelaar, Wim Jiskoot, Jun Yang, and Marc T. M. Koper. Cathodic corrosion of a bulk wire to nonaggregated functional nanocrystals and nanoalloys. *ACS Applied Materials & Interfaces*, 10(11):9532–9540, 2018.

[31] S. C. Abrahams, A. P. Ginsberg, and K. Knox. Transition metal-hydrogen compounds. II. The crystal and molecular structure of potassium rhenium hydride, K2ReH9. *Inorganic Chemistry*, 3(4):558–567, 1964.

[32] Stewart F. Parker. Spectroscopy and bonding in ternary metal hydride complexes—potential hydrogen storage media. *Coordination Chemistry Reviews*, 254(3):215–234, 2010.

[33] A. I. Yanson, P. V. Antonov, P. Rodriguez, and M. T. M. Koper. Influence of the electrolyte concentration on the size and shape of platinum nanoparticles synthesized by cathodic corrosion. *Electrochimica Acta*, 112:913–918, 2013.

[34] Michelle L. Personick and Chad A. Mirkin. Making sense of the mayhem behind shape control in the synthesis of gold nanoparticles. *Journal of the American Chemical Society*, 135(49):18238–18247, 2013.

[35] Ali Seifitokaldani, Christine M. Gabardo, Thomas Burdyny, Cao-Thang Dinh, Jonathan P. Edwards, Md Golam Kibria, Oleksandr S. Bushuyev, Shana O. Kelley, David Sinton, and Edward H. Sargent. Hydronium-induced switching between CO2 electroreduction pathways. *Journal of the American Chemical Society*, 140(11):3833–3837, 2018.

[36] Christine M. Gabardo, Ali Seifitokaldani, Jonathan P. Edwards, Cao-Thang Dinh, Thomas Burdyny, Md Golam Kibria, Colin P. O'Brien, Edward H. Sargent, and David Sinton. Combined high alkalinity and pressurization enable efficient CO2 electroreduction to CO. *Energy & Environmental Science*, 11(9):2531–2539, 2018.

[37] Stephanie Nitopi, Erlend Bertheussen, Soren B. Scott, Xinyan Liu, Albert K. Engstfeld, Sebastian Horch, Brian Seger, Ifan E. L. Stephens, Karen Chan, Christopher Hahn, Jens K. Nørskov, Thomas F. Jaramillo, and Ib Chorkendorff. Progress and perspectives of electrochemical CO2 reduction on copper in aqueous electrolyte. *Chemical Reviews*, 119(12):7610–7672, 2019.

[38] N. Gupta, M. Gattrell, and B. MacDougall. Calculation for the cathode surface concentrations in the electrochemical reduction of CO2 in KHCO3 solutions. *Journal of Applied Electrochemistry*, 36(2):161–172, 2006.

[39] Hideaki Kita, Hiroshi Nakajima, and Kimitaka Hayashi. Electrochemical oxidation of CO on Au in alkaline solution. *Journal of Electroanalytical Chemistry and Interfacial Electrochemistry*, 190(1):141–156, 1985.

[40] Paramaconi Rodriguez, Nuria Garcia-Araez, Andrey Koverga, Stefan Frank, and Marc T. M. Koper. CO electroxidation on gold in alkaline media: A combined electrochemical, spectroscopic, and DFT study. *Langmuir*, 26(14):12425–12432, 2010.

[41] Flemming Besenbacher, Erik Lægsgaard, and Ivan Stensgaard. Fast-scanning STM studies. *Materials Today*, 8(5):26–30, 2005.

[42] Jun Wang, Monica McEntee, Wenjie Tang, Matthew Neurock, Arthur P. Baddorf, Petro Maksymovych, and John T. Yates. Formation, migration, and reactivity of Au-CO complexes on gold surfaces. *Journal of the American Chemical Society*, 138(5):1518–1526, 2016.

[43] Nakkiran Arulmozhi, Thomas J. P. Hersbach, and Marc T. M. Koper. Nanoscale morphological evolution of monocrystalline Pt surfaces during cathodic corrosion. *Proceedings of the National Academy of Sciences*, page 202017086, 2020.

[44] Stefano Mezzavilla, Sebastian Horch, Ifan E. L. Stephens, Brian Seger, and Ib Chorkendorff. Structure sensitivity in the electrocatalytic reduction of CO2 with gold catalysts. *Angewandte Chemie*, 131(12):3814–3818, 2019.

[45] Matteo Duca, Paramaconi Rodriguez, Alexei I. Yanson, and Marc T. M. Koper. Selective electrocatalysis on platinum nanoparticles with preferential (100) orientation prepared by cathodic corrosion. *Topics in Catalysis*, 57(1):255–264, 2014.

4

Clean and Reproducible Voltammetry of Copper Single Crystals with Prominent Facet-Specific Features Using Induction Annealing

Although copper is widely used as an electrocatalyst for the CO_2 reduction reaction, often little emphasis is placed on identifying exactly the facet distribution of the copper surface. Furthermore, because of differing surface preparation methodologies, reported characterization voltammograms (where applicable) often vary significantly between laboratories, even for surfaces of supposedly the same orientation. In this work, we describe a surface preparation methodology involving the combination of induction annealing and well-documented electrochemical steps, by which reproducible voltammetry for copper surfaces of different orientations can be obtained. Specifically, we investigated copper surfaces of the three principal orientations: (111), (100) and (110), and a representative polycrystalline surface. We compared these surfaces to surfaces reported in the literature prepared via either electropolishing or UHV-standard methodologies, where we find induction preparation to yield improvements in surface quality with respect to electropolished surfaces, though not quite as good as those obtained by UHV-preparation.

This chapter has been published in
Raaijman, S. J.; Arulmozhi, N.; da Silva, A.H.M.; Koper, M. T. M., *J. Electrochem. Soc.* **2021**, *168* (9) 096510

4.1. Introduction

With a paradigm shift in climate-related research, copper has found itself at the frontier of investigations into electrochemical carbon dioxide reduction (i.e., the CO_2 reduction reaction, CO2RR) due to its unique propensity to generate > $2\,e^-$ and C2+ products from CO_2. The product spectrum is found to be strongly influenced by both potential[1–3] and the specific facet distribution at the interface[4, 5] with e.g., ethylene formation having higher yields at lower overpotentials on the {100} plane compared to the {111} and {110} faces.[4, 6, 7] This shows the importance of identifying and reporting the types of electrochemically active sites present on copper surfaces used to study the CO2RR. Means of characterizing differing copper sites have been described previously in the works of e.g., Jović and Jović[8, 9], Schouten *et al.*[10], and more recently in more detail by Engstfelt *et al.*[11], Bagger *et al.*,[12] Maagaard *et al.*[13], Sebastián-Pascual *et al.*[14, 15], and Tiwari *et al.*[16–18] However, metallic copper proves to be very exacting in terms of its treatment, both prior to and during electrochemical characterization – often leading to surfaces prepared under similar conditions exhibiting substantial differences in their electrochemical fingerprint.[11, 18]

Surface preparation, specifically, plays an important role in obtaining reproducible surfaces. Considering copper's propensity to oxidize, it is not possible to employ the current default preparation methodology for (more) noble metals: i.e., flame annealing under ambient conditions, as first introduced by Clavilier *et al.*[19] As such, different preparatory treatments were established for copper surfaces. These methodologies are electrochemical in nature: several copper layers are removed by forming, and subsequently dissolving, copper oxides[20] through subjecting the surface to oxidizing potentials in concentrated phosphoric acid solution (generally with respect to a copper or graphite counter electrode in a two-electrode configuration).[2, 10] However, this so-called electropolishing is anisotropic, and thus the resulting facet distribution will be a function of applied potential and polarization time. Since potentials are commonly applied in a two-electrode configuration, the exact potential at the electrode interface is ill-defined, leading to further discrepancies between different samples and surfaces prepared in different laboratories.

Therefore, although we have means of preparing and characterizing (single-crystalline) copper surfaces, we currently lack exact methodologies to systematically and consistently generate reproducible surfaces that yield identical results among different laboratories. In this work, we extend the commonly employed methodologies for the preparation of copper surfaces with induction annealing to obtain improved surface reproducibility with relatively little impact on experimental complexity. We will describe a set of experimental steps consisting of a combination of electropolishing, electromagnetic induction heating, and specific electrochemical treatments that yield reproducible copper surfaces with clear facet-specific adsorption features for commonly studied copper surfaces; Cu(111), Cu(100), Cu(110) and Cu(poly). We will compare our results to results obtained by electropolishing only, and to surfaces prepared in ultra-high vacuum (UHV), which would be the preferred methodology but is more cumbersome and also not widely available.

4.2. Experimental

4.2.1. Chemicals, electrochemistry and cells

All solutions were made by dissolving appropriate amounts of chemicals in Milli-Q water (Millipore, resistivity $\geq 18.2\ M\Omega \cdot cm$). The chemicals: H_3PO_4 (85%, p.a., Merck), H_2SO_4 (96%, ACS reagent, Honeywell), H_2O_2 (35%, Ph. Nord, Merck), HNO_3 (65%, Ph. Eur., Boom), $KMnO_4$ (ACS reagent, Sigma Aldrich), NaOH (99.99%, trace metals basis, Sigma Aldrich) for preparing electrolyte, and NaOH (30.4%, Suprapur, Supelco) for the $10\ M$ oxidation experiment in Figure 4.8, were used without further purification. Gases, H_2 (Linde 5.0) and Ar (Linde, 5.0), were used as received.

The experimental work was conducted using monocrystalline disk-type Cu(111), Cu(100) and Cu(110) electrodes (Surface Preparatory Labs, oriented to $\leq 0.1°, d = 8\ mm$), and spherical bead-type and disk-type polycrystalline Cu(poly) working electrodes (WEs). Cu(poly) disk-type electrodes were made by machining a Cu foil (99.995%, Mateck) into the desired shape and dimension (disk of $d = 10\ mm$) and laser welding a copper wire to the backside. Cu(poly) spherical bead-type electrodes of ca. $2-3\ mm$ in diameter were made by melting a copper wire (99.9999%, metals basis, Puratronic) into a droplet via induction annealing under oxygen-free atmosphere (H_2 or Ar). Surface impurities were removed by briefly etching (ca. $5\ s$) the resulting bead electrode in concentrated nitric acid (65%), and re-melting the bead (but not allowing it to grow larger). This etching/remelting cycle was repeated ca. 4 times to remove the majority of visible surface contaminants.

WEs were cleaned either by mechanical polishing followed by sonication and electropolishing (for the machined Cu(poly) disk-type electrode) or via induction annealing (all other electrodes) prior to each measurement, with the exact methodologies described in more detail in the supporting information (SI). Characterization CVs ($0.1\ M$ NaOH) were obtained following facet-specific procedures involving insertion at particular potentials and pre-cycling in specific potential windows prior to measuring the 'full-scale' CVs given in this work. Exact parameters are detailed in the SI. A reversible hydrogen electrode (RHE) (Hydroflex, Gaskatel) was used as a reference electrode (RE). All potentials in this work are reported vs. RHE unless specified otherwise. A platinum spiral ($99.99+\%$) was used as a counter electrode (CE), and was cleaned in concentrated piranha solution ($3:1\ v/v$ mix of H_2SO_4 and H_2O_2) overnight after disassembly of the cell to remove any copper contaminants. After piranha exposure, Pt CEs were flame annealed prior to insertion into the cell.

Glassware and plasticware were cleaned in acidified aqueous permanganate solution for $12+\ hours$ ($0.5\ M$ H_2SO_4 $+1\ g{\cdot}L^{-1}$ $KMnO_4$). Prior to starting experiments, the leftover cleaning solution was removed by rinsing with Milli-Q water and washing with diluted piranha solution (diluted to $> 95\ vol\%$ water) to remove manganese dioxide and permanganate residue. Next, glassware/plasticware was rinsed three times and boiled five times in Milli-Q water to remove piranha residue.

A one-compartment fluorinated ethylene propylene (FEP) cell, fitted with ETFE gas tubes and holes for the RE and CE, was used for electrochemical measurements. Electrolyte solutions were prepared by dissolving appropriate amounts of chemicals in Milli-Q water. Argon was passed through and above the electrolyte to remove any dissolved gases. Prior to closing the electrical circuit, argon flow through the electrolyte was stopped while argon flow above the electrolyte was initiated or maintained. Disk electrodes were measured in hanging meniscus configuration, whereas spherical bead-type electrodes were inserted with the entirety of the bead submerged, with the electrolyte level reaching to where the bead was connected to the wire. Where applicable, CVs were normalized to the geometric surface area, except in the case of spherical bead-type Cu(poly) electrodes, which were normalized to their OH-adsorption charge as measured between $-0.25\ V < E < +0.44\ V$ after correcting for the double layer current. The value used for conversion of OH-adsorption charge to area was $128.1\ \mu C \cdot cm^{-2}$, which was determined as described in the SI.

4.2.2. Instruments and Software

A BioLogic VSP-300 potentiostat controlled via their proprietary software EC-Lab was used for all electrochemical measurements. Literature CVs were extracted from their respective sources in image form and converted to numeric data using the shareware 'DataThief III'. Data editing and plotting was done using the software Igor. Mass flow controllers (SLA5850, Brooks) were digitally controlled via the manufacturer's proprietary software. Where applicable, mechanical polishing was conducted on a Forcipol 1 machine (Metkon), post-polishing ultrasonication was done in a Bandelin Sonorex RK 25 H ultrasonicator and RF heating was applied via a 2.4 kW Ambrell EASYheat model 0224 fitted with a Flowmax water cooling solution.

4.2.3. Normalization of literature CVs

Digitized literature CVs were edited in a number of ways to facilitate comparison to our CVs. Firstly, they were manually shifted horizontally to achieve symmetry of the main adsorption feature around the x-axis (to offset ORR-related current). Secondly, where applicable, the potential was shifted to best align key adsorption features (any such shifts are specified in the legend). Thirdly, they were scaled such that they yielded identical double layer (DL) thicknesses (defined as $i_{forward\ scan}^{average} - i_{backward\ scan}^{average}$) within a potential region where all CVs of the same surface orientation exhibited (apparent) capacitive behavior. Specifically, these regions were $+0.225\ V < E < +0.275\ V$, $+0.17\ V < E < +0.24\ V$ and $-0.10\ V < E < +0.10\ V$ for Cu(111), Cu(100) and Cu(110) surfaces, respectively. The potential boundaries were chosen as large as possible to average out any inaccuracies from the image to data transcription process. Although we will refer to these areas as double layer regions, an important secondary consideration in picking these particular boundaries was the degree of overlap between CVs of different sources. As such, these regions are not necessarily representative of what we would consider ideal locations for determining the double layer capacity for these surfaces.

4.3. Results and discussion

4.3.1. Literature comparison

To verify the quality of the surfaces obtained via our methodology, CVs of the three basal planes ({111}, {100} and {110}) are compared to recent literature discussing UHV-prepared crystals and electropolished surfaces from sources that report CVs with clear facet-specific features (Figures 4.1-4.3). The CVs we report were measured in $0.1\ M$ NaOH, whereas it is common in recent literature to use $0.1\ M$ KOH. Cations of different identity may have an effect on peak intensity: Engstfeld *et al.* show peak suppression for the Cu(100)-specific feature in KOH compared to NaOH electrolyte[11], although Tiwari *et al.* show only minor differences exists for Cu(111) when comparing KOH and NaOH electrolytes.[18] DFT calculations predict that the presence of a cation should have little effect on adsorption energies on copper surfaces (and thus the CV)[21], but no systematic experimental study exists (to the best of our knowledge). Other experimental conditions, such as molarity ($0.1\ M$) and scan rate ($\nu = 50\ mV \cdot s^{-1}$) are the same for all discussed CVs, as is the cell material (plastic) for all but one of the CVs (electropolished Cu(110) by Huang *et al.*[22], which was likely measured in glass judging by their reported Cu(111) CV, though not specified in text).

Cu(111) literature comparison

In Figure 4.1, CVs of Cu(111) as obtained via various preparation methods are depicted. Black represents a UHV-prepared surface[17], with an electropolished sample by the same group shown in orange.[17] Another electropolished crystal, from a different group, is shown in red[15], and the CV obtained by us is in blue. As can be seen, all CVs exhibit a strong reversible adsorption feature centered around $+0.1\ V$[18], which has been assigned to OH-adsorption on {111} terraces.[17, 23] An additional {111}-related peak is seen for the blue CV at $+0.455\ V$ (presumably O-adsorption, further elaborated in a later section). However, scanning to such oxidative potentials results in irreversible surface changes thus necessitating reannealing of the crystal to regain surface ordering.

Comparing the black (UHV) and orange (electropolished) CVs we find that an electropolished surface measured by the same group exhibits suppressed intensity for the OH-adsorption feature; a common characteristic for electropolished samples. However, fair comparison between differing sources is impeded by a specific characteristic of the {111} facet: namely that it apparently requires active cycling. Specifically, by only briefly applying a standby potential before initiating cycling, such as done by Sebastián-Pascual *et al.* for their electropolished CV (red)[15], the DL-normalized {111}-specific feature at $+0.1\ V$ becomes more pronounced compared to Tiwari *et al.*'s UHV-prepared surface.[17] Considering we employ the same electrochemical methodology, also our CV (blue) exhibits a similarly more intense OH-adsorption feature.

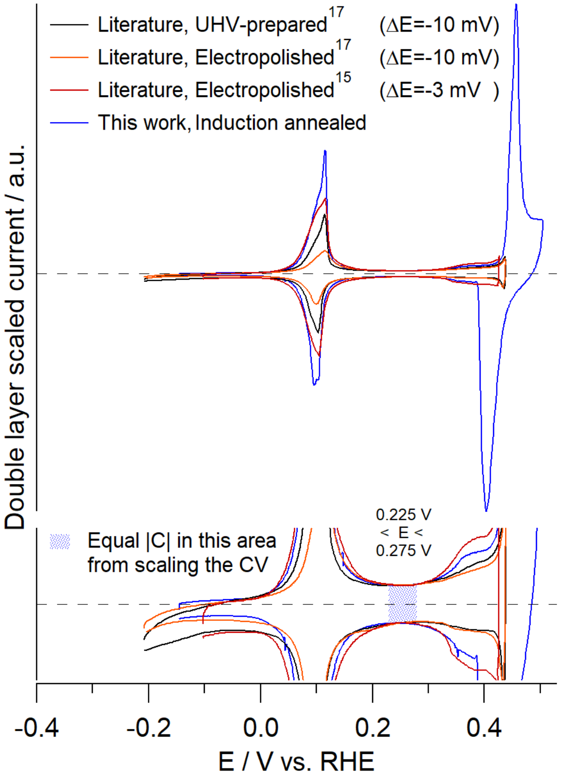

Figure 4.1: Comparison of literature reported CVs of Cu(111) with an induction annealing-prepared sample. CVs have been manually shifted up/down to reach the maximum amount of symmetry around the x-axis of the main adsorption features. CVs have been scaled to the absolute charge of the CV region represented by the blue dotted box, with the potential boundaries as specified in the image. δE values represent the amount by which literature CVs were manually adjusted to align the key adsorption feature at $+0.1!\ V$ with the induction annealed CV.

If this alternative measuring strategy would result in an increased number of terrace sites, and thereby yield increased charge of the adsorption feature (i.e., surface roughening), one would expect the double layer thickness (i.e., total surface capacitance) to similarly increase. However, normalizing by the charging current (as determined between $+0.225\ V < E < +0.275\ V$) does not resolve the charge discrepancy (e.g., compare the red and black lines). Considering this argument relies heavily on the assumption that certain regions of the CV are purely (pseudo-) capacitive in nature, we point to a publication by Maagaard *et al.*[13] wherein they show that introducing step-site defects in a Cu(111) crystal leads to (small) increases in the electro-sorption charge of the {111}-specific feature which is similarly reflected in a small increase in current in the double layer region we defined previously. Furthermore, their step-rich surface exhibits an additional oxidative feature near $+0.29\ V$ and cathodic feature near $-0.04\ V$, both of which are not observed in our Cu(111) CV nor in those reported by Sebastián-Pascual *et al.*[15] Additional proof against electrochemical roughening comes from ref [18] where they show via ex-situ STM of a Cu(111) crystal pre- and post-electrochemical characterization ($0.1\ M$ KOH) that cycling between $-0.2\ V < E < +0.45\ V$ leads to *"...no major structural changes..., suggesting that the Cu(111) surface is relatively stable under these conditions"*.

An alternative explanation for the discrepancy in peak intensity might be that the CVs reported by Tiwari *et al.*[17] and Maagaard *et al.*[13] were measured in KOH electrolyte, whereas we and Sebastián-Pascual *et al.*[15] used NaOH electrolyte. However, those same authors (in the SI of another one of their publications[18]) report only minor differences for a CV of Cu(111) when measuring in either KOH or NaOH. Hence, also differences in the solution cations are unable to explain this difference. Therefore, we tentatively propose instead that the charge associated with this feature reflects the state of the surface in the electrochemical environment, with the increased intensity being an indicator of surface quality and long-range ordering of the atoms making up the terraces at the metal|electrolyte interface.

Further differences between UHV-prepared Cu(111) CVs and electropolished / induction annealed surfaces can be observed with regards to the amount of crystal defects (as visible from charge in the region $+0.32\ V < E < +0.42\ V$). To start, the orange (electropolished) CV actually exhibits a lower quantity of defect sites than the UHV-prepared surface by the same group (black). However, this surface also exhibits severe suppression of the main OH-adsorption feature, thus the defect density is still increased with respect to the UHV sample. The other non-UHV surfaces (red, blue) both exhibit increased amounts of defect sites as compared to the UHV-prepared surface, which is more in line with expectations considering that surface preparation involving electropolishing introduces defects into the surface. However, whereas generally defect density increases as a surface is electropolished more, the number of defect sites for our induction annealed surface was found to be stable with respect to time (not depicted) – even though periodic electropolishing was applied when an experiment resulted in irreversible surface changes. Actually, the majority of the defects present in the surface originated from our initial attempts at cleaning the crystal; a methodology which has since been replaced by a milder technique that introduces fewer defects.

Overall, a Cu(111) crystal prepared via induction annealing exhibits the features indicative of clean $\{111\}$ terraces, with a relatively lower defect-to-terrace sites ratio ($Q_{defects} : Q_{terraces}$) than electropolished surfaces, although not as good as a UHV-prepared Cu(111) crystal. Furthermore, it was found (not depicted) that the quantity of step defects did not increase with additional electropolishing when post-induction annealing was employed, contrary to what is observed for surfaces that are not annealed after such treatment. Finally, it was observed that the exact electrochemical methodology has a strong influence on the intensity of the $\{111\}$-terrace specific OH-adsorption feature at ca. $+0.1\ V$, where shorter periods at a constant polarization potential followed by constant cycling result in more a pronounced feature. Similar sensitivity of Cu(111) with respect to the initial polarization period (potential and/or time) has been reported before[9], but in that work the resulting CV exhibits clear signs of contamination associated with impurities related to alkaline glass leaching.[18] As such, it is unclear if the sensitivity towards the initial polarization time we observe in the absence of impurities is the result of the same phenomenon as the effect they observe in the presence of foreign surface adsorbates – especially considering that they also report the CV to evolve with successive cycling, which we do not observe.

Cu(100) literature comparison

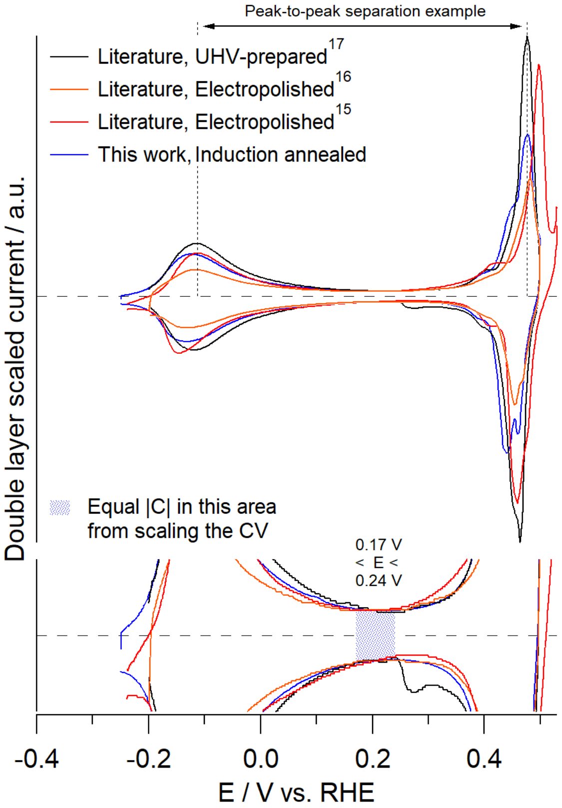

Figure 4.2: Comparison of literature reported CVs of Cu(100) with an induction annealing-prepared sample. CVs have been manually shifted up/down to reach the maximum amount of symmetry around the x-axis of the main adsorption features. CVs have been scaled to the absolute charge of the CV region represented by the blue dotted box, with the potential boundaries as specified in the image.

In Figure 4.2, CVs are depicted for Cu(100) as prepared via different methodologies. Black shows the electrochemical signal of a UHV-prepared surface[17], with an electropolished example by the same group in orange.[16] An electropolished surface published by Sebastián-Pascual *et al.* is shown in red[15], and finally the CV obtained by us via induction annealing is depicted in blue. The {100} facet exhibits two specific features: a reversible feature around $-0.1\ V$ ascribed to OH-

Table 4.1: Peak-to-peak separation of the two oxidative {100}-terrace adsorption features for the different Cu(100) crystals. These values are meant mostly for illustrative purposes, as they are of limited accuracy due to the transcription process converting images to numeric data.

Crystal	**Peak separation (mV)**	**Δ compared to UHV (mV)**
Cu(100), UHV (black)	591	0
Cu(100), Electropolished (orange)	597	6
Cu(100), Electropolished (red)	610	19
Cu(100), Induction annealed (blue)	599	8

adsorption[9, 17, 24, 25], and another reversible feature at ca. $+0.475\ V$[11] (which is likely due to O-adsorption, addressed in more detail in a later section). It is important to note that it has been reported that copper {100} terraces are not stable when cycled in the potential window used for electrochemical surface characterization[25] as commonly employed in prevalent literature and also in this work.[9–11, 17] However, it has recently been shown that adventitious oxygen in the electrolyte has a significant effect on the voltametric behavior of a Cu(100) surface[11], and large amounts of oxygen (as evidenced by the overall cathodic current) are observed in the work reporting about the instability of the terrace sites.[25] In this work, we shall presume that a Cu(100) surface is stable under the employed characterization conditions (as implied by the reproducibility of the CV with successive cycling, not depicted), so long as the electrolyte is properly deaerated.

The Cu(100) CVs from different sources show better agreement than in the case of Cu(111), exhibiting reasonably comparable intensities for the feature near $-0.1\ V$, although showing some more variability in the second feature (ca. $+0.475\ V$). Comparing the UHV-prepared surface (black) with the electropolished surface from the same group (orange) shows once again that the electropolished sample exhibits overall suppression of the facet-specific adsorption features. Additionally, it can be seen that the second feature is shifted to slightly more oxidative potentials (see also Table 4.1, where the peak-to-peak distance is given – with a visual representation of the meaning of this separation distance, using the UHV-sample as an example, given in Figure 4.2). Comparing the electropolished sample by Sebastián-Pascual *et al.*[15] (red) with the orange electropolished sample shows that the former exhibits more prominent OH-adsorption features, but at the cost of i) reduced symmetry of the feature near $-0.125\ V$, and ii) a more substantial shift of the second adsorption feature (Table 4.1).

If we compare the surface prepared via induction annealing (blue) with the other literature reported crystals, it is in-between the electropolished and UHV-prepared samples. E.g., the intensity of the feature at $-0.125\ V$ agrees well with that of the electropolished sample with more prominent features (red), but is suppressed in comparison to the UHV-prepared surface (black). But, the level of symmetry is greater than the red sample, matching that of the black sample. As for the second feature near $+0.475\ V$, we find that its location matches well with that of the UHV-prepared sample (though its peak-to-peak distance is still slightly increased,

Table 4.1), as opposed to the red trace which exhibits a significant shift towards more oxidative potentials. However, the intensity of the feature is lower than either of those surfaces – though it has been reported that this feature is very sensitive to the presence of trace amounts of oxygen in the solution, with higher peak intensities associated with increased oxygen content[11] (with our system having very little oxygen).

Comparing the same points with the second electropolished surface (orange) is more favorable, with the induction annealed surface better matching the features of a properly prepared UHV-sample in most instances though they both exhibit similar levels of symmetry for the first peak. Finally, it can be observed that the induction annealed CV has a shoulder near $+0.445\ V$ (its location matching well with the second feature of Cu(111)), which is more prominent than for the literature samples. Similar to Cu(111), we attribute this higher density of crystal defects in our sample to our initial crystal cleaning attempts and we expect these to be present to a lesser degree if new crystals are cleaned employing the alternative electropolishing procedure as described in the experimental section.

Overall, the CV of a Cu(100) crystal as-prepared via induction annealing is found to be a compromise between the CVs obtained after UHV surface preparation and electropolishing. The OH-adsorption feature near $-0.125\ V$ exhibits good symmetry, but is suppressed in intensity as compared to a UHV-prepared surface, though more pronounced and symmetrical than after electropolishing. The second $\{100\}$-terrace specific feature near $+0.475\ V$ is suppressed in intensity compared to all literature-reported surfaces (possibly related to differences in the amount of oxygen present in solution), but matches well in its location with that of a UHV-prepared surface. However, the amount of defect sites present in the crystal was significantly worse than the other surfaces – which we posit should not be as prominent if milder cleaning procedures are employed for newly procured crystals.

Cu(110) literature comparison

In Figure 4.3, various Cu(110) CVs are depicted with the signal of a UHV-prepared surface shown in black[17] and an electropolished crystal from the same group shown in orange,[16] an electropolished surface published by Huang *et al.* (likely measured in a glass cell) depicted in red[22], and the characterization CV obtained in this work via induction annealing shown in blue. This facet is reported to have two facet-specific regions; one OH-adsorption feature[17] located near $-0.3\ V$ and an additional feature near $+0.335\ V$ (for which we will discuss the corresponding adsorbates later). However, we found that scanning to the potential boundaries where the former peak is located resulted in severe suppression of the second feature. Increasing the lower potential boundary to more positive values resulted in more stable voltammetry at the cost of not seeing this cathodic feature at $-0.3\ V$. Considering the apparent instability of the CV in this wider potential window, combined with the fact that most published CVs stop at more positive potentials (including many of the Cu(110) CVs reported by the group that identified the feature at $-0.3\ V$[17]), we shall exclude this particular adsorption feature from our discussion.

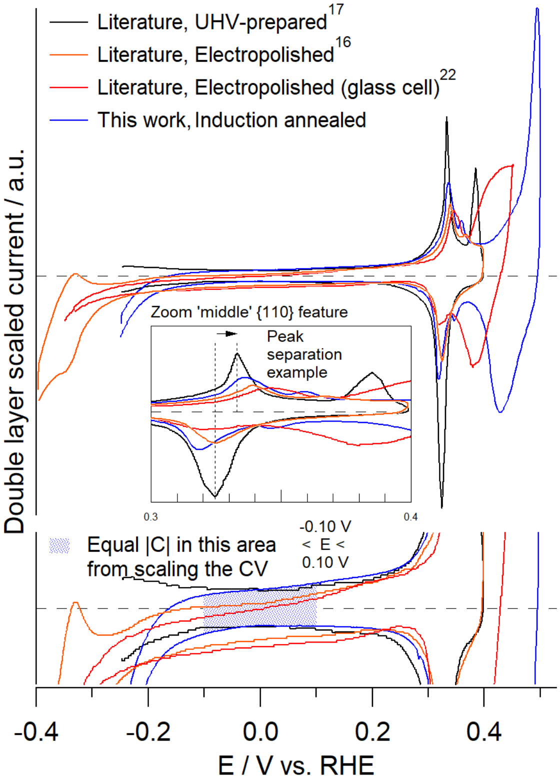

Figure 4.3: Comparison of literature reported CVs of Cu(110) with an induction annealing-prepared sample. CVs have been manually shifted up/down to reach the maximum amount of symmetry around the x-axis of the main adsorption features. CVs have been scaled to the absolute charge of the CV region represented by the blue dotted box, with the potential boundaries as specified in the image.

Starting with the electropolished crystal by Huang *et al.* (red)[22], we see a mostly featureless region between $-0.25\ V < E < +0.05\ V$ and a faint, broad feature between $+0.05\ V < E < +0.25\ V$ (the region where {111} terraces adsorb OH). Going more positive we find a symmetrical feature at ca. $+0.33\ V$ that is related to {110} terraces (a measure for the peak symmetry as visually represented in Figure 4.3, is given in Table 4.2). Finally, we observe a large oxidative 'hump' between $+0.35\ V < E < +0.45\ V$, which (to the best of our knowledge) is not specific to {110} terrace sites and we shall thus attribute to crystal defects. Next we shall discuss the electropolished sample reported by Tiwari *et al.*[16] (orange). Their CV exhibits a more symmetrical (Table 4.2) and comparatively sharper {110} feature, the same broad featureless region at lower potentials, and is missing most of the defect-related peaks present for the red crystal – although a scrutinizing eye can observe a faint reversible peak between $-0.25\ V < E < -0.05\ V$ (representing OH-adsorption on {100} terraces). However, the CV does have an additional feature in the form of a defect-related minor oxidative spike near $+0.367\ V$, although

Table 4.2: Peak separation between the maxima of the oxidative and reductive waves of the {110} feature at ca. $+0.33\ V$. These values are meant mostly for illustrative purposes, as they are of limited accuracy due to the transcription process converting images to numeric data.

Crystal	**Peak separation (mV)**
Cu(110), UHV (black)	9
Cu(110), Electropolished (orange)	15
Cu(110), Electropolished (red)	25
Cu(110), Induction annealed (blue)	18

no associated peak in the negative-going scan direction is observed (possibly it is irreversible to such an extent that it overlaps with the cathodic {110} feature).

A UHV-prepared crystal (black)[17] similarly shows a virtually featureless region between $-0.25\ V < E < +0.30\ V$, followed by a sharp, symmetrical {110}-related adsorption feature – although the cathodic wave exhibits increased charge compared to the anodic wave. At more positive potentials, an oxidative can be seen spike (ca. $+0.385\ V$) whose origin is not elaborated on in the original paper.[17] Seemingly, this spike has no counterpart in the negative-going scan direction, although it is likely potential-shifted due to non-reversibility and happens to overlap with the cathodic {110}-related feature, considering the charge mismatch between the cathodic and anodic waves of said feature. Interestingly, the location of the spike at $+0.385\ V$ matches well with where {100} step sites exhibit adsorption-related charge, as deduced from the reversible peak in this area present for the CV of a Cu(211) crystal.[16] However, that crystal does not exhibit the same shift (i.e. irreversibility) of the desorption wave to lower potentials. Possibly the UHV-prepared Cu(110) surface, under electrochemical conditions, exists in a (partially) reconstructed state that exposes {100} step-like surface sites, considering that ordinarily highly reversible adsorption features are observed for single crystalline surfaces (though this is speculative).

An induction annealed crystal (blue) is again a compromise; being somewhere in-between an electropolished and a UHV-prepared surface. The double layer region up to $+0.30\ V$ is mostly featureless, although a prominent reductive 'tail' (presumably HER) is observed at the lower end of the potential range, and a minor amount of {111} terraces can be argued to be present as judged from a small amount of excess charge in the potential region between $+0.05\ V < E < +0.25\ V$. A clear, reversible {110}-specific feature is observed, but its intensity is suppressed compared to the UHV-prepared sample, although more prominent than for the electropolished surfaces. A reversible defect-related spike is seen near $+0.36\ V$ (at slightly more cathodic potentials than what is observed for the orange sample, and symmetrical contrary to the orange CV). Furthermore, by extending the positive potential window, an additional (irreversible) {110}-terrace specific feature is observed at $+0.494\ V$. An interesting empirical finding is that the Cu(110) surface is relatively stable even when scanning to $+0.50\ V$, exhibiting reproducible voltammetry (not depicted).

A final consideration is with regards to the reversibility of the {110} feature, with all non-UHV samples exhibiting decreased reversibility compared to a UHV-prepared surface (Table 4.2). However, considering the mismatch between the charge of the anodic and cathodic waves for the UHV sample, it is likely that the cathodic wave is a convolution of two features. This may influence the metric we use to represent peak symmetry (e.g., the potential difference between the maxima of the anodic and cathodic waves, respectively) depending on the exact location of the (hypothesized) secondary feature. Hence, we consider peak symmetry to be of limited value as a means of comparison.

4.3.2. Properties of induction annealed crystals

Cu(111)

We shall now briefly discuss the characteristic CV of an as-measured Cu(111) surface prepared by induction annealing, following the electrochemical methodology described in this work. To this end, a standalone CV of Cu(111) with different levels of magnification and varying degrees of x-axis compression is depicted in Figure 4.4. Firstly, it can be observed that there exist two apparent 'double layer' regions: places where seemingly only capacitive current is observed, namely between $-0.15\ V < E < 0\ V$ and between $+0.2\ V < E < +0.3\ V$. However, the charging current in these two windows is not identical and, considering that the second region exhibits larger currents, it is probable that this latter region is not purely capacitive in nature. Similar behavior is also visible in the literature, though in that work it is more evident at a scan rate of $100\ mV \cdot s^{-1}$.[13] We hypothesize that adsorption phenomena on {111} terrace sites with high step density take place in this region. This statement is based on two observations. Firstly, Maagaard *et al.* show that the CV for a Cu(111) surface develops an additional oxidative feature at ca. $+0.28\ V$ upon roughening of the surface.[13] Secondly, in a work discussing CO oxidation on Cu single crystals, Tiwari *et al.*[16] report an electropolished CV for Cu(211) (which has a 3x{111}{100} structure), which shows a very broad feature between ca. $-0.02\ V < E < +0.25\ V$ – a window that is basically an extension of the region where {111} terraces are normally observed. Hence, this region should preferably be avoided if one wishes to determine the double layer capacity (C_{DL}), with the lower potential window ($-0.15\ V < E < 0\ V$) being more suitable for that purpose.

A second observation is that it is entirely possible, in practice, to obtain oxygen-free CVs for this facet (and copper in general), although this does require a properly sealed cell and generous amounts of argon bubbling. The significance of this observation lies in the fact that most literature work has substantial amounts of oxygen present (as judged from a lack of symmetry around the x-axis, especially at lower potentials), and it is unclear what kind of influences the presence and/or reduction of oxygen may have on the stability and adsorption behavior of (different types of) copper (sites). Having ORR current contribute to the CV may also lead to a misinterpretation of copper-specific behavior. E.g., signs of early onset HER due to increasing the number of defect sites and/or the number of {110} terrace sites in a copper surface might be misinterpreted as reduction of trace amounts of oxygen (such behavior can be seen to occur in Figure 4.8).

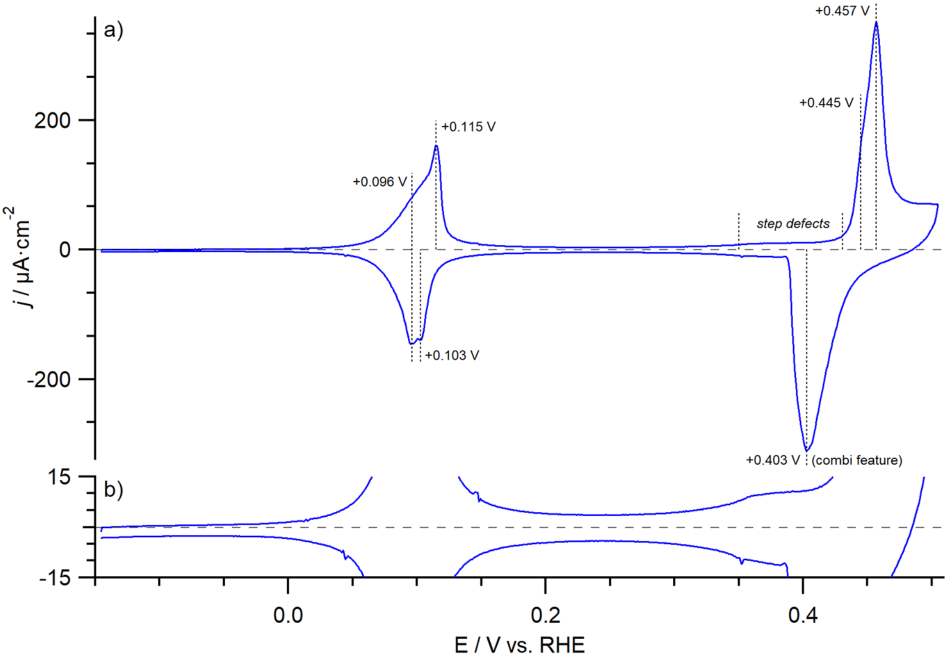

Figure 4.4: Normalized (geometric area) CV of Cu(111) as obtained after preparation via induction annealing, employing the electrochemical procedure described in the experimental section. Measured in $0.1\ M$ NaOH at scan rate $\nu = 50\ mV \cdot s^{-1}$.

As a third consideration, we shall discuss in more detail the {111} terrace-specific adsorption features in alkaline electrolyte. Specifically, there is the commonly reported[9, 10, 13, 17] reversible OH-sorption feature[12, 17, 23] near $+0.1\ V$ (peak A), which is actually a convolution of a broad peak located at more cathodic potentials and a narrower (i.e., sharper) peak located at more anodic potentials (ca. $+0.096\ V$ and $+0.115\ V$, respectively – Figure 4.4a). This binary nature is likely related to the average width of the terraces, as becomes evident when comparing the CV of a UHV-prepared surface (having large {111} terraces) with the CVs of electropolished Cu(111) (having overall smaller {111} terraces) (Figure 4.1, black vs. orange and red, respectively). From this, it can be seen that a UHV-prepared surface has a strong feature at $+0.115\ V$, and the broad peak at $+0.096\ V$ manifests as more of a shoulder, whereas electropolished surfaces are better described as consisting of mostly a broad feature, having a relatively smaller charge-contribution of the sharper spike at $+0.115\ V$.

Additionally, there exists a second, irreversible, adsorption feature at more oxidative potentials (ca. $+0.45\ V$, peak B) which is again best described as a convolution of two peaks: a peak centered around $+0.457\ V$, which has a shoulder at ca. $+0.445\ V$ (Figure 4.4a). Using similar reasoning, we ascribe this duality to O-adsorption on smaller and larger {111} terrace sites, where it is likely that the feature at $+0.445\ V$ is due to O-adsorption on smaller terraces as we observe

Table 4.3: Reaction schemes for OH and O adsorption on copper.

$$\mathrm{Cu_2O + H_2O + 2\,e^- \rightleftharpoons 2\,Cu + 2\,OH^-},\ E^0 = +0.41\ V \text{ vs. RHE } (pH13) \tag{R1}$$

$$\mathrm{nCu + OH^- \rightleftharpoons Cu_{\mathit{n}}OH_{ads} + e^-} \tag{R2}$$

$$\mathrm{Cu_{\mathit{n}}OH_{ads} + OH^- \rightleftharpoons Cu_{\mathit{n}}O_{ads} + H_2O + e^-} \tag{R3}$$

$$\mathrm{2\,CuOH \rightleftharpoons Cu_2O + H_2O} \tag{R4}$$

this peak as well in the form of a defect peak in our Cu(100) crystal (Figure 4.5a). Considering the close proximity of this second feature to the equilibrium potential of Cu_2O formation ($+0.45\ V$ vs. $+0.41\ V$, Reaction R1 in Table 4.3[26]), it is likely that this feature is due to O-adsorption. If true, we would expect the charge associated with the OH-adsorption feature to be equal to the charge associated with the second feature as per the stoichiometry of Reactions R2 and R3 in Table 4.3 (where we have opted to not use "Cu_2O_{ads}" and "$CuOH_{ads}$" to avoid confusion with the formation of bulk oxides and CuOH, which is believed to be an existing but highly unstable species that is rapidly converted into Cu_2O via Reaction R4 in Table 4.3).[27–29] To substantiate the hypothesis that the second feature is related to O-adsorption, we mathematically deconvoluted the voltammogram into its individual constituents, which allows for an approximate quantification of the charges associated with each of the peaks that make up the CV (Figure C.8). From our deconvolution, we estimate that the ratio of peak A to peak B $\approx 0.9 : 1$, which we consider sufficiently close to the theoretically expected value of $1 : 1$ to tentatively assign this second adsorption feature to O-adsorption.

A final consideration is regarding the charge associated with the OH-adsorption feature. The value we calculate is equal to $107\ \mu C \cdot cm_{geo}^{-1}$, although this value does contain the charge contribution between $+0.1\ V < E < +0.25\ V$ as well (without this contribution, we find $101\ \mu C \cdot cm_{geo}^{-1}$). This value is significantly higher than the value reported by Tiwari *et al.*[17] ($79\ \mu C \cdot cm_{geo}^{-1}$) whose value corresponds to a coverage of 1/4th of a monolayer, with our calculated charge being closer to a coverage of 1/3rd of a monolayer instead. Considering that the OH-adsorption charge we find for the other basal planes agrees much better with literature (see next sections), and taking into account that this difference in charge for OH-adsorption on Cu(111) persists even when correcting for the double layer capacity (as discussed previously), we are currently unable to explain this discrepancy.

Cu(100)

The CV of an induction annealed Cu(100) surface as obtained in this work is given in Figure 4.5. Regarding the {100} specific features, a clear OH-adsorption feature[9, 17, 24, 25] is observed at ca. $-0.125\ V$ as is a (previously reported)[11] second feature near $+0.477\ V$. Regarding the nature of the adsorbing species for this anodic feature, we can use the same logic as previously. By mathematically deconvoluting the CV (Figure C.9), we find that the charge ratio of the OH-adsorption peak with

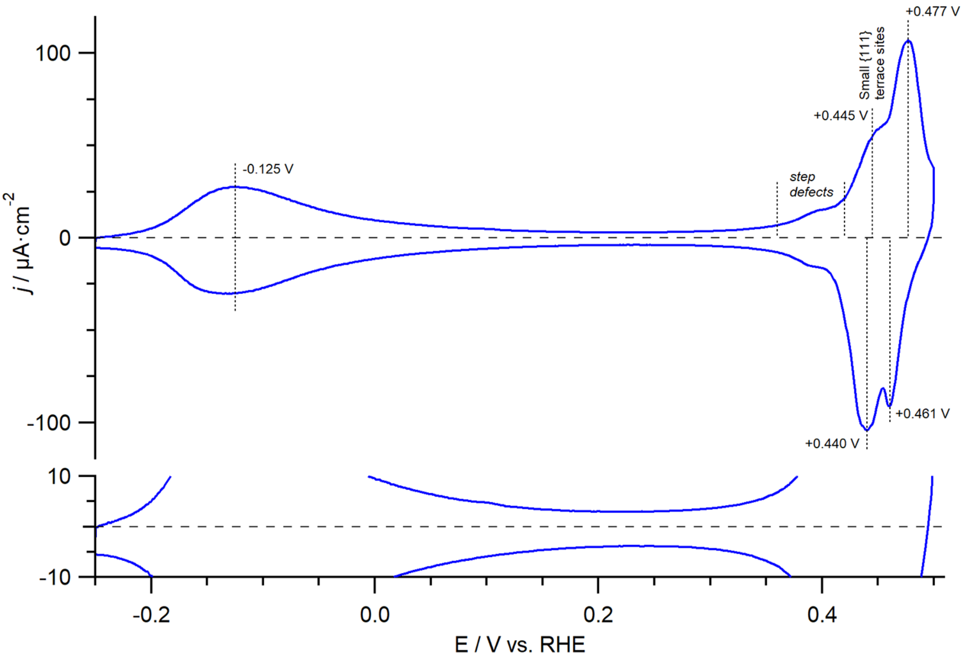

Figure 4.5: Normalized (geometric area) CV of Cu(100) as obtained after preparation via induction annealing, employing the electrochemical procedure described in the experimental section. Measured in $0.1\ M$ NaOH at scan rate $\nu = 50\ mV \cdot s^{-1}$.

respect to the second peak is (again) ca. $0.9 : 1$. Hence, we believe the feature at $+0.477\ V$ to be due to O-adsorption on {100}-terrace sites. Aside from this, we found (empirically) that the exact location of the second peak seems to depend on the quality of the surface (Figure 4.2), shifting to more oxidative potentials for surfaces with a higher defect density. As for the charge associated with the OH-adsorption feature, we find $68.7\ \mu C \cdot cm_{geo}^{-1}$ – which is in reasonable agreement with the theoretical value reported by Tiwari *et al.*[17] ($59\ \mu C \cdot cm_{geo}^{-1}$).

As a final consideration, we observe a larger-than-usual amount of defect sites in the form of a shoulder near $+0.445\ V$ (which we believe to be small {111} terrace sites), with literature reported CVs not commonly showing such an clear shoulder (though it is generally present, Figure 4.2). Interestingly, these terrace sites exhibit a much higher (apparent) reversibility than what we find for a Cu(111) crystal (Figure 4.4). Possibly, the reversibility of adsorption on these sites is a function of terrace size, with smaller terraces exhibiting increased reversibility. Alternatively, our assignment of this feature to {111} terraces might be erroneous, though we are not aware of any other surface sites that (may) give rise to an adsorption feature in this region. This peak was found to increase over time with repeated electropolishing under our initially employed electropolishing conditions (not depicted), but stabilized after switching to a milder electropolishing methodology (see experimental section). This milder form of electropolishing should result in better quality

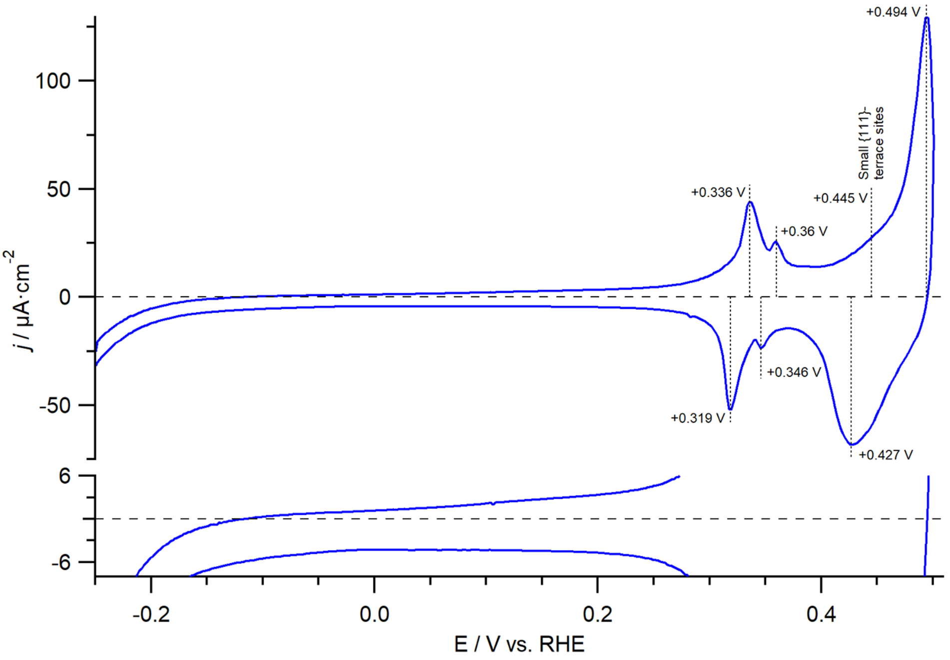

Figure 4.6: Normalized (geometric area) CV of Cu(110) as obtained after preparation via induction annealing, employing the electrochemical procedure described in the experimental section. Measured in $0.1\ M$ NaOH at scan rate $\nu = 50\ mV \cdot s^{-1}$.

surfaces with fewer defects.

Cu(110)

A typical characterization CV obtained for Cu(110) as obtained after induction annealing and electrochemical treatment as described in this work is depicted in Figure 4.6. Preparing this particular facet via induction annealing was found to be challenging, with strongly suppressed peak intensities observed for the {110}-specific feature after quenching the crystal in pure hydrogen (the default treatment employed for the other surfaces). Lowering the cooling rate, and/or changing the annealing atmosphere or cooling atmosphere all yielded similar results. Quench-cooling in pure argon looked promising, but resulted in the {110}-specific peak location shifting and becoming unstable during electrochemical cycling, transforming to yield the same suppressed CV as obtained in other instances. Eventually, we found that evolving large amounts of hydrogen (presumably) leads to restructuring of the surface to yield CVs with a peak intensity that compared favorably with literature. However, this methodology comes at a cost: preparing a Cu(110) crystal this way yields a CV that exhibits 'tailing' (likely HER) at potentials below $-0.1\ V$, which is not observed in published literature – although the presence of oxygen could potentially mask this effect to a certain extent.

Regarding the {110}-terrace specific peaks, a reversible adsorption feature is observed at ca. $+0.33\ V$ and an additional irreversible feature is observed near $+0.494\ V$. Assigning the adsorbates associated with these two features is requires a bit more work than for the previous surfaces. OH-adsorption has been shown to correlate well with the potential of zero charge (pzc) for copper[15] with Cu(110) having the most negative pzc out of the three basal planes.[30] As such, the expected location of the OH-adsorption feature of Cu(110) would be at more negative potentials than for Cu(100) and Cu(111). To this end, Tiwari *et al.*[17] show that a {110}-specific adsorption feature exists at ca. $-0.3\ V$. However, the charge they determined experimentally to be associated with this feature is $25\ \mu C \cdot cm_{geo}^{-1}$, which is about half of the charge they expect based on their theoretical modeling ($54\ \mu C \cdot cm_{geo}^{-1}$). As their modelling predicts OH to bind atop the atoms making up the rows in the (110) surface, they conclude that Cu(110) likely exists in a (110)-(1x2) missing row reconstructed state, which would account for half of the charge missing. Interestingly, CV deconvolution (Figure C.10) of our system yields a very similar estimated charge for the feature at $+0.33\ V$ ($25.8\ \mu C \cdot cm_{geo}^{-1}$ vs. theoretically $27\ \mu C \cdot cm_{geo}^{-1}$). Furthermore, if we calculate the charge ratio of the peak with respect to the feature at $+0.494\ V$ (which we expect is related to O-adsorption), we find a ratio of ca. $1.06 : 2$. Finally, considering the equilibrium potential for Cu_2O formation ($+0.41\ V$, Reaction R1 in Table 4.3), it is rather unlikely that the feature at $+0.33\ V$ involves O-adsorption. Rather, it is more probable to be related to OH-adsorption.

Combining all these considerations can reasonably be done in two possible ways. Firstly, it is possible that a second, {110} terrace-specific, OH-adsorption site exists for a Cu(110)-(1x2) surface – which would likely be the surface sites that are exposed after removing every other row of atoms. In this case, a difference in adsorption strength would result in differing peak locations, but a similar total charge may be observed if the adsorbates are spaced approximately equally as in the case for adsorption on the top of the row. An alternative possibility is a potential-induced lifting of the reconstruction, where the surface reverts back to a Cu(110) surface at more anodic potentials. In such a case, an adsorption feature would be expected after lifting of the reconstruction, equal in charge to the first feature. Both instances would result a ratio of $1 : 2$ when calculating the ratio between either of the two cathodic (OH-adsorption) features and the adsorption feature at $+0.494\ V$, if the latter is O-adsorption. Although we cannot determine which of these options is correct from the current data, based on these evidences we are fairly confident in assigning the feature at $+0.33\ V$ to OH-adsorption and the feature at $+0.494\ V$ to O-adsorption.

4.3.3. Cu(poly): induction annealing vs electropolishing

Depending on research objectives it may be important to study surfaces that encompass all types of sites simultaneously, for instance as a means of determining the overall catalytic properties of a material in one measurement. Polycrystalline surfaces lie at the heart of such experiments as they consist of, by definition, many different crystallites of various orientations and dimensions. Though polycrystalline surfaces are more often than not studied for their relative simplicity, a properly conducted study using such surfaces can still provide a wealth of information on the overall behavior of a given material.

The methodology for preparing such polycrystalline copper surfaces generally encompasses procuring a sheet of material, machining it to the desired shape and dimensions, and then mechanically polishing it as a means of both decreasing the roughness factor (R_f = EASA/geometric area) as well as cleaning of the surface. An electrode prepared as such is expected to yield reasonably reproducible surfaces, so long as the starting material is of comparable purity. However, it is known that mechanically polished copper surfaces (even after sonication) do not yield CVs exhibiting the expected adsorption features of a copper surface,[11, 31] which can be interpreted as the copper surface being blocked by residues of the polishing process. Hence, an additional (anisotropic) electropolishing step is often applied, wherein the copper surface is oxidized in concentrated (phosphoric[2, 10]) acid solution and the electrogenerated oxides subsequently dissolve.[20] However, because the exact surface treatments employed by different laboratories vary slightly (e.g., polishing with finer slurries or different polishing materials, sonicating for varying time periods possibly in different solvents, electropolishing at different potentials or in electrolytes of differing compositions), reported characterization CVs for copper exhibit large differences between different laboratories, yet are all called polycrystalline.[11] In this work, we found that preparing polycrystalline spherical bead-type copper electrodes via induction annealing is an easy and quick method for producing clean copper surfaces with a consistent and wide site distribution that exhibit single-crystal like adsorption features when following the surface preparation and electrochemical procedure described in the experimental section.

In Figures 4.7a and 4.7b, we present the CVs of a mechanically polished + electropolished copper disk electrode (Cu(poly)$_{\text{Mech}}$) and an induction-grown + induction annealed spherical bead electrode (Cu(poly)$_{\text{Induct}}$) in red and blue, respectively. Both were measured as per the electrochemical methodology described in the experimental section. To verify that the differing normalization techniques between these two samples (geometric vs. electrochemically active area, see experimental section) would not influence the result we determined the roughness factor of the disk-type electrode from its OH-adsorption charge, finding $R_f = 1.02$ – which we believe is sufficiently close for fair comparison. The Cu(poly)$_{\text{Mech}}$ CV does exhibit some residual oxygen for which we are unsure to what degree it affects the differences we shall discuss. We shall proceed assuming it is of negligible influence.

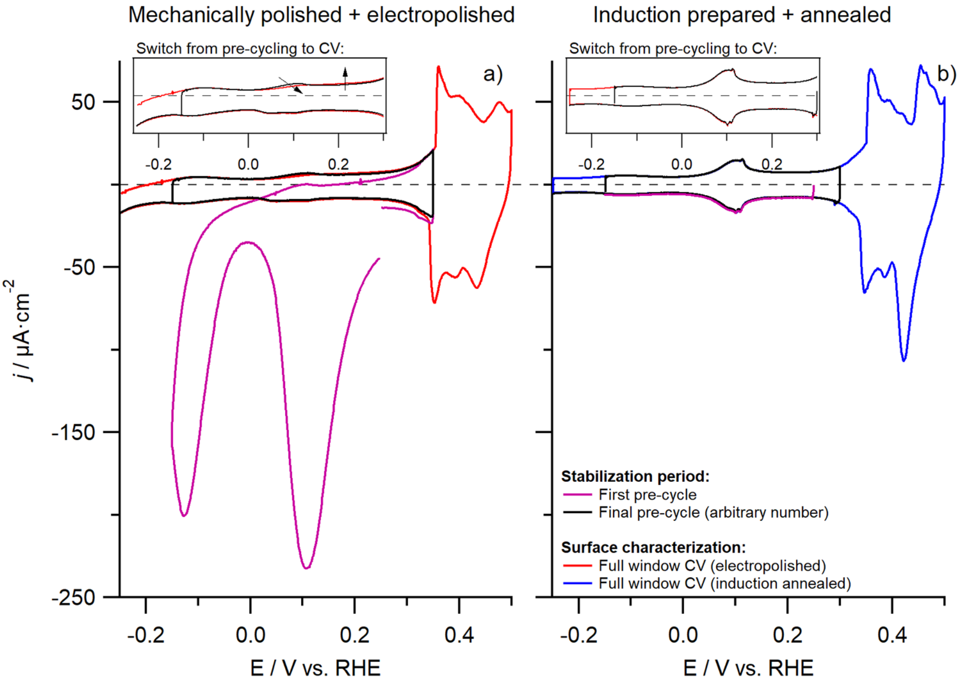

Figure 4.7: Typical copper CV ($0.1\ M$ NaOH, scan rate $\nu = 50\ mV \cdot s^{-1}$) obtained after a) mechanical polishing + electropolishing treatment and b) induction annealing treatment. In purple, the first CV after establishing electrolyte contact is depicted, while the last pre-characterization cycle (i.e., initial cycling in a smaller potential window to stabilize the surface and remove oxygen) is depicted in black. In red and blue are shown the full-window characterization CVs for the electropolished and induction annealing-prepared surfaces, respectively.

The greatest difference between these two samples can be seen in the first pre-cycling CV (purple); namely, that an electropolished electrode is initially covered by a layer of copper oxide, whereas the induction annealed surface is not. Though the former can be considered unavoidable under normal laboratory conditions (having to expose the electrode to ambient conditions for brief periods), it affects the surface. Specifically, the $\{111\}$ terrace OH-adsorption feature at $+0.1\ V$ significantly differs between the red and blue CVs, both in shape and in intensity. Whereas this feature is reminiscent of a Cu(111) single crystal (Figure 4.1) for the Cu(poly)$_{\text{Induct}}$ electrode, the Cu(poly)$_{\text{Mech}}$ disk is found to exhibit less overall charge in this area, irreversibility, and a cathodic feature that seems split into two. This split is also observed if 'long' (ca. $> 10\ s$) standby potentials ($E = -0.25\ V$) are applied to surfaces containing $\{111\}$ terrace sites (including Cu(111)) (Figure C.2), though the Cu(poly)$_{\text{Mech}}$ electrode was not subjected to such treatment. Hence, it is likely that the peak splitting is instead related to i) the electropolishing step or ii) the initial presence of an oxide film. Additional changes related to this peak arise when the lower vertex potential is decreased from $-0.15\ V$ to $-0.25\ V$ (compare the low potential region of the red and blue lines). In the case of a Cu(poly)$_{\text{Induct}}$

surface, we find that decreasing the lower potential boundary has negligible effect on the CV, whereas in the case of a Cu(poly)$_{\text{Mech}}$ surface we find that it leads to a redistribution of the charge of the anodic at ca. $+0.1\ V$ feature to overall more cathodic potentials (illustrated by the arrows in the inset in Figure 4.7a).

Overall, it can be said that the {111} terrace sites present on the surface of an electropolished electrode do not exhibit behavior that is representative of well-ordered, large {111} terraces; even though it is clearly possible to obtain an electrochemical signal reminiscent of the behavior of well-defined terraces with a polycrystalline electrode as evidenced by the CV for an induction annealed surface. Considering that the OH-adsorption behavior of {111} terrace sites on an electropolished surface differs from that observed for a Cu(111) crystal, it is likely that their electrochemical properties (e.g., catalytic activity) similarly differ to a certain extent.

The second important difference between the two polycrystalline surfaces is their facet distribution, as evidenced by the various peaks in the CV, and the relative charges associated with those peaks (with respect to one another). Specifically, besides OH-adsorption on {100} and {111} terrace sites ($-0.125\ V$ and $+0.1\ V$, respectively), a copper surface also exhibits a number of (distinct) peaks between $+0.35\ V < E < +0.50\ V$, whose individual current densities differ significantly between the two electrodes. That particular potential window can be split into two regions. Firstly, there is the window between $+0.35\ V < E < +0.44\ V$, which can be assigned to (OH-)adsorption on various step sites by realizing that this window is where single crystals of the principal orientations show charge unrelated to their primary sites (i.e., defect sites). Likely the adsorbate is OH, as the CV up to $+0.44\ V$ is found to be reversible (see e.g., Figures C.3 and C.7) and the alternative (O-adsorption) is generally irreversible (previously discussed) – though it can theoretically be either when taking into consideration the potential. The second region is between $+0.44\ V < E < +0.50\ V$ and is the region where O-adsorption on the terraces is observed.

Both regions exhibit clear differences when comparing the two surfaces, which can be interpreted as these surfaces having differing (ratios of) electrochemically active sites. These differences in surface facet distribution can likely be attributed to the anisotropic nature of the electropolishing step, where such treatment results in surfaces having a changed (preferential) site distribution compared to the starting surface. Considering that anisotropy favors certain types of sites over other types of sites, it involves both the preferential creation as well as the preferential removal of particular sites, where specifically the removal of sites may invalidate the measurement if e.g., the purpose of the experiment is to obtain the average activity of all possible sites simultaneously. The methodology for preparing a bead-type electrode which does not have such bias in surface site distribution is described in the SI.

Finally, induction annealing of a polycrystalline surface enjoys the same advantage as induction annealing copper single crystals; namely high surface reproducibility. A polycrystalline surface is the best way of illustrating reproducibility, exactly because it contains a wide assortment of different types of surface sites.

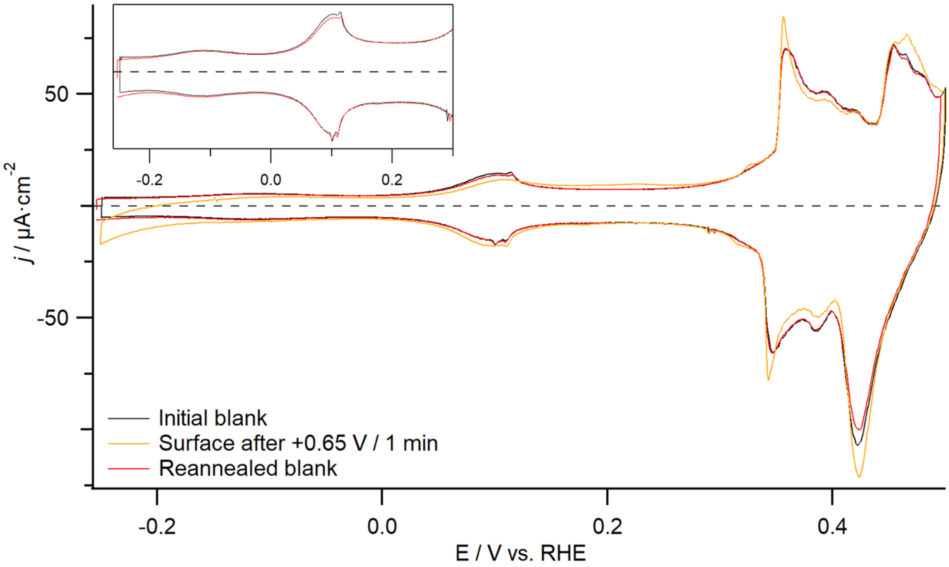

Figure 4.8: Illustration of the reproducibility of a polycrystalline surface after having been regenerated via induction annealing-treatment. In black, the initially obtained CV is depicted, whereas in orange the state of the surface is depicted after having been oxidized at $+0.65\ V$ for $60\ seconds$ in $10\ M$ NaOH. In red, the surface has been reannealed to recover its initial state. All CVs were measured in $0.1\ M$ NaOH at scan rate $\nu = 50\ mV \cdot s^{-1}$.

This is illustrated in Figure 4.8, where we depict the CV of an induction annealed Cu(poly) CV as obtained initially (black), after having been oxidized at $+0.65\ V$ for $60\ seconds$ in $10\ M$ NaOH (orange), and after having been reannealed and characterized again (red). The oxidative treatment introduces a clear change in the facet distribution at the interface (compare black to orange). However, after reannealing, the surface is fully recovered to its initial state (compare red and black) seeing as these CVs are virtually indistinguishable from one another (with the difference in the negative going scan being due to a slight mismatch in the anodic potential).

4.4. Conclusions

In this work, we cleaned and prepared copper single crystalline surfaces via a combination of electropolishing, induction annealing and very detailed electrochemical surface characterization methods. These methodologies were found to yield reproducible CVs, where the number of crystal defects did not increase with time. Furthermore, the CVs obtained in this manner compared favorably with literature reported CVs, although the quality was generally not on par with UHV-prepared surfaces. However, they were found to be of higher quality than what is reported for electropolished surfaces.

Induction annealing was also applied to polycrystalline surfaces, and a decreased site bias was observed compared to electropolished samples. Furthermore, induction annealing was found to be capable of recovering even significantly altered surfaces such as after anisotropic oxidation/reduction cycles.

References

[1] Yoshio Hori, Katsuhei Kikuchi, and Shin Suzuki. Production of CO and CH4 in electrochemical reduction of CO2 at metal electrodes in aqueous hydrogencarbonate solution. *Chemistry Letters*, (11):1695–1698, 1985.

[2] Kendra P. Kuhl, Etosha R. Cave, David N. Abram, and Thomas F. Jaramillo. New insights into the electrochemical reduction of carbon dioxide on metallic copper surfaces. *Energy & Environmental Science*, 5(5):7050–7059, 2012.

[3] Hori Yoshio, Kikuchi Katsuhei, Murata Akira, and Suzuki Shin. Production of methane and ethylene in electrochemical reduction of carbon dioxide at copper electrode in aqueous hydrogencarbonate solution. *Chemistry Letters*, 15(6):897–898, 1986.

[4] Y. Hori, I. Takahashi, O. Koga, and N. Hoshi. Electrochemical reduction of carbon dioxide at various series of copper single crystal electrodes. *Journal of Molecular Catalysis A: Chemical*, 199(1):39–47, 2003.

[5] Ichiro Takahashi, Osamu Koga, Nagahiro Hoshi, and Yoshio Hori. Electrochemical reduction of CO2 at copper single crystal Cu(S)-[n(111)×(111)] and Cu(S)-[n(110)×(100)] electrodes. *Journal of Electroanalytical Chemistry*, 533(1–2):135–143, 2002.

[6] Federico Calle-Vallejo and Marc T. M. Koper. Theoretical considerations on the electroreduction of CO to C2 species on Cu(100) electrodes. *Angewandte Chemie International Edition*, 52(28):7282–7285, 2013.

[7] F. Sloan Roberts, Kendra P. Kuhl, and Anders Nilsson. High selectivity for ethylene from carbon dioxide reduction over copper nanocube electrocatalysts. *Angewandte Chemie*, 127(17):5268–5271, 2015.

[8] V. D. Jović and B. M. Jović. EIS and differential capacitance measurements onto single crystal faces in different solutions: Part II: Cu(111) and Cu(100) in 0.1 M NaOH. *Journal of Electroanalytical Chemistry*, 541:13–21, 2003.

[9] Vladimir Jović and Borka Jović. Surface reconstruction during the adsorption/desorption of oh species onto Cu(111) and Cu(100) in 0.1 M NaOH solution. *Journal of the Serbian Chemical Society*, 67(7):531–546, 2002.

[10] Klaas Jan P. Schouten, Elena Pérez Gallent, and Marc T.M. Koper. The electrochemical characterization of copper single-crystal electrodes in alkaline media. *Journal of Electroanalytical Chemistry*, 699:6–9, 2013.

[11] Albert K. Engstfeld, Thomas Maagaard, Sebastian Horch, Ib Chorkendorff, and Ifan E. L. Stephens. Polycrystalline and single-crystal Cu electrodes: Influence

of experimental conditions on the electrochemical properties in alkaline media. *Chemistry – A European Journal*, 24(67):17743–17755, 2018.

[12] Alexander Bagger, Rosa M. Arán-Ais, Joakim Halldin Stenlid, Egon Campos dos Santos, Logi Arnarson, Kim Degn Jensen, María Escudero-Escribano, Beatriz Roldan Cuenya, and Jan Rossmeisl. Ab initio cyclic voltammetry on Cu(111), Cu(100) and Cu(110) in acidic, neutral and alkaline solutions. *ChemPhysChem*, 20(22):3096–3105, 2019.

[13] Thomas Maagaard, Aarti Tiwari, Ib Chorkendorff, and Sebastian Horch. On the possibilities and considerations of interfacing ultra-high vacuum equipment with an electrochemical setup. *ChemPhysChem*, 20(22):3024–3029, 2019.

[14] Paula Sebastián-Pascual, Stefano Mezzavilla, Ifan E. L. Stephens, and María Escudero-Escribano. Structure-sensitivity and electrolyte effects in CO2 electroreduction: From model studies to applications. *ChemCatChem*, 11(16):3626–3645, 2019.

[15] Paula Sebastián-Pascual, Francisco J. Sarabia, Víctor Climent, Juan M. Feliu, and María Escudero-Escribano. Elucidating the structure of the Cu-alkaline electrochemical interface with the laser-induced temperature jump method. *The Journal of Physical Chemistry C*, 2020.

[16] Aarti Tiwari, Hendrik H. Heenen, Anton Simon Bjørnlund, Degenhart Hochfilzer, Karen Chan, and Sebastian Horch. Electrochemical oxidation of CO on Cu single crystals under alkaline conditions. *ACS Energy Letters*, 5(11):3437–3442, 2020.

[17] Aarti Tiwari, Hendrik H. Heenen, Anton Simon Bjørnlund, Thomas Maagaard, EunAe Cho, Ib Chorkendorff, Henrik H. Kristoffersen, Karen Chan, and Sebastian Horch. Fingerprint voltammograms of copper single crystals under alkaline conditions: A fundamental mechanistic analysis. *Journal of Physical Chemistry Letters*, 11(4):1450–1455, 2020.

[18] Aarti Tiwari, Thomas Maagaard, Ib Chorkendorff, and Sebastian Horch. Effect of dissolved glassware on the structure-sensitive part of the Cu(111) voltammogram in KOH. *ACS Energy Letters*, 4(7):1645–1649, 2019.

[19] J. Clavilier, R. Faure, G. Guinet, and R. Durand. Preparation of monocrystalline Pt microelectrodes and electrochemical study of the plane surfaces cut in the direction of the {111} and {110} planes. *Journal of Electroanalytical Chemistry and Interfacial Electrochemistry*, 107(1):205–209, 1980.

[20] G. Yang, B. Wang, K. Tawfiq, H. Wei, S. Zhou, and G. Chen. Electropolishing of surfaces: theory and applications. *Surface Engineering*, 33(2):149–166, 2017.

[21] Alexander Bagger, Logi Arnarson, Martin H. Hansen, Eckhard Spohr, and Jan Rossmeisl. Electrochemical CO reduction: A property of the electrochemical interface. *Journal of the American Chemical Society*, 141(4):1506–1514, 2019.

[22] Yun Huang, Albertus D. Handoko, Pussana Hirunsit, and Boon Siang Yeo. Electrochemical reduction of CO2 using copper single-crystal surfaces: Effects of CO* coverage on the selective formation of ethylene. *ACS Catalysis*, 7(3):1749–1756, 2017.

[23] V. Maurice, H. H. Strehblow, and P. Marcus. In situ STM study of the initial stages of oxidation of Cu(111) in aqueous solution. *Surface Science*, 458(1):185–194, 2000.

[24] B. J. Cruickshank, Douglas D. Sneddon, and Andrew A. Gewirth. In situ observations of oxygen adsorption on a Cu(100) substrate using atomic force microscopy. *Surface Science*, 281(1):L308–L314, 1993.

[25] Julia Kunze, Vincent Maurice, Lorena H. Klein, Hans-Henning Strehblow, and Philippe Marcus. In situ STM study of the anodic oxidation of Cu(001) in 0.1 M NaOH. *Journal of Electroanalytical Chemistry*, 554-555:113–125, 2003.

[26] William M. Haynes, David R. Lide, and Thomas J. Bruno. *CRC handbook of chemistry and physics: a ready-reference book of chemical and physical data*. 97 edition, 2017.

[27] S. M. Abd el Haleem and Badr G. Ateya. Cyclic voltammetry of copper in sodium hydroxide solutions. *Journal of Electroanalytical Chemistry and Interfacial Electrochemistry*, 117(2):309–319, 1981.

[28] Marcel Pourbaix. Atlas of electrochemical equilibria in aqueous solution. *NACE*, 307, 1974.

[29] Inna L. Soroka, Andrey Shchukarev, Mats Jonsson, Nadezda V. Tarakina, and Pavel A. Korzhavyi. Cuprous hydroxide in a solid form: does it exist? *Dalton Transactions*, 42(26):9585–9594, 2013.

[30] O. Koga, T. Matsuo, N. Hoshi, and Y. Hori. Charge displacement adsorption of carbon monoxide on [110] zone copper single crystal electrodes in relation with PZC. *Electrochimica Acta*, 44(6):903–907, 1998.

[31] David Reyter, Marek Odziemkowski, Daniel Bélanger, and Lionel Roué. Electrochemically activated copper electrodes: surface characterization, electrochemical behavior, and properties for the electroreduction of nitrate. *Journal of the Electrochemical Society*, 154(8):K36, 2007.

5

Morphological stability of copper surfaces under reducing conditions

Though copper is a capable electrocatalyst for the CO_2 reduction reaction (CO2RR), it rapidly deactivates to produce mostly H_2. This has been hypothesized to occur because of potential-induced morphological restucturing leading to facet redistribution at the surface which in turn results in a shift of catalytic activity to favour H_2 formation over CO2RR. Here, we investigate the veracity of this hypothesis by studying the changes in the voltammetry of Cu(111), Cu(100), Cu(110) and polycrystalline copper after being subjected to strongly cathodic conditions. The basal planes were chosen as model catalysts, whilst polycrystalline copper served to study the overall behavior of defect-rich facets (i.e., undercoordinated sites). We found that all surfaces exhibited (perhaps surprisingly) high stability when subjected to strongly cathodic potentials in concentrated alkaline electrolyte ($10\ M$ NaOH). Proof for morphological stability under CO2RR-representative conditions ($60\ min$ at $-0.75\ V$ in $0.5\ M$ $KHCO_3$) was obtained from identical location scanning electron microscopy, where the mesoscopic morphology for a nanoparticle-covered copper surface was found unchanged to within the instrument accuracy. Observed changes in voltammetry under such conditions, we found, were unreliable due to electrode fouling. We show that reported restructuring is likely due to oxidation, with (brief) oxidation periods ($+0.50\ V, 1\ min$) leading to changes in the facet distribution upon subsequent cathodic treatment. Therfore we posit that it is accidental oxidation/reduction cycles that are responsible for many groups observing morphological instability of copper.

This chapter has been adapted with permission from
Raaijman, S. J.$^{=}$; Arulmozhi, N.$^{=}$; Koper, M. T. M., *ACS Appl. Mater. Interfaces* **2021**, *13* (41) 48730–48744
Copyright 2021 American Chemical Society.

5.1. Introduction

From an electrochemical perspective, the CO_2 reduction reaction (CO2RR) is a potentially lucrative pathway for the valorization of a harmful waste product: CO_2. Although catalyst selectivity and activity for this reaction are currently unfit for industrial application, many different types of functionalized carbon-containing products can be obtained via direct CO_2 reduction on e.g., copper electrodes, where > 2 electron-products are of particular interest. However, besides having sub-optimal selectivity and activity[1–5], copper is also prone to deactivation during CO2RR.[6, 7] There are various theories as to the source for this deactivation, ranging from electrode fouling by reaction products (e.g., graphitic carbon[8]) and solution impurities[6, 7], to oxidation and reduction driven surface restructuring due to strain resulting from mismatching lattice parameters[9], to evolution of surface morphology due to dissolution of surface oxides[10, 11], to cathodic corrosion (CC) [12, 13] and potential-induced surface restructuring[12, 14–17], to dissolved copper species playing an active role in the catalytic process.[18]

Of these theories, changing surface morphology under purely cathodic CO2RR conditions[12, 14, 16, 17, 19–21] has been gaining popularity. In this case, changes in the distribution of surface sites would be responsible for variability of the product spectrum. Experimental reports of platinum[13, 22, 23], rhodium[24, 25], and gold[25, 26] surfaces undergoing massive restructuring at sufficiently cathodic potentials through a process called cathodic corrosion provide credibility to this theory. Such restructuring during CC has been hypothesized to result from cathodic dissolution mediated by the formation of (ternary) metal hydrides.[24] Given that CO2RR and carbon monoxide reduction (CORR) usually take place under conditions at which cathodic corrosion may occur (i.e., strongly negative potential, high local alkalinity), CC could be a relevant deactivation mechanism for copper electrodes.

In this work, we investigate the (in-)stability of various different copper facets under strongly cathodically corrosive conditions by investigating the evolution in cyclic voltammetry after cathodization in concentrated alkali electrolyte to determine if CC can explain the reported morphology changes of copper under cathodic (CO2RR) conditions. We compare those results to scanning electron microscopy (SEM) experiments conducted on a nanostructured surface prior to- and after running CO2RR to provide relevance to the CO2RR community. Importantly, all experiments were carried out such that accidental surface oxidation was minimized. Both cyclic voltammetry and SEM evidences reported herein indicate that copper is actually stable under purely reducing conditions, and we show that morphological changes as reported in literature are likely related to accidental oxidation/reduction cycles, as opposed to being the result of cathodic corrosion during CO2RR conditions.

5.2. Experimental

5.2.1. Chemicals and electrochemistry

Single-compartment electrochemical cells were made out of fluorinated ethylene propylene bottles (FEP) with appropriately sized machined inlets and outlets for the working electrode (WE), counter electrode (CE) (Pt, $99.99+\%$), reference electrode (RE, Gaskatel Hydroflex) and ETFE gas tubes. All electrochemical experiments were conducted in such cells. All potentials in this work are reported versus the reversible hydrogen electrode (RHE) unless otherwise specified. Because of reference accuracy limits in the hydroxide environment in combination with high flowrates of argon, the CVs were found to be accurate to within $\pm 3\ mV$, which was manually corrected for post-measurement. A standalone annealing compartment made from borosilicate glass and quartz, described elsewhere[27] was mounted on top of the electrochemical cell to enable the annealing of copper crystals in oxygen-free conditions. Argon (Linde, 5.0) was passed through the electrolyte to remove any gases and switched to blanket the solution during electrochemical measurements, unless otherwise specified. In the instances where experiments are conducted in a differing electrolyte (e.g., $10\ M$ NaOH, bicarbonate solution) than the blank electrolyte ($0.1\ M$ NaOH), the working cell was switched by unmounting the standalone annealing compartment (with the electrode located inside of it, protected against oxidation by isolating the compartment by closing a key and purging with hydrogen), removing the previous cell and mounting a new cell. After switching the working cell, the electrolyte of the newly-connected cell was purged for ca. $5\ minutes$ to remove any oxygen that was introduced by having to open the cell prior to mounting the annealing compartment on top.

Electrolyte solutions were prepared by dissolving appropriate amounts of chemicals used as received in Milli-Q water (Millipore; resistivity $\geq 18.2\ M\Omega \cdot cm$). Blank voltammograms were conducted in $0.1\ M$ NaOH (99.99%, trace metals basis, Sigma Aldrich), cathodic corrosion experiments were conducted in $10\ M$ NaOH (30.4%, Suprapur, Supelco), CO2RR experiments were conducted in $0.5\ M$ $KHCO_3$ (99.95%, trace metals basis, Sigma Aldrich) purged with CO_2 (Linde, 4.7) for at least half an hour. Glassware, plasticware and other relevant parts were oxidatively cleaned in acidic ($0.5\ M$ H_2SO_4, 96%, ACS reagent, Honeywell) permanganate ($1\ gL^{-1}$ $KMnO_4$, 99%, ACS reagent, Sigma Aldrich) overnight. Before starting experiments, the permanganate solution was poured out and leftover traces of the solution removed via rinsing with Milli-Q water and washing in a dilute sulfuric acid/peroxide (H_2O_2, 35%, Ph. Nord, Merck) mix. After washing, residues of the acid washing process were removed by boiling in Milli-Q water for five times.

Platinum CEs were stored in concentrated piranha solution ($3 : 1\ v/v$ $H_2SO_4 : H_2O_2$) after disassembly of the electrochemical cell to prevent copper contamination/alloying. Prior to use, Pt electrodes were rinsed with Milli-Q water and flame annealed with a butane torch. Copper electrodes were cleaned via induction annealing under reducing atmosphere, with the full details described elsewhere.[27] Disk-type electrodes were measured in hanging meniscus configuration, whereas spherical bead-type electrodes were inserted into the electrolyte in their entirety up until where the bead connected to the wire. Cut disk-type electrode CVs were normalized to the geometric surface area, and spherical bead-type Cu(poly) electrodes were normalized to their OH-adsorption charge (determined between $-0.25\ V < E < +0.44\ V$) using $128.1\ \mu C \cdot cm^{-2}$.[27] Exact crystal pre-treatment and measurement methodologies, including information on CV peak assignments, are described in a separate work.[27]

5.2.2. Spherical single crystal growth

Spherical single crystals used as is, or as the substrate for the anisotropically roughened electrodes used during identical location SEM investigations, were prepared via the methodology described by Arulmozhi and Jerkiewizc[28], albeit with an alternate nozzle-type that allowed for a central hydrogen-oxygen flame surrounded by an inert argon column. A brief summary of the growth process is as follows.

a. A copper bead was grown from high purity Cu wire (99.9999%, metals basis, Puratronic) via induction annealing in an oxygen-free environment

b. Impurities that migrated from the bulk to the surface were removed by dissolution in concentrated HNO_3 (65%, Ph. Eur., Boom), after which the bead was thoroughly rinsed with Milli-Q water.

c. The bead was briefly remolten (but not grown larger) and allowed to solidify again as per step a), and additional impurities that migrated to the surface were removed as per step b). Re-melting and subsequent surface dissolution/cleaning steps were repeated ca. $5\ times$.

d. The high purity bead electrode was then mounted a few millimeter above the nozzle in a duplicate of the crystal-growing setup as described in [28]. The nozzle, however, was replaced by a different type that allowed for a central flame surrounded by an outer flame, but instead of supplying fuel for an outer flame, argon was fed – resulting in a central flame surrounded by a 'protective' argon blanket.

e. A flame comprised of hydrogen and oxygen in a ratio that was just barely hot enough for melting copper (for our setup, $500 : 57\ sccm$ H_2 : Ar) was used in conjunction with an argon blanket ($800\ sccm$) and positioned such that ca. 75% of the copper bead was molten.

f. After a brief stabilization period (ca. $5 - 15\ minutes$) the nozzle was then gradually decreased in height via a computer-controlled micro-actuator located at the base of the micro-torch, allowing for the copper melt to slowly solidify.

g. After the entirety of the (now single crystalline) bead had solidified, the flowrate of the Ar blanket was increased to $1500\ sccm$ in one step and the oxygen content of the flame lowered in ca. 20% increments until reaching zero over a period of ca. $30\ seconds$.

h. Subsequently, the hydrogen flowrate was gradually reduced in ca. 1% increments, whilst the argon flowrate was increased in 1% increments until the hydrogen flame extinguished from a lack of oxygen (coming from the ambient air, diffusing through the argon blanket). Decreasing the hydrogen flowrate to ca. $100\ sccm$ resulted in the flame being unable to persist for our system.

i. Then, the crystal was allowed to cool to room temperature in the reducing atmosphere of ca. $2000 : 100$ Ar : H_2 for ca. $10 - 15\ min$.

5.2.3. Anisotropic roughening

Creation of anisotropic roughness with μm-scale morphology was obtained in a controlled manner by using a strategy reported by Sloan *et al.*[29] Briefly, we cycled the electrode in CO_2-purged bicarbonate ($0.1\ M$) electrolyte with $4\ mM$ KCl from $-0.75\ V$ to $+0.70\ V$, and back down to $-1.5\ V$ at a scan rate $\nu = 5\ mV \cdot s^{-1}$. Then, $-1.5\ V$ was applied for another ca. $5\ minutes$. The exact potentials and number of cycles (i.e., 1) were adjusted from the original work so as to prevent losing anisotropic effects due to over-oxidation, with a period at highly reducing potentials included to guarantee full reduction of the surface.

5.2.4. Interfacing between electrochemistry and SEM

In case of post-electrochemical treatment investigation of the surface via SEM, the following methodology was employed to limit surface oxidation of the crystals. It is very important to make sure the surface is completely dry prior to exposure to air where it cannot be avoided, so as to decrease the rate at which the surface oxidizes.

a. Finish the electrochemical experiment

b. Break electrical contact and increase hydrogen flow to several $L \cdot min^{-1}$ (adjusted manually, exact flowrate unknown).

c. Move electrode up, to where the annealing compartment of the setup is connected to the electrochemical cell (see [27])

d. Move the entirety of the annealing compartment containing the electrode up, breaking the link with the electrochemical cell. This action creates an opening where the annealing compartment is now exposed to ambient conditions but as this location is the path of least resistance for the hydrogen to flow, the crystal is still under reducing conditions provided the hydrogen flow is sufficiently high.

e. Move the crystal slightly down, so that it is sticking out of the annealing compartment a few millimeters.

f. Thoroughly rinse the crystal with Milli-Q water (ca. $30\ seconds$), being careful to only wet the crystal surface and not to allow water to flow up to (and down from) where the connecting wire of the crystal is attached to the electrode holder.

g. Move the crystal up through the keyhole to inside of the annealing compartment and close the key, creating a water-locked isolated environment.

h. Decrease hydrogen flow to several hundred sccm (exact flowrates unknown), making sure that the gas is exiting through the water lock.

i. Dry the electrode in the annealing compartment under active hydrogen flow for ca. $15 - 30\ minutes$.

j. Stop hydrogen flow and take the electrode out of the setup. Fixate the electrode in a SEM holder, and place the holder in a desiccator or other type of vessel that can be depressurized. Attach the desiccator with crystal inside to a pump and depressurize to ca. $1 - 5\ mbar$, and close off the desiccator. Total exposure of the (dry) crystal to ($1\ atm$ of) air during this period is ca. $45 - 60\ seconds$.

k. Move the desiccator to where the SEM is located and place the crystal in the SEM chamber, close it off and start pumping down. During this period, the (dry) crystal is exposed to ($1\ atm$ of) air for another ca. $30 - 45\ seconds$.

5.2.5. Instruments and software

All electrochemical experiments were conducted with a VSP-300 potentiostat from BioLogic, controlled with their proprietary software EC-Lab. Where applicable, gas flowrates were controlled via mass flow controllers from Brooks (SLA5850) via their proprietary software. Data editing and plotting was done using the software Igor. The SEM was operated under high vacuum ($\leq 8 \cdot 10^{-6}\ mbar$), with micrographs collected with beam settings of $15\ kV$ and $0.40\ nA$ utilizing an Everhart-Thornley detector. SEM images have been subjected to post-acquisition editing in photoshop, possibly having been i) rotated, ii) cropped and/or iii) having had their contrast and brightness adjusted.

5.3. Results and discussion

5.3.1. Cathodic surface stability from CV studies

To study if copper undergoes cathodic restructuring, experiments were conducted under literature-reported conditions that maximize the chance of cathodically-induced morphological changes occurring: high alkalinity, high cation concentration, and strongly negative potentials.[13, 22–25] Stability studies were conducted in $10\ M$ NaOH at the maximum cathodic potential that could be applied by our potentiostat with 85% iR correction turned on, being $-1.75\ V$ vs. RHE. Furthermore, our experimental setup was carefully constructed such that it allowed us to fully prevent surface oxidation unless deliberately induced via electrochemical means. Experiments were performed in the absence and presence of surface oxides to determine the effect of oxidation on the apparent cathodic stability of copper. Where applicable, pre-oxidation was done at $+0.50\ V$ considering that this potential is only a few millivolts positive of the open circuit potential (OCV) for copper in our electrochemical environment. Corrosion times (cathodic and anodic) were set at $1\ minute$, so as to minimize any possible influences of contaminants and to prevent electrolyte heating from influencing the results. Experiments for longer time periods, at different cathodic potentials, and under different electrolyte conditions are described in the second half of this work.

Characterization CVs ($0.1\ M$ NaOH) obtained after cathodization in both the absence (Figure 5.1) and presence (Figure 5.2) of surface oxides are compared to their initial characterization CVs (blank CVs), to study the cathodic stability of metallic copper and how the presence of a native oxide layer influences this stability. Reference inaccuracies resulted in upper potential limits varying ca. $3\ mV$, which actually influences the results slightly considering the upper potential we employ in this work is right at the onset of bulk copper oxidation. Therefore, depending on the exact situation, we may forego discussing changes in the negative going scan, especially if those differences are located close to the upper potential limit of the CV. Considering that all surfaces exhibit comparable behavior under purely cathodic conditions, we shall discuss the results of cathodic-only experiments ($1\ min$ at $-1.75\ V$ in $10\ M$ NaOH) first, depicted in Figure 5.1, where the initial blank CV for the various surfaces is shown in black and the CV obtained after cathodization in red.

The CV of a Cu(111) surface after one minute of cathodization is depicted in Figure 5.1a. Various insets depicting magnifications of the double layer regions and main OH-adsorption feature are included for clarity. We find that the CVs before (black) and after (red) cathodization are strikingly similar if we ignore a minor cathodic offset of the CV between $-0.15\ V < E < +0.30\ V$ as that can be attributed to trace amounts of oxygen in the electrolyte (not actually influencing the CV shape, only resulting in a cathodic offset). Actually, only one difference is observed, namely that the twinned cathodic OH-adsorption feature for the {111}-terraces at $+0.1\ V$ shows a minute increase in charge for the more positively located peak (denoted by an arrow in the inset), though this effect is virtually absent in the anodic feature. In our previous work[27] we hypothesize that the split nature of the {111}-specific OH-adsorption feature is a function of terrace length, with a broader adsorption feature located at more negative potentials being related to relatively smaller terraces and a sharp feature located at slightly more positive potentials being related to (very) large terraces. If the narrower {111}-specific feature indeed relates to larger terraces, as we propose, then the CV we obtain after applying cathodic potentials denotes an increase in the number of such larger terraces. This minor increase in surface crystallinity is very likely a result of the fact that we reanneal the surface prior to conducting cathodization experiments, having resulted in a marginally smoother surface. From the (absence of) observed differences, we conclude that the copper {111} face is stable against purely cathodic conditions.

The same experiment was also conducted on Cu(100) and is depicted in Figure 5.1b, where black denotes the blank and red the CV after cathodization. An inset depicting the 'pre-cycling' phase is included as we found that {100} terraces reconstruct during this period if the surface had been treated cathodically (but not after induction annealing, i.e., before the blank). During this phase (inset Figure 5.1b) we find that the {100}-specific OH-adsorption feature at $-0.125\ V$ is initially fairly asymmetrical but becomes increasingly symmetrical with successive cycling (e.g., going from the blue to the purple CV) although the initial level of symmetry is never regained, even if the number of cycles during this period is increased (not depicted).

These observations for pre-cycling carry over to the full-window post-cathodization characterization CV (red) where it can be seen that the cathodic peak at $-0.125\ V$ is

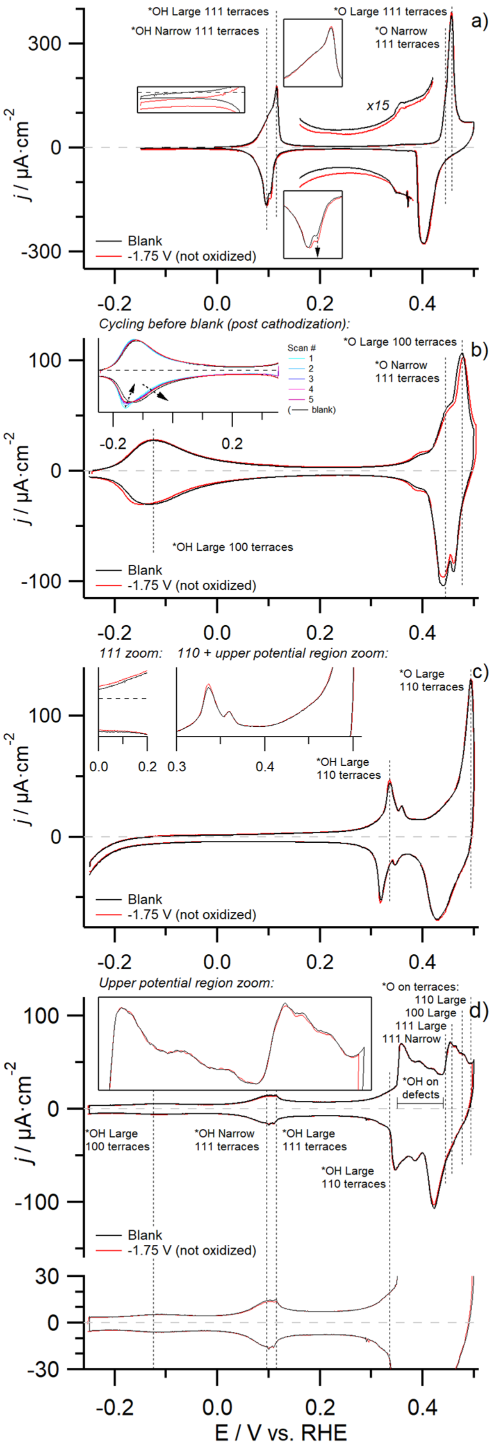

Figure 5.1: The effect of applying a cathodization period on the characterization CV (0.1 M NaOH, $\nu = 50\ mV \cdot s^{-1}$) of copper surfaces of various orientations devoid of initial surface oxides. Panels a-d) represent the voltammograms obtained prior to- (black) and after (red) a cathodization period (1 min at $-1.75\ V$, 85% iR corrected) in 10 M NaOH for an a) Cu(111), b) Cu(100), c) Cu(110) and d) Cu(poly) surface.

shifted to slightly more negative potentials thus resulting in decreased reversibility of the overall feature. Additionally, it can be seen that the reversible defect-related peak located at $+0.38\ V$ exhibits increased charge, signifying an increase in defect sites. As a third difference we find that the {100}-specific O-adsorption feature at $+0.477\ V$ shifts to slightly more positive potentials whilst slightly decreasing in maximum intensity, resulting in decreased current in the region $+0.42\ V < E < +0.48\ V$ and increased current for $E > +0.48\ V$. We believe that the positive shifting of this feature signifies a decrease in average {100} terrace width, which matches with the observed increase in defect density. These minor CV changes for Cu(100) could possibly be the result of (partially) irreversible potential-induced surface reconstruction at negative potentials. Such cathodic reconstruction of the {100} face has been reported by Matsushima *et al.*[15] who show via in-situ scanning tunneling microscopy that, under sufficiently negative potentials in $0.1\ M$ $HClO_4$, a fraction of the atoms at the Cu(100) surface form rows that are slightly elevated with respect to the rest of the surface. If this so-called hydrogen-induced reconstruction[15] is not fully reversible, it can reasonably explain the minor differences observed in our cyclic voltammetry, considering that the CV changes we discuss represent an overall decrease in surface crystallinity. Although we find that the {100} face is not perfectly stable under cathodic-only conditions, the changes are still relatively minor.

CVs of a Cu(110) surface before (black) and after (red) cathodic polarization are shown in Figure 5.1c. Post-cathodization voltammetric behavior similar to that of a Cu(111) surface is observed, i.e., mostly an absence of change. One minute difference can be observed by looking at the amount of anodic and cathodic charge associated with the {110}-feature located at ca. $+0.33\ V$, which is found to increase slightly – signifying a small increase in surface crystallinity. This minor increase in crystallinity is not so strange, considering that the methodology we employ for generating a stable {110} surface involves evolving large amounts of hydrogen at very negative potentials, similar to the cathodic treatment we use for the results depicted in this figure. No other deviations are observed, and thus we arrive at the same conclusion as for the other two faces: the {110} facet is stable under cathodically corrosive conditions.

Finally, we depict CVs of Cu(poly) in Figure 5.1d. By their nature, polycrystalline surfaces contain a higher fraction of undercoordinated sites such as step and kink defects. This is evident from the presence (and intensity) of a number of additional features between $+0.35\ V < E < +0.44\ V$. Due to the different sizes of crystallites present on the surface, it will also contain a wider gamut of terrace sizes. Hence, experiments on a Cu(poly) electrode can provide additional insights into the cathodic stability of more reactive, and therefore generally assumed more catalytically active, sites. Investigation of the CV after the experiment (red) shows very little change compared to the initially obtained blank CV (black). Scrutinizing closely, small deviations can be seen around $+0.1\ V$, and between $0.44\ V < E < 0.48\ V$, which relate to changes in {111} terrace sites and {100} terrace sites, respectively. The small decrease in OH-adsorption on {111} terraces ($+0.1\ V$) can actually be attributed to the fact that we sweep the potential to $E < -0.15\ V$, which has been reported in literature to result in suppression of the associated anodic feature.[30] Taking into consideration that the negative potential limit was slightly more negative after cathodization due to reference inaccuracies, the minor difference at ca. $+0.1\ V$ is likely caused by the slight variation in lower CV boundaries. This leaves a diminutive difference in O-adsorption related to {100}-terrace sites ($+0.477\ V$), which is in line with what we discussed previously for Cu(100), namely that likely some irreversibility is associated with lifting the hydrogen-induced reconstruction of this face. Therefore, we conclude that also a defect-rich Cu(poly) surface is stable under strongly cathodic conditions, with mostly {100} terrace-sites being mildly impacted.

A second set of experiments was conducted based on the notion that it is challenging to guarantee oxygen-free, non-oxidizing conditions when utilizing default literature procedures, surface preparation methodologies and prevalent experimental setups. To this end, a pre-oxidation step ($1\ min$ at $+0.50\ V$, close to the OCV of Cu in our system) prior to cathodization was purposely included in a set of control experiments, to compare the cathodic stability of copper in the presence of a native oxide film with our results in the absence of surface oxides. Pre-oxidation investigations at more positive potentials were also investigated for Cu(110) and Cu(poly) surfaces, considering that they exhibited very mild changes at $+0.50\ V$. The results are depicted in Figure 5.2, where initially obtained blank CVs (black) for the various surfaces under investigation are compared to the characterization CV as obtained after pre-oxidation cathodization experiments in $10\ M$ NaOH (red) where the surface was first pre-oxidized ($1\ min$ at $+0.50\ V$), prior to stepping the potential to cathodic potentials ($1\ min$ at $-1.75\ V$).

The effect of adding a pre-oxidation step on the cathodic stability of a Cu(111) surface can be determined by comparing the CVs in Figure 5.1a (absence of oxidation) with those in Figure 5.2a (presence of oxidation). To determine this effect, we first have to analyze what CV changes occur for a surface that has been pre-oxidized before cathodization by comparing the initial CV (black) to the CV obtained after the experiment (red) in Figure 5.2a. A first difference can be seen at the negative potential limit of the CV ($E < 0\ V$), where excess cathodic charge is observed after pre-oxidation plus cathodization treatment. Considering that this current is not related to the ORR (its onset being at too negative a potential for that – e.g., compare it to the more positive onset for ORR-related current in the red trace in Figure 5.1a), we tentatively attribute it to the hydrogen evolution reaction (HER) instead. Second, we see that the oxidative {111}-terrace peak at $+0.1\ V$ shows reduced peak intensity which looks to be associated with increased charge at slightly more positive potentials (ca. $+0.105\ V$). Additionally, a new anodic feature is observed to develop at ca. $+0.235\ V$. Furthermore, we find that the reversible defect-related feature around $+0.35\ V$ grows in intensity. None of these effects were observed in the absence of a pre-oxidation treatment. Lastly, we observe increased charge of the more positive peak of the cathodic feature at $+0.1\ V$. This is in agreement with what we observe in the absence of surface oxidation, though in that instance the anodic charge did not decrease.

The increased HER activity of a pre-oxidized and subsequently cathodized Cu(111)

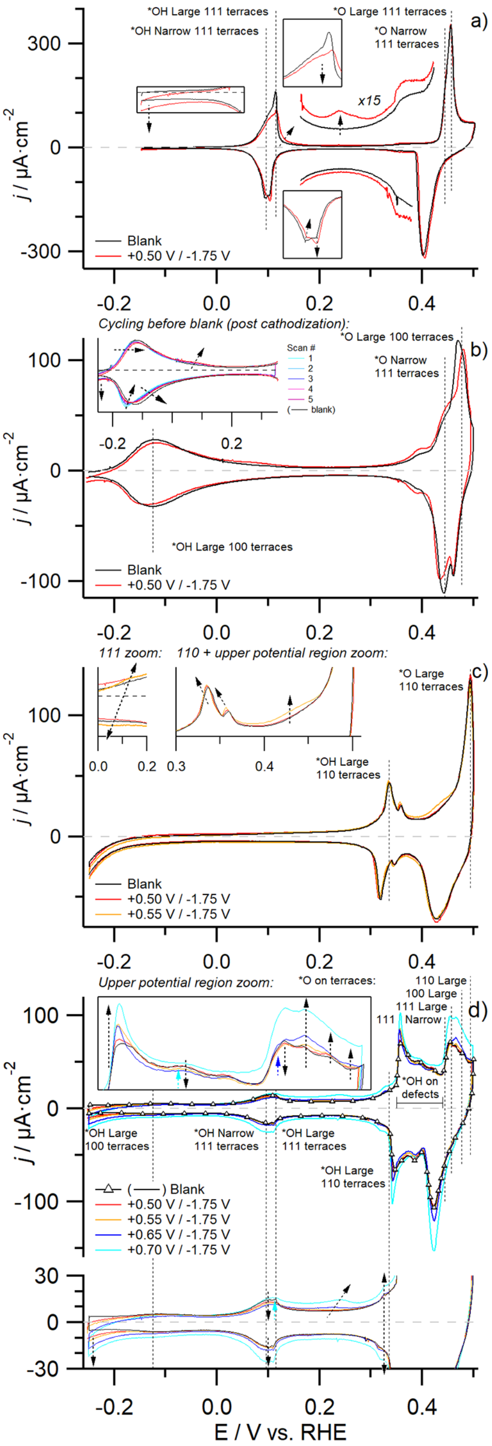

Figure 5.2: The effect of applying a pre-oxidation period followed by a cathodization period on the characterization CV ($0.1\ M$ NaOH, $\nu = 50\ mV \cdot s^{-1}$) of copper surfaces of various orientations devoid of initial surface oxides. Panels a-d) represent the voltammograms obtained prior to- (black) and after (red) a pre-oxidation period ($1\ min$ at $+0.50\ V, 85\%$ iR corrected) followed by a cathodization period ($1\ min$ at $-1.75V, 85\%$ iR corrected) in $10\ M$ NaOH for an a) Cu(111), b) Cu(100), c) Cu(110) and d) Cu(poly) surface. More positive oxidation potentials were also investigated for the Cu(110) ($+0.55\ V$ only) and Cu(poly) electrodes, which are depicted in orange, blue and cyan for $1\ min$ of oxidation at $+0.55\ V, +0.65\ V$ and $+0.70\ V$, respectively.

surface, combined with the appearance of a new, irreversible anodic feature at $+0.235\ V$ and an increase in charge of the feature at $+0.35\ V$ all indicate additional defect sites. This is corroborated by the fact that we observe the peak intensity of the $\{111\}$-specific OH-adsorption feature at $+0.1\ V$ going down, whilst simultaneously seeing an increase in charge in the region located at slightly more positive potentials. We hypothesize this represents a decrease in average terrace width, considering that a literature-reported Cu(211) CV (denoting a 3(111)x(100) surface) exhibits a similar broad charge contribution at potentials positive of $+0.1\ V$.[31] We realize that it is peculiar that the increase in oxidative charge at $E > +0.1\ V$ that we attribute to small-width $\{111\}$ terraces is not matched by a similar increase in cathodic charge in the negative-going scan, as is the fact that the suppression of charge of the anodic feature at $+0.1\ V$ is (mostly) absent for the cathodic feature. A possible explanation for this would revolve around the irreversible nature of O-adsorption on $\{111\}$ terrace sites as evidenced by the asymmetry of the feature at $+0.457\ V$. Possibly, shorter (i.e., defect rich) terraces are influenced more strongly by oxygen desorption resulting in reconstruction of these sites in the reverse scan direction. Overall, by comparing the respective CV changes of Cu(111) when it has been cathodized either in the absence or in the presence of a pre-oxidation step, it is clear that surface oxides negatively impact the stability of $\{111\}$ terrace sites under cathodic conditions – and thus, by association, are likely to result in changing their morphology.

Next, we study the effect of the presence of surface oxides on the cathodic stability of Cu(100). The characterization CVs of this face after cathodization in the absence and presence of a pre-oxidation period are shown in Figures 5.1b and 5.2b, respectively. Once again, an inset with the pre-cycling CVs is provided in Figure 5.2b with the initial blank CV and CV after pre-oxidation plus cathodization treatment depicted in black and red in the submain figure, respectively. In line with our initial discussion for this facet, already during the pre-cycling phase surface reconstruction is apparent. Specifically, for the pre-oxidized and subsequently cathodized electrode, we observe the following behavior during this initial phase (inset Figure 5.2b). Firstly, similar to a non-oxidized surface, we observe that the feature at $-0.125\ V$ starts off asymmetrically, but becomes more symmetrical with successive cycling (going from the blue to the purple line), with the cathodic peak shifting to more positive potentials. Again, the initial symmetry of the feature is not fully recovered. In contrast with cathodic-only treatment, a number of additional changes are observed during this pre-cycling period in the case of pre-oxidation. Aside from the cathodic peak at ca. $-0.125\ V$ shifting, the oxidative peak is actually observed to shift slightly as well. Furthermore, the total charge of the $\{100\}$ adsorption feature is observed to diminish. Additionally, an anodic shoulder grows in at ca. $+0.075\ V$; relatively close to where one would expect $\{111\}$ terraces to contribute charge (+0.1 V) although no associated cathodic peak is observed. Finally, HER activity at negative potentials ($E < -0.2\ V$) increases with successive cycling.

All of these effects carry over when we compare the full-window characterization CV (red) with the initial blank CV (black): excess cathodic charge is observed for

$E < 0.2\ V$, the {100} adsorption feature at $-0.125\ V$ is overall less symmetrical and exhibits suppressed charge, and an oxidative 'bump' near $+0.075\ V$ is visible. The suppression of the overall charge of the OH-adsorption feature was not observed in the case of a cathodic-only treated Cu(100) crystal (Figure 5.1b), nor was the formation of a feature near $+0.075\ V$. Additional observed changes for the full-window CV are that more crystal defects are present as indicated by increases in charge for both the step-related feature at ca. $+0.38\ V$ and the {111}-terraces related shoulder near $+0.445\ V$. Increases in the number of step sites was also observed without surface oxidation, but increases in {111} terrace sites were not. Finally, the {100} O-adsorption feature ($+0.477\ V$) is observed to both decrease in intensity and shift towards more positive potentials. This agrees with what we observed in the absence of surface oxidation, but is more pronounced after pre-oxidation.

From the combination of increased HER activity, the appearance of a new feature at $+0.075\ V$, an increase in the charge of the reversible defects-related feature near $+0.38\ V$ and the growth of the shoulder at ca. $+0.445\ V$ (likely related to the formation of small {111} terrace sites[27]) it is clear that additional defects are being formed in the surface. Similar to the previous discussion, this is corroborated by the loss of symmetry and decrease in intensity of the {100}-related feature near $-0.125\ V$, for which we know from a literature-reported Cu(911) CV (denoting a 5(100)x(111) surface)[32] that the OH-feature for shorter {100} terraces is located at more negative potentials. We also observe the {100}-specific O-adsorption feature at $+0.475\ V$ to shift to more positive potentials (making it overall less reversible) and decrease in intensity, both of which can be similarly interpreted as the behavior observed for the main OH-adsorption feature at $-0.125\ V$: a decrease in surface crystallinity. Considering that these changes are more numerous and more pronounced than for the cathodic-only experiment, it is clear that the presence of surface oxides results in decreased stability of {100} terrace sites and thus increases the likelihood of morphological evolution taking place.

Next, we investigate the effect of pre-oxidation on the cathodic stability of Cu(110), with Figures 5.1c and 5.2c showing the CVs obtained before (black) after (red) cathodization in the absence and presence of a pre-oxidation period at $+0.50\ V$, respectively. Due to the very small differences observed for a pre-oxidation potential of $+0.50\ V$ (red), an additional experiment was conducted at $+0.55\ V$ (orange). When carefully scrutinized, both samples exhibit the same CV changes, but we will discuss the latter since there the changes are more prominent. When comparing the orange trace to the initial blank (black), we observe the following. Firstly, we find increased HER activity at potentials $E < -0.1\ V$. Secondly, a reversible feature near $+0.1\ V$ develops, being a clear indication of the formation of {111}-terrace sites. Thirdly, the amount of charge of the {110}-specific OH-adsorption feature at $+0.33\ V$ is found to increase slightly, similar to the non-oxidized sample. However, we see an additional change for this feature, being a shift to slightly more negative potentials. Further differences are observed in the form of increased charge for the symmetrical, defect-related feature at ca. $+0.35\ V$, which is additionally observed to also shift to slightly more negative potentials. Finally, we observe increased charge in the potential range $0.375\ V < E < 0.46\ V$, where both defect sites and $\{111\}$ terraces exhibit adsorption behavior.

Compared to Cu(111) and Cu(100), Cu(110) exhibits less prominent changes when pre-oxidized, necessitating an increase in the oxidation potential from $+0.50\ V$ to $+0.55\ V$ to observe changes of similar magnitude as seen for pre-oxidized $\{111\}$ and $\{100\}$ surfaces. However, the overall conclusion after comparison of CV behavior in the absence and presence of surface oxides is in agreement with previously discussed faces: oxidation negatively impacts the cathodic stability of Cu(110).

Lastly, we also investigated the behavior of a Cu(poly) electrode, depicted in Figures 5.1d and 5.2d, for cathodization in the absence and presence of pre-oxidation, respectively. Considering such a surface is easily remade if irreversible surface damage is observed, a wider range of pre-oxidation potentials was investigated. Specifically, depicted in Figure 5.2d in red, orange, blue and cyan are, respectively: $+0.50\ V, +0.55\ V, +0.65\ V$ and $+0.70\ V$ (with $+0.60\ V$ falling in-between $+0.55\ V$ and $+0.65\ V$, not depicted). At the bottom of the figure a narrower current range is provided, giving a clearer view of the changes in the region between $-0.25\ V < E < +0.35\ V$. Considering that the voltammetric behavior we observe is (almost) identical up to a pre-oxidation potential of $+0.65\ V$ (blue), we shall discuss that particular datapoint.

Similar to the principal faces, we find that a pre-oxidized and subsequently cathodized polycrystalline copper surface exhibits increased HER activity at $E < -0.1\ V$. This increase is likely related to an increase in defect density, although it may also signify an increase in the number of $\{110\}$ terrace sites or a combination of the two. Due to increased HER current, it becomes difficult to ascertain if the $\{100\}$ OH-adsorption feature at $-0.125\ V$ is changing or not because of convolution effects. However, clear changes are observed for OH-adsorption on $\{111\}$ terraces, with the anodic peak at $+0.1\ V$ exhibiting decreased current density, although this is not reflected in a decrease of the associated cathodic peak (which stays equal for $+0.50\ V$ and $+0.55\ V$, and conversely increases in the case of $+0.65\ V$). Concomitantly with the decrease of the anodic peak at $+0.1\ V$, an increase in anodic (but not cathodic) charge is observed in the potential window that directly follows, between ca. $+0.1\ V < E < +0.3\ V$. Similar behavior was observed for Cu(111), where we hypothesized it represents a decrease in average terrace width, whilst the mismatch between anodic and cathodic charge trends is possibly related to the irreversibility of oxygen adsorption resulting in reconstruction of the (defect-rich) terraces.

Increased charge at $+0.33\ V$ is also observed, signifying that additional $\{110\}$ terraces are present. Then, between $+0.35\ V < E < +0.44\ V$ (where OH adsorbs on defects) we find increased charge centered around $+0.356\ V$, whilst the rest of the window remains equal ($+0.42\ V < E < +0.44\ V$) or decreases in charge ($+0.37\ V < E < +0.42\ V$). Taken together, this represents anisotropic surface restructuring with some types of defects increasing and other types of defect sites decreasing in abundance. In the upper potential region of the CV (*O region, $E \geq +0.44\ V$) we see the following. Between $+0.44\ V < E < +0.458\ V$ (O-adsorption on $\{111\}$ terraces) a small decrease in charge is observed for pre-oxidation at $+0.50\ V$

and $+0.55\ V$. However, from $+0.65\ V$ on, the charge starts increasing. The initial decrease can readily be explained by anisotropic effects, with the (originally fully reduced) $\{111\}$ terrace sites being lost as they interconvert into other types of sites when oxidized and subsequently reduced. However, as a reversal in behavior is observed with peak charge increasing for $E \geq +0.65\ V$, a secondary process operating in parallel with the first mechanism must exist via which new terrace sites form. Likely, this additional pathway has to do with the creation of pits in the surface through dissolution and/or the formation of deposits through electroplating of (in-operando generated) Cu ions. The last section of the CV ($E > +0.458\ V$) exhibits monotonous increase in charge as a function of pre-oxidation potential, representing increases in the amount of both $\{100\}$ and $\{110\}$ terrace sites.

Clearly, oxidation and subsequent reduction of copper is anisotropic; with some types of defect and terrace sites decreasing and other types of defect and terrace sites increasing, representing their interconversion. However, as the pre-oxidation potential is increased, the initial stages of surface roughening can be observed as evidenced by the reversal of the behavior of O-adsorption on $\{111\}$ terraces (decreasing to increasing as oxidation potential is increased). This roughening of the surface becomes more pronounced as the pre-oxidation potential is increased to $+0.70\ V$ (Figure 5.2d, cyan), with the entirety of the CV exhibiting increased current density. This represents an increase in the number of every type of site, which can only be valid if overall surface area is increasing (i.e., roughening of the surface). Such roughening (i.e., changing morphology) can be explained if we either start forming pits in the surface via dissolution[11] and/or start forming particles atop the surface (e.g., due to redeposition phenomena). Roughening of copper in the absence and presence of a pre-oxidation period is further investigated in the following section, where we use SEM to investigate various locations on a spherical single crystal.

5.3.2. Microscopy study of surface roughening in the absence and presence of copper oxides

So far, we employed CV studies to investigate the (absence of) change in surface morphology of various copper substrates under purely cathodic conditions. Supporting evidence for the voltammetric behavior observed in the presence and absence of a pre-oxidation period is provided in the form of SEM imaging. For this study, a spherical single crystal was used as a model catalyst considering that it allows for comparison of substrates of (initially) comparable crystallographic orientation. The exact procedure was as follows. Firstly, the single crystal was pre-oxidized in $10\ M$ NaOH at $+0.70\ V$ for $1\ minute$ prior to being cathodized at $-1.75\ V$ for $1\ minute$ (equal electrochemical treatment to the cyan trace in Figure 5.2d), whereafter it was moved to the SEM for investigating the morphology. Exact imaging locations were documented to allow for re-visiting them later on. Then, the crystal was (mostly) recovered to its initial state by flame annealing it in a H_2/O_2 flame for ca. $30\ min$ near the melting point of copper (CV reproducibility depicted in Figure D.1). Next, a cathodic-only experiment was conducted by applying $-1.75\ V$ for $5\ minutes$ in $10\ M$ NaOH, where the experiment duration was intentionally increased five-fold (from $1\ min$ to $5\ min$) as preliminary results indicated no discernible roughening after $1\ min$ of cathodization (not depicted). After rinsing and drying, the crystal was then moved to the SEM and manually positioned to match as best as possible its orientation during the previous experiment based on the visible (static) locations of the $\{100\}$ and $\{111\}$ planes. Then, previously investigated locations were revisited and imaged again. As the orientation of the crystal in the SEM chamber was manually adjusted between experiments, the incidence angle of the electron beam with respect to the surface normal is not exactly equal between corresponding sets of images nor is it necessarily always exactly perpendicular to the surface. Furthermore, slight mismatches of this angle between images are exacerbated by the fact that the surface has a curvature in all directions, considering that the study was conducted on a spherical single crystal. The micrographs obtained for both conditions are depicted in Figure 5.3 in the form of numbered pairs (e.g., $\underline{1}$ and 1), for which we estimate that the respective sets of images between the different experiments were located within $< 100\ \mu m$ of each other on the surface (yielding comparable initial substrates).

By imaging various spots along the vertices of a stereographic triangle, we were able to investigate a wide variety of substrates and obtain results that should be representative of the overall behavior of a polycrystalline surface. And because we employ a spherical single crystalline surface, we can compare locations on the crystal for different experiments that were initially of the same crystallographic orientation. Hence, we can relate changes in morphology to changes in experimental conditions in an unbiased manner as substrate-directing effects are mitigated (contrary to if similar experiments were to be conducted on polycrystalline surfaces). We compare the final morphology of a surface that was treated purely cathodically ($-1.75\ V, 5\ min$) with that of a surface that was firstly oxidized ($+0.7\ V, 1\ min$) and then treated cathodically ($-1.75\ V, 1\ min$) to determine the influence of surface oxidation on the morphological restructuring of copper.

In Figures 5.3a and 5.3c, we show the overall profile of the crystal after cathodization ($-1.75\ V$) in the presence of pre-oxidation at $+0.70\ V$ and in the absence of pre-oxidation, respectively. In these subfigures, the contrast and brightness of the $\{111\}$ plane were adjusted independently to enhance its visibility. The original single-crystalline nature of the crystal is clear from Figure 5.3a, considering that the anisotropic oxidation resulted in distinct regions on the surface that repeat as expected of the symmetry of the FCC unit cell (see e.g., here[33] for further information). In Figure 5.3c (in the absence of oxidation) no such distinct regions are observed, but the $\{100\}$ and $\{111\}$ basal planes (denoted by the □ and ○ symbols, respectively) could be located, which then allowed for determination of the location of the $\{110\}$ plane, completing the stereographic triangle. 'Proof' that the main facets as indicated by the symbols are indeed located where we claim is provided in the form of close-ups of those regions given in Figure 5.3g, where the top row was obtained in the presence of pre-oxidation and the bottom row in the absence of pre-oxidation. In Figure 5.3e, a rotated and magnified view of Figure 5.3a is presented, with numbering added to represent the approximate locations where micrographs were obtained.

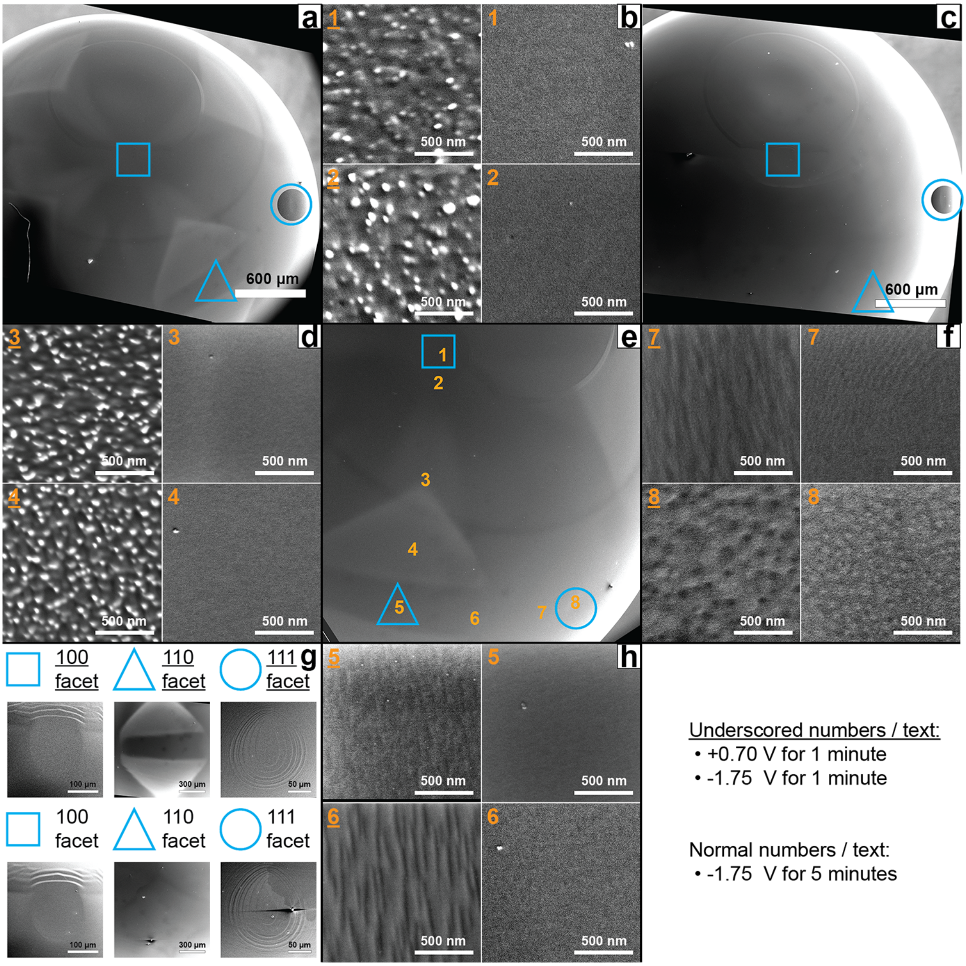

Figure 5.3: Comparison of close-proximity location SEM images for an identical spherical single crystal that was either subjected to a cathodic-only period ($-1.75\ V$ for $5\ min$) or firstly pre-oxidized ($+0.7\ V$ for $1\ min$) before applying a cathodic period ($-1.75\ V$ for $1\ min$) in $10\ M$ NaOH. Overview images for the pre-oxidized and cathodic-only treated crystal are given in panels a) and c), respectively. Close-ups of the basal planes (represented by the following symbols: □ for $\{100\}$, ▵ for $\{110\}$ and ○ for $\{111\}$) are provided in panel g), where only two out of three need to be visible for accurate determination of the location of a stereographic triangle. Approximate imaging locations along the vertices of the stereographic triangle as defined by the three respective basal planes are represented by the numbers in orange in panel e). High-magnification micrographs of the locations matching the numbering of panel e) are depicted in panels b), d), f) and h), with the number matching the location given in the top-left corner where side-by-side sets represent micrographs obtained in matching locations for either cathodic corrosion in the presence of a pre-oxidation step (left-hand side, with underscored numbering) or in the absence of pre-oxidation (right-hand side, with normal numbering).

Having established the crystallinity of the surface and determined the location of one of the stereographic triangles, we now investigate a number of locations along the vertices of the triangle to represent the cathodic stability of copper of various crystallographic orientations in Figures 5.3b, d, f and h. In each of these subfigures, the morphology of two different spots on the surface in the presence of pre-oxidation (left-hand side) are compared to representative locations without oxidation (right-hand side), with numbers in the top-left corner of the respective images matching the locations given in Figure 5.3e. Comparing the surface morphologies in Figures 5.3b, d and h, we find that surface roughening is below the detection limit of the SEM in the case of cathodic-only treatment ($-1.75\ V, 5\ min$), requiring random traces of dust for focusing. However, clear anisotropic roughening is present if a pre-oxidation step ($+0.70\ V, 1\ min$) is included prior to cathodization ($-1.75\ V, 1\ min$). An exception to this is seen in Figure 5.3f, wherein locations close to the $\{111\}$ face are depicted. In this case, some (albeit less) roughness is also observed in the case of cathodic-only treatment. This actually agrees with small changes in voltammetry (Figure D.1) observed after recovery of the surface via H_2/O_2 annealing, considering that the $\{111\}$ terrace-related OH-adsorption peak ($+0.1\ V$) exhibited slightly increased charge after flame annealing compared to the CV obtained prior to the pre-oxidation experiment. As such, we are unsure if the roughness we observe from SEM near the $\{111\}$ face is because of the cathodic treatment, or because the annealing treatment failed to fully recover the surface to its initial state.

The key take-away from this measurement is that a partially oxidized surface results in significant roughening during cathodization, whereas a fully reduced surface yields no observable roughening. Furthermore, the roughening under pre-oxidized conditions is anisotropic, in agreement with CV results (Figure 5.2d). Although we realize that the spatial resolution of the SEM is limited, the results we obtain are in line with what we observe also from voltammetry: high stability of copper with respect to purely cathodic conditions that is negatively impacted by the presence of surface oxides.

5.3.3. (Absence of) time-dependent morphological change

Up to now, the results reported here have been regarding the stability of copper under aggressively cathodic potentials ($-1.75\ V$ vs. RHE) in strongly alkaline media ($10\ M$ NaOH) for relatively brief periods of time ($1\ min$, except for the cathodic-only SEM data reported in Figure 5.3; $5\ min$). We realize that such conditions may not represent the reported morphological instability of copper during CO2RR operation, considering that electrolyte composition and experiment duration differ significantly, implying that possible effects by e.g., (adsorption of) carbonaceous species are not included. To this end, we performed voltammetric studies before and after the following experiments: i) equal conditions as discussed so far ($-1.75\ V$ in $10\ M$ NaOH) but for increased reaction times ($5, 15$ and $60\ min$, Figures 5.4a and 5.4b, respectively) and ii) employing CO2RR-representative conditions ($60\ min$ at $-0.75\ V$ in $0.5\ M$ $KHCO_3$, Figure 5.4c). The upper boundary of $60\ min$ was chosen based on literature-reported chronoamperometry data exhibiting a clear trend of decreasing CO2RR activity of various copper surfaces on this timescale by multiple authors.[7, 10, 21, 34, 35]

Blank CVs ($0.1\ M$ NaOH) obtained prior to and after extended cathodization periods in either $10\ M$ NaOH or $0.5\ M$ $KHCO_3$ are depicted in Figure 5.4, where close-ups of relevant regions are provided as insets and trends discussed in text denoted by arrows. Figure 5.4a depicts CVs obtained initially (i.e., the blank) and after 5 and $15\ minutes$ of cathodization ($-1.75\ V$) in $10\ M$ NaOH in black, yellow and blue, respectively. Unlike for $1\ min$ of reaction time (Figure 5.1d) under otherwise identical conditions, minor changes in voltammetry can be observed in this instance. Specifically; a small increase in HER activity (denoted by increased cathodic current for $E < -0.1\ V$), suppression of the anodic (but not cathodic) $\{111\}$ OH-adsorption feature at $+0.1\ V$, and suppressed current density (both anodic and cathodic) between $+0.35\ V < E < +0.50\ V$. Here, the suppressed charge for $E > +0.35\ V$ denotes, from a concerted electrochemical and copper-centric perspective, a decrease in the total number of electrochemically addressable copper sites, considering every type of site contributes charge somewhere in this region. Although certain situations involving surface restructuring might lead to an overall decrease in number of active sites (see supporting information), they are unlikely.

Reasonably, if surface morphology is indeed changing to the degree as reported in literature, one would expect to see certain types of sites increase in relative abundance with other types of sites decreasing in abundance, whilst simultaneously observing an increase in the total number of surface sites as changes in morphology bring about a shift in the site distribution and furthermore lead to (reportedly) overall smaller surface deposits. Exactly such behavior can be seen in e.g., Figure 5.2d where irreversible oxidation and reduction results in changes in relative site abundances and (for increasingly positive oxidation potentials) increases in overall surface area. However, this ‘common sense’ scenario is in disagreement with the voltammetry results in Figure 5.4a.

Increasing the reaction time to $60\ min$ ($-1.75\ V, 10\ M$ NaOH, Figure 5.4b) provides us with additional information: all CV changes observed for 5 and $15\ minutes$ become more prominent after $60\ minutes$, although suppression of the anodic feature at $+0.1\ V$ cannot be ascertained since this region is now masked by new features that develop. These additional features comprise, specifically, three new anodic peaks at ca. $-0.125\ V, +0.05\ V$ and $+0.2\ V$, and two new cathodic features near $+0.1\ V$ and $-0.1\ V$ (where the latter is actually a convolution of two peaks). The locations of these new features do not match with where the various types of possible copper sites are known to adsorb, considering that a Cu(poly) surface contains all kinds of possible sites and yet these newly developing features do not match in their location with any of the adsorption features observed for such a surface. Neither does their asymmetrical nature agree with the reversibility of OH adsorption on copper sites. Interestingly, when we use cyclic voltammetry to investigate what happens to a polycrystalline copper surface under CO2RR-representative conditions ($60\ min$ at $-0.75\ V$ in $0.5\ M$ $KHCO_3$ + CO_2 (g), Figure 5.4c), similar CV behavior is observed as after $60\ min$ at $-1.75\ V$ in $10\ M$ NaOH, though less pronounced. We also found the same behavior in less concentrated bicarbonate electrolyte ($-0.75\ V$

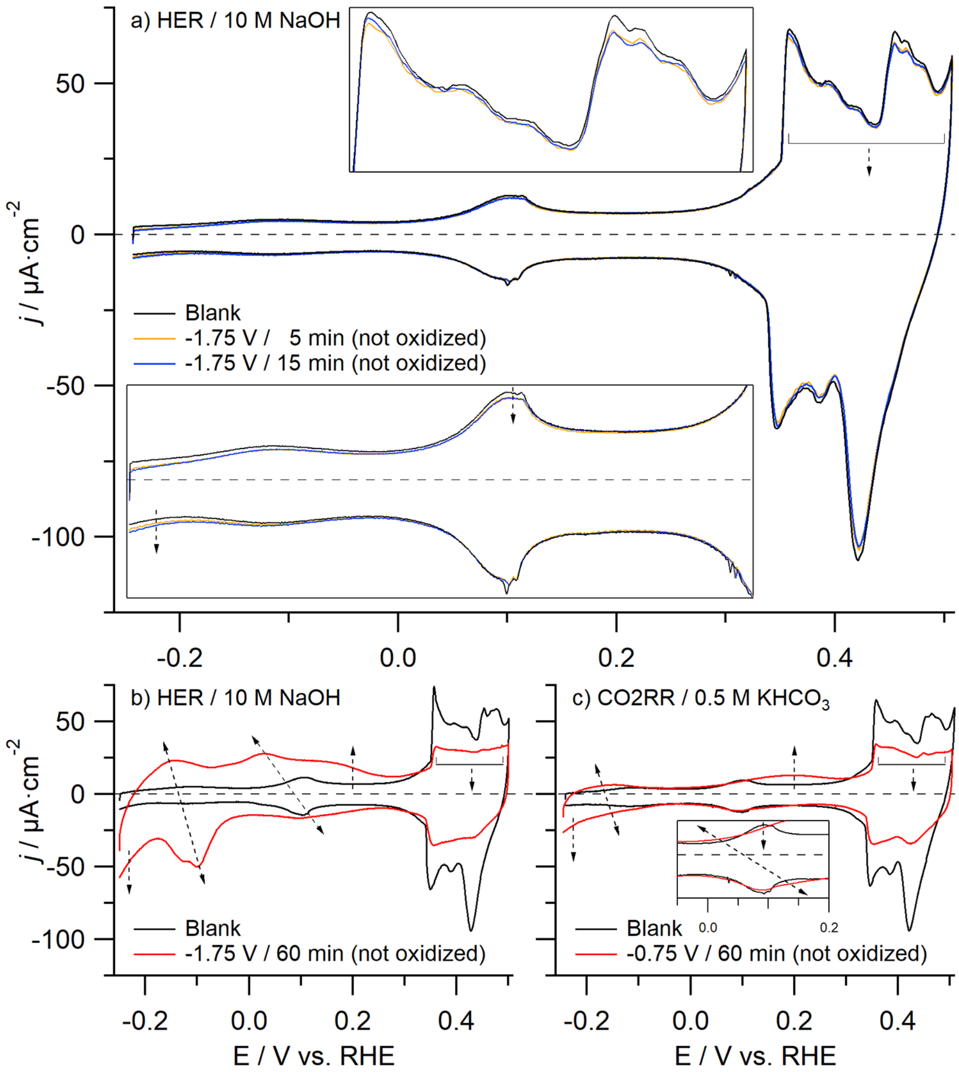

Figure 5.4: Changes in the characterization CVs ($0.1\ M$ NaOH, $\nu = 50\ mV \cdot s^{-1}$) of Cu(poly) surfaces after being subjected to purely cathodic conditions ($5 - 60\ min$) under various conditions. In panels a) and b) the CVs obtained after cathodization at $-1.75\ V$ in $10\ M$ NaOH for 5 (orange) and $15\ minutes$ (blue), and after $60\ minutes$ (red), are compared to their respective blank CVs ($0.1\ M$ NaOH, $\nu = 50\ mV \cdot s^{-1}$) (black). In panel c) the characterization CVs ($0.1\ M$ NaOH, $\nu = 50\ mV \cdot s^{-1}$) obtained before (blank, in black) and after (red) $60\ minutes$ of CO$_2$ reduction at $-0.75\ V$ in $0.5\ M$ KHCO$_3$ are depicted. Reported potentials are 85% iR corrected.

in $0.1\ M$ $KHCO_3$, Figure D.3) for various reaction times, with CV changes already evident within $1\ min$ and becoming more pronounced with increased reaction duration. This apparent independence on reaction conditions was further verified from CV studies after performing CO reduction in $10\ M$ NaOH at both $-0.75\ V$ and $-0.40\ V$ (Figures D.4 and D.5, respectively) for reaction times between 1 and $30\ min$ (e.g., comparable conditions to Figures 5.1d and 5.4a). Also in this instance, near-identical CV trends were observed after reaction in the absence and presence of CO, irrespective of the exact applied potential ($-1.75\ V$ vs. $-0.75\ V$ and $-0.40\ V$). Namely, an absence of change in voltammetry after $1\ min$, and CV suppression effects plus increased HER after extended reaction duration.

In summary, voltammetric studies for longer timeframes ($5-60\ min$) under various different reaction conditions resulted in comparable CV trends. Specifically, studies employing strong ($-1.75\ V$, without CO) and weak ($-0.75\ V$ and $-0.40\ V$, with CO) cathodic potentials in $10\ M$ NaOH showed independence of the potential and presence of CO. Similar results (apparent independence of exact reaction conditions) were also obtained when investigating reduction ($-0.75\ V$) in different concentrations of bicarbonate electrolyte: $0.1\ M$ and $0.5\ M$ $KHCO_3$. Because of the similar voltammetry results obtained under these various conditions, which were furthermore difficult to reconcile with the expected behavior of clean copper, we started doubting the applicability of this CV-centric approach for studying copper stability for extended-duration experiments.

To verify if the voltammetric data was representative of changing copper morphology or otherwise, extended-time control experiments that did not rely on CV were performed by conducting identical-location SEM studies on a micro-roughened copper surface prior to- and after $60\ min$ of CO2RR at $-0.75\ V$ in $0.5\ M$ $KHCO_3$. Taking into consideration the considerable changes observed in voltammetry after $60\ minutes$ of cathodization (both in $10\ M$ NaOH and $0.5\ M$ $KHCO_3$, Figures 5.4b and 5.4c) we would reasonably expect to be able to see such changes via SEM, if indeed the changes in voltammetry are representative of the redistribution of copper sites at the interface resulting from changing morphology. E.g., CV changes of similar magnitude were observed in Figure 5.2d, and resulted in easily identifiable roughening in the SEM (Figure 5.3). The basis for this study was an anisotropically (Figure D.2) roughened spherical single crystal (halide-induced roughening procedure described in the experimental section) that retained its macroscopic anisotropy resulting from its initial single-crystallinity but exhibited facet-dependent nanoscale morphology after roughening.

After the roughening procedure, the crystal was rinsed and dried under reducing atmosphere and moved to the SEM, where multiple easily identifiable spots of various morphologies were imaged. Next, it was transferred to the electrochemical setup where it was subjected to $-0.75\ V$ in $0.5\ M$ $KHCO_3$ for $60\ min$ under constant CO_2 bubbling. Deactivation on this timescale for this electrode is evident from the current response of the system (Figure D.6). Copper-catalyst deactivation under similar conditions; ca. $1\ hour$ of CO2RR at potentials between $-1\ V < E < -0.7\ V$ in bicarbonate electrolyte between $0.1\ M$ and $0.5\ M$ for both unpurified and prepurified electrolytes has also been observed by other authors. E.g., see current traces reported by Kuhl *et al.*[34], Wang *et al.*[35], and Wuttig *et al.*[7] Additionally, Popovic *et al.*[10] write about the morphological evolution of copper on a similar timescale and under similar conditions (i.e., $50\ min$ at $-0.70\ V$ in $0.1\ M$ $KHCO_3$). After conducting CO2RR, the electrode was rinsed, dried and moved to the SEM once again. As described in a previous section (accompanying Figure 5.3), the crystal was manually positioned to match as best as possible its previous orientation using the surface anisotropy. Because of this manual step, the incidence angle of the electron beam with respect to the surface normal will deviate slightly between the two datasets, with this mismatch being exacerbated by the curvature of the surface. Previously imaged sites were re-located and a follow-up set of micrographs was taken for each location.

The results of this experiment are shown in Figure 5.5, where micrographs of various spots on the surface exhibiting different morphologies on the mesoscale (ca. $50-200\ nm$ range) obtained before (left-hand side) and after (right-hand side) CO2RR are depicted. Mesoscale surface stability after one hour of reaction time can be investigated by comparing Figures 5.5a, c, e, and g with Figures 5.5b, d, f, and h for micrographs of the surface prior to- and after CO2RR, respectively. Insets show a magnification of a region located within the associated full-sized images. The discussion for this particular experiment is straightforward: the surface was found to be virtually unchanged to within the detection limits for our system. Overall shapes and locations of the variously sized and oriented microparticles located in these images remain static. If anything, there can be observed one difference between Figures 5.5e and 5.5f; an additional particle being located near the bottom-middle for Figure 5.5f, which we believe is likely dust. Though the resolution of the SEM is limited, a copper surface is commonly believed to undergo signification changes under CO2RR conditions on the length-scale we investigate and should be easily visible in the insets provided in Figure 5.5.[21] However, as we are very careful to minimize surface oxidation at every step of the experiment, we find that deposits tens of nanometers in size (i.e., highly reactive and therefore unstable) exhibit high stability within the timeframe and resolution of our system.

Although SEM is incapable of resolving the (distribution of) facets at the interface (one would need atomically resolved and preferably in-situ techniques for such information), CV evidence (which is structure sensitive) for short timeframes under cathodic conditions in $10\ M$ NaOH on the three basal planes and defect-rich polycrystalline copper indicated no discernible surface changes, which is in good qualitative agreement with the SEM data provided in both Figure 5.3 ($5\ min$ at $-1.75\ V$ in $10\ M$ NaOH) and Figure 5.5 ($60\ min$ at $-0.75\ V$ in $0.5\ M$ $KHCO_3$), as also there we observe no morphological differences to within the limits of our instrument in absence of surface oxidation. However, the SEM data in Figure 5.5 evidently disagrees with the CV data obtained for such longer time periods (Figure 5.4c), based on which we would expect, at a minimum, identifiable change in morphology on the ca. $50\ nm$ scale, if indeed the CV evolution is representative of a changing distribution of facets at the interface. From these results, we believe that the cyclic voltammetry results obtained after $5-60\ minutes$ of reduction are not related to changes in surface morphology as induced by the negative interfacial potential.

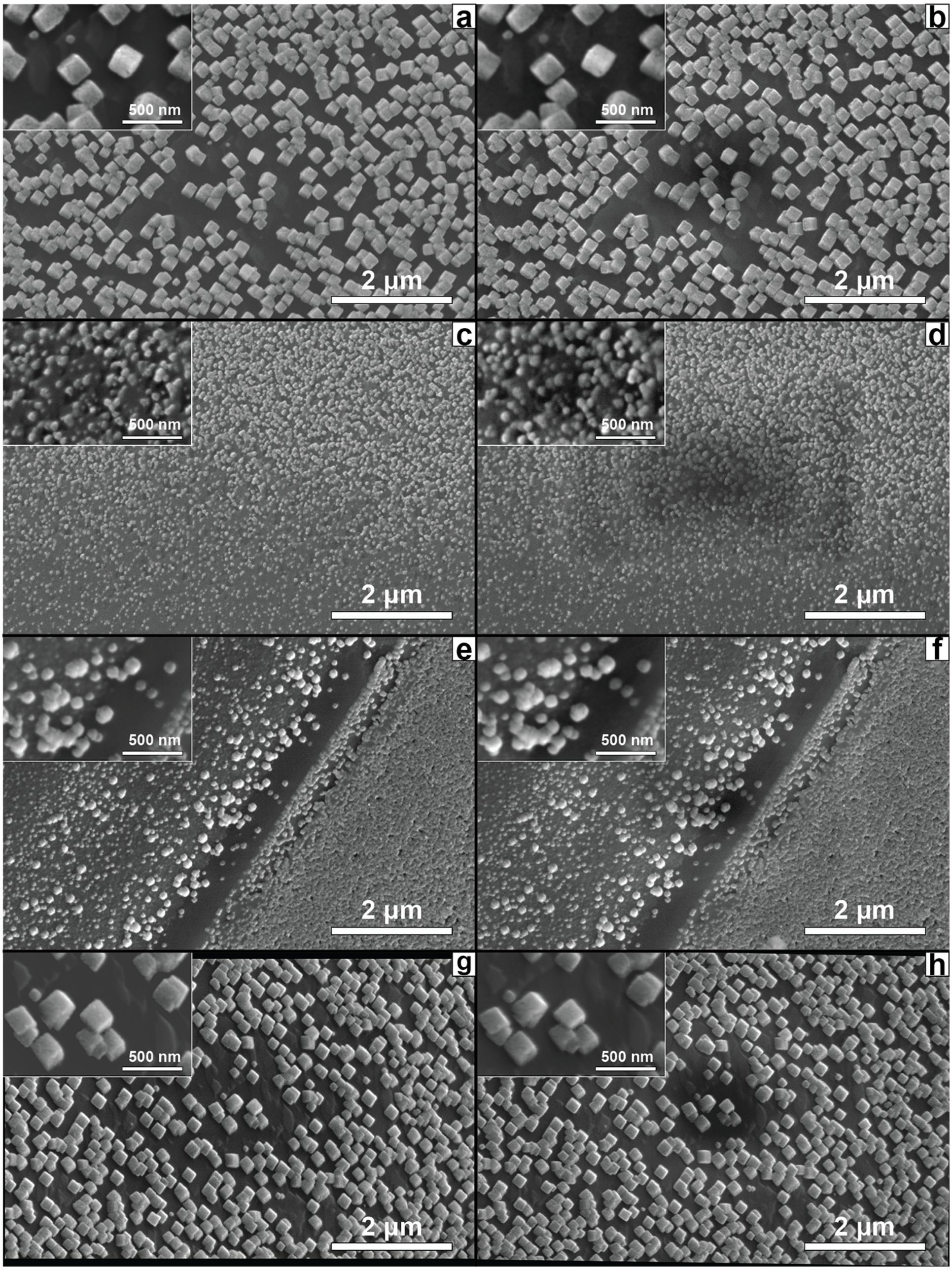

Figure 5.5: Identical location SEM of an electrochemically roughened spherical single crystal electrode before (left-hand: a, c, e and g) and after (right-hand: b, d, f and h) $60\ min$ of CO2RR at $-0.75\ V$ vs. RHE in $0.5\ M$ KHCO$_3$ for various locations on the crystal.

Neither can we attribute the observed CV trends to unintended oxidation, considering the behavior is very different from the changes we see when comparing CVs obtained for pre-oxidized surfaces (Figure 5.2) and cathodic-only treated surfaces (Figure 5.1). Hence, we posit that the changes in voltammetry after extended reaction duration must be related to something other than cathodically induced and/or anodically induced morphological surface evolution. We suggest the changes may instead be related to the blocking of copper sites with foreign species, as that would agree with the appearance of non-copper features in the CV which become more prominent as a function of time, together with the suppression of adsorption charge of known copper sites.

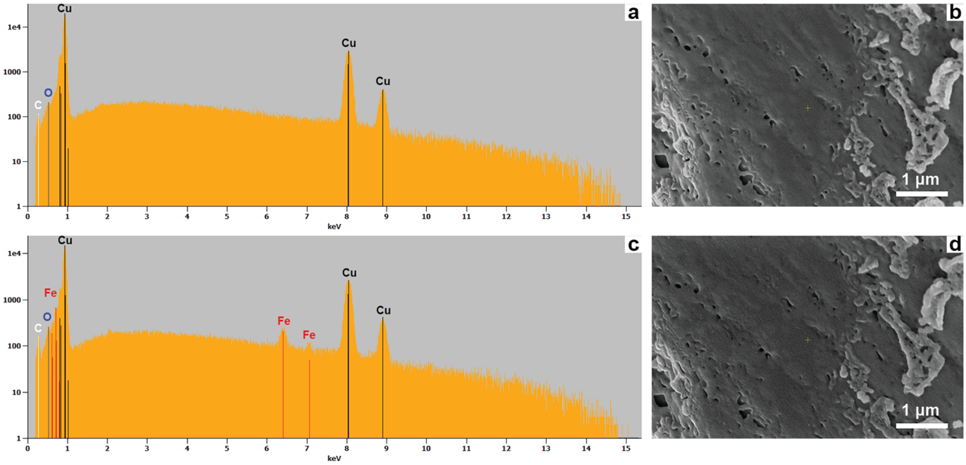

Figure 5.6: Surface morphology and elemental analysis results before and after ca. $5\ hours$ of CO2RR at $-0.75\ V$ in saturated $KHCO_3$ solution under constant CO_2 (g) purging for an arbitrary location on a nitric acid-cleaned polycrystalline bead electrode. Panels a) and c) show the EDX spectrum obtained prior to- and after CO2RR whilst b) and d) show the accompanying SEM micrographs for where EDX was performed.

To investigate this hypothesis, we conducted the following experiment. Firstly, a Cu(poly) bead-type electrode was grown and cleaned as per steps (a-c) of single crystal growth described in the experimental. After a final HNO_3 etching and Milli-Q rinsing step, it was not remolten. Rather it was briefly (ca. $10\ s$) annealed inductively in pure hydrogen to remove the oxide layer, but at much lower temperatures than used normally (i.e., decreased instrument power) so as to prevent migration of bulk contaminants to the surface. The crystal was cooled down in hydrogen, moved to the SEM and had its elemental composition investigated via energy-dispersive X-ray spectroscopy (EDX) for various locations to verify that the surface was devoid of contaminants to within the accuracy of the apparatus. Thereafter, the crystal was moved to our controlled-atmosphere electrochemical setup and CO2RR was carried out in saturated $KHCO_3$ solution (with sufficient $KHCO_3$ added to nominally reach $2\ M$) under constant CO_2 bubbling at $-0.75\ V$ for ca. $5\ hours$. Finally, the surface was rinsed under reducing conditions, dried in hydrogen, and moved back to the

SEM where EDX was performed once more. Results representative of the overall observed behavior are depicted in Figure 5.6 with additional locations provided in Figures D.7 and D.8.

Although more convincing proof and a more detailed discussion of the morphological stability of copper is provided in the previous section, the respective micrographs in shown Figures 5.6b and 5.6d (before and after CO2RR, respectively) agree with those data: little to no change in surface morphology can be seen. However, elemental analysis shows a different story; with EDX showing no Fe prior to CO2RR (Figure 5.6a) but iron being clearly visible after (Figure 5.6c). Identical observations were made for various regions on the crystal located hundreds of μm apart and having differing morphologies (see e.g., Figures D.7 and D.8), all exhibiting no distinguishable changes in morphology but with traces of iron present after the experiment. Hence, we believe that the changes in cyclic voltammetry that we observe when reaction time is increased (Figure 5.4) are most probably related to fouling by solution impurities rather than changes in the distribution of facets at the surface resulting from morphological evolution.

5.4. Conclusions

The cathodic stability of the various principal surfaces of copper, together with a defect-rich polycrystalline surface, was investigated under known highly cathodically corrosive conditions[13, 23] as well as under commonplace CO2RR conditions. The stability of these surfaces was found to be exquisite under purely cathodic potentials, so-long as oxide formation was entirely avoided (Figure 5.1). However, allowing the surface to partially oxidize resulted in rapid changes in the distribution of active sites at the surface (Figure 5.2). The morphological stability under cathodic-only conditions for both HER at $-1.75\ V$ in $10\ M$ NaOH and CO2RR at $-0.75\ V$ in $0.5\ M$ $KHCO_3$ + CO_2 (g) for prolonged times was corroborated by SEM, with no surface roughening observed to within the accuracy of the equipment for both instances when surface oxidation was absent (Figures 5.3 and 5.5, respectively). Voltammetric data after such prolonged reaction times (Figure 5.4) proved to be unreliable, showing very different behavior from CV results obtained for shorter periods of time (Figure 5.1, no changes), exhibiting instead the development of features unrelated to copper, where various different electrolytes and reaction conditions all yielded comparable results. We show that the mismatch between CV data and SEM data after cathodization for extended periods of time is related to electrode fouling as determined via SEM+EDX, where surface morphology was found static but elemental analysis showed iron to be present after reaction (Figure 5.6 and Figures D.7/D.8).

Our findings are in contradiction with current literature, wherein it is often proposed that the catalyst deactivation observed for Cu surfaces is possibly due to changes in surface morphology resulting in facet redistribution[12, 14, 19–21, 36], as induced in some manner by the reaction environment (e.g., due to the applied potential[12, 16, 17], or due to (CO2RR intermediate-related) adsorbates[37], or due to the local pH[36, 38], or other factors). However, a comparatively much simpler explanation underlying reported changes in surface morphology exists: accidental surface oxidation and subsequent anisotropic (Figures 5.2 and 5.3) reduction of the surface (likely in concert with dissolution and redeposition) as also proposed by Popovic *et al.*[10], where the rate of reduction of these oxides is likely to influence the final morphology. Such unintended (partial) surface oxidation is easily achieved, considering that the open circuit potential for copper falls within the region where surface oxidation takes place[11] and with increasingly complicated setups becoming more prevalent, increasing also the likelihood of minor experimental errors. In agreement with this theory, we show that brief oxidation ($1\ min$) at potentials very close to the open circuit potential of copper ($+0.50\ V$ vs. RHE), resulted in appreciable differences in cyclic voltammetry (Figure 5.2) denoting anisotropic surface restructuring. Thus, we conclude that oxidation-reduction cycles are at the basis of the reported morphological changes for copper, with the thickness of such (accidentally formed) oxide layers, their subsequent (rate of) reduction, and the number of such oxidation/reduction cycles yielding the various (changes in) morphologies reported. This agrees well with Speck and Cherevko[11] who report the absence of copper dissolution at negative potentials down to $-1\ V$ vs. RHE, stating: *"...but further oxidation at open circuit potential results in dissolution."*

As a final consideration we would like to point out that the conclusions we draw in this work may contradict with conclusions of other authors on this topic, however the data we base our (and others their) conclusions on are not necessarily in disagreement with other data. This is best illustrated by two recent works by Simon *et al.*[12], and by Popovic *et al.*[10] In the former, in-situ EC-AFM images are presented showing that a Cu(100) surface imaged at open circuit in $0.1\ M$ $KHCO_3$ changes its morphology once CO2RR conditions are applied, with the resulting surface morphology being a function of the applied potential. However, it is also stated that *"...[We] performed CO2RR... over extended periods of time [..., but AFM] images reveal no obvious morphological changes on the surface over the reaction times studied..."*.[12] Hence, the change in morphology occurred after stepping from open circuit to their potential of interest, which agrees well with our proposed mechanism of oxidation-induced morphological change, which in the case of Simon *et al.*[12] would be the result of starting at open circuit potential. Similarly, Popovic *et al.*[10] show degradation of a ca. $500\ nm$ radius Cu nanoparticle, but their study also contains periods at open circuit translating to successive oxidation and reduction cycles. In our work we employ extremely cathodic potentials, resulting in the electrolyte near the surface being supersaturated with hydrogen when we disconnect the electrical circuit. Thereafter, we rinse briefly under strong hydrogen flow and dry our electrodes in an isolated environment under high hydrogen flow. Hence, we minimize such oxidation that would occur at open circuit potentials, and can show that the CV does not change after brief periods of cathodization. Though contamination effects prohibit us from providing the same type of proof for prolonged periods of time, identical location SEM measurements serve to show that the morphology is stable, at least on the length-scale reported on by Popovic *et al.*[10]

References

[1] Matthew Jouny, Wesley Luc, and Feng Jiao. General techno-economic analysis of CO2 electrolysis systems. *Industrial & Engineering Chemistry Research*, 57(6):2165–2177, 2018.

[2] Md Golam Kibria, Jonathan P. Edwards, Christine M. Gabardo, Cao-Thang Dinh, Ali Seifitokaldani, David Sinton, and Edward H. Sargent. Electrochemical CO2 reduction into chemical feedstocks: From mechanistic electrocatalysis models to system design. *Advanced Materials*, 31(31):1807166, 2019.

[3] Jared Sisler, Shaihroz Khan, Alexander H. Ip, Moritz W. Schreiber, Shaffiq A. Jaffer, Erin R. Bobicki, Cao-Thang Dinh, and Edward H. Sargent. Ethylene electrosynthesis: A comparative techno-economic analysis of alkaline vs membrane electrode assembly vs CO2–CO–C2H4 tandems. *ACS Energy Letters*, 6(3):997–1002, 2021.

[4] Jun Tae Song, Hakhyeon Song, Beomil Kim, and Jihun Oh. Towards higher rate electrochemical CO2 conversion: From liquid-phase to gas-phase systems. *Catalysts*, 9(3):224, 2019.

[5] Sumit Verma, Byoungsu Kim, Huei-Ru “Molly” Jhong, Sichao Ma, and Paul J. A. Kenis. A gross-margin model for defining technoeconomic benchmarks in the electroreduction of CO2. *ChemSusChem*, 9(15):1972–1979, 2016.

[6] Y. Hori, H. Konishi, T. Futamura, A. Murata, O. Koga, H. Sakurai, and K. Oguma. “deactivation of copper electrode” in electrochemical reduction of CO2. *Electrochimica Acta*, 50(27):5354–5369, 2005.

[7] Anna Wuttig and Yogesh Surendranath. Impurity ion complexation enhances carbon dioxide reduction catalysis. *ACS Catalysis*, 5(7):4479–4484, 2015.

[8] David W. DeWulf, Tuo Jin, and Allen J. Bard. Electrochemical and surface studies of carbon dioxide reduction to methane and ethylene at copper electrodes in aqueous solutions. *Journal of The Electrochemical Society*, 136(6):1686–1691, 1989.

[9] Dan Ren, Nian Tee Wong, Albertus Denny Handoko, Yun Huang, and Boon Siang Yeo. Mechanistic insights into the enhanced activity and stability of agglomerated Cu nanocrystals for the electrochemical reduction of carbon dioxide to n-propanol. *Journal of Physical Chemistry Letters*, 7(1):20–24, 2016.

[10] Stefan Popovic, Marjan Bele, and Nejc Hodnik. Reconstruction of copper nanoparticles at electrochemical CO2 reduction reaction conditions occurs via two-step dissolution/redeposition mechanism. *ChemElectroChem*, (DOI: 10.1002/celc.202100387), 2021.

[11] Florian D. Speck and Serhiy Cherevko. Electrochemical copper dissolution: A benchmark for stable CO2 reduction on copper electrocatalysts. *Electrochemistry Communications*, 115:106739, 2020.

[12] Georg H. Simon, Christopher S. Kley, and Beatriz Roldan Cuenya. Potential-dependent morphology of copper catalysts during CO2 electroreduction revealed by in-situ atomic force microscopy. *Angewandte Chemie International Edition*, 60(5):2561–2568, 2021.

[13] Alexei I. Yanson, Paramaconi Rodriguez, Nuria Garcia-Araez, Rik V. Mom, Frans D. Tichelaar, and Marc T. M. Koper. Cathodic corrosion: A quick, clean, and versatile method for the synthesis of metallic nanoparticles. *Angewandte Chemie International Edition*, 50(28):6346–6350, 2011.

[14] Youn-Geun Kim, Jack Hess Baricuatro, Alnald Javier, John Mathew Gregoire, and Manuel P. Soriaga. The evolution of the polycrystalline copper surface, first to Cu(111) and then to Cu(100), at a fixed CO2RR potential: A study by operando EC-STM. *Langmuir*, 30(50):15053–15056, 2014.

[15] Hisayoshi Matsushima, Andriy Taranovskyy, Christian Haak, Yvonne Gründer, and Olaf M. Magnussen. Reconstruction of Cu(100) electrode surfaces during hydrogen evolution. *Journal of the American Chemical Society*, 131(30):10362–10363, 2009.

[16] Thanh Hai Phan, Karla Banjac, Fernando P. Cometto, Federico Dattila, Rodrigo García-Muelas, Stefan J. Raaijman, Chunmiao Ye, Marc T. M. Koper, Núria López, and Magalí Lingenfelder. Emergence of potential-controlled Cu-nanocuboids and graphene-covered Cu-nanocuboids under operando CO2 electroreduction. *Nano Letters*, 21(5):2059–2065, 2021.

[17] Beatriz Roldán Cuenya, Fabian Scholten, Khanh-Ly C. Nguyen, Jared P. Bruce, and Markus Heyde. Identifying structure-selectivity correlations in the electrochemical reduction of CO2: comparison of well-ordered atomically-clean and chemically-etched Cu single crystal surfaces. *Angewandte Chemie International Edition*, (DOI: 10.1002/anie.202103102), 2021.

[18] Rosa M. Arán-Ais, Fabian Scholten, Sebastian Kunze, Rubén Rizo, and Beatriz Roldan Cuenya. The role of in situ generated morphological motifs and Cu(i) species in C2+ product selectivity during CO2 pulsed electroreduction. *Nature Energy*, 5(4):317–325, 2020.

[19] Youn-Geun Kim, Jack H. Baricuatro, and Manuel P. Soriaga. Surface reconstruction of polycrystalline Cu electrodes in aqueous KHCO3 electrolyte at potentials in the early stages of CO2 reduction. *Electrocatalysis*, 9(4):526–530, 2018.

[20] Youn-Geun Kim, Alnald Javier, Jack H. Baricuatro, Daniel Torelli, Kyle D. cummins, Chu F. Tsang, John C. Hemminger, and Manuel P. Soriaga. Reprint

of: Surface reconstruction of pure-Cu single-crystal electrodes under CO-reduction potentials in alkaline solutions: A study by seriatim ECSTM-DEMS. *Journal of Electroanalytical Chemistry*, 793:113–118, 2017.

[21] Stefan Popović, Milutin Smiljanić, Primož Jovanovič, Jan Vavra, Raffaella Buonsanti, and Nejc Hodnik. Stability and degradation mechanisms of copper-based catalysts for electrochemical CO2 reduction. *Angewandte Chemie International Edition*, 59(35):14736–14746, 2020.

[22] Thomas J. P. Hersbach, Alexei I. Yanson, and Marc T. M. Koper. Anisotropic etching of platinum electrodes at the onset of cathodic corrosion. *Nature Communications*, 7:12653, 2016.

[23] A. I. Yanson, P. V. Antonov, P. Rodriguez, and M. T. M. Koper. Influence of the electrolyte concentration on the size and shape of platinum nanoparticles synthesized by cathodic corrosion. *Electrochimica Acta*, 112:913–918, 2013.

[24] Thomas J. P. Hersbach, Ian T. McCrum, Dimitra Anastasiadou, Rianne Wever, Federico Calle-Vallejo, and Marc T. M. Koper. Alkali metal cation effects in structuring Pt, Rh, and Au surfaces through cathodic corrosion. *ACS Applied Materials & Interfaces*, 10(45):39363–39379, 2018.

[25] Thomas J. P. Hersbach, Vladislav A. Mints, Federico Calle-Vallejo, Alexei I. Yanson, and Marc T. M. Koper. Anisotropic etching of rhodium and gold as the onset of nanoparticle formation by cathodic corrosion. *Faraday Discussions*, 193(0):207–222, 2016.

[26] Stefan J. Raaijman, Nakkiran Arulmozhi, and Marc T. M. Koper. Anisotropic cathodic corrosion of gold electrodes in the absence and presence of carbon monoxide. *Journal of Physical Chemistry C*, 124(52):28539–28554, 2020.

[27] S.J. Raaijman, N.Arulmozhi, and M.T.M.Koper. Clean and reproducible voltammetry of copper single crystals with prominent facet-specific features using induction annealing. (manuscript submitted for publication), 2021.

[28] Nakkiran Arulmozhi and Gregory Jerkiewicz. Design and development of instrumentations for the preparation of platinum single crystals for electrochemistry and electrocatalysis research. Part 1: Semi-automated crystal growth. *Electrocatalysis*, 7(6):507–518, 2016.

[29] F. Sloan Roberts, Kendra P. Kuhl, and Anders Nilsson. High selectivity for ethylene from carbon dioxide reduction over copper nanocube electrocatalysts. *Angewandte Chemie*, 127(17):5268–5271, 2015.

[30] Paula Sebastián-Pascual, Francisco J. Sarabia, Víctor Climent, Juan M. Feliu, and María Escudero-Escribano. Elucidating the structure of the Cu-alkaline electrochemical interface with the laser-induced temperature jump method. *The Journal of Physical Chemistry C*, 2020.

[31] Aarti Tiwari, Hendrik H. Heenen, Anton Simon Bjørnlund, Degenhart Hochfilzer, Karen Chan, and Sebastian Horch. Electrochemical oxidation of CO on Cu single crystals under alkaline conditions. *ACS Energy Letters*, 5(11):3437–3442, 2020.

[32] Klaas Jan P. Schouten, Elena Pérez Gallent, and Marc T.M. Koper. The electrochemical characterization of copper single-crystal electrodes in alkaline media. *Journal of Electroanalytical Chemistry*, 699:6–9, 2013.

[33] Nakkiran Arulmozhi, Derek Esau, Ram P. Lamsal, Diane Beauchemin, and Gregory Jerkiewicz. Structural transformation of monocrystalline platinum electrodes upon electro-oxidation and electro-dissolution. *ACS Catalysis*, 8(7):6426–6439, 2018.

[34] Kendra P. Kuhl, Etosha R. Cave, David N. Abram, and Thomas F. Jaramillo. New insights into the electrochemical reduction of carbon dioxide on metallic copper surfaces. *Energy & Environmental Science*, 5(5):7050–7059, 2012.

[35] Lei Wang, Stephanie A. Nitopi, Erlend Bertheussen, Marat Orazov, Carlos G. Morales-Guio, Xinyan Liu, Drew C. Higgins, Karen Chan, Jens K. Nørskov, Christopher Hahn, and Thomas F. Jaramillo. Electrochemical carbon monoxide reduction on polycrystalline copper: Effects of potential, pressure, and pH on selectivity toward multicarbon and oxygenated products. *ACS Catalysis*, 8(8):7445–7454, 2018.

[36] Wei Luo, Lei Hu, Yimin Xv, Jian Zhou, Wentao Xv, and Mi Yan. Electrochemical corrosion behavior and surface passivation of bulk nanocrystalline copper in alkaline solution. *Anti-Corrosion Methods and Materials*, 2020.

[37] Phil De Luna, Rafael Quintero-Bermudez, Cao-Thang Dinh, Michael B. Ross, Oleksandr S. Bushuyev, Petar Todorović, Tom Regier, Shana O. Kelley, Peidong Yang, and Edward H. Sargent. Catalyst electro-redeposition controls morphology and oxidation state for selective carbon dioxide reduction. *Nature Catalysis*, 1(2):103–110, 2018.

[38] Yaran Zhao, Xiaoxia Chang, Arnav S. Malkani, Xuan Yang, Levi Thompson, Feng Jiao, and Bingjun Xu. Speciation of Cu surfaces during the electrochemical CO reduction reaction. *Journal of the American Chemical Society*, 142(21):9735–9743, 2020.

6

Samenvatting

Het onderzoek beschreven in dit proefschrift is gebaseerd op twee hoofdpunten, te wezen 'hoe verloopt de katalytische reductie van koolstofdioxide (CO_2) naar producten bestaande uit (ketens van) twee of meer koolstoffen' en '(hoe) kunnen we bestaande processen aanpassen om deze reactie te verbeteren'. Beide onderwerpen hebben een industriële insteek, alhoewel de uiteindelijke uitvoering een meer fundamenteel karakter heeft aangenomen. De gedachte achter het eerste vraagstuk is hoe we waardevolle(re) producten kunnen maken uit koolstofdioxide via electroreductie, waarbij producten welke bestaan uit langere koolstofketens over het algemeen meer industriële toepassingen hebben en zodoende een hogere kostprijs genieten. De uiteindelijke uitwerking van dit vraagstuk zoals beschreven in dit proefschrift is in de vorm van een mechanistisch georiënteerd onderzoek, met een focus op hoe een elektrokatalysator het maken van chemische bindingen tussen individuele koolstofatomen faciliteert. Het industriële belang van dit onderzoek is dus gerelateerd aan het vervaardigen van producten met meerwaarde uit goedkope grondstoffen: koolstofdioxide en water, terwijl de wetenschappelijke relevantie voortvloeit uit het feit dat er momenteel nog veel onenigheid bestaat over hoe exact de vorming van een chemische binding tussen twee koolstoffen geschied tijdens de elektrochemische omzetting van CO_2.

Ter invulling van het tweede vraagstuk (bestaande technologieën verbeteren) is er in dit proefschrift onderzoek uitgevoerd naar de (mogelijke) veranderingen in de (oppervlakte-)structuur van verscheidene metallische katalysatoren onder reducerende (=kathodische) omstandigheden in het bijzijn van, of gedurende de actieve omzetting van, koolstofdioxide en/of koolstofmonoxide (CO). Deze invalshoek is relevant voor de chemische industrie aangezien de katalytische activiteit voor de reductie van koolstofdioxide sterk afhankelijk is van de oppervlaktestruktuur, en eventuele veranderingen in de struktuur dus invloed hebben op hoe de reactie verloopt en daarmee de procesefficiëntie. Wetenschappelijk gezien is deze vraaginvulling ook interessant: over de instabiliteit van metallische katalysatoren onder reductive reactiecondities is momenteel nog weinig bekend, gezien zulke omstandigheden volgens conventionele wijsheid juist resulteren in metaaloppervlakken van hoge stabiliteit.

De uitwerkingen van de onderzoeksresultaten zijn beschreven in hoofdstukken 2-5. Specifiek, hoofdstuk 2 is toegewijd aan het eerste hoofdpunt (mechanisme vorming koolstof-koolstof ketens), terwijl hoofdstukken 3 t/m 5 betrekking hebben tot het tweede hoofdpunt (instabiliteit oppervlakken onder CO_2-reductie omstandigheden). De resultaten besproken in hoofdstuk 2 zijn als volgt. Onderzoek was verricht naar de reductie van koolstofmonoxide met zilver (Ag) als elektrokatalysator. Alhoewel zilver niet de ideale kandidaat is voor het vormen van C2+ producten (de overkoepelende term voor stoffen die twee of meer koolstofatomen bevatten), zijn er voor dit systeem theoretische berekeningen gepubliceerd die voorspellen dat zilver een betere elektrokatalysator zou zijn voor de vorming van ethanol (H_3CCH_2OH) dan de vooralsnog beste katalysator voor de vorming van C2+ producten; koper (Cu). Koolstofdioxide werd in dit proefschrift vervangen met koolstofmonoxide als reactant, gezien de auteurs van de theoretisch-georiënteerde publicatie speculeerden dat de geschillen tussen hun voorspellingen en experimentele data van anderen verklaard zou kunnen worden door aan te nemen dat koolstofmonoxide vrijwel meteen het oppervlak verlaat nadat het gevormd wordt en zodoende niet de kans heeft verder te reageren. De vorming van koolstofmonoxide uit koolstofdioxide is algemeen geaccepteerd als de eerste stap in de reductie van koolstofdioxide naar C2+ producten, en zodoende is het bestuderen van CO als reactant representatief voor het verwachte mechanisme als CO_2 gereduceerd zou worden.

Met inachtneming van deze punten, was de experimentele uitvoering als volgt. Mechanistische aspecten van de CO_2-reductie-reactie aan zilver werden onderzocht, door CO te reduceren bij verschillende potentialen en de beschikbaarheid van CO aan het oppervlak werd gemanipuleerd door de druk te variëren. De gevormde C2+ producten werden geanalyseerd als functies van aangelegde potentiaal en reactant druk, waarbij overeenkomsten en verschillen tussen het gedrag van de gevormde producten gebruikt kunnen worden om (onderdelen van) het mechanisme te achterhalen. De volgende conclusies konden worden getrokken uit de resultaten van het onderzoek. Ten eerste, is een zilver katalysator inderdaad in staat om C2+ producten te vormen uit CO(2), zolang de bezettingsgraad van CO aan het oppervlak voldoende hoog is. Hiernaast wordt er meer van dit soort producten gevormd, als de druk, en daarmee de bezettingsgraad aan CO, verhoogd wordt. Bij de hoogste druk onderzocht (ca. $60\ bar$) is ethanol het meest gevormde product als we kijken naar specifiek C2+ producten. Deze conclusie zijn in overeenstemming met de hypothese geuit in het theoretische onderzoek dat door middel van berekeningen voorspelde dat zilver een goede katalysator zou zijn voor de vorming van ethanol uit CO_2 maar waarschijnlijk gelimiteerd wordt door de beschikbaarheid aan CO op het oppervlak. Ten tweede konden we geen ethyleen (H_2CCH_2) waarnemen tijdens onze metingen, waaruit we concluderen dat dit molecuul geen rol speelt als tussenstap voor de vorming van de gedetecteerde producten met ketens van 3 koolstofatomen: n-propanol (mechanisme C2 naar C3 producten). Ook dit is in overeenstemming met de theoretische berekeningen, gezien daaruit naar voren komt dat zilver slecht in staat is om de laatste $C-O$ binding te breken en dus moeite heeft ethyleen te vormen. Deze specifieke eigenschap van zilver is ook terug te zien in het waargenomen productspectrum: alle gedetecteerde C2+ producten bevatten minimaal één C−OH groep. Ten derde tonen ethanol en propanol sterke overeenkomsten in hun gedrag als functie van potentiaal en druk. Hieruit kan worden opgemaakt dat ze een gedeelde voorganger hebben in hun vormingsmechanisme. Gezien de afwezigheid van de vorming van ethyleen, de goede overeenstemming met de theoretische voorspellingen voor het katalytisch gedrag van zilver, en experimentele resultaten in de literatuur over acetaldehyde reductie aan koper, concluderen we dat deze gedeelde voorganger tussen C2 en C3 producten waarschijnlijk een acetaldehyde-achtig intermediar is.

In hoofdstuk 3 bekijken we de stabiliteit van een goud katalysator onder sterk alkalische omstandigheden in de aanwezigheid en afwezigheid van CO. Het gekozen alkalische milieu is bekend als een belangrijke component in het destabiliseren van oppervlakken onder kathodische potentialen, en is gebruikt als een benadering voor de lokale omgeving van het oppervlak gedurende industriële CO_2-reactie omstandigheden. De experimentele uitvoering was als volgt. De stabiliteit van sferische goud eenkristallen werd onderzocht door middel van elektrosorptie metingen en door het oppervlak te bestuderen via een rasterelektronenmicroscoop. De structuurgevoeligheid van zuurstof elektrosorptie geeft een beeld van wat er gebeurt met de gemiddelde oppervlaktesamenstelling, terwijl de combinatie van de regelmaat van een sferisch eenkristal samen met foto's van het oppervlak een beeld schetst van de (in-)stabiliteit van individuele facetten. Uit de resultaten van dit onderzoek konden we de volgende conclusies trekken. De belangrijkste conclusie is dat de instabiliteit van goud onder de geteste omstandigheden structuurafhankelijk is. Een tweede conclusie is dat er twee verschillende processen verantwoordelijk zijn voor de uiteindelijke verandering in de oppervlaktestructuur: het oplossen van goud van relatief gezien instabielere oppervlakken (110-type facetten, en facetten met hogere stappendichtheid), en het groeien van goud uit oplossing op plekken met specifieke structuur (111- en 100-type facetten) wat leidt tot de formatie van deeltjes op de oppervlakken met deze specifieke geometrieën, en drastische veranderingen van de facetten waar goud oplost. De gemiddelde actie van deze twee processen leidt tot oppervlakken welke meer 111-type facetten en minder 110-type facetten bevatten, wat een negatieve invloed heeft op de katalytische activiteit van polykristallijn goud voor de reductie van CO_2. Ten derde nam de snelheid waarmee het oppervlak veranderde toe, als CO aanwezig was in de buurt van het oppervlak. Hieruit kunnen we concluderen dat koolstofmonoxide een negatieve impact heeft op de kathodische stabiliteit van goud, wat we toeschrijven aan het feit dat het maken van een Au−CO binding (tijdens CO adsorptie) de sterkte van de Au−Au bindingen van goud met zijn omgeving verzwakt en daarmee de goudatomen aan het oppervlak destabiliseert.

In hoofdstuk 4 rapporteren we het adsorptie-gedrag van koperoppervlakken met verschillende structuren in alkalisch milieu. Deze informatie is nodig voor het uitvoeren van elektrosorptie metingen zoals ook gebruikt in hoofdstuk 3. Echter, in het geval van goud was deze informatie al beschikbaar, terwijl de literatuur betreffende het facet-specifieke adsorptiegedrag van koper nog onvolledig was. Door de standaard methode voor koper oppervlaktevoorbereiding te vervangen met een inductieverhitting-gebaseerde methode in combinatie met een zuurstofvrije reactieomgeving, konden we onze metingen uitvoeren aan volledig metallische oppervlakken. De experimentele uitvoering was als volgt. Koper elektrodes met specifieke oppervlaktestructuren werden schoongemaakt door deze te verwarmen tot dicht bij het smeltpunt voor enkele minuten in een reducerende waterstofatmosfeer, waarna ze de tijd kregen af te koelen naar kamertemperatuur. Nadien werd er een intern pad geopend tussen de elektrochemische cel gelegen onderaan de opstelling, en de bovenzijde van de opstelling, waar het kristal voorbereid kan worden door middel van verwarming. Het kristal werd daarna verplaatst van de bovenzijde naar de onderzijde, waar elektrochemische metingen uitgevoerd konden worden. Het adsorptiegedrag van ieder kristal werd bepaald door elektrisch contact te maken met het elektrolyt en de potentiaal stapsgewijs te veranderen en de resulterende stroom te meten (cyclische voltammetrie). Door de elektrochemische procedures te optimaliseren, konden we de reproduceerbaarheid van de resultaten garanderen. De conclusies die we op konden trekken uit de resultaten zijn als volgt. Ten eerste: met de juiste oppervlaktebehandeling, exacte elektrochemische stappen, en een zuurstofvrije omgeving kunnen zeer reproduceerbare oppervlakken verkregen worden. Ten tweede: door de standaard oppervlaktebehandeling voor koper (elektrochemisch oplossen in zuur) te vervangen met een inductieverwarming-gebaseerde behandeling, kunnen oppervlakken met hogere kristalliniteit verkregen worden. Ten derde kunnen we uit de ladingen geassocieerd met de adsorptiepieken aantonen dat de 111, 100 en 110 vlakken allemaal een uniek gelegen O-adsorptie piek hebben naast de reeds bekende facet-specifieke OH-adsorptie pieken. Laatstens concluderen we dat de exacte liggingen van de OH- en O-adsorptiepieken voor de 111 en 100 vlakken in het cyclisch voltammogram worden beïnvloed door de lengtes van de terrassen.

In hoofdstuk 5 onderzoeken we de kathodische stabiliteit van koperoppervlakken met verschillende structuren onder diverse omstandigheden. De methodologie is vergelijkbaar met die in hoofdstuk 3: de stabiliteit van een reeks koperkristallen werd onderzocht door middel van elektrosorptie metingen en door het oppervlak te bekijken via een rasterelektronenmicroscoop, waar de structuurgevoeligheid van hydroxide en zuurstof elektrosorptie een beeld geeft van wat er gebeurt met de gemiddelde oppervlaktesamenstelling, terwijl foto's van identieke locaties op de elektrodes een beeld schetsen van de (in-)stabiliteit van oppervlakken met verschillende morfologie. De stabiliteit in zowel sterk alkalisch milieu ($10\ M$ NaOH elektrolyt, bekend als belangrijke factor in het destabiliseren van metallische oppervlakken), als standaard reactie omstandigheden voor het omzetten van CO_2 ($0.5\ M$ $KHCO_3$ elektrolyt) hebben we getest, om een indruk te krijgen of de aanwezigheid van koolstofdioxide, CO_2-gerelateerde producten, en CO_2-gerelateerde ionen in oplossing (HCO_3^-, CO_3^{2-}) invloed hebben op de stabiliteit van koper tijdens kathodische omstandigheden. De conclusies die we konden trekken zijn als volgt. In tegenstelling tot goud, is koper onder kathodische omstandigheden in sterk alkalisch milieu stabiel: elektrosorptie metingen bewijzen dat de verdeling van facetten aan het oppervlak gelijk blijft voor korte-termijn experimenten. De tweede conclusie is dat onder CO_2-reactie omstandigheden, mits alleen katodische potentialen worden aangelegd, een koperoppervlak ook stabiel is. Deze conclusie komt van identieke-locatie elektronenmicroscoopfoto's voor- en na $6\ uur$ reactie, waar de foto's identiek aan elkaar zijn tot op een schaal van ca. $50 - 100\ nanometer$ (de maximum resolutie van de meting). Echter, als het koperoppervlak per ongeluk (of expres) wordt geoxideerd door naar oxidatieve potentialen te gaan, dan veranderd een koperoppervlak significant binnen $1\ minuut$. Vandaar dat de laatste conclusie is, dat iedereen die rapporteert dat koper niet stabiel is gedurende CO_2-reactie omstandigheden, waarschijnlijk niet voorzichtig genoeg hun experimenten uitvoert en per ongeluk hun koperoppervlak de kans geeft (deels) te oxideren.

A

Supporting information for Chapter 2: High-pressure CO electroreduction at silver produces ethanol and propanol

A.1. Supporting experimental

A.1.1. Chemicals

All solutions were prepared by dissolving appropriate amounts of chemicals, used as received unless otherwise indicated, in high purity Milli-Q water (Millipore, $18.2\ M\Omega\cdot cm$). All experiments were conducted in $300\ mL$ $0.5\ M$ KOH (99.95%, Alfa Aesar) electrolyte purged and pressurized with carbon monoxide (Linde, 4.7), whilst the counter electrode compartment was purged with nitrogen (Linde, 2.0).

A.1.2. Electrochemistry

Potentials were controlled via either a Solartron (Energylab XM with 2A booster) or Autolab (PGSTAT302N) potentiostat in a three-electrode configuration. Solution resistances were determined via impedance before the start of the experiment and at regular intervals during the measurement, but reported potential values are not corrected for ohmic drop. High-pressure electrochemical cell and product detection. A home-made three-compartment electrochemical cell designed to fit inside an autoclave (Premex, Hastelloy C22, 600 mL) was used for all experiments reported in this work (Figure A.1). The autoclave had a total of three gas inlets (CE compartment, WE compartment topside (not used) and WE backside) and two gas

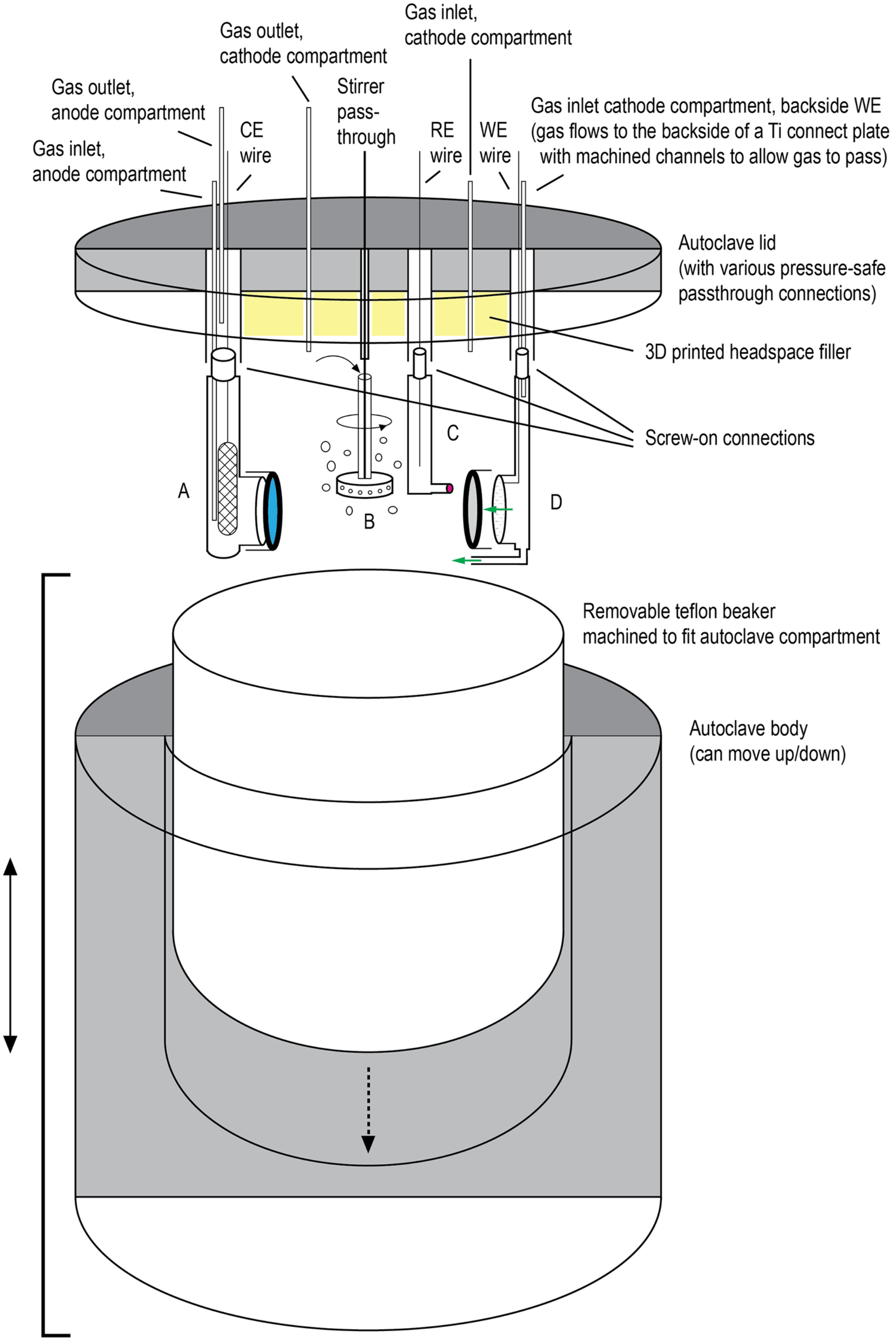

Figure A.1: Schematic of the high-pressure setup.

outlets (CE and WE compartment outlets). The inlets of the autoclave were attached to calibrated mass flow controllers (Brooks, Delta Smart II) connected to their respective gas bottles, whilst the outlet was attached to a back-pressure regulator (Equilibar) to regulate pressure inside the reaction chamber and allow for constant flow. Outflows of excess gases for counter and working compartments were united downstream, but the existence of a constant net positive flux for both compartments prevented mixing at points located upstream. After, exhaust gas was led through a dehumidifier (Perma Pure, MD-050-24S-2) prior to being introduced into a gas chromatograph (G.A.S, CompactGC 4.0).

The electrochemical cell was comprised of two sections: a bottom and a top half. The lower half contained the electrochemical cell and consisted of a cylindrical PTFE beaker that was machined to precisely fit the bottom of the autoclave. The top half of the cell was affixed to the top of the autoclave, and housed a series of machined plastic pieces that extended down into the PTFE beaker upon assembly. Specifically, the top contained a total of five elements: separate housings for both the counter (Figure A.1, A) and reference electrodes (Figure A.1, C), a machined component capable of flowing gases along the back of the working electrode into the reaction vessel (Figure A.1, D), a vertical stirring rod (Figure A.1, B), and a final piece of 3D printed solid plastic (3D printed with Form labs 2 SLA 3D printer using FLGPC02 resin) that was shaped so as to fill the empty spaces in-between the other components above the electrolyte level (Figure A.1, yellow sections). Electrical contact with the outside was established via pass-through Swagelok fittings located in the top of the autoclave.

The counter electrode (platinum mesh, 99.9%, Alfa Aesar) was housed in a rectangular enclosure made out of PEEK with an internal volume of ca. $20\ mL$. The anolyte was isolated from the rest of the cell via an anion exchange membrane (AEM, Fumasen, FAB-PK-130) of ca. $7\ cm^2$. The anolyte was constantly purged with nitrogen to facilitate mixing and the removal of bubbles, whilst also serving as an internal standard for gas quantification. The membrane separating the two compartments was replaced daily, or alternatively after each experiment (for experiments $> 12\ h$).

A home-made Ag/AgCl wire in contact with KCl solution made up the reference electrode. Prior to each experiment the AgCl layer was renewed by submerging the silver wire (99.9%, Alfa Aesar) in a $0.1\ M$ HCl solution (Ph. Eur., Merck) and applying a current of $+20\ mA$ for $20\ seconds$ vs. a Pt wire to form a silver chloride overlayer, which is the electrochemical equivalent of some commonly employed[1, 2] chemical treatments to generate a AgCl layer. Then, the wire was thoroughly rinsed with Milli-Q water, after which it was submerged in a machined Luggin capillary made from Kel-F containing ca. 10 mL AgCl saturated (0.16 M) 3 M KCl solution (Merck). The tip of the Luggin capillary was located in close proximity to the bottom-half of the working electrode surface (ca. $1\ mm$ away) and terminated with a PEEK frit with $2\ \mu m$ pores (Idex, A-710) to separate the working electrolyte from the reference solution. The working electrode assembly was comprised of an open-ended hollow rod that allowed for gases to be introduced to the reaction vessel. Electrical contact with the working electrode was established through the backside of the WE via a circular titanium plate (connected to a lead) that had flow channels machined into it to allow gases to reach the backside of the electrode. However, no means of closing the lower end of the tube were present. Thus, gases could also flow past the backside of the electrode and out of the bottom tube into the electrolyte. A silver GDE (Dioxide Materials, Ag/ionomer coating on carbon paper) was cut to size and used as received, with a total geometric area of $1\ cm^2$ exposed to the electrolyte. The working electrode was replaced for each individual measurement.

A.1.3. IR drop determination

Solution resistances were determined at the start of each experiment via impedance spectroscopy near the open circuit potential and assumed to be equal to the measured real impedance at $10\ kHz$[3], which varied between 4.8 and $5.5\ \Omega$ for all experiments reported in this work. Potentials as we report them ($V\ vs.\ Ag|AgCl|KCl_{3\ M}$) can be converted to the reversible hydrogen electrode (RHE) scale via Equation A.1, and the ohmic resistance compensated to obtain the 'real' interfacial potential via Equation A.2 where conventional signage for cathodic (negative) and anodic (positive) current applies. Using a standard potential of $E^{3\ M\ \mathrm{Cl}^-}_{Ag|AgCl} = +0.21\ V\ vs.\ SHE$, a pH of 13.7 for our $0.5\ M$ KOH electrolyte, an R value of $5\ \Omega$, and $-0.5\ A$ of current at the most negatively applied potential of $-4.5\ V$ (see Figure A.6, considering $1\ cm^2$ of area), we obtain a 'real' potential of ca. $-1\ V\ vs.\ RHE$.

$$V\ vs.\ RHE = V\ vs.\ Ag|AgCl|KCl_{3M} + E^{3\ M\ \mathrm{Cl}^-}_{Ag|AgCl}(V) + pH * 59.1 * 10^{-3}(V) \quad \text{(A.1)}$$

$$V_{real} = V_{applied} - i(A) * R_u(\Omega) \quad \text{(A.2)}$$

A.1.4. Cleaning

Organic and metallic contaminants were removed from the cell body by submerging in acidified ($0.5\ M$ H_2SO_4, Ph. Eur, Merck) permanganate solution ($1\ g \cdot L^{-1}$ $KMnO_4$, Baker Chemicals) for a minimum of $12\ h$, which was rinsed with dilute piranha solution followed by thorough rinsing with Milli-Q water prior to use. The upper compartment housing the electrode compartments were cleaned by storing in Milli-Q water and rinsing them prior to use. All parts of the cell in direct contact with electrolyte were made of various chemically inert polymers (PTFE, PEEK or Kel-F), to prevent metal ion leaching by the highly alkaline electrolyte.

A.1.5. Product analysis

The gaseous cell exhaust was sampled at regular intervals ($1\ to\ 6\ times/hr$) via gas chromatography, with the sampling frequency depending on reactant gas inflow ($15-150\ mL_n \cdot min^{-1}$) with lower flows (and less frequent sampling intervals) being used for experiments that necessitated longer reaction times (i.e. lower currents). The addition of a known flow of inert gas (nitrogen) was used as an internal standard to calculate the flows of the individual components. After each experiment, a liquid sample was taken from the catholyte and analyzed via NMR with DMSO as an internal standard similar to the procedure as described by Kuhl et al.[3]

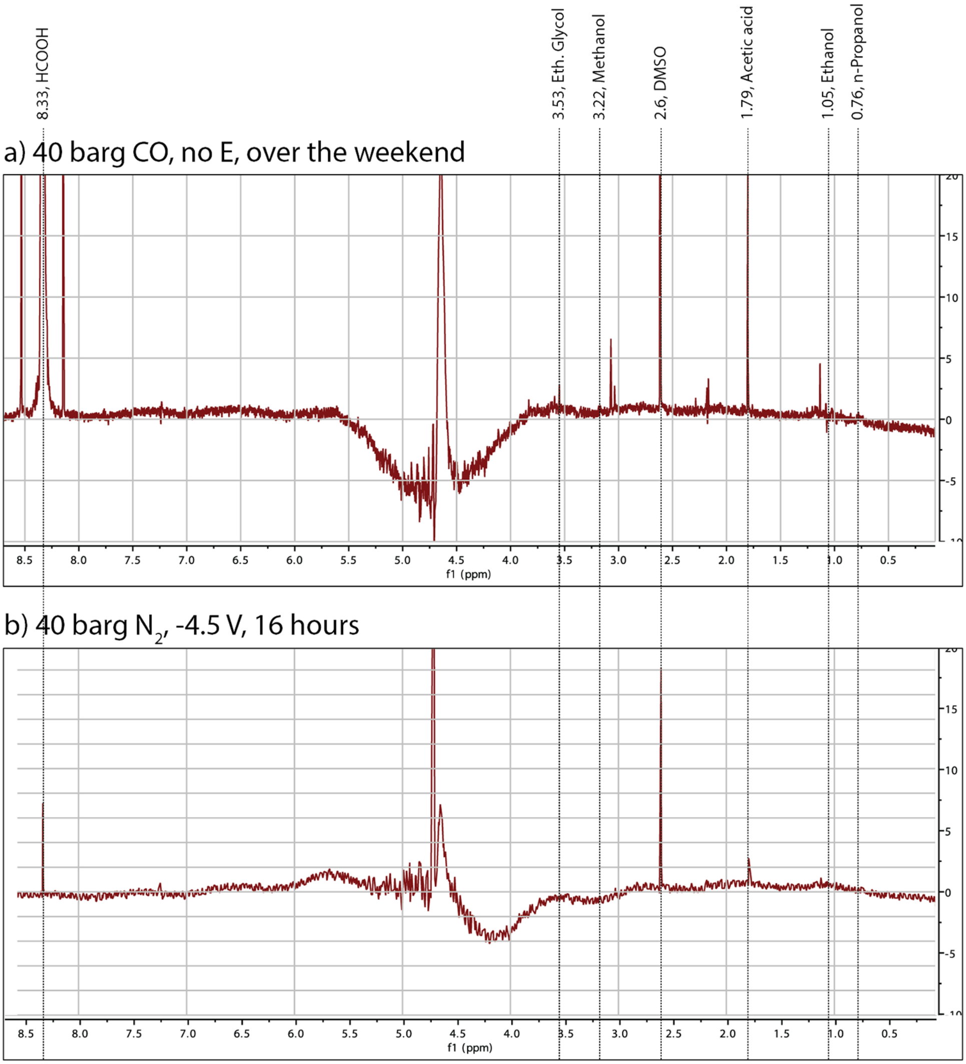

Figure A.2: NMR spectra control experiments.

A.2. Control experiments to verify product origin

Two measurements were performed so as to verify that the origin of products is electrochemical in nature, with the electrolyte composition investigated via NMR for products (Figure A.2). Firstly, the reactor was set up identically as discussed previously and pressurized to $40\ barg$ of CO, including continuous gas flow. However, no potential was applied to the WE. This condition was kept for $> 60\ hours$, and the 'electrolyte' was analyzed for products (Figure A.2a). In this instance, two liquid (and no gaseous) products discussed in the main text were observed: formic acid and acetic acid. Formic acid formation from CO + OH^- has been addressed in the main text, but the fact that we see acetic acid is peculiar. Although its formation rate is much below what we observe in the presence of an applied potential (it is about 35% of the lowest formation rate detected in this work i.e., for $10\ barg$ of CO at $-2\ V$), one would not expect its formation at all in absence of an applied potential. This trace of acetic acid may originate from a reaction between CH_4 and CO_2.[4] Carbon dioxide will be present in minor quantities due to the reverse water-gas shift reaction ($CO + H_2O \rightleftharpoons CO_2 + H_2$), whilst methane is present as an impurity in the CO gas (and we also observe in the GC). Although this reaction is unfavorable, and the quantities of required reactants are low, it may serve as an explanation for the trace of acetic acid we observe, even in the absence of an applied potential.

As for the second control experiment, we applied $-4.5\ V$ under $40\ barg$ of N_2. In this instance, no appreciable quantities of any kind of product other than hydrogen were observed (although a small spike representing formic acid can be seen, likely originating from traces of CO left in the dead spots of the system as we also found from GC, but its concentration is insignificant).

A.3. Formation rates for non-CORR products

The observed formation rates for H_2 and HCOOH are depicted in Figure A.3.

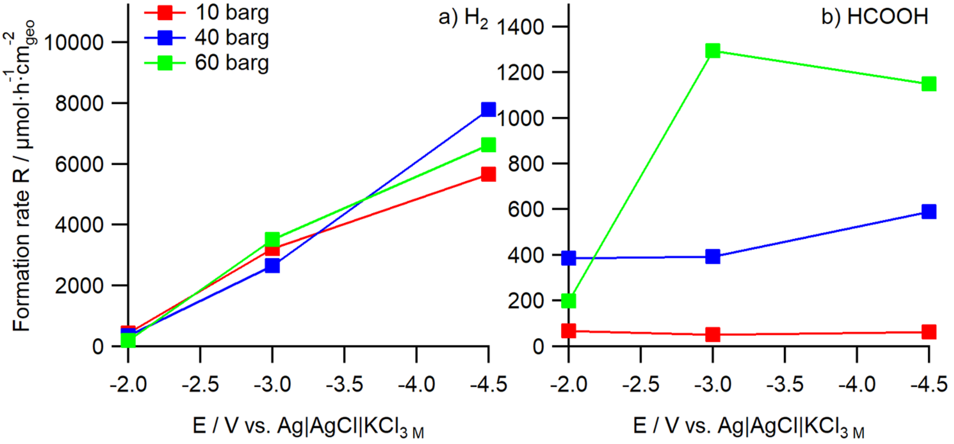

Figure A.3: Area-normalized formation rates for non-CORR products.

A.4. Electrochemical response of the system

Partial current densities for the CORR-related products discussed in the main text are depicted in Figure A.4, and the partial current density for hydrogen is shown in Figure A.5. Beware of the difference in scale between the two figures (μA vs mA for Figures A.4 and A.5, respectively). Total system current densities for the various investigated conditions are depicted in Figure A.6.

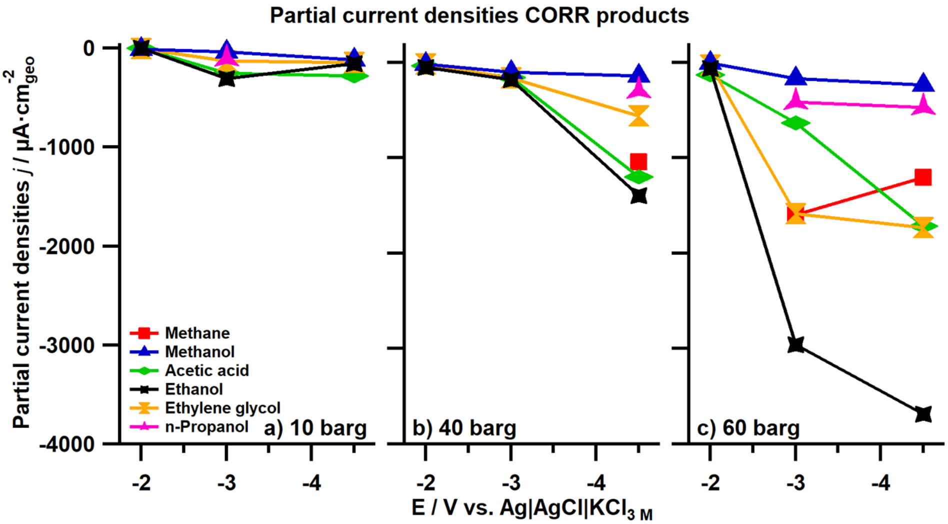

Figure A.4: Partial-current density equivalent plot of Figure 2.1 in the main text.

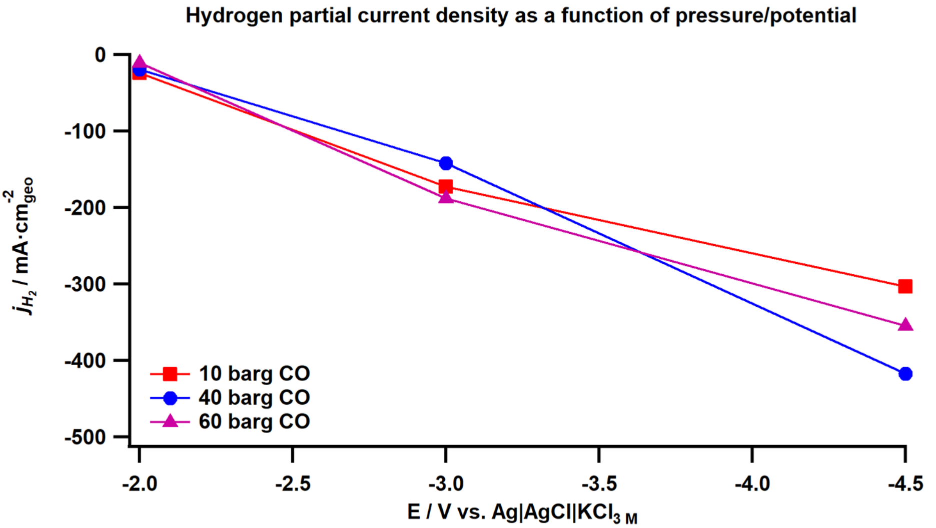

Figure A.5: Pressure-dependent partial current density of hydrogen.

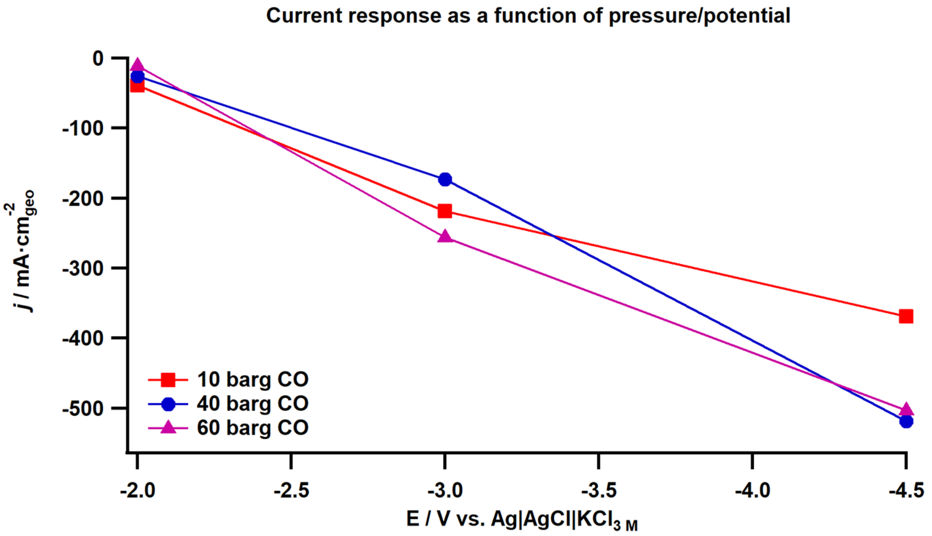

Figure A.6: Total current densities for the various investigated conditions.

Faradaic efficiencies for the measurements discussed in the main text are provided in Table A.1. Two main points stand out. Firstly, CORR products are the minority species, which is reflected in low faradaic efficiency values for these products. Secondly, not all current in the system is accounted for. The latter we explain by the fact that our reactor at the time of measuring did not have a perfect seal (an issue that has since been addressed), allowing part of the hydrogen to escape the system. Considering that hydrogen accounts for the vast majority of the current, a loss of hydrogen (as it is very fugacious) through to a small leak in the system has large repercussions for the total faradaic efficiency. However, this issue is expected to have little to no influence on the identities and quantities of solution-phase products, as they are not meaningfully present in the gas phase due to their lower vapor pressure, and therefore should not significantly influence our discussion. Regarding methane, which would be affected, it is only sporadically observed (to rise above the always present baseline due to trace impurities in the CO bottle) and due to this does not match any trend, even if there is a larger error bar for those instances where it is observed.

Table A.1: Faradaic efficiencies of observed reaction products during CORR on Ag.

Faradaic efficiencies (%):

		Ethylene glycol	MeOH	Acetic acid	EtOH	n-PrOH	H_2	CH_4	Sum
10 barg	-2 V	0.003	0.023	0.001	0.002	0.000	60.960	0.000	60.990
	-3 V	0.058	0.017	0.116	0.139	0.049	79.078	0.000	79.457
	-4.5 V	0.039	0.032	0.076	0.042	0.000	82.287	0.000	82.476
40 barg	-2 V	0.077	0.074	0.135	0.203	0.000	73.742	0.000	74.231
	-3 V	0.094	0.059	0.092	0.104	0.000	82.092	0.000	82.442
	-4.5 V	0.108	0.027	0.231	0.270	0.057	80.544	0.201	81.439
60 barg	-2 V	0.283	0.051	1.175	0.584	0.000	96.618	0.000	98.710
	-3 V	0.620	0.066	0.247	1.154	0.161	73.374	0.623	76.246
	-4.5 V	0.345	0.047	0.341	0.732	0.094	70.505	0.239	72.303

A.5. Summarized literature-reported C-C bond formation mechanisms

Reaction schemes summarizing the various proposed formation pathways for C2 and C3 products (in A3 format) are provided at the very end of the supporting information. Subsets of mechanisms proposed by the same groups have been combined into single schemes using color coding to distinguish separate publications. Different reaction mechanisms are indicated by different letters (going from A to J), combined with either -C2 or -C3 to denote if a proposed pathway leads to C2 or C3 products. Mechanisms with the same lettering are proposed by the same group(s) of people (e.g., A-C2 and A-C3 would represent the mechanism by which C2 and C3 products are formed, respectively, as proposed by the same group). References to the various publications are provided in the individual schemes, together with the color coding used for each scheme (i.e., which color belongs to which reference). Proposed reaction schemes that are similar in nature (e.g., having similar types of intermediates, overlapping steps etc.) have been grouped together as follows for C2 formation schemes: A-B, C-E, F-H, and I. The proposed mechanism J-C3 does not have a corresponding C2 mechanism, though they refer to the work represented by the mechanisms A-C2 and A-C3.

[this page has been left blank intentionally for the digital edition]

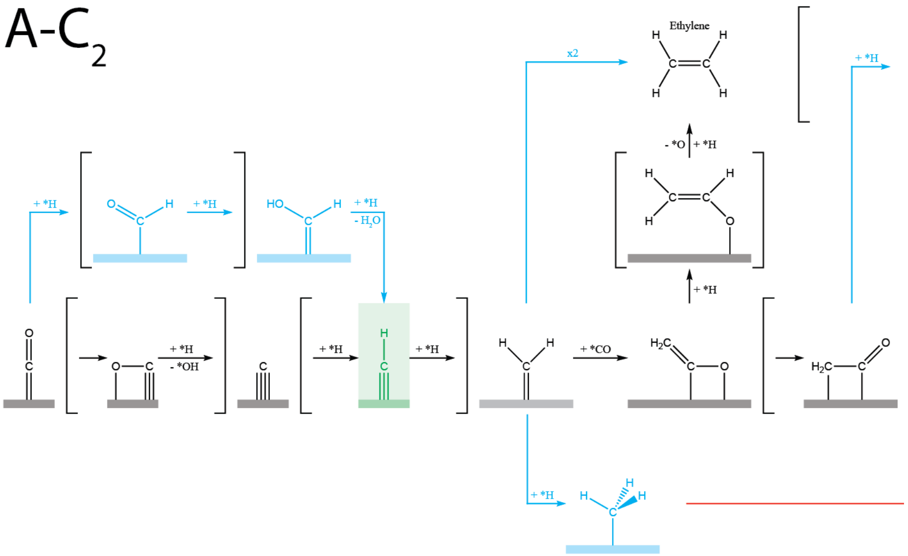
A-C_2

🟦 Blue Cu(poly): Hori, Y. (Takahashi, R.), Formation of hydrocarbons in the electrochemical reduction of carbon dioxide at a copper elec-

🟥 Red Cu(100) terraces with (110) steps: Wang, X. (Strasser, P), Morphology and mechanism of highly selective Cu(II) oxide nanosheet

🟩 Green Cu(poly): Ikeda, S. (Noda, H.), Electrochemical Mass Reduction of Carbon Dioxide using Cu-Loaded Gas Diffusion Electrodes II.

Black Cu(poly): Hori, Y. (Murata, A.), Electrochemical Reduction of CO at a Copper Electrode. J Phys Chem B 1997, 101 (36), 7075-7081.

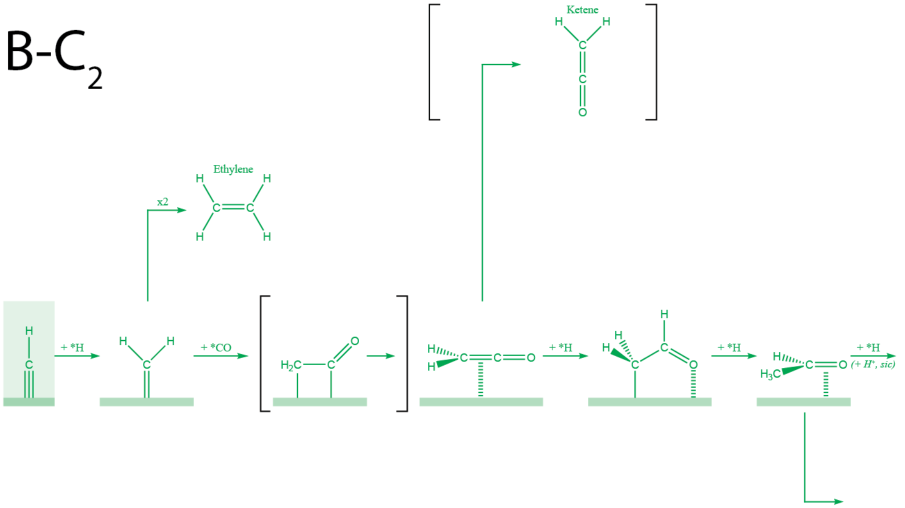
B-C_2

Figure A.7: Left-half

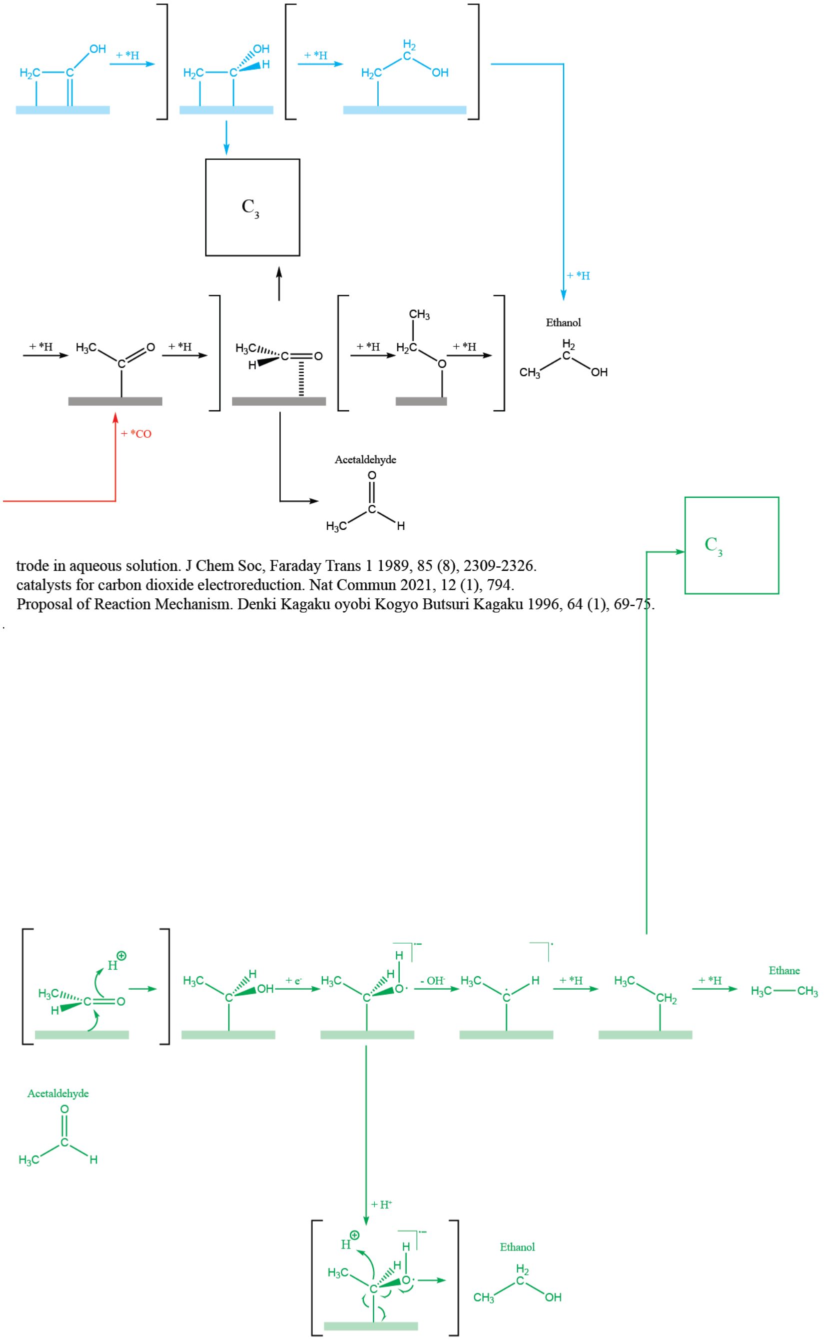

trode in aqueous solution. J Chem Soc, Faraday Trans 1 1989, 85 (8), 2309-2326.
catalysts for carbon dioxide electroreduction. Nat Commun 2021, 12 (1), 794.
Proposal of Reaction Mechanism. Denki Kagaku oyobi Kogyo Butsuri Kagaku 1996, 64 (1), 69-75.

Figure A.7: Right-half

C-C$_2$

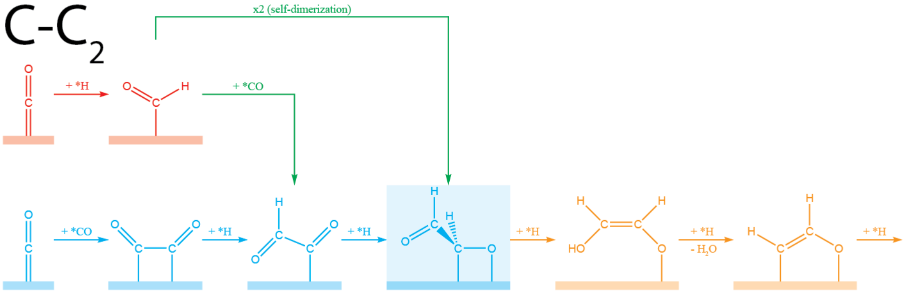

Orange	Cu(211): Bertheussen, E. (Chorkendorff, I), Acetaldehyde as an Intermediate in the Electroreduction of Carbon Monoxide to Ethanol on
Red	Cu(211): Peterson, A. A. (Nørskov, J. K.), How copper catalyzes the electroreduction of carbon dioxide into hydrocarbon fuels. Energy
Green	Cu(211): Montoya, J. H. (Nørskov, J. K.), Insights into C-C Coupling in CO2 Electroreduction on Copper Electrodes. ChemCatChem
Blue	Cu(100) & Cu(111): Montoya, J. H. (Nørskov, J. K.), Theoretical Insights into a CO Dimerization Mechanism in CO2 Electroreduction. J
Black	Cu(poly): Kuhl, K. P. (Jaramillo, T. F.), New insights into the electrochemical reduction of carbon dioxide on metallic copper surfaces.

D-C$_2$

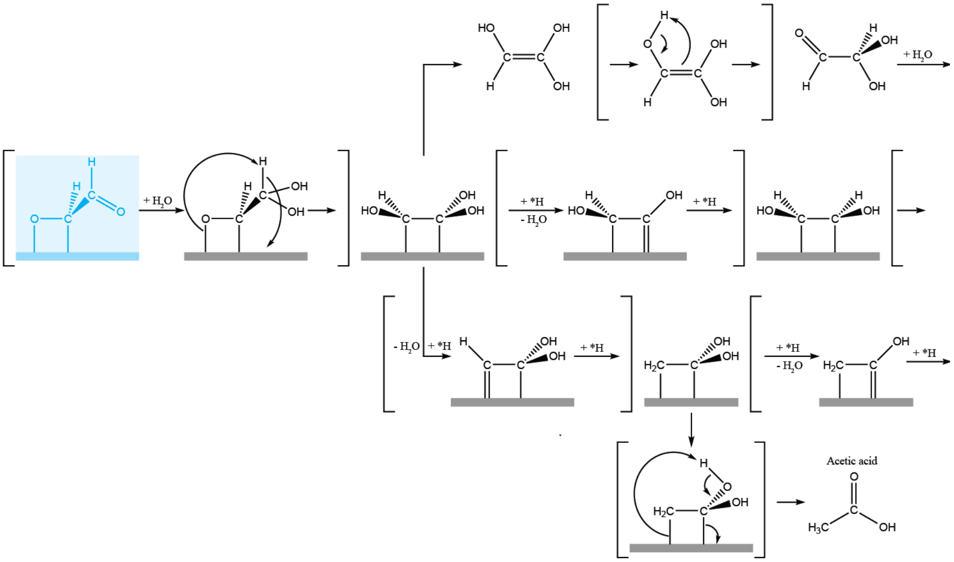

Figure A.8: Left-half

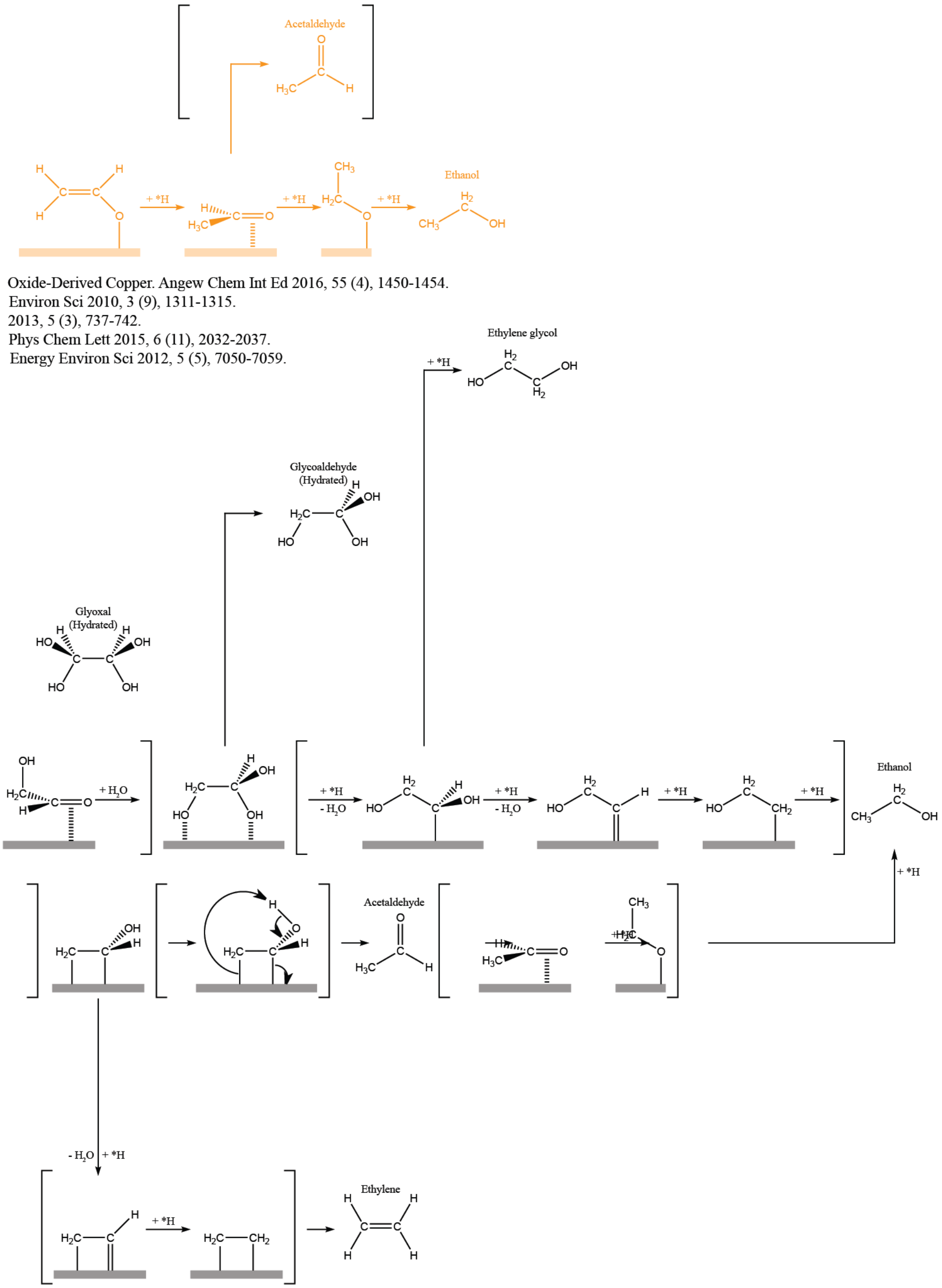

Oxide-Derived Copper. Angew Chem Int Ed 2016, 55 (4), 1450-1454.
Environ Sci 2010, 3 (9), 1311-1315.
2013, 5 (3), 737-742.
Phys Chem Lett 2015, 6 (11), 2032-2037.
Energy Environ Sci 2012, 5 (5), 7050-7059.

Figure A.8: Right-half

E-C_2

Blue Cu(poly): Kuhl, K. P. (Jaramillo, T. F.), New insights into the electrochemical reduction of carbon dioxide on metal-
Black Cu(poly): Shah, A. H. (He, T.), Revisiting Electrochemical Reduction of CO2 on Cu Electrode: Where Do We Stand

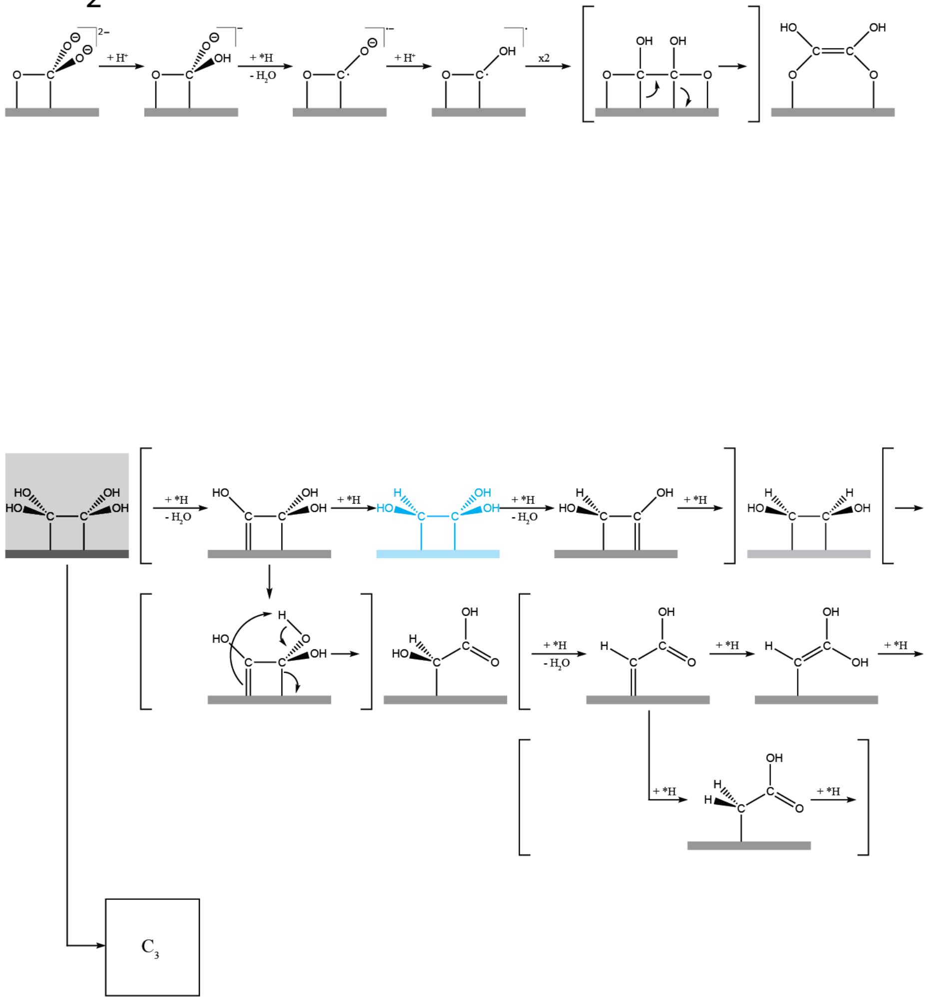

Figure A.9: Left-half

lic copper surfaces. Energy Environ Sci 2012, 5 (5), 7050-7059.
about the Intermediates? J Phys Chem C 2018, 122 (32), 18528-18536.

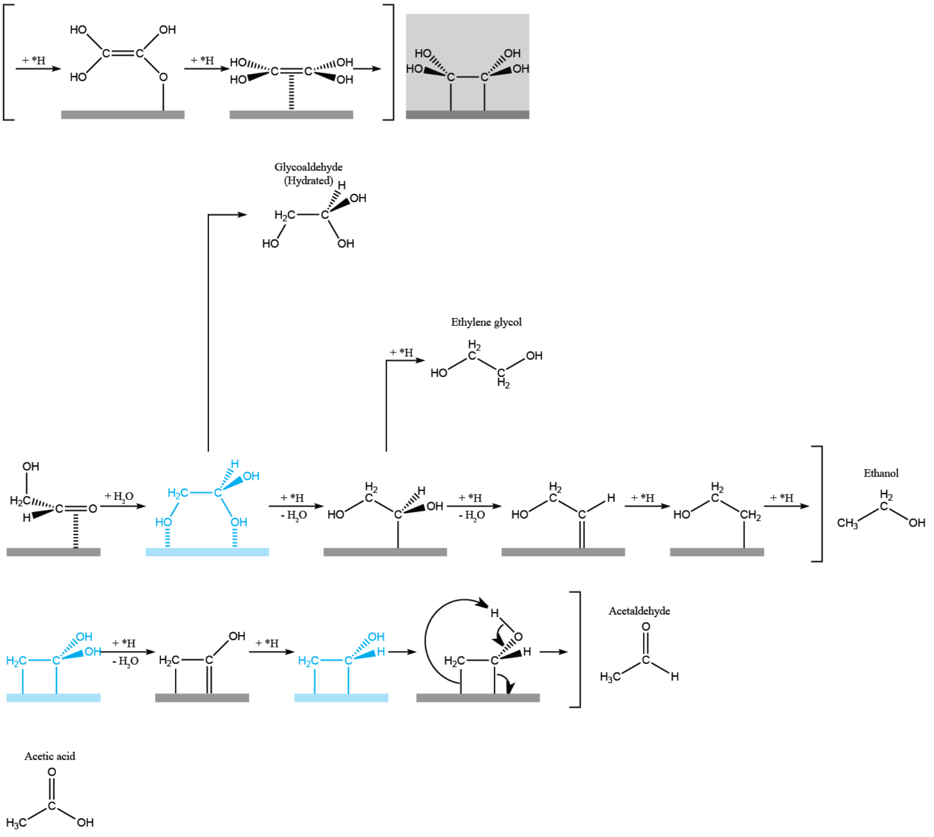

Figure A.9: Right-half

F-C_2

Green	Cu(100): Calle-Vallejo, F. (Koper, M. T. M.), Theoretical Considerations on the Electroreduction of CO to C2
Red	Ag, Cu & Au(100): Hanselman, S. (Calle-Vallejo, F.), Computational Comparison of Late Transition Metal (100)
Blue	Cu(211): Liu, X. (Chan, K), pH effects on the electrochemical reduction of CO(2) towards C2 products on step-

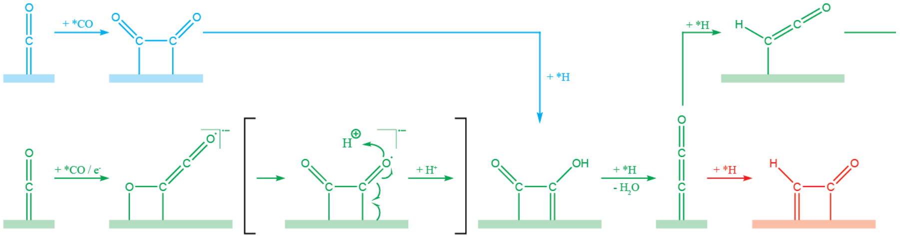

G-C_2

Black	Cu(100): Luo, W. (Asthagiri, A.), Facet Dependence of CO2 Reduction Paths on Cu Electrodes. ACS Catal 2016,
Orange	Cu(111): Nie, X. (Asthagiri, A.), Reaction mechanisms of CO2 electrochemical reduction on Cu(1 1 1) deter-

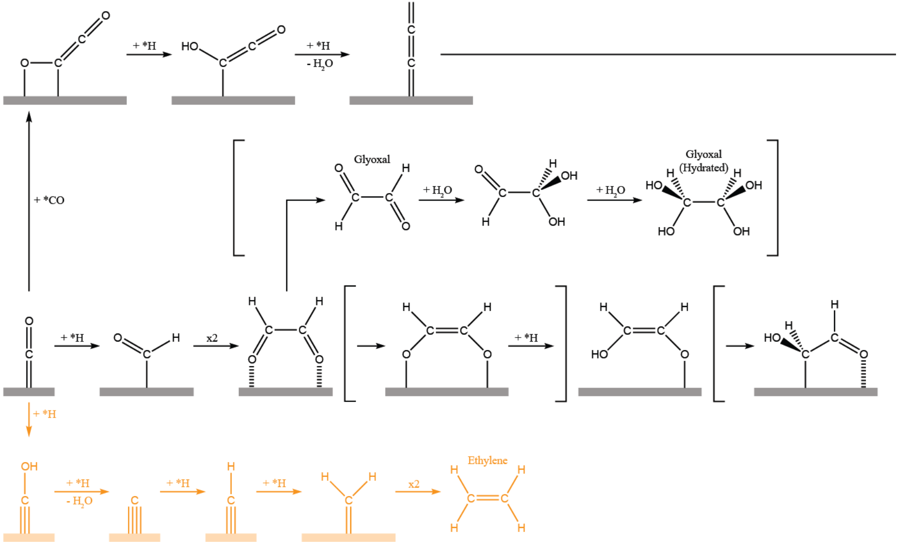

Figure A.10: Left-half

Species on Cu(100) Electrodes. Angew Chem Int Ed 2013, 52 (28), 7282-7285.
Surfaces for the Electrocatalytic Reduction of CO to C2 Species. ACS Energy Letters 2018, 3 (5), 1062-1067.
ped copper. Nat Commun 2019, 10 (1), 32.

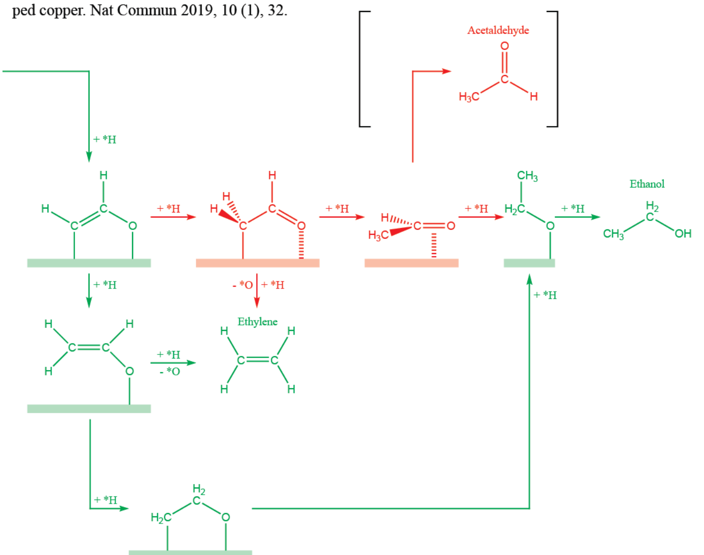

6 (1), 219-229.
mined with density functional theory. J Catal 2014, 312, 108-122.

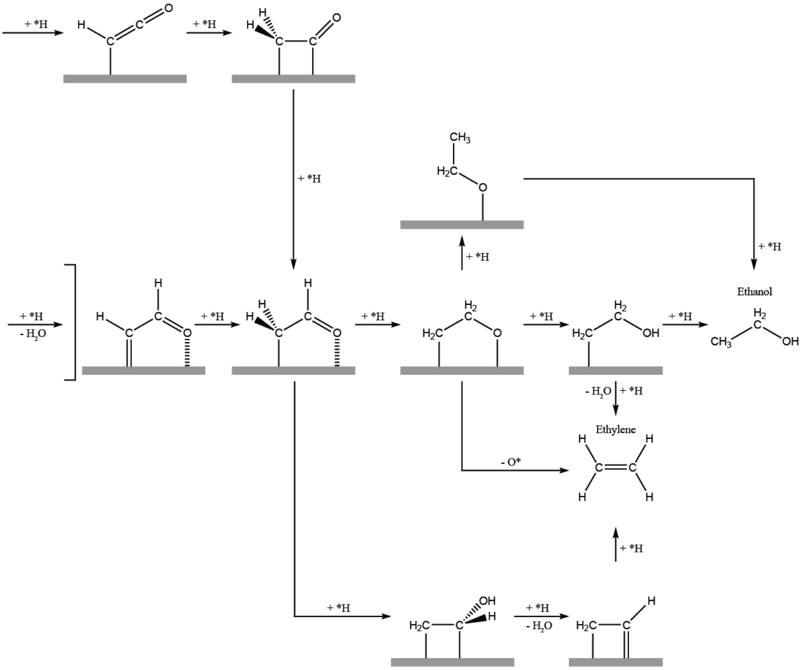

Figure A.10: Right-half

H-C_2

Black Cu(100): Garza, A. J.; Bell, A. T.; Head-Gordon, M., Mechanism of CO2 Reduction at Copper Surfaces: Path-

Red Only Cu(100) and only at low overpotential

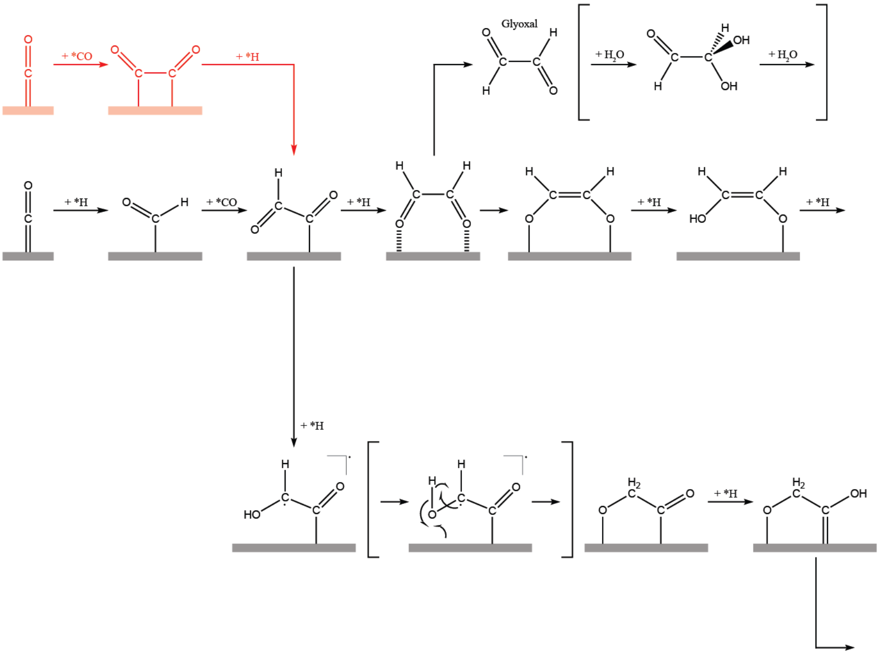

Figure A.11: Left-half

ways to C2 Products. ACS Catal 2018, 8 (2), 1490-1499.

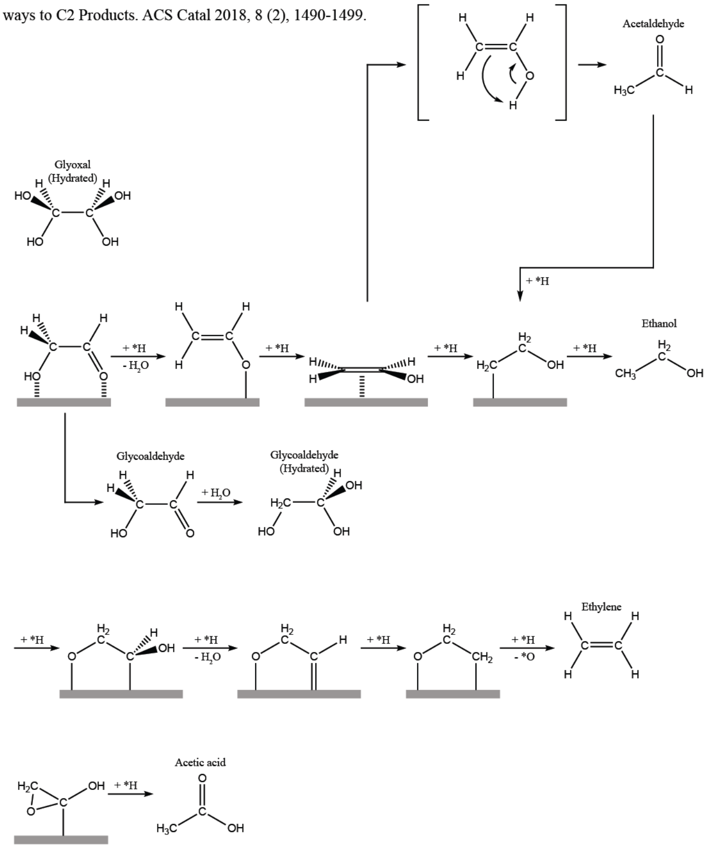

Figure A.11: Right-half

i-C$_2$

Red Cu(100): Cheng, T. (Goddard, W. A.), Full atomistic reaction mechanism with kinetics for CO reduction on Cu(100) from ab
Blue Cu(100): Lum, Y. (Ager, J. W.), Electrochemical CO Reduction Builds Solvent Water into Oxygenate Products. J Am Chem
Black Cu(100): Xiao, H. (Goddard, W. A.), Atomistic Mechanisms Underlying Selectivities in C1 and C2 Products from Electro-

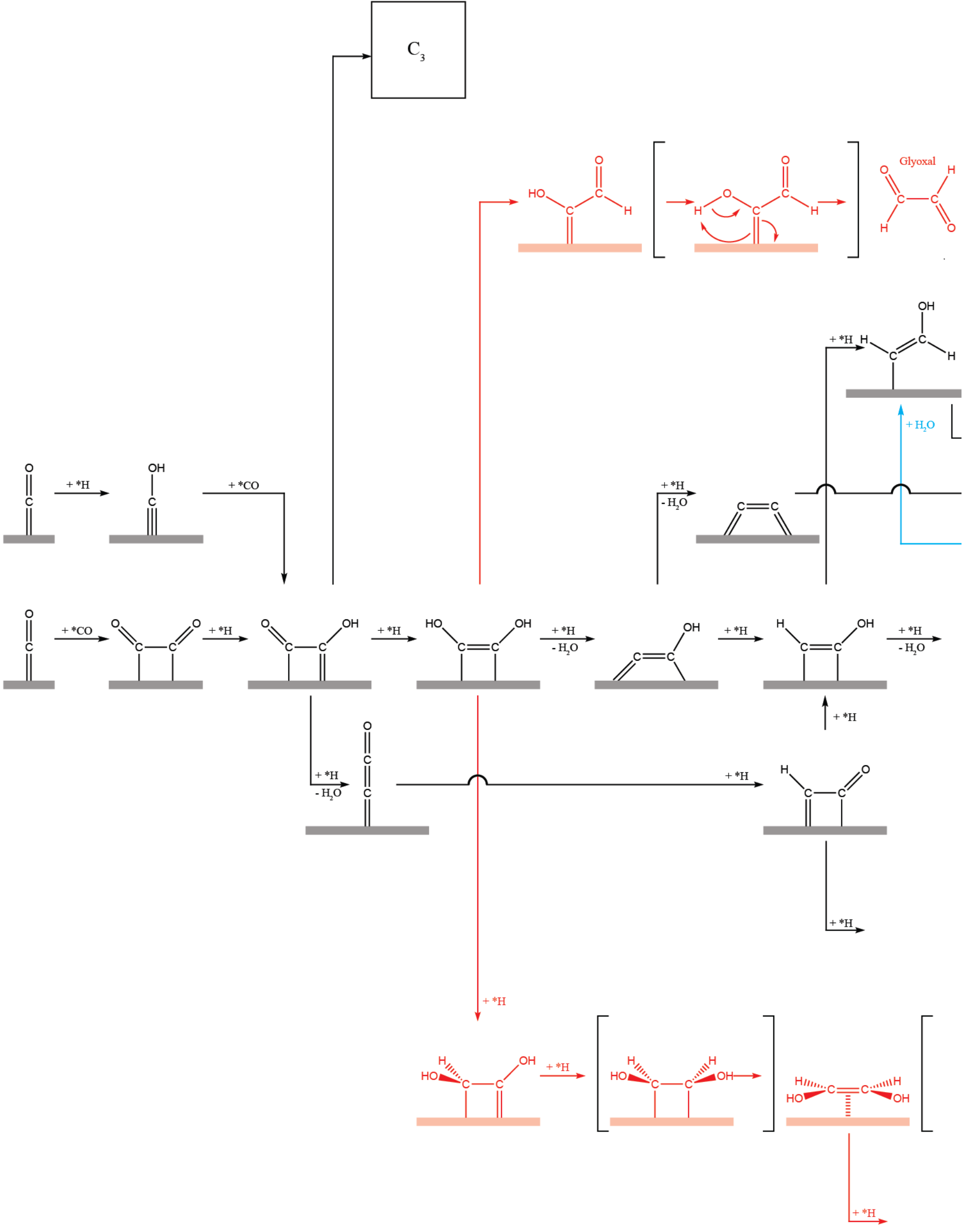

Figure A.12: Left-half

initio molecular dynamics free-energy calculations at 298 K. PNAS 2017, 114 (8), 1795-1800.
Soc 2018, 140 (30), 9337-9340.
chemical Reduction of CO on Cu(111). J Am Chem Soc 2017, 139 (1), 130-136.

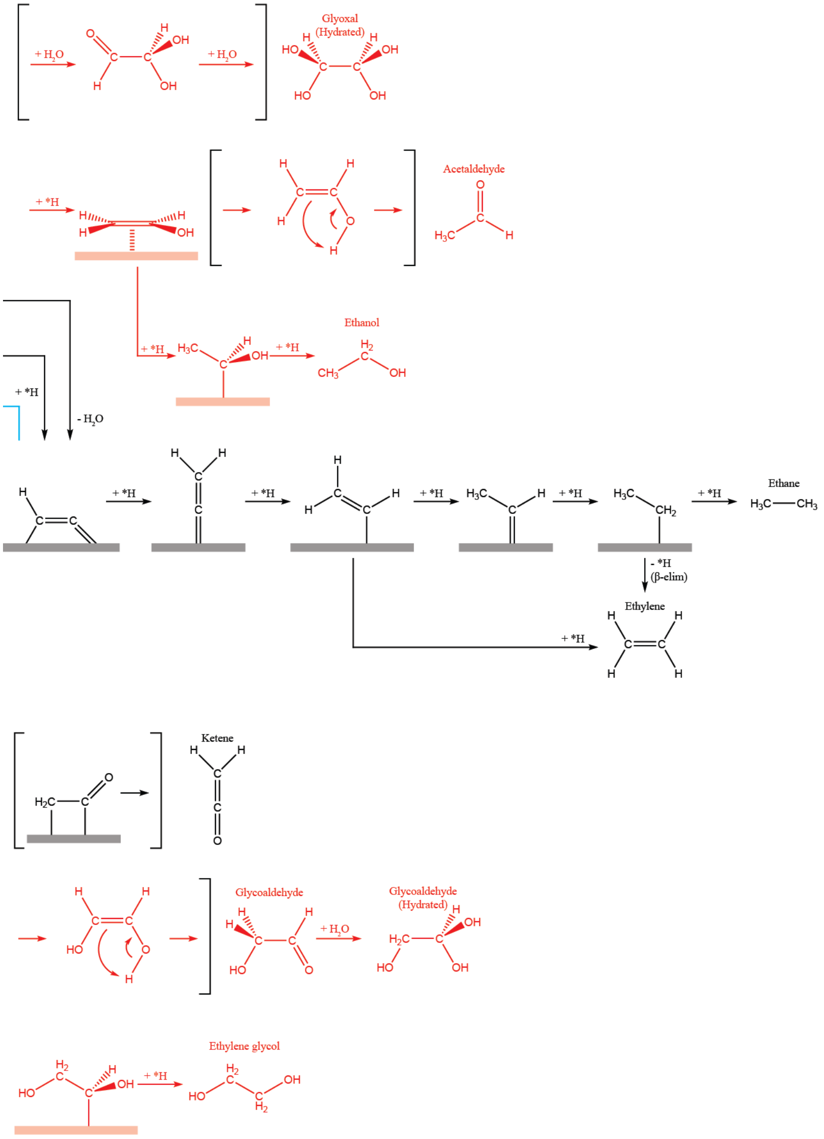

Figure A.12: Right-half

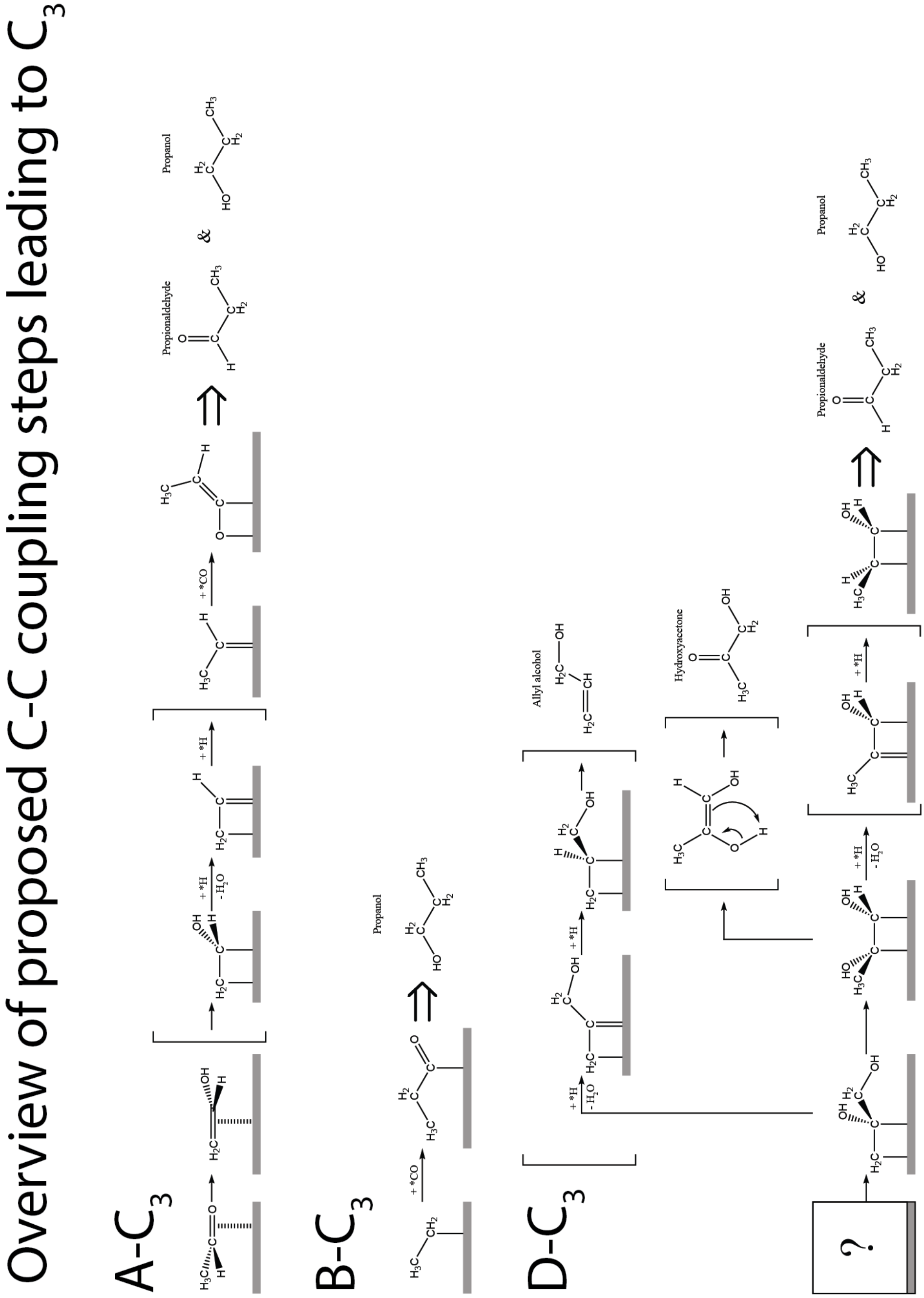

Figure A.13: Top-half

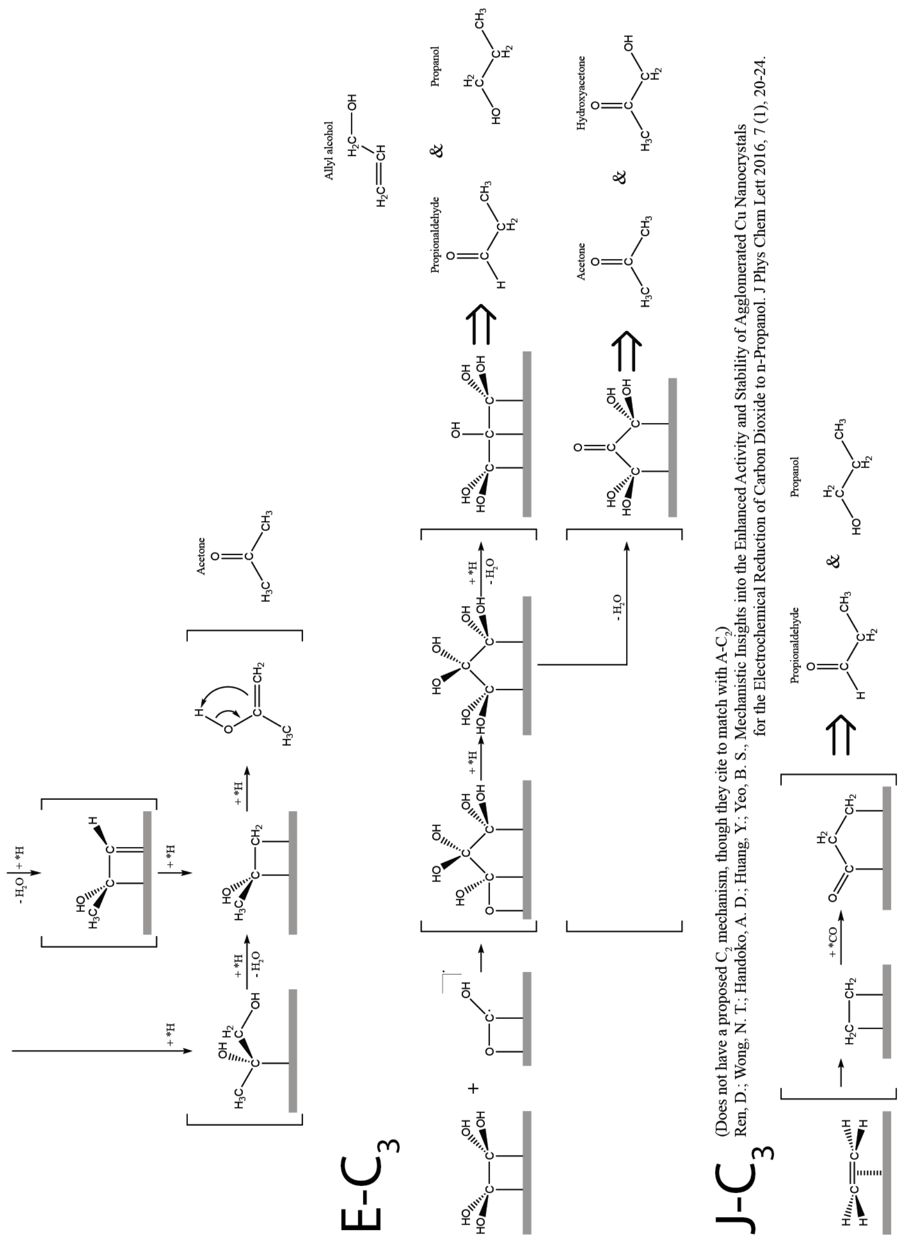

(Does not have a proposed C_2 mechanism, though they cite to match with A-C_2)
Ren, D.; Wong, N. T.; Handoko, A. D.; Huang, Y.; Yeo, B. S., Mechanistic Insights into the Enhanced Activity and Stability of Agglomerated Cu Nanocrystals for the Electrochemical Reduction of Carbon Dioxide to n-Propanol. J Phys Chem Lett 2016, 7 (1), 20-24.

Figure A.13: Bottom-half

References

[1] Rebecca Barlag, Frazier Nyasulu, Rachel Starr, Jenna Silverman, Phyllis Arthasery, and Lauren McMills. A student-made silver–silver chloride reference electrode for the general chemistry laboratory: ~10 min preparation. *Journal of Chemical Education*, 91(5):766–768, 2014.

[2] Gaston A. East and M. A. del Valle. Easy-to-make Ag/AgCl reference electrode. *Journal of Chemical Education*, 77(1):97, 2000.

[3] Kendra P. Kuhl, Etosha R. Cave, David N. Abram, and Thomas F. Jaramillo. New insights into the electrochemical reduction of carbon dioxide on metallic copper surfaces. *Energy & Environmental Science*, 5(5):7050–7059, 2012.

[4] Esther M. Wilcox, George W. Roberts, and James J. Spivey. Direct catalytic formation of acetic acid from CO2 and methane. *Catalysis Today*, 88(1):83–90, 2003.

B

Supporting information for Chapter 3: Anisotropic Cathodic Corrosion of Gold Electrodes in Absence and Presence of Carbon Monoxide

B.1. SEM-visible onset of corrosion for {111} and {110} faces

The observable onset of corrosion for the {111} and {110} facets as visible from SEM micrographs is depicted in Figure B.1, where panels a, b represent micrographs for the {111} face prior to (no crystallites observed) and after (crystallites visible) the onset of corrosion, respectively, and panels c, d show the {110} face without pitting and with pitting (the corrosion mode for that face), respectively.

B.2. Substrate pitting of {111} and {100} faces from SEM

Although the main corrosion mode for the {111} and {100} facets is in the form of crystallite growth, the initial substrate does exhibit a certain degree of pitting as well. This is evident from Figure B.2, where panels a, b depict close-ups of the substrate beneath the crystallites for the {111} and {100} faces, respectively.

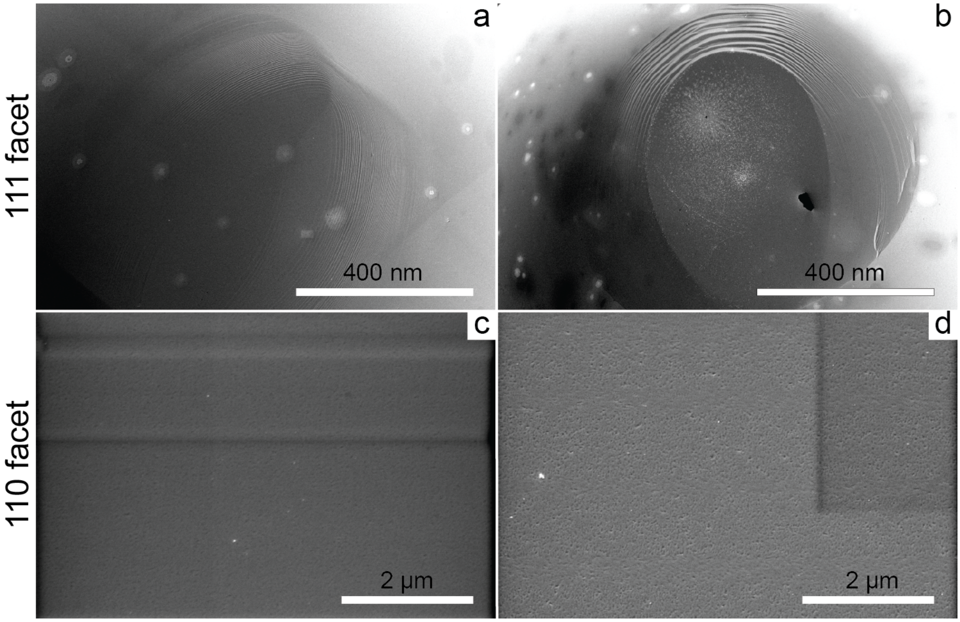

Figure B.1: Onset of corrosion-induced morphological changes as visible from SEM for the {111} facet corroded for a) 5 $minutes$ at –1.2 V_{RHE} and for b) 7.5 $minutes$ at –1.2 V_{RHE}, and for the {110} facet corroded for c) 2.5 $minutes$ at –1.1 V_{RHE} and for d) 5 $minutes$ at –1.1 V_{RHE}.

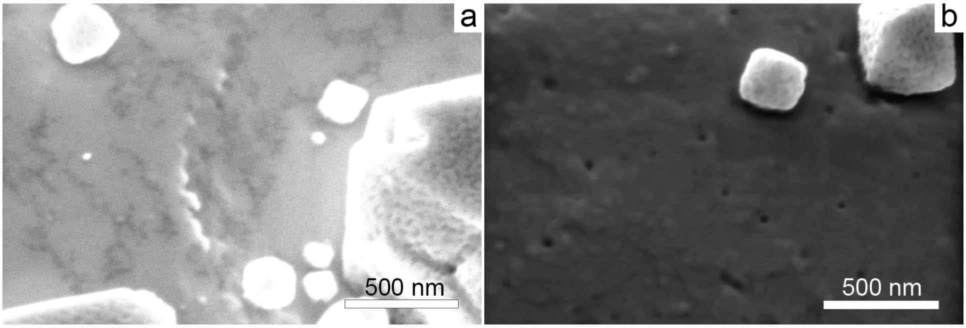

Figure B.2: Corrosion of initial substrate on which nanocrystallites grow for a) the {111} plane corroded for 7.5 $minutes$ at –1.3 V_{RHE} and b) the {100} plane corroded for 7.5 $minutes$ at –1.3 V_{RHE}.

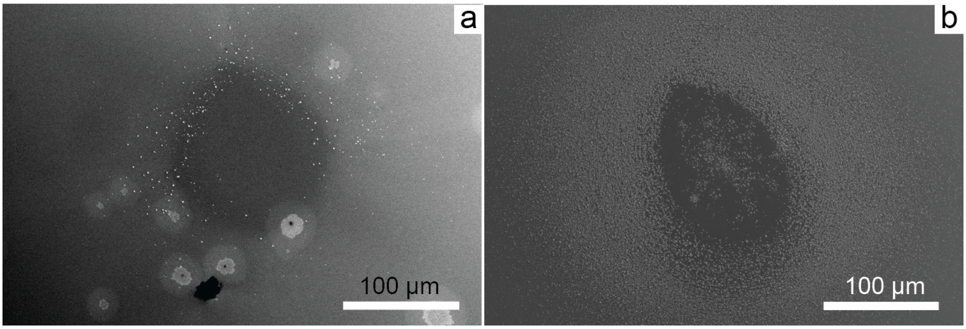

Figure B.3: Location of nanocrystallite formation on the {100} face at the early stages of corrosion after a) $2.5\ minutes$ at $-1.3\ V_{RHE}$ and for longer corrosion times; i.e., for b) $5\ minutes$ at $-1.3\ V_{RHE}$.

B.3. Onset location crystallites {100} face

Although corrosion of the {100} face results in crystallite formation on and near this face, growth starts from the edges of this face at the onset of corrosion as depicted in Figure B.3 where in panel a is shown a micrograph obtained near the observed onset of crystallite formation and is compared to corrosion for extended time in panel b. It can be seen that initially crystallites form at the edges of the facet, whereas for longer corrosion times crystallites form also on the actual {100} face.

B.4. Absence of crystallite formation during extended corrosion at decreased cathodic potential

Proof that crystallite formation is not the result of dissolution and redeposition of the counter electrode is provided in the form of long-term corrosion at (slightly) decreased cathodic potentials in Figure B.4. This is evident from the global overview of a spherical single crystal when $-1\ V_{RHE}$ is applied for $1.5\ hours$ in the presence of CO. Although considerable contamination is present (in the form of white 'blobs'), no crystallites were observed on this surface.

B.5. Imperfect double layer signals for cut Au crystals

The double layer signals for the (cut) single crystalline surfaces we employ in this work (Figure B.5) differ from established literature for the single crystalline gold basal planes (although the important features are present).[1–6] We attribute the deviations with respect to specifically the double layer region to mainly two points. Firstly; the crystals used herein started off with a certain fraction of defect sites which affects average terrace sizes and adds new types of adsorption sites and, secondly; minute traces of oxygen were present in the electrolyte during some of

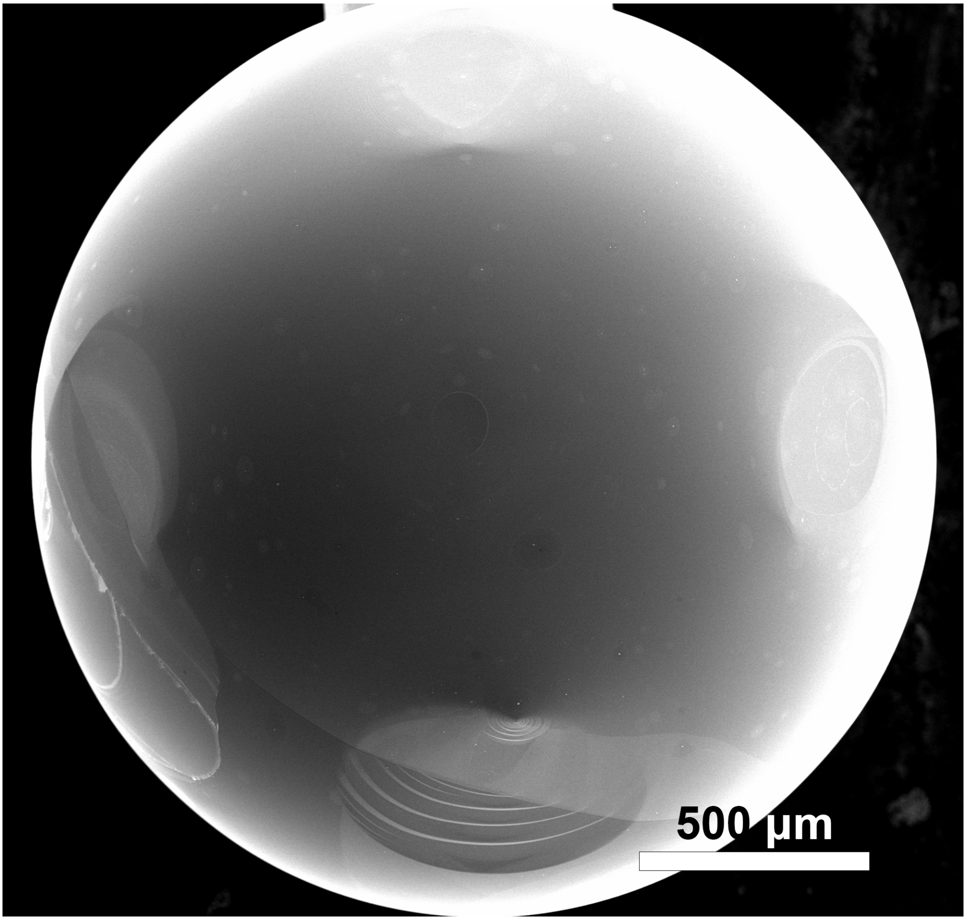

Figure B.4: Overview of a gold spherical single crystal after corrosion for 1.5 $hours$ at -1 V_{RHE} in the presence of CO.

the measurements. Additionally, the scan rate employed in this work ($80\ mV{\cdot}s^{-1}$) is also different from what is commonly used in double layer investigations ($10\ mV{\cdot}s^{-1}$) which influences charging currents. Finally, an imperfect meniscus, which would expose a small fraction of the sides of the crystal, may also result in the behavior of the double layer observed. The presence of defect sites is seen also in the gold oxide region, evident from current in the potential regions attributed to step-sites as described in Table 3.1 (main text). To the best of our knowledge, there exists no literature that systematically investigates the changes of the double-layer region when step-site defects are introduced. Irrespectively, as can clearly be seen from the hydroxide/oxide adsorption regions as shown in this work, the majority feature for the differently cut single crystals matches the feature that is attributed to the respective basal planes.

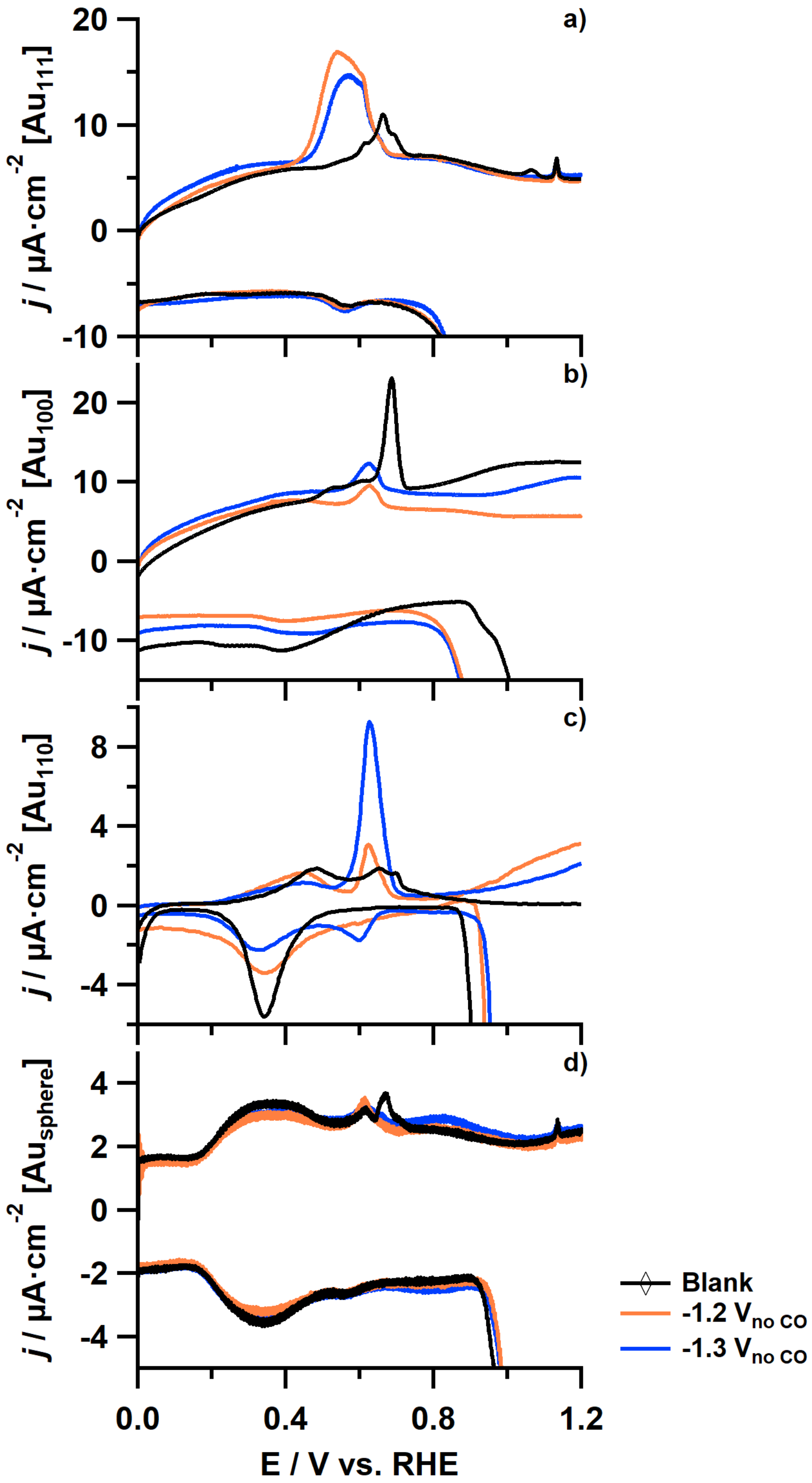

Figure B.5: Zoom of the CV DL region for gold crystals corroded in $10\ M$ NaOH for $2.5\ minutes$ in the absence (solid lines) and presence (dashed lines) of CO at $-1.2\ V_{RHE}$ (orange) and $-1.3\ V_{RHE}$ (blue) (85% iR corrected) for a) Au(111), b) Au(100), c) Au(110) and d) Au(spherical) electrodes, compared with their respective CVs prior to corrosion (black).

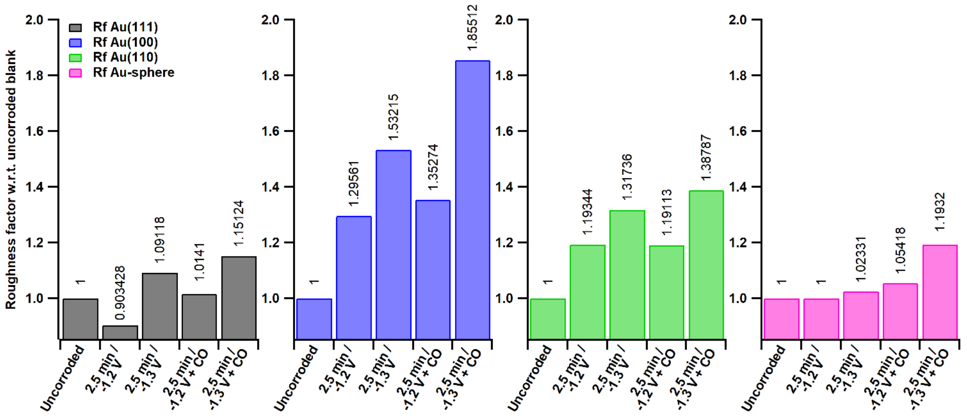

Figure B.6: Roughness factors for crystals with different crystallographic orientations (Au(111), black bars; Au(100), blue bars; Au(110), green bars; Au(sphere), pink bars) before and after cathodic corrosion in $10\ M$ NaOH for $2.5\ minutes$ at -1.2 and $-1.3\ V_{RHE}$, in the absence and presence of CO (going from left to right).

B.6. Crystal roughness determination

Roughness factors after corrosion (see Figure B.6) were determined by integrating the oxidation current in the CV obtained after corrosion at potentials more positive than $0.9\ V$ vs. RHE after subtraction of the double layer current, and dividing this charge by the charge that was similarly calculated from the CV obtained prior to corrosion. The double layer current was determined either mathematically via eq. B.1 for CVs that exhibited a symmetrical double layer region between $0 < E < 0.15\ V$ vs. RHE, or otherwise by manually shifting the CV down whilst carefully considering that the oxidation current in the region between $0.9 < E < 1.3\ V$ vs. RHE didn't fall below zero.

$$i_{DL} = \frac{1}{2} \cdot (\bar{i}_{\text{forward}} - \bar{i}_{\text{backward}}) \text{ between } 0 \leq E \leq 0.15\ V \qquad \text{(B.1)}$$

References

[1] T. H. Dretschkow and T. H. Wandlowski. The kinetics of structural changes in anionic adlayers on stepped Au(111)s electrodes from sulfuric acid solutions. *Berichte der Bunsengesellschaft für physikalische Chemie*, 101(4):749–757, 1997.

[2] Ludwig A. Kibler. *Preparation and characterization of noble metal single crystal electrode surfaces*. International Society of Electrochemistry, 2003.

[3] D. M. Kolb. Reconstruction phenomena at metal-electrolyte interfaces. *Progress in Surface Science*, 51(2):109–173, 1996.

[4] O. M. Magnussen, J. Wiechers, and R. J. Behm. In situ scanning tunneling microscopy observations of the potential-dependent (1 × 2) reconstruction on Au(110) in acidic electrolytes. *Surface Science*, 289(1):139–151, 1993.

[5] H. Striegler, P. Skoluda, and D. M. Kolb. On the stability of unreconstructed Au(100)-(1×1) at negative potentials in aqueous sulfate solution. *Journal of Electroanalytical Chemistry*, 471(1):9–13, 1999.

[6] Koji Yoshida, Akiyoshi Kuzume, Peter Broekmann, Ilya V. Pobelov, and Thomas Wandlowski. Reconstruction and electrochemical oxidation of Au(110) surface in 0.1 M H2SO4. *Electrochimica Acta*, 139:281–288, 2014.

C

Supporting information for Chapter 4: Clean and Reproducible Voltammetry of Copper Single Crystals with Prominent Facet-Specific Features Using Induction Annealing

C.1. Copper cleaning and characterization

Two different cleaning methodologies were employed in this work. The first cleaning method is a commonly employed electropolishing[1–3] treatment, and was conducted on disk-type Cu(poly) electrodes. Briefly, the copper disk was polished with increasingly smaller sizes of alumina polishing paste (Buehler) on polishing cloth (Buehler), starting at $5\ \mu m$ and decreasing down to $1\ \mu m$ on a polishing machine until a shiny finish was obtained. Thereafter, the electrode was rinsed with and subsequently sonicated in Milli-Q water for at least $15\ min$. Finally, the surface was electropolished at $+3\ V$ vs. a graphite CE (99.9995%, metals basis, Alfa Aesar) in $66\ wt\%$ H_3PO_4 prior to electrochemical characterization (described in a later section).

The second cleaning method (used for all other surfaces in this work) is as follows. Copper electrodes were rinsed with Milli-Q water and then placed in an isolated induction annealing compartment with gas inlets and a water-locked gas outlet for controlled-atmosphere annealing. Reductive atmosphere was applied by purging pure H_2 (Linde 5.0) for disk-type single crystals, or a mix of H_2 and Ar of ca. $50 : 50\ vol\%$ for spherical bead-type Cu(poly) crystals, with the total gas flow kept at $300\ sccm$ (standard cubic centimeters per minute) via mass flow controllers. Mixing hydrogen and argon was necessary for spherical bead-type Cu(poly) crystals due to instrument power limitations with the required gas ratio depending on crystal dimensions, but the argon content was kept as low as possible due to the trace oxygen impurities commonly present in argon. The power of the RF-heating instrument was adjusted to fine-tune crystal temperature as judged by the color, with crystals being heated to having an orange-to-yellow glow ($950 \pm 50\ ^{\circ}C$) and kept there for ca. $5\ min$. After annealing, electrodes were quench-cooled in pure hydrogen for ca. $5\ minutes$ (methodology: increase H_2 flow to $1000\ sccm$, halt Ar flow, stop induction current), although cooling time was increased for crystals annealed for longer periods because of increased heating of the surrounding parts. The exact setup is depicted in Figure C.1, which is based on the designs of others as previously reported[4–8], with the key difference being the introduction of a valve that allows for uncoupling the annealing environment from the electrochemical cell.

After the crystal had reached room temperature, an internal pathway from the annealing section (compartment 1, Figure C.1) to the electrochemical cell below (compartment 2, Figure C.1) was established by turning a key with a sufficiently large keyhole to allow for the crystal to pass through. At this point the argon flow through the electrolyte ($0.1\ M$ NaOH) is halted, and instead argon flow is directed to blanket the electrolyte. By opening the key, the annealing compartment and electrochemical cell are now internally connected and thus their initially separate atmospheres can mix; $1000\ sccm$ of H_2 of the annealing compartment (on top) with Ar from the bottom compartment (argon flow was manually adjusted until the electrolyte surface was close to vibrating due to the gas pressure, exact flowrate unknown). Prior to lowering the crystal and closing the electrical circuit, an ‘insertion potential’ was pre-applied. The electrode was lowered through the keyhole, and a meniscus established under electrochemical control. After establishing electrochemical contact, the hydrogen flow in the annealing section is halted and replaced by $1000\ sccm$ of argon. The electrochemical steps and applied potentials vary slightly with the crystallographic orientations of the crystals, and are described in detail in the following subsections.

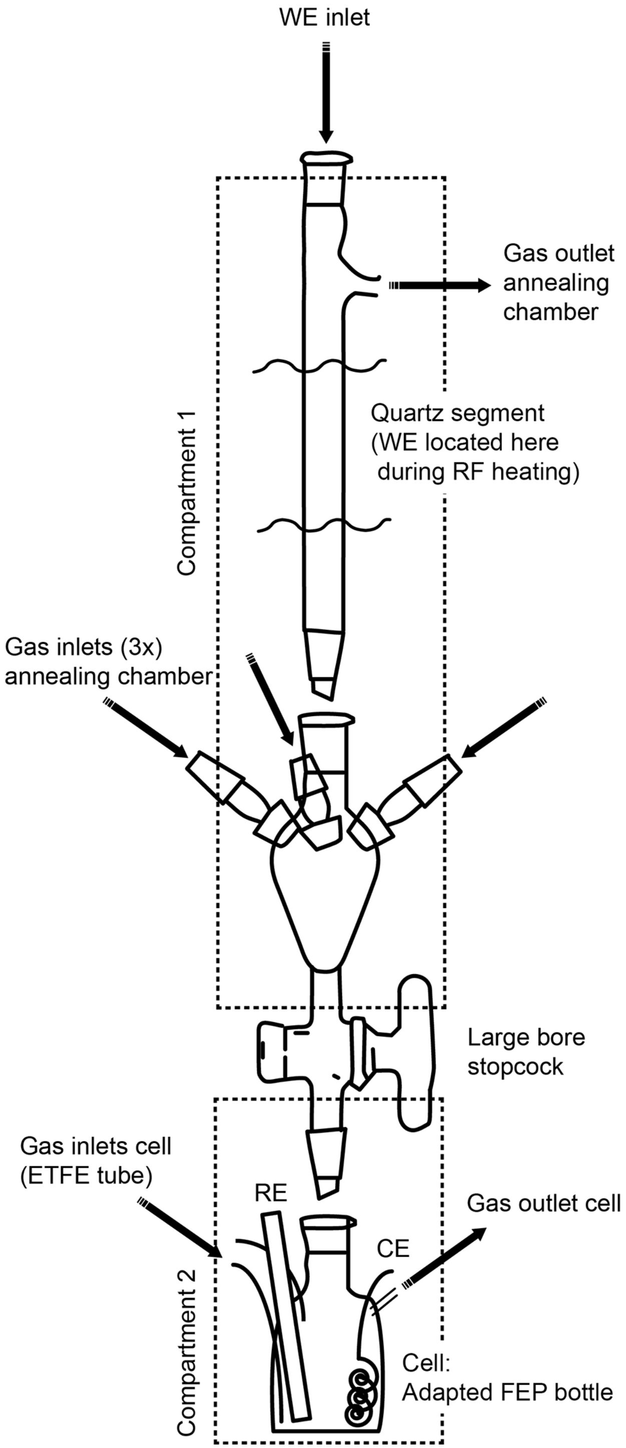

Figure C.1: Components that make up the controlled atmosphere induction annealing + electrochemistry setup. All parts not specifically labeled are made out of borosilicate glass.

C.1.1. Cu(100) characterization

By following the methodology described in this section, stable and symmetrical CVs for Cu(100) electrodes should be obtained, given clean and oxygen-free atmosphere and electrolyte.

a. Establish initial electrochemical contact with the electrolyte at $0\ V$ vs. RHE (i.e., apply $0\ V$ prior to closing the electrical circuit). After establishing contact, adopt a hanging meniscus configuration and allow for the contact current to decrease and stabilize; ca. $-100\ pA \cdot cm_{geo}^{-2}$ is normally achieved in properly deaerated electrolyte solution after 1 to $15\ minutes$.

b. After reaching a sufficiently low and stable contact current, conduct a linear sweep (LS) from $0\ V$ to $-0.25\ V$ (scan rate $\nu = 50\ mV \cdot s^{-1}$).

c. At this point, start a pre-cycling period in order to stabilize (and possibly reconstruct, when accidentally starting with a slightly oxidized crystal) the $\{100\}$ terraces. Scan in the potential window $-0.25\ V < E < +0.35\ V$ vs. RHE at a scan rate $\nu = 50\ mV \cdot s^{-1}$ for a number of times (ca. 5) to obtain a symmetrical $\{100\}$-feature at $-0.125\ V$. For a properly annealed and (mostly) defect-free crystal, pre-cycling CVs should change little, if at al.

d. After pre-cycling, measure one final CV in the potential window $-0.25\ V < E < +0.50\ V$ at scan rate $\nu = 50\ mV \cdot s^{-1}$ (the characterization CV).

This final window was chosen to encompass the known adsorption features of $\{111\}$, $\{100\}$ and $\{110\}$ sites, but leads to irreversible changes for certain facets. Hence, after measuring this full window it is important to rinse and reanneal the surface. The surface after reannealing will be identical to the surface as characterized via CV in the final step. Alternatively, one can either halt at step c) and work with that surface without the need for reannealing, or decrease the upper potential limit in step d) to $+0.44\ V$ and continue without the need for reannealing.

C.1.2. Cu(111) and Cu(poly) characterization

A defining characteristic of (surfaces containing) $\{111\}$ terrace sites is the fact that those particular sites seemingly reconstruct when fixed potentials are applied for extended periods of time ($> 10\ s$). In practical terms, if the (any) potential is held constant for protracted periods, the $\{111\}$-specific OH-adsorption feature is found to diminish in intensity, and traces of an additional (cathodic) feature start to manifest. This effect is more pronounced if the potential is scanned to $E < -0.15\ V$, and very clear when comparing the CV of a polycrystalline electrode that was actively cycled without a standby period with an electrode that was firstly kept at $-0.25\ V$ for ca. $60\ seconds$ before commencing cycling (Figure C.2, black and red lines, respectively). Specifically, it can be seen that the main $\{111\}$ terrace feature at $+0.1\ V$ for the black line exhibits increased current density, and the red line shows a cathodic 'shoulder' near ca. $+0.025\ V$. Although these measurements were conducted on two different crystals (with the red line specifically having some inaccuracy in its calculated electrochemically active surface area due to traces of

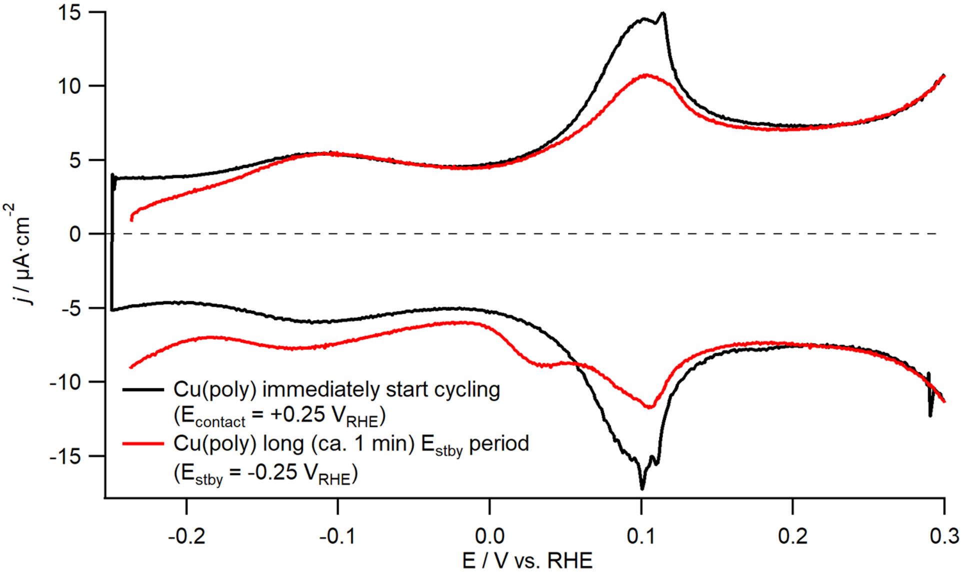

Figure C.2: Comparison of two Cu(poly) electrodes, one measured with only a brief ($< 10\ s$) standby period ($+0.25\ V$) followed by active cycling ($-0.15\ V < E < +0.425\ V$, black) and one measured after a prolonged standby period ($-0.25\ V$, ca. $90\ s$) followed by active cycling ($-0.25\ V < E < +0.425\ V$, red).

oxygen), the differences between them are representative of what is observed if the same surface would be subjected to the two different initial treatments.

Currently, we are unsure as to what causes this behavior, and what these differences mean exactly for the state of the surface. However, staying at a fixed potential for prolonged periods of time results in a weakening in intensity, decreased reversibility and the development of an additional cathodic feature. These signs are all opposite of what one would expect for a single crystalline surface of high quality; considering those generally exhibit high reversibility and intense facet-specific features. Therefore we consider the surface obtained without a standby period to be better representative of clean {111} terrace sites with long-range ordering, especially considering that those CVs compare favorably with recent literature reported voltammograms on a UHV-prepared Cu(111) crystal.

One can obtain voltammograms with a pronounced {111}-terrace specific adsorption feature by initiating the measurement with only a brief standby period followed by cycling – a methodology that is employed by Sebastián-Pascual *et al.*[9, 10] (provided in greater detail to us in a personal communication), which served as the basis for the procedure used in this work as described below.

a. Make initial electrochemical contact with the electrolyte at $+0.25\ V$ vs. RHE for Cu(111)/Cu(poly) electrodes. However, immediately after establishing electrolyte contact and making the meniscus (a process that should take only a few seconds), sweep the potential from $+0.25\ V$ to $-0.15\ V$.

b. After reaching $-0.15\ V$, start a pre-cycling period in the potential window $-0.15\ V < E < +0.425\ V$. This pre-cycling step is necessary to allow for the sides of the crystal to dry and any ORR-related current to diminish, as no stabilization period at any fixed potential was found usable. Generally, a total of 5 cycles was sufficient for the CV to become symmetrical around the x-axis, denoting the absence of oxygen-related current. Similarly to Cu(100), the pre-cycling CVs should change little, if at all, for a properly annealed and (mostly) defect-free crystal. However, the main {111} terrace feature around $+0.1\ V$ is very sensitive to the presence of electrolyte contamination and/or surface defects, which manifests itself in a decrease in charge of the OH-adsorption feature with successive cycling. Generally, increasing argon flow, reannealing the crystal or replacing the electrolyte was found to remedy this.

At this point, the methodology diverges for Cu(111) and polycrystalline surfaces. Cu(111):

c. After the pre-cycling period, measure one final CV in the potential window $-0.15\ V < E < +0.50\ V$ at scan rate $\nu = 50\ mV \cdot s^{-1}$ (the characterization CV). Please note that the cathodic boundary is slightly more positive than for Cu(100), since the {111} terraces were found to be unstable at potentials $E < -0.15\ V$.

Cu(poly):

c. After pre-cycling, extend the lower CV boundary from $-0.15\ V$ to $-0.25\ V$ and measure one final CV in the potential window $-0.25\ V < E < +0.50\ V$ at scan rate $\nu = 50\ mV \cdot s^{-1}$ (the characterization CV). Extending the lower boundary will generally result in the {111} feature diminishing slightly in intensity, but will allow for the presence of the full {100} OH-adsorption feature.

Due to irreversible changes occurring at the upper potential limit, reannealing the surface after characterization is advised. The surface after reannealing will be identical to the surface that was characterized just prior to annealing. Alternatively, one can either halt at step b) and use that surface for the next experiment without the need for reannealing or decrease the upper potential limit in step c) to $+0.44\ V$ and continue without the need for reannealing.

C.1.3. Cu(110) characterization

Contrary to Cu(100) and Cu(111) surfaces, the Cu(110) surface is found to be unstable under the typical surface treatment employed in this work. Specifically, it is found that annealing (and, more importantly, cooling) in pure hydrogen atmosphere results in a (presumably) reconstructed surface with a strongly suppressed {110}-terrace feature (around $+0.33\ V$). Changing the annealing and/or cooling atmosphere to be a mix of argon and hydrogen (of several different compositions) was found to always result in a surface with unstable and/or strongly suppressed {110}-specific OH adsorption feature. Hence, a special electrochemical treatment (step b) was introduced to obtain literature- representative CVs. The following methodology should result in clean, stable and reproducible Cu(110) CVs.

a. Establish initial electrochemical contact at open circuit (E_{oc}).

b. Apply a potential of $-10\ V$ vs. RHE for $30\ seconds$ whilst bubbling argon through the solution (exact cathodic potential not important, so long as it results in large amounts of cathodic current – i.e., several $hundreds$ of $mA \cdot cm_{geo}^{-2}$).

c. This step is a combination of a number of actions:

   c.1. Lift the electrode and break contact with the electrolyte (and stop controlling the potential). Purge the solution with argon for a few minutes to remove the hydrogen and oxygen produced in step b). Every now and again, make and break the meniscus (keeping the electrode at open circuit) to remove dissolved gases in the droplet attached to the surface of the crystal.

   c.2. Change the argon flow to blanket the solution, re-establish meniscus at open circuit.

   c.3. Run a linear sweep from E_{oc} to $0\ V$.

   c.4. Pre-cycle the crystal in the potential window $0\ V < E < +0.3\ V$ for a few cycles (ca. $2-3$). Determine if the CV quickly becomes symmetrical around x-axis. If the CV becomes symmetrical and stable, go to next step. If there is still oxygen (indicated by a lack of symmetry), go back to step c1). Often, repeating step c) in full is necessary for $2-3$ times.

d. Extend the lower CV boundary from $0\ V to - 0.25\ V$, and measure one final CV in the potential window $-0.25\ V < E < +0.50\ V$ at scan rate $\nu = 50\ mV \cdot s^{-1}$ (the characterization CV).

Considering that preparing this surface is more intricate than the other surfaces described, it is not advised to reanneal the surface after characterization. Instead, one can rinse the electrode (preferably under hydrogen atmosphere), dry the top of the electrode with a piece of paper (in the case of a disk), and transfer to a working cell to conduct experiments. The $\{110\}$ facet seems more resistant to oxidation than the other faces, and the cycling up to $+0.50\ V$ does not seem to lead to irreversible oxidation (so long as it is for brief periods). If the rinsing and transfer periods are sufficiently short ($< 1\ min$), reproducible CVs can be obtained via this method.

C.2. Mechanically polished single crystals cleaning procedure

To remove any residues related to the mechanical polishing process, cut single crystals (as-received from the supplier) were treated as described below. This cleaning was found to be necessary, considering that as-received crystals exhibited additional features in the CV unrelated to the adsorption peaks expected for surfaces of their orientation. It is important to note that the cleaning procedure described below is destructive in nature, and will introduce additional defects into the surface.

Initially the electropolishing methodology as described by Schouten *et al.*[3] and Engstfeld *et al.*[11] was employed in this work for cleaning copper single crystals as per step a). However, this methodology was found to be too aggressive and later on we switched to a milder electropolishing method described by Sebastián-Pascual *et al.*[9, 10, 12] (alternative a). It is strongly advised to employ this alternative electropolishing step (if electropolishing is required), considering that it yields similarly clean surfaces but introduces fewer step-site defects.

The exact cleaning methodology was as follows.

a. The crystal is electropolished by subjecting the electrode to $+2\ V$ vs. a copper CE in $66\ wt\%$ H_3PO_4 solution for $10\ seconds$, followed by $30\ seconds$ at $0\ V$.

(Milder alternative:)

a. The crystal is electropolished at $+1.8\ V$ vs. a Cu CE for $5\ seconds$ in a $10:2:2\ vol\%$ electrolyte of $\mathrm{H_2SO_4} : \mathrm{H_3PO_4} : \mathrm{H_2O}$ which was freshly prepared at the start of the day (hygroscopic action increases the water content over time and results in increased currents at similar potentials, leading to more step defects being generated). Expected (peak) currents during electropolishing: ca. $+300-400\ mA \cdot cm_{geo}^{-2}$

b. The crystal is then thoroughly rinsed with Milli-Q water and ultrasonicated in a clean water bath for ca. $10\ minutes$ without being in contact with the sides or bottom of the container.

c. The crystal was thoroughly rinsed with Milli-Q water again, and inductively annealed close to the melting temperature of the material for ca. $5\ minutes$ under H_2 flow, after which it was quench-cooled down to room temperature in increased H_2 flow for another ca. $5\ min$. After taking out the electrode from the annealing compartment, the color should not change as a color change indicates oxide formation (i.e., the crystal has not cooled down sufficiently).

d. Steps a-c) were repeated a minimum of $5\ times$.

Finally, the crystal was electropolished once more (i.e., step a) after which it was thoroughly rinsed and annealed for ca. $15\ min$ (i.e., step c, but for longer). It is then cooled in hydrogen atmosphere, and subsequently electrochemically characterized to ascertain the quality of the surface. In this work, these steps were sufficient to yield surfaces that showed features comparable to what is reported in literature, and thus no additional actions were undertaken.

C.3. Procedure for recovery of defective cut single crystals

Depending on the situation, it is possible that the CV obtained after an experiment does not match that of a clean, well-defined surface. In such instances, two approaches were employed to recover the initial surface structure. As a first option, the crystal would be inductively annealed as described in the surface preparation section, and then electrochemically characterized to determine if this was sufficient to recover the surface. If the crystal was found to change in the right direction but not fully recover, a longer annealing period was conducted (ca. $15 - 30\ minutes$) and the crystal characterized again.

However, at times, annealing (multiple times, and/or for longer periods) was not sufficient to recover the defective crystal to its initial state. In such cases, the same methodology as described for cleaning mechanically polished surfaces was employed, but steps a-c) were only conducted once (i.e., skipping step d), followed by a long (ca. $15\ min$) annealing step. Then the surface was cooled in a stream of H_2 and electrochemically characterized to verify its structural integrity. This second methodology was repeated until a good surface was obtained, but generally in this work a single treatment was sufficient.

C.4. EASA determination from OH adsorption for Cu(poly) electrodes

To facilitate easier comparison between literature-reported CVs and/or catalytic activities, it is common practice to report data in current density to account for surface area effects. In the case of copper, authors often normalize their data via the geometric area of their surface. However, this form of normalization relies on the inherent assumption that the surface itself is perfectly flat – i.e., has a roughness factor (R_f = 'real area'/geometrical area) of 1. More often than not, this assumption is invalid. To this end, it has been proposed that it is more accurate to determine the so-called electrochemically active surface area (EASA), so as to better represent the actual number of electrochemically addressable sites present at the interface and normalize data using this value.

In this regard, a methodology much employed in the literature for determining this EASA area for copper electrodes is via the double-layer capacity.[13, 14] Briefly, by scanning a small potential window considered purely capacitive in nature at different scan rates, one can determine the total surface capacitance (denoted here C_{tot}, in $Farad$) as the slope by plotting the double layer current (A) as a function of scan rate ($V \cdot s^{-1}$), see Equation C.1.

$$i_{DL}(A) = C_{tot}(F) * \frac{\delta E}{\delta t}(\frac{V}{s}), \text{ where } C_{tot}(F) = C_{DL}(\frac{F}{A}) * A_{Electrochemical} \quad \text{(C.1)}$$

Then, by comparing the total capacitance to a reference value (C_{DL}, labeled C* by Trasatti and Petrii[14]), we can theoretically determine the EASA as per Equation C.2.

$$A_{Electrochemical} = C_{tot}(F)/C_{DL}(\frac{F}{A}) \quad \text{(C.2)}$$

Although this methodology indeed provides an estimate of the number of electrochemically addressable surface sites, it requires the existence of a potential window where purely capacitive behavior is observed, and its accuracy depends strongly on the availability and validity of a reference capacitance value for the system under consideration (which may vary with the type of electrolyte, and/or the potential window wherein it is measured). In literature, researchers tend to use capacitive surface area measurements via two alternate strategies. Firstly, some measure the total capacitance of their system as per Equation C.1 and determine the area using a literature reference value for C_{DL}. This literature value is generally taken to be $28\ \mu F \cdot cm^{-2}$ (though sometimes reported[15, 16] as $29\ \mu F \cdot cm^{-2}$) in $0.1\ M$ $HClO_4$ for polycrystalline copper as per a publication from 1995 wherein they generalize the capacitance determined for platinum and gold to copper, citing the *'...apparent independence of the capacitance value of the metal'*.[17] Additionally, there are those whom determine their own reference value by measuring the total capacitance of a finely polished surface of known geometric area and assumed surface roughness factor of 1, where they obtain C_{DL} by dividing their obtained C_{tot} by the geometrical area of their surface. Theoretically, these two methods should yield fairly similar (or rather, identical) results, considering they describe the same thing. However, they generally do not, as is illustrated in Table C.1, which summarizes a (by no means exhaustive) number of publications that determined (and used instead) their own reference capacity value for copper under various conditions (original capacitance source included).

From Table C.1, we can clearly see that that there is a rather large spread for the reported reference capacitance, even when it is measured in the same electrolyte ($28 - 78\ \mu F \cdot cm^{-2}$). The differences become even more striking when comparing between differing electrolytes ($4 - 264\ \mu F \cdot cm^{-2}$), showing not only the importance of having a reliable reference in the system under consideration, but also the apparent inaccuracies associated with double layer capacitance surface area determination.[18] In part, these inaccuracies are the result of defining a certain substrate as having a R_f value of 1, which is generally not thoroughly verified (and is difficult to verify for copper, as oxidation/reduction cycles may change the roughness). Additionally, further variability can be related to (differences in) the facet distribution at the interface for surfaces prepared by different groups as some facets are more open than others, resulting in differing capacitance values for differing faces with the total capacitance being the summation of the capacitances of the various sites that make up the surface.

Because of these reasons, researchers investigating non-copper systems generally use other means of determining the real surface area, with electrochemical surface titration-types of methods being popular. Examples include hydrogen and oxygen adsorption studies (e.g., H_{upd} on Pt[19] and surface oxidation of Au[20]), or the deposition of a monolayer of a foreign metal through underpotential deposition (UDP)[14, 21], where the former is more common than the latter.[14, 18] Such electrochemical titration studies are also possible for copper systems, considering that copper is known to yield well-separated adsorption features in hydroxide solution[1, 22, 23], where it is reported that the charge of specific features in the CV can be associated to the geometric areas of particular facets.[23]

Table C.1: Various literature-reported values for C_{DL} as measured in differing laboratories and (possibly) under different conditions /electrolytes.

Reported C_{tot} (μF)	**Reported area (cm^2)**	**Capacitance C_{DL} ($\frac{\mu F}{cm^2}$)**	**Electrolyte**	**Scan rates ($mV \cdot s^{-1}$)**	**Surface**	**Ref**
4	$\pi * 0.52 = 0.785$	5.1	CO_2-saturated 0.1 M $KHCO_3$	Not reported, nor available from cited sources	Cu(100)	[24]
n/a	n/a	16	CO_2-saturated 0.1 M $CsHCO_3$	Not reported, nor available from cited sources	Cu_2O thin film	[25]
n/a	n/a	28	0.1 M $HClO_4$	20, 50, 100, 200, 500	Pt and Au "platinum and gold electrode"	[17]
51	1.13	45.1	0.1 M $HClO_4$	10, 20, 40, 60, 80, 100 (from cited source)	Cu(poly)	[26]
18	$\pi * 0.32 = 0.283$	63.7	1 M NaOH	"...10 to 80"	Cu(poly)	[27]
n/a	n/a	78	0.1 M $HClO_4$	10, 20, 40, 60, 80, 100	Cu(poly)	[28]
n/a	n/a	264	0.1 M KOH	5, 10, 20, 50, 100	Cu(poly)	[29]

With this information in mind, we decided to attempt as best we could to correlate the current integral of a polycrystalline copper surface to its geometrical area, so as to obtain a reference value by which the EASAs of other copper electrodes can be determined via adsorption studies (instead of by their capacitance values). The exact methodology for this process is described in the following section, where we also try to specify all of the assumptions that we must necessarily make for enabling us to determine such a reference adsorption charge density value.

Firstly, we require a clean and flat polycrystalline surface for which we can consistently and accurately expose a known geometrical area to the electrolyte solution. To this end, we opted for preparing a spherical polycrystalline electrode (i.e., droplet at the end of a wire), which we then polished down to about half-way the bead with silicon carbide sandpaper (Hermes, 2500 grid) to yield a bead-type electrode (i.e., a half-sphere at the end of a wire) which was further mechanically polished with diamond slurries (Buehler) of successively smaller sizes from $5\ \mu m$ down to $1\ \mu m$ to yield a mirror finish. Cleaning of the initial spherical droplet was done as per the methodology described elsewhere in this work (briefly, through a number of iterations of: melting of the bead followed by HNO_3 etching and rinsing with Milli-Q water). Further surface cleaning after mechanical polishing was also performed as described elsewhere in this work (briefly, through a number of iterations of: sonicating the electrode in Milli-Q water for ca. $15\ min$, followed by electropolishing, then rinsing with Milli-Q water and induction annealing in inert atmosphere for ca. $5\ min$).

Considering that the 2D geometry of the resulting surface is determined by the polishing angle with respect to the surface normal of the initial spherical bead (ranging from a perfect circle to oval, depending on the angle), the resulting surface was photographed and the resulting image analyzed to correlate the pixel count of the surface to the area of an item of known dimensions to determine geometric surface area as a more accurate representation of the area as opposed to measuring the diameter and calculating the geometric area by assuming the electrode is perfectly circular. This geometrical area was found to be $0.11\ cm^2_{geo}$.

At this point, we make two assumptions in order to continue our investigation:

(1) The cleaning has led to the successful removal of all surface impurities and/or any contaminants still present on the surface do not contribute to the charge of the CV nor do they block copper surface sites.

(2) The resulting surface is atomically flat (i.e., we define it as having a R_f of 1).

As for the validity of these assumptions, no foreign adsorption features are observed during cyclic voltammetry which would signify the presence of contaminants, which gives credence to assumption (1). Regarding assumption (2), the mechanical polishing and especially electropolishing steps introduce roughness, but this roughness is reduced by the induction annealing step. Still, it is unlikely that the surface is fully atomically flat, but we will have to make this assumption nonetheless.

At this point, we had to decide in what potential window we should determine the charges associated with electro-sorption processes. We opted for measuring in the potential window $-0.25\ V < E < +0.44\ V$, considering that we found that this window exhibits reversible features which is indicative of fast and, importantly, non-destructive adsorption phenomena, whilst encompassing facet-specific adsorption features for all of the basal planes and (likely, see main text) defect sites. This empirical upper potential limit agrees well with the most cathodic tabulated oxidation reaction of copper (Reaction R1).[30] Further indication of the non-destructive nature of the processes occurring in this window is in the form of dissolution studies, wherein it is reported that no copper is detected in solution for potentials $E < 0.5\ V$ vs. RHE during cyclic voltammetry in $0.05\ M$ KOH.[31] The cyclic voltammogram in this window, as obtained for the surface discussed throughout this section, is depicted in Figure C.3.

$$\mathrm{Cu_2O + H_2O + 2\,e^- \rightleftharpoons 2\,Cu + 2\,OH^-}, E^0 = +0.41\ V \text{ vs. RHE } (pH13) \qquad \text{(R1)}$$

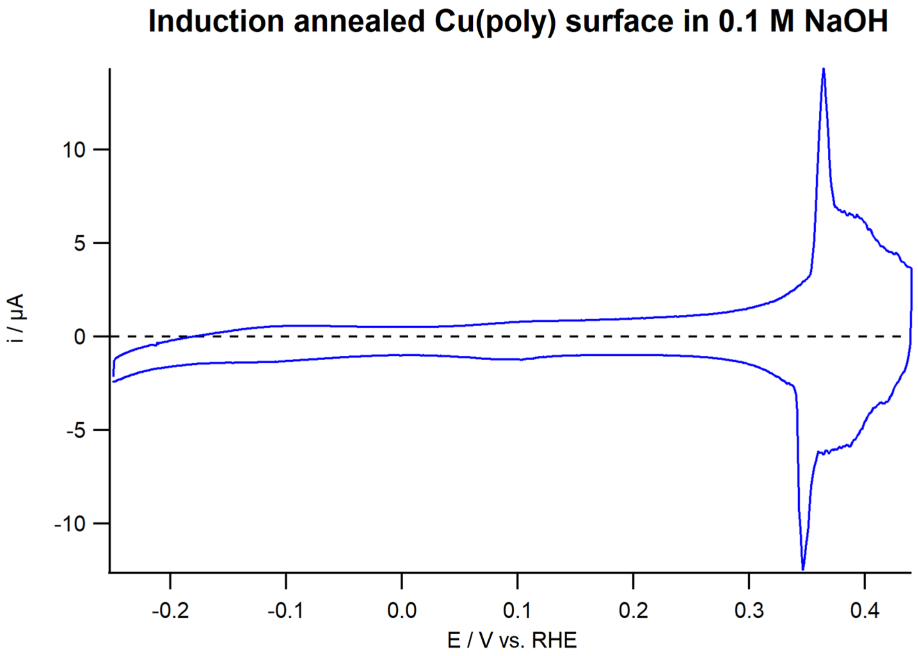

Figure C.3: CV of a mechanically polished and thoroughly cleaned, inductively annealed polycrystalline copper bead-type electrode in $0.1\ M$ NaOH (scan rate $\nu = 50\ mV \cdot s^{-1}$) in the window exhibiting reversible adsorption/desorption behavior.

Though this CV (Figure C.3) is adequate in the sense that it exhibits only features that are related to adsorption phenomena involving copper sites, with clear indication of the presence of a number of different surface sites, it has a minor issue: there is a slight contribution of ORR current at the cathodic end of the CV ($E < +0.1\ V$). This parasitic current contribution was found to be virtually impossible to remove. Although we tentatively ascribe this current to ORR (considering already the region at ca. $0\ V$ is not symmetrical around the x-axis), it may also be related to increased HER on defect sites, or possibly a combination of both.

In order to be able to continue our investigation from this point, we make two additional assumptions:

(3) The adsorption processes occurring on the surface are fully reversible in the potential window that we investigate.

(4) The oxygen concentration in the system is constant, resulting in equal contributions of ORR current at a given potential in both the positive going scan and the negative going scan.

Both assumptions are relatively ‘safe’, considering that the CV looks symmetrical (providing validity to assumption (3)) and considering that multiple successive scans result in the same CV (not depicted) without the ORR current contribution changing for either scan direction (leading to assumption (4)).

Under these conditions, the charge contributions of the CV can be divided as follows.

$$\text{Positive going scan: } Q^{f}_{total} = Q^{+}_{adsorption} + Q^{+}_{DL} + Q^{-}_{ORR} \tag{C.3}$$

$$\text{Negative going scan: } Q^{b}_{total} = Q^{-}_{desorption} + Q^{-}_{DL} + Q^{-}_{ORR} \tag{C.4}$$

where Q^{+} denotes an anodic current integral and Q^{-} denotes a cathodic current integral. Additionally, from the assumption that the adsorption processes are fully reversible we can state: $Q^{+}_{adsorption} = -Q^{-}_{desorption}$, and similar reasoning applies to the double layer charge since the scan boundaries are equal for the positive- and negative-going scans: $Q^{+}_{DL} = -Q^{-}_{DL}$. If we now subtract the total charge of the negative-going scan (Q^{b}_{total}) from the total charge of the positive-going scan (Q^{f}_{total}), the ORR contribution cancels out, see Equation C.5. Please note that it is irrelevant if the parasitic (faradaic) current contribution is related to ORR or HER (or a combination of both): so-long as the charge contribution(s) is (are) equal during both scan-directions, they cancel out.

$$\begin{aligned} Q^{f}_{total} - Q^{b}_{total} &= (Q^{+}_{adsorption} + Q^{+}_{DL} + Q^{-}_{ORR}) - (Q^{-}_{desorption} + Q^{-}_{DL} + Q^{-}_{ORR}) \\ &= (Q^{+}_{adsorption} + Q^{+}_{DL} + Q^{-}_{ORR}) + (Q^{+}_{adsorption} + Q^{+}_{DL} - Q^{-}_{ORR}) \\ &= 2 * (Q^{+}_{adsorption} + Q^{+}_{DL}) \end{aligned} \tag{C.5}$$

Now, if we can determine what the double-layer capacity is for our system we could calculate Q^{+}_{DL} and thereby work out the total adsorption-related charge contribution to our CV. We found empirically that the current in the area of the CV between $-0.250\ V < E < -0.235\ V$ was a decent descriptor of surface area; indicative that this area is mostly dictated by capacitive behavior, and therefore we used this region to calculate the double-layer charging current via Equation C.6.

$$i_{DL} = \frac{1}{2} * \left\{ \frac{1}{n} * \sum_{1}^{n} i^{f}(E_n) - \frac{1}{m} * \sum_{1}^{m} i^{b}(E_m) \right\} \tag{C.6}$$

Here, n and m signify the total number of individual datapoints of the CV in the previously defined potential window for the positive-going scan direction and negative-going scan direction, respectively, and $i^{f}(E_n)$ and $i^{b}(E_m)$ denote the currents at the individual potentials associated with datapoints n and m, respectively. For this equation to be valid, we rely once again on assumption (4); that ORR-related faradaic currents cancel out when subtracting the currents for the positive- and negative-going scan directions. The as-calculated value for i_{DL} of the electrode we have been discussing (Figure C.3) was $0.60\ \mu A$ at a scan rate $\nu = 50\ mV \cdot s^{-1}$.

One might argue that it is more accurate to determine (through Equation C.1) the total surface capacitance from scan rate dependency studies of the double-layer

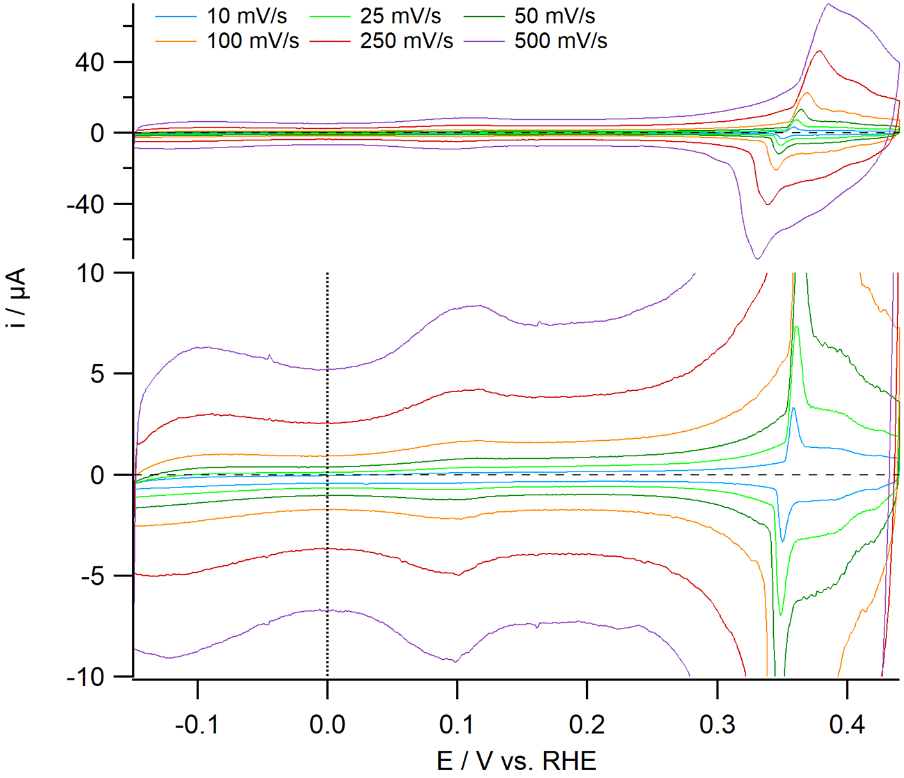

Figure C.4: Scan rate dependency of a polished polycrystalline copper surface in $0.1\ M$ NaOH.

charging current obtained experimentally via Equation C.6, and then back-calculate the theoretical charging current at a particular scan rate from the capacitance. By doing so, besides improved accuracy of the charging current value, one would obtain an additional surface-indicative metric (system capacity, C_{tot}) from basically a single blank CV measurement (just requiring some additional cycling at various scan rates). To briefly address this, we cycled our electrode in the potential window $-0.15\ V < E < +0.44\ V$ (for the scan rate dependency study we increased the lower CV boundary from $-0.25\ V$ to $-0.15\ V$ since $\{111\}$ terrace sites are not fully stable below $-0.15\ V$ – see main text) at various scan rates (specifically, $10, 25, 50, 100, 250$ and $500\ mV \cdot s^{-1}$) so-as to be able to determine double-layer currents (i_{DL}) at these scan rates. Please mind that the faster scan rates we employ are only viable for surfaces of low roughness. The CVs obtained under these conditions are depicted in Figure C.4.

From the changes in the voltammetry as a function of scan rate, we determined that the area around $0\ V$ exhibited the most capacitive-like behavior (thinnest double-layer with a reasonably stable current although only in a small window). Therefore, we decided to calculate the i_{DL} at each scan rate in the window $-0.005\ V <$

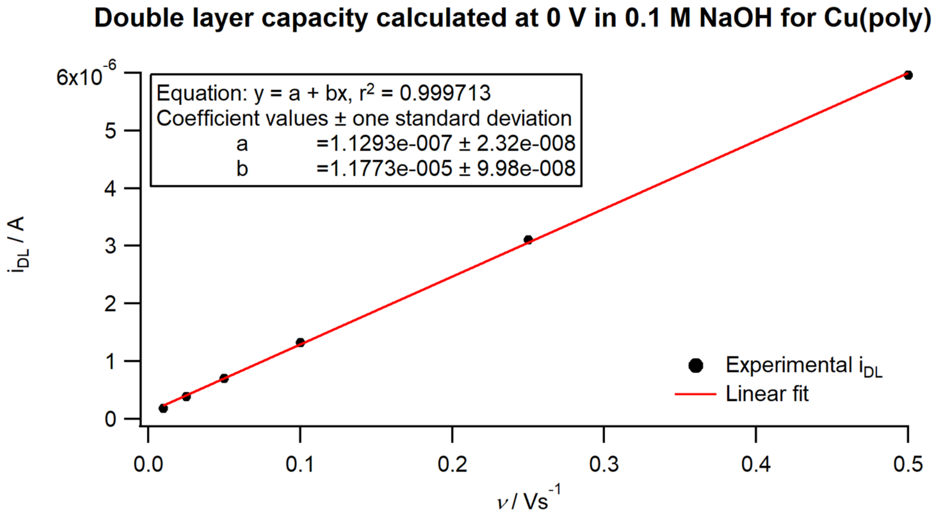

Figure C.5: Total double layer capacity (Ctot) of the polished polycrystalline copper electrode discussed in text, as calculated via Equation C.1 using experimentally determined charging currents as per Equation C.6.

$E < +0.005\ V$ (i.e., $0\ V \pm 5\ mV$) via Equation C.6. However, even though we determined this region seemed most suitable for obtaining the double layer capacity, it must be noted that {100}-terrace sites do yield adsorption-related charge in this window (see main text) albeit a relatively minor amount.

At this point we have the required information for determining the total capacitance, with the results of the linear regression for our flat polycrystalline surface being depicted in Figure C.5. As can be seen from the textbox insert in the figure, the total capacitance we find for our system under our applicable conditions ($0.1\ M$ NaOH, determined at $0\ V$) is $11.77\ \mu F$ (from which we can also calculate the reference capacitance by dividing by the surface area, being $0.11\ cm^2_{geo}$: $C_{DL} = 107\ \mu F \cdot cm^{-2}$). Now we can back-calculate the expected double-layer charging current at a scan rate $\nu = 50\ mV \cdot s^{-1}$ (the scan rate used for the blank CV in Figure C.3) via Equation C.1, yielding $i_{DL} = 0.59\ \mu A$ which is virtually identical to the i_{DL} value we found from our empirically determined DL region of the CV ($-0.250\ V < E < -0.235\ V$, $0.60\ \mu A$). For future calculations, we shall use $i_{DL} = 0.59\ \mu A$, however, in practice, both methods seem suitable for obtaining the double-layer charging current, and both are used in this work depending on the circumstances.

After this brief intermezzo, we now have all the information we require to extract the charge that is due to adsorption processes taking place during the copper CV. Depending on the type of software one uses; it may be easiest to positive-shift the entire CV until all currents are ≥ 0. Then, the positive-going and negative-going scans can be individually integrated, and the latter subtracted from the former, as is visually represented in Figure C.6. For the polycrystalline surface discussed so

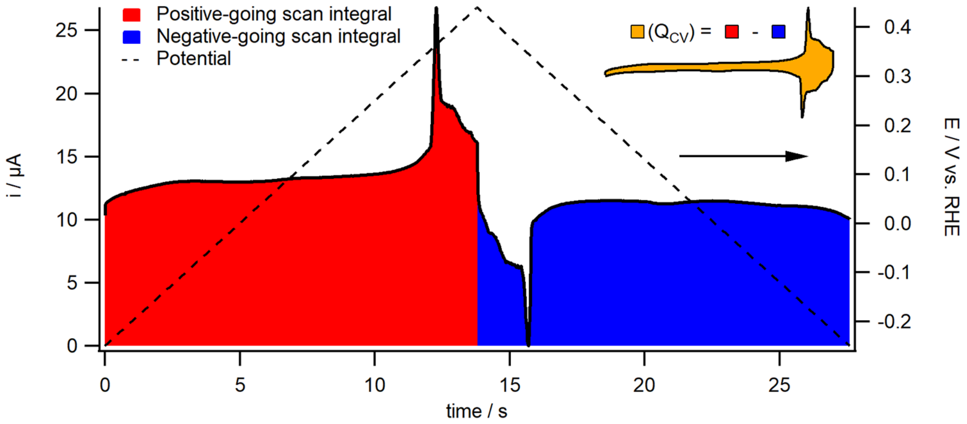

Figure C.6: Visual representation of the charges discussed in text, and what regions they represent.

far in this segment, the charge encompassed by the CV ($Q_{CV} = Q^{f}_{total} - Q^{b}_{total}$) was equal to $44.31\ \mu C$.

Finally, we can now determine the area-normalized charge associated with adsorption phenomena on copper via Equation C.7. The part where we multiply the double-layer current by a number of CV parameters is nothing more than the time it takes to finish one full cycle of the voltammogram. The resulting reference charge we obtain find is $128.1\ \mu C \cdot cm^{-2}$.

$$\frac{Q^{+}_{adsorption}(C)}{A_{geo}(cm^2)} = \frac{1}{A_{geo}(cm^2)} * \frac{1}{2} * \left\{ \left(Q^{f}_{total}(C) - Q^{b}_{total}(C) \right) - i_{DL}(A) * 2 * \frac{E_{max}(V) - E_{min}(V)}{scan\ rate \frac{V}{s}} \right\} \tag{C.7}$$

Now, we shall have to make one final assumption in order to use this value for generic EASA determination in our system:

(5) The site distribution of the mechanically polished, subsequently electropolished finally and induction annealed polycrystalline electrode we used to obtain this reference value is representative for all polycrystalline surfaces

The validity of this final assumption is difficult to ascertain. As a first indication, we can deduce if the value we have calculated makes logical sense by comparing our result for polycrystalline copper to literature-reported values for single crystalline surfaces. In this case, Tiwari *et al.*[23] report that the facet-specific adsorption features for {111}, {100} and {110} should theoretically yield adsorption charge densities of respectively 79, 59 and $27\ \mu C \cdot cm^{-2}$. However, the terraces are not fully covered with OH, having instead the equivalent of between $1/4$ to $1/3$ of a monolayer coverage when considering a Cu:OH ratio of $1:1$ as a full ML. Comparatively, step sites are more reactive than terrace sites, and thus a higher coverage can reasonably be expected for such sites, which happen to make up a significant portion of a polycrystalline surface. Therefore, we believe that the fact that the reference value we obtained for polycrystalline copper ($128.1\ \mu C \cdot cm^{-2}$) is somewhat higher than the range of values reported by Tiwari *et al.*[23] seems reasonable at least.

However, this still does not directly address how applicable assumption (5) is to polycrystalline surfaces of differing site distributions. For now, the best answer to this question is simply to use this methodology of surface normalization, and see how surfaces with different facet distributions compare. To this end, the mechanically polished electrode we have discussed throughout this section is compared to a spherical bead-type polycrystalline electrode (for which it is not possible to readily determine the geometrical surface area) in Figure C.7. From comparing the blue line (polished bead-type electrode) with the red line (spherical bead-type electrode) it is evident that the facet distribution at the interface for these two electrodes is rather different from the fact that they exhibit very different charge contributions in differing regions of the CV. However, after calculating the total adsorption charge for these two surfaces and normalizing the CVs to their respective EASAs, we find that the voltammograms 'look' as one would empirically expect two similarly sized surfaces to behave, though this is decidedly not a convincing argument.Slightly less subjective 'proof' of the normalized CVs representing very similar areas is that the

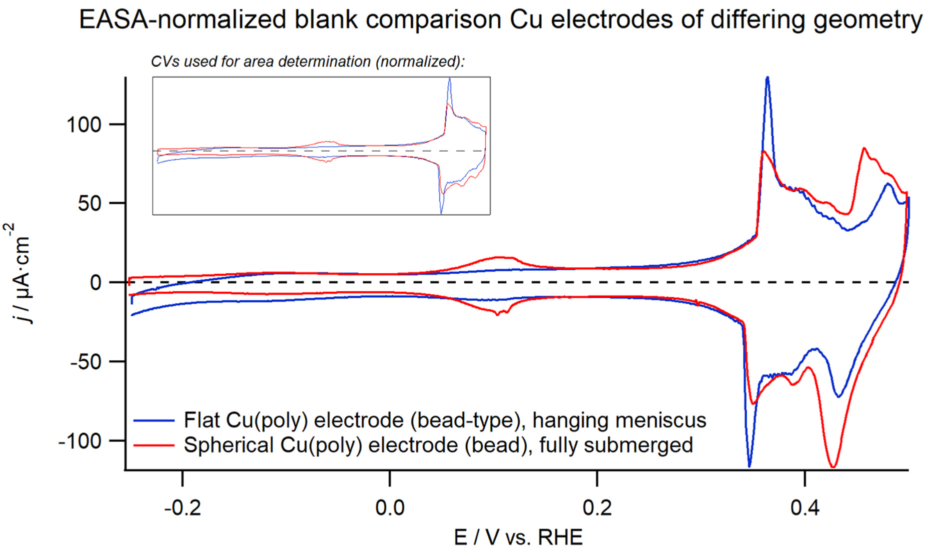

Figure C.7: Two "adsorption EASA-normalized" copper surfaces of strongly different geometry (2D circular vs. 3D spherical) and reasonably different surface-site distribution (as evidenced by the differing intensities at identical potentials in the CVs).

double-layer thickness in the pseudo-capacitive region between $-0.25\ V < E < +0.35\ V$ is very similar between the two surfaces, even though we do not scale directly to this value (it is, however, an integral part of the calculation – as is inherent to surface titration methods).

C.5. Single crystal CV peak deconvolution

C.5.1. Deconvolution of a Cu(111) CV

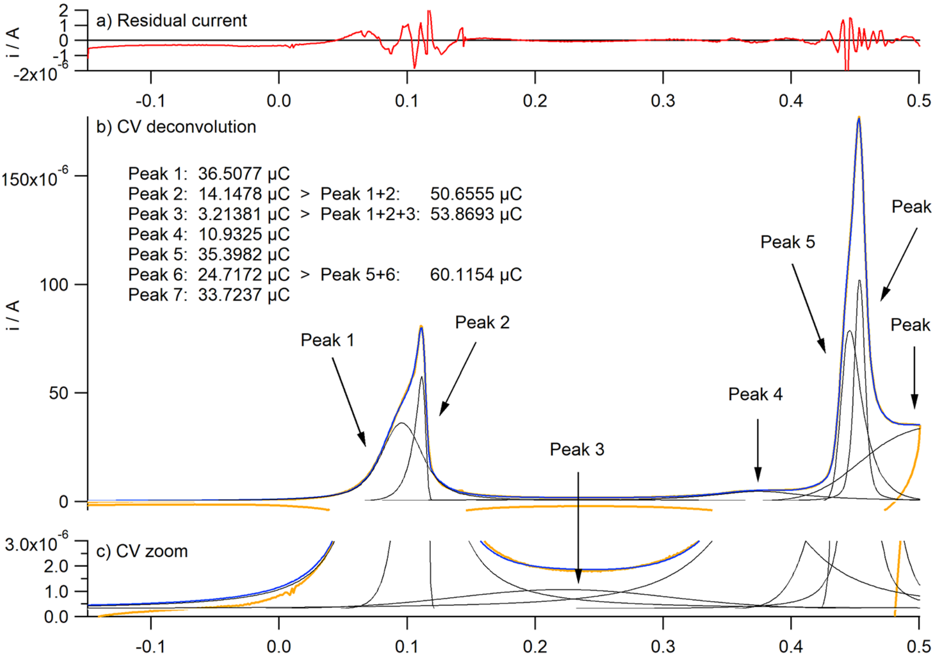

Figure C.8: Mathematical deconvolution of a Cu(111) CV into a sum of individual peaks. In a) the difference in current between the measured CV and the sum of the optimized peaks (red) is given. In b) the locations, shapes and labels of the individual modelled peaks (black) are depicted and compared to the measured CV (orange) and the sum of the optimized peaks (blue). In c) a close-up of b) is given to show the location and shape of peak 3.

In Figure C.8 we have modelled a Cu(111) CV by fitting the observed features to a number of distinct peaks (of varying shapes, e.g., Guassian, Lorentzian, and/or a combination of an Exponential and Gaussian function was used, depending on which fit best the shape of each peak). Considering our belief that {111} terraces with high defect density (i.e., having very narrow widths) yield an adsorption signal at potentials $-0.02\ V < E < +0.25\ V$, we added a representative peak in this region in our deconvolution model (labelled 'peak 3'). Empiric evidence for the existence of this additional peak can derived from the fact that fitting without this peak yields a considerably worse goodness of fit (not depicted). After separating the individual components, the OH-adsorption charge (sum of the peaks located between $-0.1\ V < E < +0.25\ V$, i.e., peaks 1-3) was estimated to be $53.9\ \mu C$ ($= 107\ \mu C \cdot cm_{geo}^{-1}$), and the adsorption charge associated with the second adsorption feature (sum of the peaks located between $+0.43\ V < E < +0.475\ V$, i.e., peaks 5 & 6) was estimated to be $60.1\ \mu C$, yielding a ratio of ca. $0.9 : 1$. It must be noted that deconvolution of a CV exhibiting such a large number of non-Gaussian features is not very accurate, but can still serve as an indication.

C.5.2. Deconvolution of a Cu(100) CV

In Figure C.9 we have modelled a Cu(100) CV by fitting the observed features to a number of distinct peaks. After separating the individual components, the OH-adsorption charge (peak 1, located at $E = -0.125\ V$) was estimated to be $34.5\ \mu C$ ($= 68.7\ \mu C \cdot cm_{geo}^{-1}$), and the charge associated with the second adsorption feature (peak 4, located at $E = 0.475\ V$) was estimated to be $37.9\ \mu C$, yielding a ratio of ca. $0.9 : 1$.

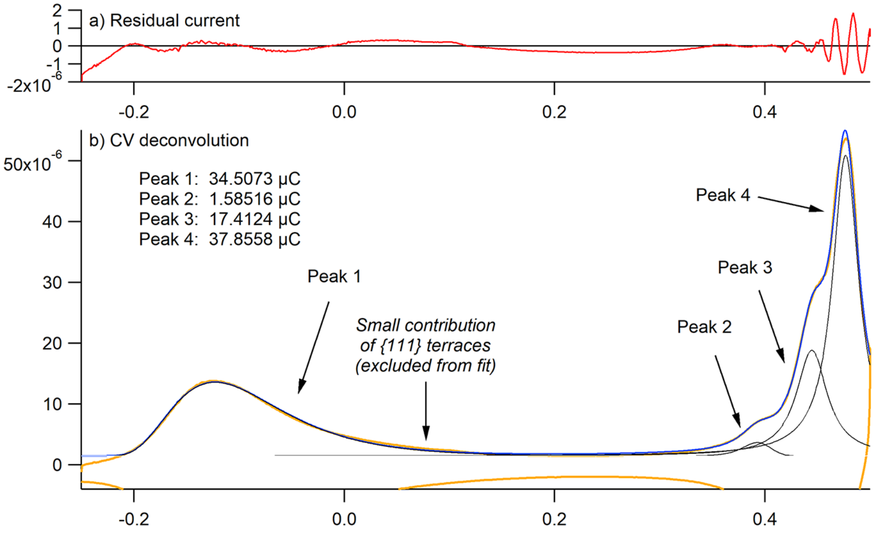

Figure C.9: Mathematical deconvolution of a Cu(100) CV into a sum of individual peaks. In a) the difference in current between the measured CV and the sum of the optimized peaks (red) is given. In b) the locations, shapes and labels of the individual modelled peaks (black) are depicted and compared to the measured CV (orange) and the sum of the optimized peaks (blue).

C.5.3. Deconvolution of a Cu(110) CV

In Figure C.10 we have modelled a Cu(110) CV by fitting the observed features to a number of distinct peaks. After separating the individual components, the OH-adsorption charge (peak 1, located at $E = +0.33\ V$) was estimated to be $13.0\ \mu C$ $(= 25.8\ \mu C \cdot cm_{geo}^{-1})$, and the adsorption charge associated with the second adsorption feature (peak 4, located at $E = +0.494\ V$) was estimated to be $24.5\ \mu C$, yielding a ratio of ca. $1.06 : 2$. Please beware that this CV was found to have the lowest goodness of fit, due a) the cathodic tail of the $\{110\}$-specific feature at ca. $+0.33\ V$ which did not conform to any of the typical peak shapes and b) the very broad charge region between $+0.38\ V < E < +0.45\ V$, which is a convolution between several differing sites located close together (i.e., various defect sites and $\{111\}$ terraces).

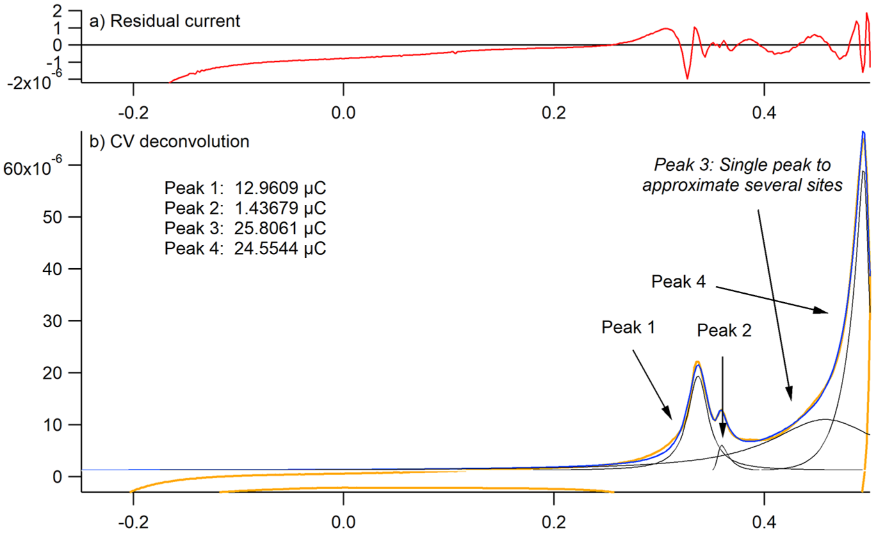

Figure C.10: Mathematical deconvolution of a Cu(110) CV into a sum of individual peaks. In a) the difference in current between the measured CV and the sum of the optimized peaks (red) is given. In b) the locations, shapes and labels of the individual modelled peaks (black) are depicted and compared to the measured CV (orange) and the sum of the optimized peaks (blue).

C.6. Preparing clean Cu(poly) with wide site distribution

The following methodology can be used for preparing bead-type polycrystalline copper electrodes. Firstly, one has to prepare a copper bead from a high purity copper wire (ideally $> 99.995\%$ purity) by melting the end of a wire into a droplet via induction heating in inert atmosphere (e.g., H_2, N_2, Ar).

- Re-melt the copper bead, but do not allow it to grow larger (to prevent additional bulk impurities from being introduced to the melt).
- After melting, allow the droplet to cool and solidify in oxygen-free atmosphere by turning off the induction current
- Take out the bead, and etch in concentrated HNO_3 (ca. $5\ seconds$, in a fume hood)
- Rinse the bead with Milli-Q water
- Go back to the first step and repeat procedure (3-5 x)
- After $3-5\ cycles$, remelt the droplet once more, but do not etch again after cooling.

After going through this process, the resulting electrode is ready for experiment after briefly annealing it $(2-5\ minutes)$ at ca. $700-800\ ^{\circ}C$ (well below the melting temperature, to prevent further bulk contaminants from migrating to the surface). Working with this type of electrode is slightly more difficult, as it is not possible to make a proper meniscus and thus experimentally challenging to expose the same amount of surface area between different experiments. However, it is possible with some practice. Additionally, small differences in exposed area between experiments can be corrected for by surface area normalization, with electrodes prepared in this way having a near identical facet distribution (and thus CV) when the total area is within $\pm 5\%$ (empirically).

References

[1] Vladimir Jović and Borka Jović. Surface reconstruction during the adsorption/desorption of OH species onto Cu(111) and Cu(100) in 0.1 M NaOH solution. *Journal of the Serbian Chemical Society*, 67(7):531–546, 2002.

[2] Kendra P. Kuhl, Etosha R. Cave, David N. Abram, and Thomas F. Jaramillo. New insights into the electrochemical reduction of carbon dioxide on metallic copper surfaces. *Energy & Environmental Science*, 5(5):7050–7059, 2012.

[3] Klaas Jan P. Schouten, Elena Pérez Gallent, and Marc T.M. Koper. The electrochemical characterization of copper single-crystal electrodes in alkaline media. *Journal of Electroanalytical Chemistry*, 699:6–9, 2013.

[4] Alexander S. Bondarenko, Ifan E. L. Stephens, and Ib Chorkendorff. A cell for the controllable thermal treatment and electrochemical characterisation of single crystal alloy electrodes. *Electrochemistry Communications*, 23:33–36, 2012.

[5] Yongchun Fu, Alexander V. Rudnev, Gustav K. H. Wiberg, and Matthias Arenz. Single graphene layer on Pt(111) creates confined electrochemical environment via selective ion transport. *Angewandte Chemie International Edition*, 56(42):12883–12887, 2017.

[6] V. Komanicky, K.C. Chang, A. Menzel, N.M. Markovic, H. You, X. Wang, and D. Myers. Stability and dissolution of platinum surfaces in perchloric acid. *Journal of the Electrochemical Society*, 153(10):B446, 2006.

[7] Ebru Özer, Benjamin Paul, Camillo Spöri, and Peter Strasser. Coupled inductive annealing-electrochemical setup for controlled preparation and characterization of alloy crystal surface electrodes. *Small Methods*, 3(8):1800232, 2019.

[8] Ebru Özer, Camillo Spöri, Tobias Reier, and Peter Strasser. Iridium(111), iridium(110), and ruthenium(0001) single crystals as model catalysts for the oxygen evolution reaction: Insights into the electrochemical oxide formation and electrocatalytic activity. *ChemCatChem*, 9(4):597–603, 2017.

[9] Sebastián Pascual Paula, Petersen Amanda Schramm, Bagger Alexander, Rossmeisl Jan, and Escudero-Escribano María. *pH and Anion Effects on Cu-Phosphate Interfaces for CO Electroreduction*. 2020.

[10] Paula Sebastián-Pascual and María Escudero-Escribano. Addressing the interfacial properties for CO electroreduction on Cu with cyclic voltammetry. *ACS Energy Letters*, 5(1):130–135, 2020.

[11] Albert K. Engstfeld, Thomas Maagaard, Sebastian Horch, Ib Chorkendorff, and Ifan E. L. Stephens. Polycrystalline and single-crystal Cu electrodes: Influence of experimental conditions on the electrochemical properties in alkaline media. *Chemistry – A European Journal*, 24(67):17743–17755, 2018.

[12] Paula Sebastián-Pascual, Francisco J. Sarabia, Víctor Climent, Juan M. Feliu, and María Escudero-Escribano. Elucidating the structure of the Cu-alkaline electrochemical interface with the laser-induced temperature jump method. *The Journal of Physical Chemistry C*, 2020.

[13] Stephanie Nitopi, Erlend Bertheussen, Soren B. Scott, Xinyan Liu, Albert K. Engstfeld, Sebastian Horch, Brian Seger, Ifan E. L. Stephens, Karen Chan, Christopher Hahn, Jens K. Nørskov, Thomas F. Jaramillo, and Ib Chorkendorff. Progress and perspectives of electrochemical CO2 reduction on copper in aqueous electrolyte. *Chemical Reviews*, 119(12):7610–7672, 2019.

[14] S. Trasatti and O. A. Petrii. Real surface area measurements in electrochemistry. *Journal of Electroanalytical Chemistry*, 327(1):353–376, 1992.

[15] Christina W. Li and Matthew W. Kanan. CO2 reduction at low overpotential on Cu electrodes resulting from the reduction of thick Cu2O films. *Journal of the American Chemical Society*, 134(17):7231–7234, 2012.

[16] Dan Ren, Jinhuan Fong, and Boon Siang Yeo. The effects of currents and potentials on the selectivities of copper toward carbon dioxide electroreduction. *Nature Communications*, 9(1):925, 2018.

[17] P. Waszczuk, P. Zelenay, and J. Sobkowski. Surface interaction of benzoic acid with a copper electrode. *Electrochimica Acta*, 40(11):1717–1721, 1995.

[18] M. Łukaszewski, M. Soszko, and A. Czerwiński. Electrochemical methods of real surface area determination of noble metal electrodes–an overview. *Int. J. Electrochem. Sci*, 11:4442–4469, 2016.

[19] V. Climent and Juan M. Feliu. Thirty years of platinum single crystal electrochemistry. *Journal of Solid State Electrochemistry*, 15(7):1297, 2011.

[20] H. Angerstein-Kozlowska, B. E. Conway, A. Hamelin, and L. Stoicoviciu. Elementary steps of electrochemical oxidation of single-crystal planes of Au—I. chemical basis of processes involving geometry of anions and the electrode surfaces. *Electrochimica Acta*, 31(8):1051–1061, 1986.

[21] Enrique Herrero, Lisa J. Buller, and Héctor D. Abruña. Underpotential deposition at single crystal surfaces of Au, Pt, Ag and other materials. *Chemical Reviews*, 101(7):1897–1930, 2001.

[22] S. M. Abd el Haleem and Badr G. Ateya. Cyclic voltammetry of copper in sodium hydroxide solutions. *Journal of Electroanalytical Chemistry and Interfacial Electrochemistry*, 117(2):309–319, 1981.

[23] Aarti Tiwari, Hendrik H. Heenen, Anton Simon Bjørnlund, Thomas Maagaard, EunAe Cho, Ib Chorkendorff, Henrik H. Kristoffersen, Karen Chan, and Sebastian Horch. Fingerprint voltammograms of copper single crystals under alkaline conditions: A fundamental mechanistic analysis. *Journal of Physical Chemistry Letters*, 11(4):1450–1455, 2020.

[24] Rosa M. Arán-Ais, Fabian Scholten, Sebastian Kunze, Rubén Rizo, and Beatriz Roldan Cuenya. The role of in situ generated morphological motifs and Cu(i) species in C2+ product selectivity during CO2 pulsed electroreduction. *Nature Energy*, 5(4):317–325, 2020.

[25] Anastasia A. Permyakova, Juan Herranz, Mario El Kazzi, Justus S. Diercks, Mauro Povia, Léa Rose Mangani, Michael Horisberger, Alexandra Pătru, and Thomas J. Schmidt. On the oxidation state of Cu2O upon electrochemical CO2 reduction: An XPS study. *ChemPhysChem*, 20(22):3120–3127, 2019.

[26] Youngkook Kwon, Yanwei Lum, Ezra L. Clark, Joel W. Ager, and Alexis T. Bell. CO2 electroreduction with enhanced ethylene and ethanol selectivity by nanostructuring polycrystalline copper. *ChemElectroChem*, 2016.

[27] David Reyter, Marek Odziemkowski, Daniel Bélanger, and Lionel Roué. Electrochemically activated copper electrodes: surface characterization, electrochemical behavior, and properties for the electroreduction of nitrate. *Journal of the Electrochemical Society*, 154(8):K36, 2007.

[28] Alisson H. M. da Silva, Stefan J. Raaijman, Cássia S. Santana, José M. Assaf, Janaina F. Gomes, and Marc T. M. Koper. Electrocatalytic CO2 reduction to C2+ products on Cu and CuxZny electrodes: Effects of chemical composition and surface morphology. *Journal of Electroanalytical Chemistry*, 880:114750, 2021.

[29] Erlend Bertheussen, Arnau Verdaguer-Casadevall, Davide Ravasio, Joseph H. Montoya, Daniel B. Trimarco, Claudie Roy, Sebastian Meier, Jürgen Wendland, Jens K. Nørskov, Ifan E. L. Stephens, and Ib Chorkendorff. Acetaldehyde as an intermediate in the electroreduction of carbon monoxide to ethanol on oxide-derived copper. *Angewandte Chemie International Edition*, 55(4):1450–1454, 2016.

[30] William M. Haynes, David R. Lide, and Thomas J. Bruno. *CRC handbook of chemistry and physics : a ready-reference book of chemical and physical data*. 97 edition, 2017.

[31] Florian D. Speck and Serhiy Cherevko. Electrochemical copper dissolution: A benchmark for stable CO2 reduction on copper electrocatalysts. *Electrochemistry Communications*, 115:106739, 2020.

D

Supporting information for Chapter 5: Morphological stability of copper surfaces under reducing conditions

D.1. Blank reproducibility spherical single crystal

The effectiveness of surface recovery via H_2/ O_2 annealing near the melting point of a copper spherical single crystal after having been oxidized at $+0.70\ V$ for $1\ minute$ is depicted in Figure D.1. In black, the blank as obtained prior to surface oxidation is depicted, and in red the blank obtained after recovering the surface via annealing after it had been oxidized. Comparison of the two blank CVs shows that facet distribution is very similar, although the red line exhibits a larger density of $\{111\}$ terrace sites as evidenced by increased charge near $+0.1\ V$ (OH-adsorption) and also near $+0.45\ V$ (O-adsorption).

D.2. Anisotropy of halide-induced roughening

Proof of the anisotropic nature of oxidation and reduction of copper in halide-containing solution is provided in Figure D.2, where a SEM image depicting the overall surface of a spherical single crystal post-treatment is provided. Various distinct regions are present on the surface, with their periodicity matching that of the three basal planes in an FCC lattice.

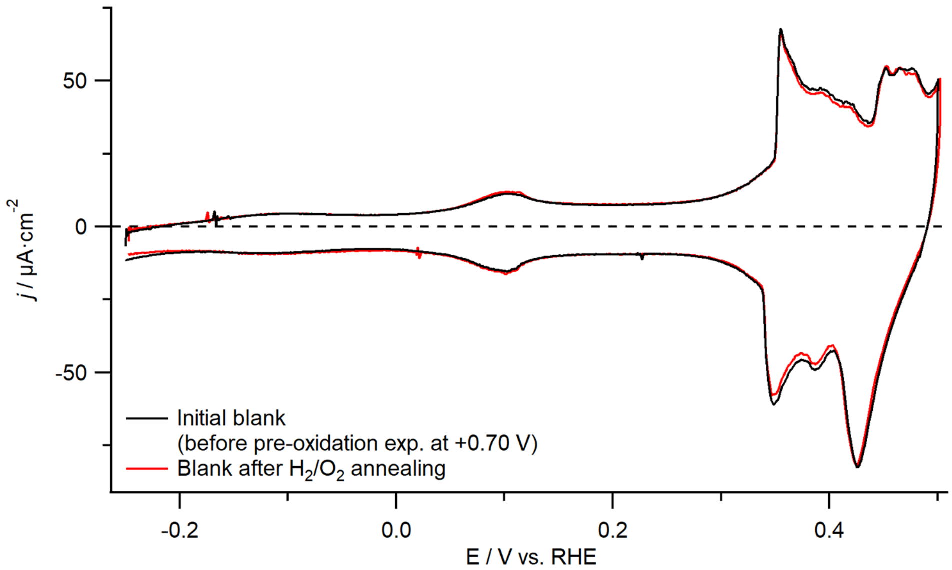

Figure D.1: Blank CV ($0.1\ M$ NaOH, $\nu = 50\ mV \cdots^{-1}$) reproducibility after a pre-oxidation + cathodization experiment ($+0.70\ V / -1.75\ V$, $1\ min$ each) after the crystal was annealed in a H_2 / O_2 flame close to the melting point for $30\ minutes$.

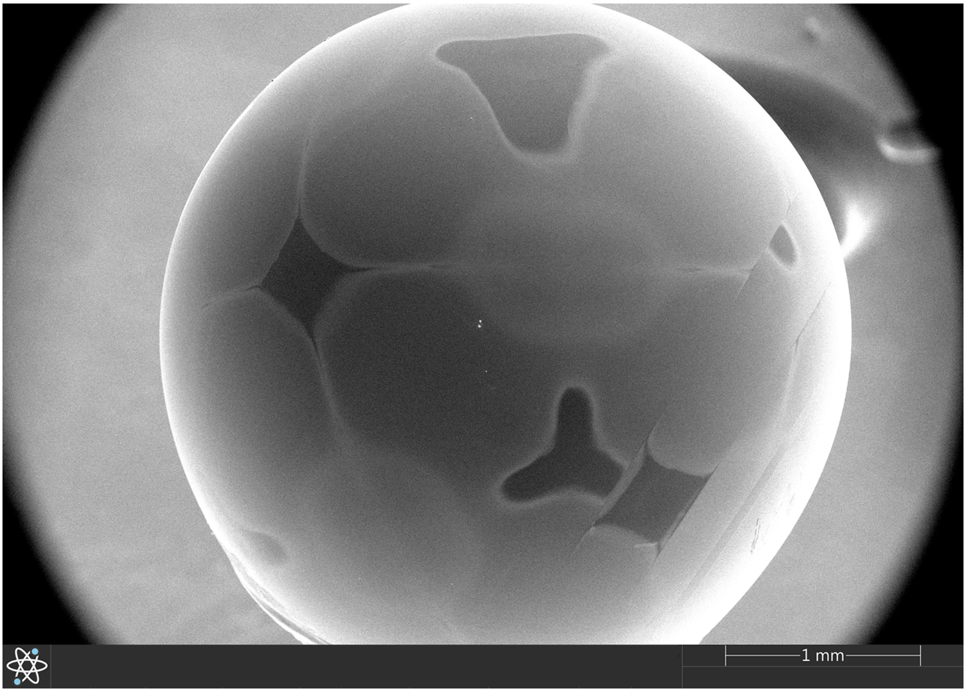

Figure D.2: Blank CV ($0.1\ M$ NaOH, $\nu = 50\ mV \cdots^{-1}$) development for a polycrystalline copper electrode as a function of reaction time during CO2RR at $-0.75\ V$ in $0.1\ M$ $KHCO_3$ electrolyte under continuous CO_2 bubbling. Voltammograms obtained after $1, 5, 15$ and $30\ minutes$ are compared to the initially obtained blank CV in red, green, blue, purple and black, respectively.

D.3. CV evolution after CO2RR in 0.1 M $KHCO_3$

The evolution of the cyclic voltammogram of a copper surface after being subjected to CO2RR at -0.75 V in 0.1 M $KHCO_3$ for varying amounts of time is depicted in Figure D.3. Clear changes are observed as reaction time is increased, indicated by the arrows in the figure. These changes correspond well with voltammetric changes observed after applying reducing conditions in both 0.5 M $KHCO_3$ and 10 M NaOH (main text).

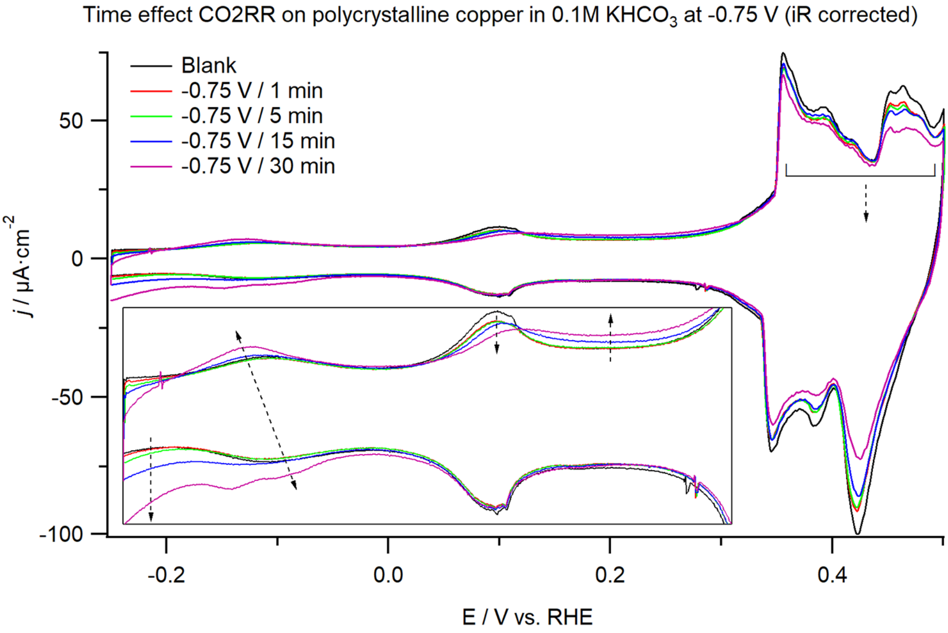

Figure D.3: Surface of a copper spherical single crystal upon anisotropic oxidation and reduction in chloride containing electrolyte (with a grain boundary visible as a result of imperfect crystal growth).

D.4. CV evolution for CORR in 10 M NaOH

Cyclic voltammetry studies were also used to investigate the effect of adding CO during cathodization in 10 M NaOH electrolyte. Furthermore, to guarantee that actual reduction of CO would occur, the applied potential was lowered from -1.75 V to both -0.75 V (Figure D.4) and -0.40 V (Figure D.5). The former potential (-0.75 V) was chosen as it is equal to the potential we used for our CO2RR studies, whereas the latter (-0.40 V) was chosen to see if the presence of CORR intermediates plays a significant role considering that -0.40 V is close to the onset of the CORR in alkaline media meaning its rate of reduction is much decreased. The changes in voltammetry are virtually identical to what is observed when we apply -1.75 V in 10 M NaOH without CO present in both cases, though the rate at which the CV changes is somewhat slower in when applying -0.40 V in the presence of CO.

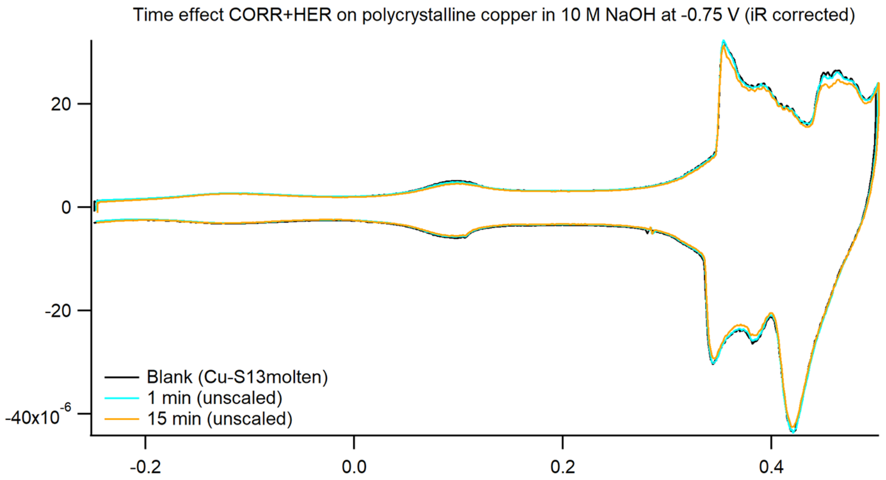

Figure D.4: Blank CV ($0.1\ M$ NaOH, $\nu = 50\ mV \cdots^{-1}$) evolution after conducting CORR experiments in $10\ M$ NaOH electrolyte with active CO bubbling at $-0.75\ V$ for various reaction times.

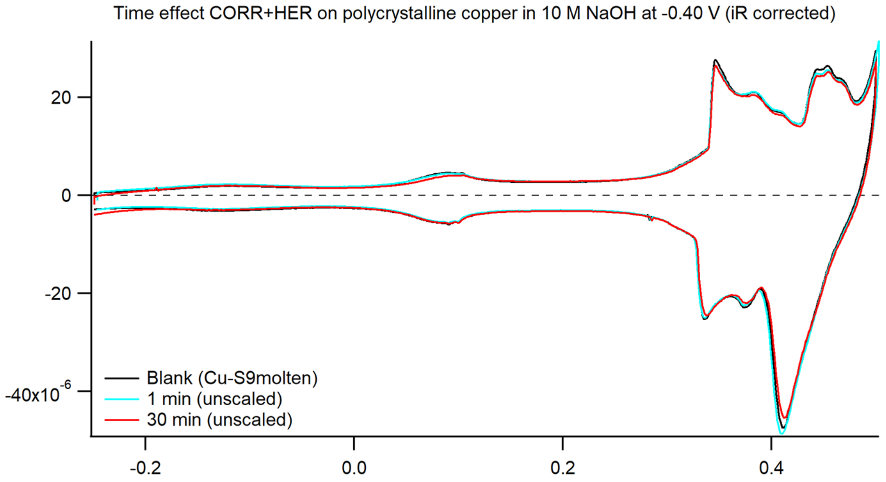

Figure D.5: Blank CV ($0.1\ M$ NaOH, $\nu = 50\ mV \cdots^{-1}$) evolution after conducting CORR experiments in $10\ M$ NaOH electrolyte with active CO bubbling at $-0.40\ V$ for various reaction times.

D.5. Electrode deactivation during CO2RR

Deactivation of the catalytic activity of the roughened spherical single crystal used for SEM studies into the long-term morphological stability of copper under CO2RR conditions ($1\ hour$ at $-0.75\ V$ in $0.5\ M$ $KHCO_3$ electrolyte under constant CO_2 bubbling) is depicted in Figure D.6, in the form of decreasing current response of the system with constant potential.

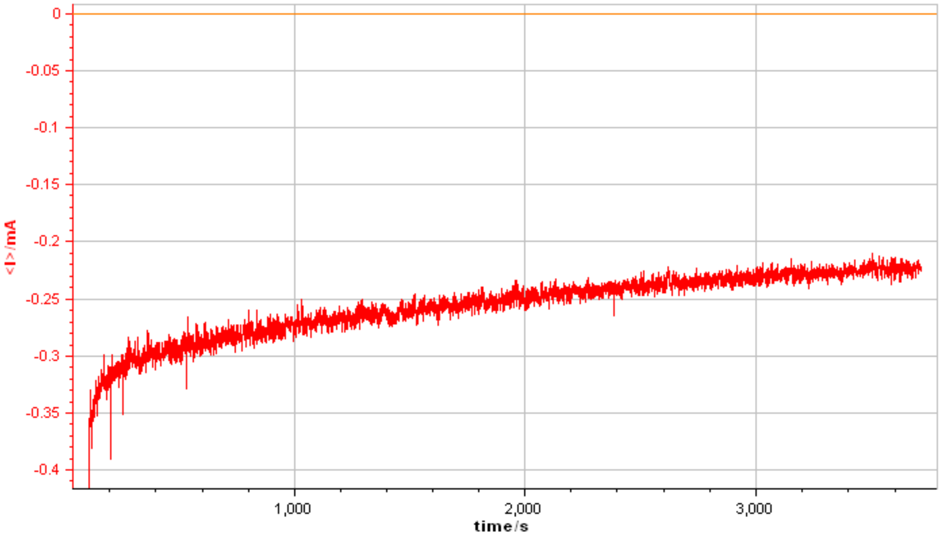

Figure D.6: Time-dependent current deactivation of roughened copper spherical single crystal surface during CO2RR conditions ($-0.75\ V$ in $0.5\ M$ $KHCO_3$ during active CO_2 bubbling).

D.6. Hypothetical morphology-change driven area reduction mechanisms

Assuming that the CV changes discussed in the main text (a decrease in the overall number of active sites, but little change in the relative abundance of the various individual types of sites) are the result of changes in morphology, the following surface restructuring-driven mechanisms can be envisioned.

E.g., one could assume that we start with a rough surface that undergoes considerable restructuring in such a manner that mesoscale and nanoscale deposits change their geometrical shapes towards such geometries that that exhibit lower surface area to volume rations (i.e., spheres). This phenomenon could explain a decrease in overall sites; however, such an explanation is rather unreasonable. Especially when we consider that the electrodes employed in this work are prepared by melting a copper wire into a droplet and allowing it to solidify resulting in a (near) spherical bead which intrinsically has a low roughness factor and low surface area to volume ratio, owing to surface-tension directed surface energy minimization effects.

Another theory that might explain a decrease in area would be to (literally) shrink the electrode radius, and thus decreasing the geometric surface area, via copper dissolution. This explanation is equally unreasonable as the former, considering the large amount of dissolution that would be required. Also, dissolution has been reported to be absent at the negative potentials we employ.[1]

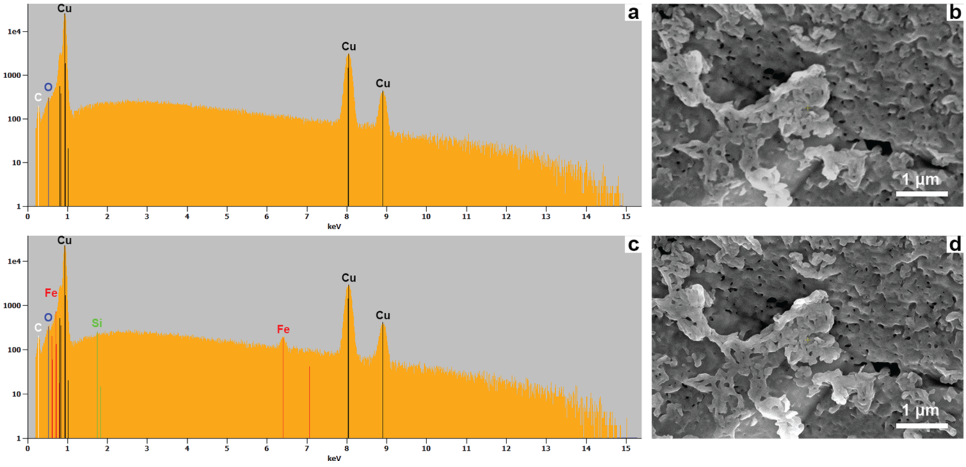

Figure D.7: Surface morphology and elemental analysis results before and after ca. $5\ hours$ of CO2RR at $-0.75\ V$ in saturated $KHCO_3$ solution under constant CO_2 (g) purging for a different location than discussed in the main text with different mesoscopic morphology on a nitric acid-cleaned polycrystalline bead electrode. Panels a and c represent the EDX spectrum a) prior to and c) after CO2RR, whilst b) and d) represent the accompanying SEM micrographs, respectively.

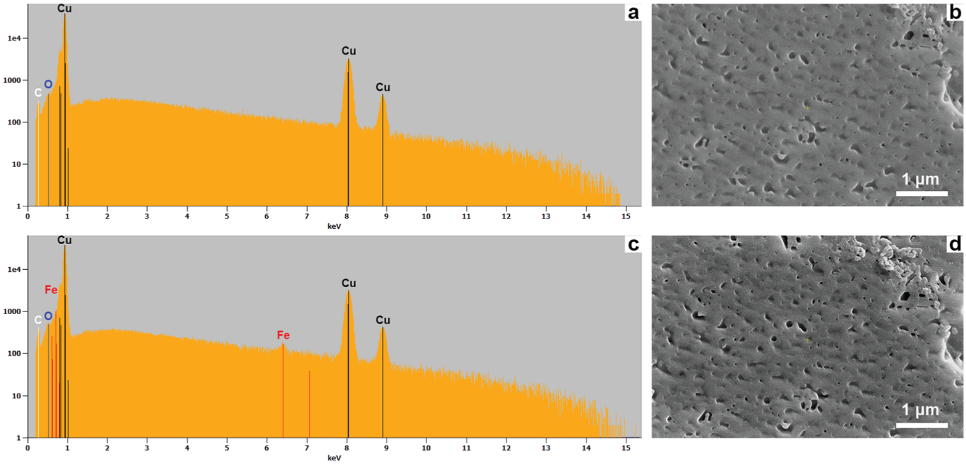

Figure D.8: Equal conditions as Figure D.7, but for a different location on the crystal. Panels a and c represent the EDX spectrum a) prior to and c) after CO2RR, whilst b) and d) represent the accompanying SEM micrographs, respectively.

D.7. EDX study of electrode fouling

Identical-location SEM + EDX experiments were conducted for multiple locations on a nitric acid-cleaned polycrystalline surface as discussed in the main text. Proof that the same observations discussed there hold also for other locations on the crystal is provided in the form of SEM micrographs before and after CO2RR ($-0.75\ V$ in saturated $KHCO_3$ for ca. $5\ hours$) with accompanying EDX signals for two other locations on the crystals in Figures D.7 and D.8.

References

[1] Florian D. Speck and Serhiy Cherevko. Electrochemical copper dissolution: A benchmark for stable CO2 reduction on copper electrocatalysts. *Electrochemistry Communications*, 115:106739, 2020.

Curriculum Vitæ

Stefan was born February 25th, 1991 in Helmond, the Netherlands. After finishing high school, he started a bachelor in chemistry, attending a joint offering by Leiden University and the Delft University of Technology. Choosing to major in courses falling in the domain of expertise of Leiden University and joining the electrochemical laboratory led by prof.dr. Koper for writing his bachelor thesis, he obtained his BSc from Leiden University in 2013. From the same university, after finishing a master thesis based on research conducted in the same laboratory, he obtained his MSc in 2016. Accumulatively, the research conducted during this period resulted in three separate publications.

The culmination of experiences resulted in the opportunity to pursue a PhD in electrochemistry, regarding the (influence of process conditions on the) electroreduction of carbon dioxide, starting 2017. This position was jointly funded by the Dutch Research Council (NWO), the Netherlands Organisation for applied scientific research (TNO) and Shell Global Solutions B.V. The first two years were spent on investigations into cation effects during the electroreduction of CO_2 by metallic copper, including method development of systems to interface gas chromatography and electrochemistry, together with some time allocated to completing teaching duties both as a TA for classes and short-term daily supervision of various (guest) interns. The results of the third through fifth years resulted in the chapters that form the basis of this thesis. Some of the results have been presented at various national and international conferences in the form of posters, with chapters 2 to 5 having been published.

Lastly, during his PhD he also employed vocational schooling as a means of broadening his knowledge by attending the following courses: 'Catalysis: an integrated approach' (2017), 'SurfCat Summer School - The science of sustainable fuels and chemicals' (2018) and 'Photo- and ElectroCatalysis at the Atomic Scale' (2019).

List of Publications

Chapter 2 is based on
Raaijman, S. J., Schellekens, M. P., Corbett, P. J., & Koper, M. T.M. High-Pressure CO Electroreduction at Silver Produces Ethanol and Propanol. *Angew. Chem. Int. Ed.* **2021**, *60* (40), 21732-21736.

Chapter 3 is based on
Raaijman, S. J.[=], Arulmozhi, N.[=], & Koper, M.T.M. Anisotropic Cathodic Corrosion of Gold Electrodes in the Absence and Presence of Carbon Monoxide. *J. Phys. Chem. C.* **2020**, *124* (52), 28539-28554.

Chapter 4 is based on
Raaijman, S. J., Arulmozhi, N., A.H.M da Silva, & Koper, M.T.M. Clean and Reproducible Voltammetry of Copper Single Crystals with Prominent Facet Specific Features Using Induction Annealing. *J. Elec. Soc.* **2021**, *168* (9), 096510

Chapter 5 is based on
Raaijman, S.J.[=], Arulmozhi, N.[=] & Koper, M.T.M. Morphological stability of copper surfaces under reducing conditions. *ACS Appl. Mater. Interfaces* **2021**, *13* (41), 48730–48744

[=] *These authors declare equal authorship*

Other publications

da Silva, A. H., Raaijman, S. J., Santana, C. S., Assaf, J. M., Gomes, J. F., & Koper, M.T.M. Electrocatalytic CO2 reduction to C2+ products on Cu and CuxZny electrodes: Effects of chemical composition and surface morphology. *J. Electroanal. Chem.* **2021**, *880*, 114750

Phan, T. H., Banjac, K., Cometto, F. P., Dattila, F., García-Muelas, R., Raaijman, S. J., Ye, C., Koper, M.T.M., López, N. & Lingenfelder, M. (2021). Emergence of Potential-Controlled Cu-Nanocuboids and Graphene-Covered Cu-Nanocuboids under Operando CO2 Electroreduction. *Nano Lett.* **2021**, *21* (5), 2059–2065

Jacobse, L., Raaijman, S. J. & Koper, M. T. M., The reactivity of platinum microelectrodes. *Phys. Chem. Chem. Phys.* **2016**, *18* (41), 28451-28457.

Diaz-Morales, O., Raaijman, S., Kortlever, R., Kooyman, P. J., Wezendonk, T., Gascon, J., Fu, W. T. & Koper, M. T. M., Iridium-based double perovskites for efficient water oxidation in acid media. *Nat. Commun.* **2016**, *7* (1), 12363.

Kwon, Y., Raaijman, S. J., Koper, M. T. M. Role of peroxide in the catalytic activity of gold for oxidation reactions in aqueous media: an electrochemical study. *ChemCatChem* **2014**, *6* (1), 79–81.

Acknowledgements

This thesis is the eventual and definite conclusion to a journey that I (unbeknownst to me at the time) began the 17th of September, 2012: the day I entered the electrochemical lab of professor Marc Koper to start my bachelor internship under the daily supervision of Youngkook Kwon. At the time I had little knowledge of science and its customs, and although I had the luck of encountering an incredible supervisor, I quickly committed my brief experience with electrochemistry to the past, considering it a dead-end road without future prospects as surely a Bachelor's degree would spell the end of my university career.

The future, however, proved me wrong in my thinking. A rather common occurrence in science, really. Two following internships in electrochemistry, under the care of Oscar Diaz-Morales and Leon Jacobse (my luck with great supervision continued), consolidated both my foundation and interest in electrochemistry. In hindsight, it is these people with their unbridled enthusiasm, patience and positive attitude towards doing science, that gave me courage for making up my mind and crossing the final bridge. To this date, my impressions of my supervisors at the time greatly contribute to my ideology of what constitutes a good scientist. And it seems this is a good location for acknowledging this, thank you for doing science as it should be done, and for guiding me on this path.

Perhaps one might wonder why my supervisor is located all the way in the third paragraph. But there is an order to things, and such an order may as well be chronological. Let the acknowledgement be as follows: there is exactly one laboratory in the world, under the supervision of one specific person, that I would ever have dared to consider my chances of being able to successfully complete a PhD to be anything other than 0%. Paired with my (rather) stubborn personality, it is quite a considerable feat that you a) offered someone like me a position, b) convinced me to actually accept the position, c) allowed me to do science the way I believe it should be done and d) somehow still managed to extract sufficient scientific data out of me to convince others into handing me a title. You are, without a doubt, a good boss to have. And I thank you, for having guided me. However, I am personally more grateful for your continued high quality contributions to the scientific community without losing your way, so to speak. You run a good group, are a good person, and contribute to great science!

And when speaking of a running a good group, I personally believe that José Dijkzeul is one of the secret weapons to keep things operational. I thank you, for all the things you do daily that I know about, and for the many more things that you do that I do not know about. Similarly to Marc, you go above and beyond. And although I may not agree a person should be expected to continually go the extra mile, as so often is, I do fully believe you deserve to be acknowledged for your contribution to the machinery that keeps scientists doing what they (presumably) do best: science.

The last section I shall keep generic, as who we are is influenced by everything and everyone near to us, in heart and mind or simply in time and space. And who we are, impacts what we do. It is a futile effort to try and quantify such things and therefore I've decided the fairest way is to average it out. Firstly, I shall thank all of my collaborators who have been working together with me, and for this exact reason have already been named as co-authors on the publications that also carry my name. Secondly (and lastly), I'd like to thank family, friends and colleagues (former and current) for being there along the way and making time for coffee, beers, conversations and help, and the occasional bout of shenanigans.